Herausgeber

Tom Lahmer Timon Rabczuk Carsten Könke

ISM-Bericht 1/2014 ISSN: 1610-7381

Institut für Strukturmechanik

Fakultät Bauingenieurwesen

Bauhaus-Universität Weimar

Marienstraße 15

D-99423 Weimar

Germany

Tel. +49 (0)3643/584504

Fax. +49(0)3643/584514

http://www.uni-weimar.de/Bauing/ism

Multiscale modeling of nanodevices based on carbon nanotubes and polymers

Multiskalige Modellierung von auf Kohlenstoffnanoröhren und Polymeren basierenden Nanobauteilen

DISSERTATION

Zur Erlangung des akademischen Grades

Doktor-Ingenieur

an der Fakultät Bauingenieurwesen

der Bauhaus-Universität Weimar

vorgelegt von

Dipl.-Ing. Junhua Zhao

Geboren am 21 April 1979 in China

Weimar, April 2013

Gutachter: Prof. Dr-Ing. Timon Rabczuk

Prof. Dr-Ing. Carsten Könke

Prof. Dr-Ing. Zhiliang Zhang

Tag der Disputation: 06 Januar 2014

ACKNOWLEDGEMENTS

I could not believe that I have the chance to do my second Ph.D in Germany yet since the Ph.D degree from Germany is my dream and very important for me. I am grateful to Prof. Rabczuk and the academic committee of Bauhaus-University Weimar who both support me to do my second Ph.D. In the process of my second Ph.D, many people gave me a lot of help in different ways. I would like to acknowledge them for their contributions.

First I would like to thank my supervisor Prof. Timon Rabczuk for his continuous inspiration, good concern and insightful comments. His efficient work gives me deep impression. Both his enthusiasm of scientific research and his open mind are highly appreciated.

I want to thank our secretaries Mrs. Marlies Terber, Mrs. Rosemarie Mayer give me a lot of help in the process.

I would like to thank Prof. Carsten Könke give me much help in my research. I would like to thank Dr. Tom Lahmer help me translate the abstract and title of the thesis.

I would also like to thank my first Ph.D (and Master) supervisor Prof. Wanlin Guo at Nanjing University of Aeronautics and Astrautics (NUAA), China. He always encourage me when I feel lose. He always gives me a lot of important suggestions based on his strong background in nanomechanics and solid mechanics. I want to thank Prof. Lifeng Wang at NUAA give me a lot of help and suggestions in my research.

I would like to thank my postdoc supervisor Prof. Zhiliang Zhang at Norwegian University of Science and Technology (NTNU), Norway. He invited me to NTNU study polymers in 2008 when I finished my first Ph.D. I learned a lot of knowledge at NTNU in two and half years. I would like to thank Dr. Shijo Nagao, Dr. Jianyang Wu, Dr. Jianying He, Dr. Xiaobo Ren, Dr. Junyan Liu at NTNU for their different help.

I would also like to thank Dr. Jin-Wu Jiang in our group. I always learn some knowledge from him when we discuss some issues together. His deeply physical background gives me a lot of help. I would like to thank Dr. Yancheng Zhang, M.S Yue Jia and Dr. Ning Wei give me much help in my research. I want to thank M.S Chao Zhang, M.S Cuixia Wang for their good concern.

In particular, I want to thank Dr. Pattabhi Budarapu give me much help and I will never forget our family's friendship.

I want to thank Dr. Cosmin Anitescu, Dr. Volkmar Zabel, Dr. Daniel Amold, Dr. Hossein Asadi, Dr. Michael Schwedler, Dr. Mohammad Silani, Dr. Hossein Talebi, Dr. Vu Bac Nam, Dr. Nhon Nguyen-Thanh and Dr. Lu for their different help in our group.

Deepest love is due to my beloved family. I am grateful to my Dad and Brothers. They always encourage and support me at any time. Most importantly, I heartily appreciate my wife. Without her support and encouragement, my thesis would have been never accomplished. My dear wife and little son are always the sweetest part of my heart.

ABSTRACT

This thesis concerns the physical and mechanical interactions on carbon nanotubes and polymers by multiscale modeling.

CNTs have attracted considerable interests in view of their unique mechanical, electronic, thermal, optical and structural properties, which enable them to have many potential applications. Carbon nanotube exists in several structure forms, from individual single-walled carbon nanotubes (SWCNTs) and multi-walled carbon nanotubes (MWCNTs) to carbon nanotube bundles and networks. The mechanical properties of SWCNTs and MWCNTs have been extensively studied by continuum modeling and molecular dynamics (MD) simulations in the past decade since the properties could be important in the CNT-based devices. CNT bundles and networks feature outstanding mechanical performance and hierarchical structures and network topologies, which have been taken as a potential saving-energy material. In the synthesis of nanocomposites, the formation of the CNT bundles and networks is a challenge to remain in understanding how to measure and predict the properties of such large systems. Therefore, a mesoscale method such as a coarse-grained (CG) method should be developed to study the nanomechanical characterization of CNT bundles and networks formation.

In this thesis, the main contributions can be written as follows: (1) Explicit solutions for the cohesive energy between carbon nanotubes, graphene and substrates are obtained through continuum modeling of the van der Waals interaction between them. (2) The CG potentials of SWCNTs are established by a molecular mechanics model. (3) The binding energy between two parallel and crossing SWCNTs and MWCNTs is obtained by continuum modeling of the van der Waals interaction between them.

Crystalline and amorphous polymers are increasingly used in modern industry as structural materials due to its important mechanical and physical properties. For crystalline polyethylene (PE), despite its importance and the studies of available MD simulations and continuum models, the link between molecular and continuum descriptions of its mechanical properties is still not well established. For amorphous polymers, the chain length and temperature effect on their elastic and elastic-plastic properties has been reported based on the united-atom (UA) and CG

MD simulations in our previous work. However, the effect of the CL and temperature on the failure behavior is not understood well yet. Especially, the failure behavior under shear has been scarcely reported in previous work. Therefore, understanding the molecular origins of macroscopic fracture behavior such as fracture energy is a fundamental scientific challenge.

In this thesis, the main contributions can be written as follows: (1) An analytical molecular mechanics model is developed to obtain the size-dependent elastic properties of crystalline PE. (2) We show that the two molecular mechanics models, the stick-spiral and the beam models, predict considerably different mechanical properties of materials based on energy equivalence. The difference between the two models is independent of the materials. (3) The tensile and shear failure behavior dependence on chain length and temperature in amorphous polymers are scrutinized using molecular dynamics simulations.

Finally, the influence of polymer wrapped two neighbouring SWNTs' dispersion on their load transfer is investigated by molecular dynamics (MD) simulations, in which the SWNTs' position, the polymer chain length and the temperature on the interaction force is systematically studied.

Kurzfassung

Die vorliegende Doktorarbeit beschäftigt sich mit den physikalischen und mechanischen Zusammenhängen von Kohlenstoffnanoröhren (CNT = carbon nanotube) und Polymeren mittels Multiskalenmodellierung. CNTs haben durch ihre einzigartigen mechanischen, elektrischen, thermischen, optischen Eigenschaften erhebliches Interesse auf sich gezogen. Ihre besonderen Eigenschaften ermöglichen viele potentielle Einsatzgebiete.

CNT kommtin vielen strukturellen Variationen vor, von der einwandigen CNT (SWCNT = single-walled carbon nanotube) über die mehrwandige CNT (MWCNT = multi-walled carbon nanotube) bis zur CNT-bündeln und -netzwerken. Die mechanischen Eigenschaften von SWCNTs und MWCNTs wurden bereits im letzten Jahrzehnt weitgehend durch Kontinuumsmodelle und Molekueldynamik (MD) Simulation untersucht. CNT-Bündel und -netzwerke weisen hervorragende mechanische Leistungen, hierarchische Strukturen und Netzwerktopologien auf. Diese Strukturen könnten als potentielle energiesparende Materialen eingesetzt.

Bei der Darstellung von Nanoverbunden bleibt die Anordnung von CNT-Bündeln und -netzwerken eine Herausforderung. Diese ist aber wichtig, um zu verstehen wie die Eigenschaften eines solch großen Systems gemessen und vorhergesagt werden können. Daher ist eine Mesoskalen-Methode some einer Grobkornmethode (CG) zu entwickelt, um die nanomechanischen Eigenschafter von CNT-Bündeln und -netzwerken zu untersuchen.

Diese Doktorarbeit liefer Beitrag zur Lösung folgendes Punkte:

(1) Explizite Lösungen für die kohäsive Energie zwischen Kohlenstoffanoröhrchen, Graphit und Schichtträger werden durch Kontinuumsmodelle der van-der-Waals-Kräfte gefunden.

(2) Das Potential zur grobkörnigen Darstellung von SWCNTs wird durch molekular-mechanische Modelle nachgewiesen.

(3) Die bindenden Energien zwischen zwei parallelen und kreuzenden SWCNTs und MWCNTs wird durch Kontinuumsmodellerierung der van-der-Waals-Kräfte zwischen ihnen festgestellt.

Kristalline und amorphe Polymere werden wegen ihrer wichtigen mechanischen und physischen Eigenschaften zunehmend in moderner Industrie als Baumaterial eingesetzt.

Für kristalline Polyethylene (PE) ist, trotz ihrer großen Bedeutung und numerischer Modellierung und Simulationen, die Verbindung zwischen molekularer und kontinuierlicher Beschreibung der mechanischen Eigenschaften noch nicht ausreichend bekannt. Für amorphe Polymere wurde der Effekt von Temperatur und Kettenlänge auf ihre elastischen und elastisch-plastischen Eigenschaften untersucht. Die Ergebnisse basieren auf der "united-atom Simulation", some Grobkorn- und MD-Simulation.

Allerdings konnten die Effekte der Kettenlänge und Temperatur auf das Bruchrverhalten noch nicht nachvollzogen warden, insbesondere unter Schubspannung. Daher ist das Verständis des molekularen Ursprungs von makroskopischem Bruchverhalten wie Bruchenergie eine fundamentale wissenschaftliche Herausforderung.

In dieser Thesis soll der Hauptbeitrag aus folgenden Punktesbestehen:

(1) Ein analytisches molekular-mechanisches Modell soll entwickelt werden, um die größenabhängigen elastischen Eigenschaften von kristallinem Polyethylen zu bestimmen.

(2) Es wird gegeigt, dass die zwei molekular-mechanischen Modelle, das "stick-spiral model" und das "beam model", stark unterschiedliche mechanische Eigenschaften der Materialien basierend auf Energiegleichstellung vorhersagen. Der Unterschied zwischen den zwei Modellen ist unabhängig vom Material.

(3) Das Fehlerverhalten unter Zug- und Schubspannung, welche abhängig von der Kettenlänge und der Temperatur von amorphen Polymeren ist, werden durch MD-Simulation eingehend geprüft.

Letztendlich wird der Einfluss von Polymeren eingewickelt in die Streuung zweier benachbarte SWNTs in ihrer Lastverlagerung durch MD Simulation analysiert, in welcher die Position der SWNTs, die Kettenlänge der Polymere und die Temperatur der Einflusskraft systematisch untersucht wird.

Contents

List of Figures

List of Tables

Chapter 1

Introduction

1.1 Background

Carbon nanotubes (CNTs) have been proposed as ideal candidates for multifarious applications including super-strong materials and nanomechanical devices due to their unique mechanical, electrical, thermal, and optical properties (Baughman et al., 2002). A fundamental understanding of their properties is thus significant to ensure the optimum performance of CNTs in potential applications. In particular, a thorough understanding of their mechanical properties is essential in designing manufacturing processes or to ensure reliability during operation of devices. The mechanical properties of CNTs have been extensively studied by continuum modeling and atomistic simulations in the past decade (Odergard et al., 2002; Zhang et al., 2002; Chang and Gao, 2003; Li and Guo, 2008) since the properties could be important in the CNT-based devices. Atomistic-based methods such as classical molecular dynamics (MD) (Iijima et al., 1996; Yakobson et al., 1996), tight-binding MD (Hernandez et al., 1998; Zhao et al., 2009), and density functional theory (Sanchez-Portal et al., 1999; Zhang et al., 2007) have been used to study the mechanical properties of CNTs. However, compared with bottom-up approaches, top-down approaches may substantially reduce the computational costs and are thus frequently used in related investigations. By equating the molecular potential energy of nano-materials to the mechanical strain energy of a representative continuum model, Odergard et al. (2002) obtained a relation between effective bending rigidity and molecular properties of a grapheme sheet. Chang and Gao (2003) established an analytical stick-spiral model (SSM) based on molecular mechanics method and for the first time derived closed-form expressions for the elastic properties of different SWCNTs. An improved model by Jiang and Guo (2011) was used to investigate the elastic properties of single-walled boron nitride nanotubes. Li and Chou (2003, 2004) presented a beam model for carbon-carbon bonds based on the molecular mechanics.

Considering the important influence of the van der Waals (vdW) interaction, Ru (2000; 2001) proposed a continuum shell model to study the buckling of double-walled CNTs. Wang et al. (2004) extended Ru's vdW model to capture the buckling characteristics of the multi-walled

CNTs. The applicability and limitations of the shell models were also discussed. Shen (2004) presented a traditional cylindrical shell model for the post-buckling of a double-walled CNT using Ru's vdW interaction model. He et al. (2005) developed a new vdW interaction model for not only the post-buckling pressure but also the pre-buckling pressure between any two layers of multi-walled CNTs, where the influence of interlayer spacing and the tube radius on the pressures were also considered. Chang (2010) developed an anisotropic shell model to investigate mechanical behavior of single-walled CNTs, in which the model can be used to effectively describe the chirality effect on mechanical properties.

Recently, the cohesive properties between double CNTs, multi-CNTs and CNT/polymer matrix have been studied systematically (Jiang et al., 2006; Lu et al., 2008). However, the above mentioned studies mainly concerned on the crucial effect of the vdW interactions on the elastic properties of the multi-walled CNTs, CNT/polymer and the crystalline PE. The crossing CNTs, CNT/graphene, and CNT/substrate are widely used in CNTs electronic devices. For instance, Fig.1.1 shows a schematic structure in the experiments (Geblinger et al., 2008; Koening et al., 2011; Wang et al., 2007). Therefore, the surface vdW forces play a key role on the mechanical behavior of the crossing CNTs, CNT/graphene and CNT/substrate (Koening et al., 2011; Wang et al., 2007). A clear understanding of the vdW interactions in these systems is crucial for their potential applications in the nanoelectromechanical systems and electronic devices.

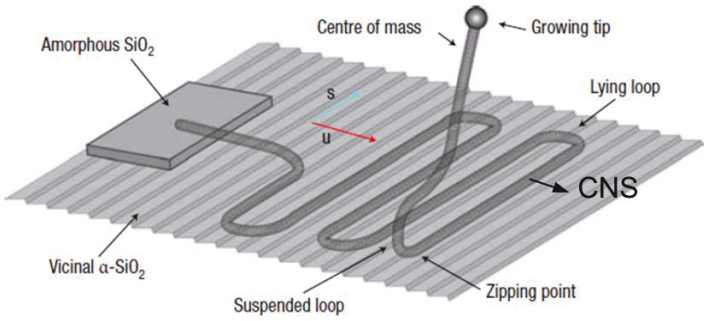

Fig. 1.1 Schematic diagram of the carbon nanotube serpentine (CNS) on a stepped substrate (Geblinger et al., 2008).

Furthermore, CNTs networks feature outstanding mechanical performance and hierarchical structures and network topologies, which have been taken as a potential saving-energy material (Xie et al., 2011). In the synthesis of nanocomposites, the formation of the CNTs bundles is a

challenge to remain in understanding how to measure and predict the properties of such large systems (Ajayan and Banhart, 2002; Kis et al., 2004). On the other hand, the dispersion of CNTs within the matrices and their interfaces are of critical importance to establish efficient load-bearing performance for large-scale applications (Cranford et al., 2010). However, this problem has not been solve satisfactorily yet. Zhigilei et al. (2005) developed a mesoscopic model of individual SWCNTs by full atom MD simulations with MFF potentials. The stretching, bending and torsion CG potentials of different SWCNTs were reported, while the non-bonded CG potentials were not considered in this work. Buehler and his group developed a mesoscale model to study the nanomechanical characterization of CNT buckypaper and bundle formation (Buehler, 2006; Cranford and Buehler, 2010; Cranford et al., 2010). Xu's group (Xie et al., 2011; Wang et al., 2012) and Li and Kröger (2012) detailed studied the mechanical properties of the two-dimensional and three-dimensional CNT networks based on the mesocale model. However, the potentials of one kind of single-walled CNT (SWCNT) (5,5) were only reported and the torsion potentials were neglected in these work, and the non-bonded potential of between the two same CG beads of (5,5) CNTs were only provided based on the full atom MD results (Buehler, 2006). Actually, the two parameters of their LJ potentials are obtained by fitting the adhesion energy at the equilibrium distance between two CNTs, and the results are only effective under small deformation by comparison with full atom MD and the CG MD simulations. These reasons lead to the limitations for further studying other kind of SWCNTs since many different SWCNTs should be often occurred under large deformation in the practical applications.

Therefore, it is significant to establish the coarse-grained (CG) potentials for different SWCNTs. At the nanoscale, the weak van der Waals interactions govern the structural organization and the mechanical properties of CNT bundles and networks (Cranford et al., 2010; Ru, 2001; Zhou et al., 2007). The interactions of individual CNTs in larger-scale structures often play a critical role in the mechanical characterization of CNT systems. How to provide accurate CG non-bonded potentials between two same CG beads (especially between two different CG beads) should be a critical issue so that the reliable results can be obtained from the CG MD simulations.

Crystalline and amorphous polymers are two of the most fundamental polymers molecular shapes that have widely been investigated by many researchers due to the important physical and chemical properties (Boyd et al., 1994; Pant et al., 1993; Zhang and Müller-Plathe, 2006). For crystalline polyethylene (PE), despite its importance and the studies of available MD simulations and continuum models (Karasawa et al., 1991; Zhao et al., 2010a; Nikolov et al., 2002), the link between molecular and continuum descriptions of its mechanical properties is still not well established. For amorphous polymers, Glass forming polymers ($T<T_g$, Tg is the glass-transition temperature) are of great industrial importance and scientific interest. Their unique mechanical properties arise from the connectivity and random-walk-like structure of the constituent chains (Shepherd, 2006). At very small strains, the response is elastic. At slightly larger strains, yielding occurs when intermolecular barriers to segmental rearrangements are overcome. Following yield, the material may exhibit strain softening, a reduction in stress to a level corresponding to plastic flow. At higher strains, the stress increases as the chain molecules orient, in a process known as strain hardening. Strain hardening suppresses strain localization (crazing, necking, shear banding) and is critical in determining material properties such as toughness and wear resistance (Hoy and Robbins, 2007; Hoy and Robbins, 2008). In the other hand, the yield point of the polymers disappears after $T>T_g$. In both amorphous and crystalline polymers, the fracture energy depends on processes that range from breaking of atomic bonds to formation of defect structures on micron and large scales (Hoy and Robbins, 2007; Hoy and Robbins, 2008). At atomic scale, the all-atoms (AA) and united-atom (UA) MD methods have been employed to simulate the mechanical performance of polymers, in which AA method means the full-atomic including interactions among all C atoms and H atoms (see Fig. 1.2), while UA method means that we treat the CH_3- or CH_2- as one UA bead. To reduce computational burdens, a CG MD method has also been developed to investigate fracture and craze of polymers. For example, the terminal (T) bead and middle (M) one of a linear polyethylene molecular chain represent CH_3-CH_2-CH_2-, and -CH_2-CH_2-CH_2-, respectively (see Fig. 1.2c and d). Recently, we have found that the chain length (CL) and temperature have a large effect on the thermomechanical properties of linear polymers (Zhao et al., 2010a; Zhao et al., 2010b; Zhao et al., 2013) based on UA and CG MD simulations.

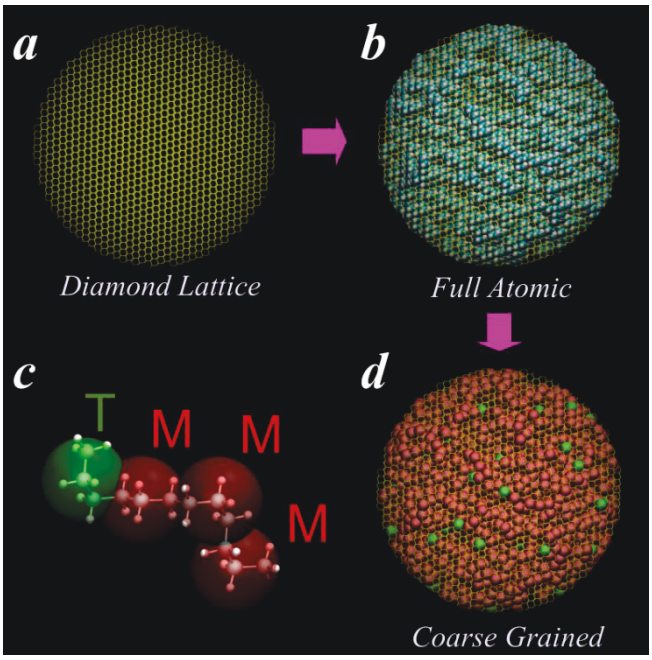

Fig. 1.2 Corase-grained (CG) molecular modelling of polyehylene nano-particles by semi-crystalline lattice method, in which the case of 200 carbon chains with constant chain length of 60 CG beads are packed into a 8nm diametric particle (The work has been done by us and was not published yet). (a) The template diamond lattice; (b) Full-atomic model generated by random walk process on the lattice; (c) CG model with terminal (T) and non-terminal middle (M) beads; (d) Final CG model obtained.

Since the UA and CG potentials limitations, the effect of the CL and temperature on the failure behavior is not understood well yet. Especially, the failure behavior under shear has been scarcely reported in previous work (See Fig. 1.2). Therefore, understanding the molecular origins of macroscopic fracture behavior such as fracture energy is a fundamental scientific challenge (Hoy and Robbins, 2007).

1.2 Objectives

This thesis is dedicated to develop a multiscale method to accurately describe the cohesive properties of CNTs and the mechanical properties of crystalline and amorphous polymers, in which the link between molecular and continuum descriptions of the properties is established well. The interrelated objectives are included as follows:

(1) Develop a molecular mechanics model to accurately describe the cohesive energy between CNTs, graphene and substrates.

(2) Determine the CG potentials of SWCNTs based on our analytical results of cohesive energy between two SWCNTs and the two stick-spiral and beam models.
(3) Establish an analytical solution of the critical length for the mechanical stability and adhesion between two SWCNTs (and MWCNTs).
(4) Develop an analytical molecular mechanics model to describe the size-dependent elastic properties of crystalline PE.
(5) Reveal the difference between the two molecular mechanics models, the stick-spiral and the beam models, in predicting the mechanical properties of materials based on energy equivalence.
(6) Propose the fracture mechanism of amorphous polymer for different chain length and temperature under uniaxial tension and shear.
(7) Reveal the effect of polymer wrapped two neighbouring SWNTs' dispersion on their load transfer.

1.3 Outline

The thesis contains nine chapters. The introduction to this study is presented in Chapter 1 and outlines the background and objectives. Seven separate articles are presented from Chapter 2 to Chapter 8.

Chapter 2 develops a molecular mechanics model to accurately describe the cohesive energy between CNTs, graphene and substrates.

The CG model for SWCNTs is established based on the stick-spiral model, beam model and continuum shell model in Chapter 3.

The critical length for the mechanical stability and adhesion between two SWCNTs (and MWCNTs) is obtained by a molecular mechanics model in Chapter 4.

Chapter 5 develops a molecular mechanics model to describe the size-dependent on the elastic properties of crystalline polyethylene.

Chapter 6 reveals the difference between the two molecular mechanics models, the stick-spiral and the beam models, in predicting the mechanical properties of materials based on energy equivalence.

Chapter 7 reveals the fracture mechanism of amorphous polymer for different chain length and temperature under uniaxial tension and shear.

Chapter 8 reveals the effect of polymer wrapped two neighbouring SWNTs' dispersion on their load transfer by MD simulations.

Chapter 9 presents the concluding remarks and suggestions for future work.

Note that the references of Chapter 1 can be seen in the other chapters.

Note that all contents of the thesis only contain some publications of my cumulative work from 2011 to 2013.

Chapter 2

A theoretical analysis of cohesive energy between carbon nanotubes, graphene and substrates*

Abstract

Explicit solutions for the cohesive energy between carbon nanotubes, graphene and substrates are obtained through continuum modeling of the van der Waals interaction between them. The dependence of the cohesive energy on their size, spacing and crossing angles is analyzed. Checking against full atom molecular dynamics calculations and available experimental results shows that the continuum solution has high accuracy. The equilibrium distances between the nanotubes, graphene and substrates with minimum cohesive energy are also provided explicitly. The obtained analytical solution should be of great help for understanding the interaction between the nanostructures and substrates, and designing composites and nanoelectromechanical systems.

2.1 Introduction

As mechanical structures enter the nanoscale regime, the van der Waals (vdW) interaction plays a significant role (Koenig et al., 2011). Carbon nanotubes (CNTs) and graphene have been proposed as one of the most promising materials for nanoelectromechanical systems due to their extremely high Young's modulus and strength. It has been well established that the mechanical behavior of CNTs and graphene is also strongly influenced by the vdW force (Yakobson et al., 1996; Ru, 2000; Ru, 2001; He et al., 2005; Jiang et al., 2006; Wang et al., 2007; Lu et al., 2007). A good understanding of the vdW interactions for two crossing CNTs, CNT/graphene and CNT/substrate is essential to ensure the optimum performance of CNTs and graphene in potential applications.

The bottom-up approaches of the atomistic-based methods such as classical molecular dynamics (MD) (Iijima et al., 1996; Yakobson et al., 1996), tight-binding MD (Hernandez et al.,

* This work has been published on <<Carbon>> 57, 108-119 (2013).

1998; Zhao et al., 2009) and density functional theory (Sanchez-Portal et al., 1999; Zhang et al., 2007; Zhang and Guo, 2008) were widely used to study the mechanical properties of the single-walled CNTs, multi-walled CNTs, boron nitride nanotubes (BNTs) and graphene sheets under uniaxial compression/tension, bending and torsion deformation. Compared with the bottom-up methods, top-down approaches may substantially reduce the computational costs and are thus frequently used in related investigations. In order to overcome limitations of atomistic simulations, some typical continuum models were developed and broadly used to clarify the elastic properties of the graphene sheets, CNTs and BNTs (Hernandez et al., 1998; Govindjee nd Sackmann, 1999; Vaccarini et al., 2000; Yoon et al., 2003; Chang, 2010) within the framework of molecular mechanics. Yakobson et al. (1996) used a traditional continuum shell model to predict the bulking of a single-walled CNT. Compared with the MD simulation, their continuum solution is considerably effective to characterize the bulkling pattern. The beam model was developed by Li and Chou (2003, 2004). They assume that the beam elements have circular cross sections and are always subjected to pure tension, pure bending and pure torsion. The theory was improved (Tserpes and Papanikos, 2005; Xia et al., 2005; To, 2006; Kasti, 2007; Wu et al.,2008; Jiang et al., 2009; Jiang et al., 2012) and extended to further calculate the five independent size- and chirality-dependent elastic moduli of single-walled CNTs using equivalent beam elements with rectangular section (Li and Guo 2008). The "stick-spiral" model (SSM) was developed by Chang and Gao (2003). An improved model by Jiang and Guo (2011) was used to investigate the elastic properties of single-walled boron nitride nanotubes. By extending the beam model and SSM to crystalline polymers (Zhao et al., 2010), we presented the SSM to investigate the size-dependent elastic properties of crystalline polyethylene (PE) (Zhao et al., 2011). Based on the united-atom MD simulations, we further verified the effectivity of the SSM in the crystalline polymers directly in which the van der Waals interaction between any two polymer chains are considered (Capaldi et al., 2004; Zhao et al., 2011). In this work, we utilized a united atom approximation in which the methyl groups (CH_2) are represented by a single "atom" or unit, and the effect of the hydrogen atoms on the polymer's configuration is accounted for in the potentials (Waheed, 2005; Shepherd, 2006). Subsequently, we extended to the beam-spring model to obtain the elastic properties of crystalline PE (Zhao et al., 2012).

Considering the important influence of the vdW interaction, Ru (Ru, 2000; Ru, 2001) proposed a continuum shell model to study the buckling of double-walled CNTs. Wang et al. (2003) extended Ru's vdW model to capture the buckling characteristics of the multi-walled CNTs. The applicability and limitations of the shell models were also discussed. Shen (2004) presented a traditional cylindrical shell model for the post-buckling of a double-walled CNT using Ru's vdW interaction model. He et al. (2005) developed a new vdW interaction model for not only the post-buckling pressure but also the pre-buckling pressure between any two layers of multi-walled CNTs, where the influence of interlayer spacing and the tube radius on the pressures were also considered.

Recently, the cohesive properties between double CNTs, multi-CNTs and CNT/polymer matrix have been studied systematically (Jiang et al., 2006; Lu et al., 2007; Lu et al., 2008). However, the above mentioned studies mainly concerned on the crucial effect of the vdW interactions on the elastic properties of the multi-walled CNTs, CNT/polymer and the crystalline PE. The crossing CNTs, CNT/graphene, and CNT/substrate are widely used in CNTs electronic devices. For instance, Fig. 2.1 shows a schematic structure in the experiments (Anantram and Leonard, 2006; Zeng et al., 2012). Therefore, the surface vdW forces play a key role on the mechanical behavior of the crossing CNTs, CNT/graphene and CNT/substrate (Hertel et al., 1998; Koenig et al, 2011). A clear understanding of the vdW interactions in these systems is crucial for their potential applications in the nanoelectromechanical systems and electronic devices.

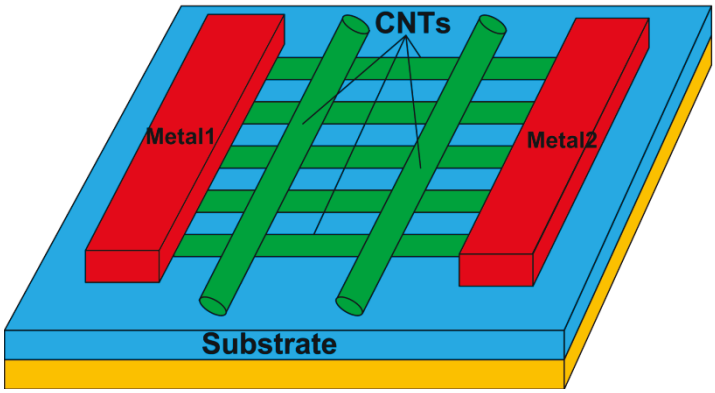

Fig. 2.1 Schematic diagrams showing the fabrication process of CNTs electronic devices.

In this paper, we obtain the closed-form expressions on the cohesive energy and the equilibrium distances between the two parallel CNTs, two crossing CNTs, CNT/graphene and CNT/substrate from a continuum model based on the Lennard-Jones (LJ) potential. The analytical expressions are validated by comparing with our MD simulation.

The paper is organized as follows: Section 2.2 shows the detailed process of the present molecular dynamics simulation. Section 2.3 describes the cohesive energy and the equilibrium distance for two crossing lines, CNT/graphene and CNT/substrate. In section 2.4, the cohesive energy for two parallel and two crossing CNTs is obtained. The paper is concluded in section 2.5.

2.2 Molecular dynamics simulation

To validate the continuum model for two crossing CNTs and CNT/graphene, all the MD simulations are performed using LAMMPS (Plimpton, 1995) with the AIREBO potential. The potential has been shown to accurately capture the bond-bond interaction between carbon atoms. The LJ cutoff radius of present AIREBO potential is chosen as 10.2 Å, and the vdW interaction is very weak and can be neglected as the distance is larger than 10.2 Å (Chang, 2007; Zhao et al., 2012). For the MD simulation, we choose the length and width $L\times W$ as 14.5×14.5 nm^2 for two graphene sheets (Cranfor and Buehler, 2011). For a CNT (50,0) parallel to a graphene sheet, the length of them are both 21.4 nm and the width of the graphene is 14.2 nm. For two infinite parallel CNTs, the length of the CNTs is 12.3 nm and the periodic boundary is applied along the center axis direction. For the crossing angle of 90 degrees, the length of the two CNTs is 21.2 nm. We keep the initial distance about 15 Å between two graphene sheets (or CNTs) where the van der Waals interactions are very weak and can be neglected. After the energy minimization, the two sheets (or CNTs) are kept as two rigid sheets (Cranfor and Buehler, 2011). The present simulation is at 0 K and the distance between two sheets or CNTs is changed with an increment of 0.1 Å per time step based on the deformation-control method, respectively. Afterwards, the structure is optimized for each displacement increment and the optimized structure is taken as the initial geometry for the next calculations. The energy minimization is performed using the conjugate-gradient method. A tolerance of relative energies between minimization iterations is set at 10^{-8} with a force tolerance of 10^{-8} to ensure a sufficiently minimized system (Plimpton, 1995).

2.3 Cohesive energy for CNT/graphene and CNT/martix

2.3.1 Cohesive energy between two parallel lines and two crossing lines

In the context of this paper, the energy of the vdW interactions (He et al., 2005; Jiang et al., 2006) is given by

$$V(h) = 4 \in \left[\left(\frac{\sigma}{h} \right)^{12} - \left(\frac{\sigma}{h} \right)^{6} \right], \tag{1}$$

where h is the distance between the interacting atoms, $\in$ is the depth of the potential, σ is a parameter that is determined by the equilibrium distance (Yakobson et al., 1996; Chang et al., 2007). It is obvious that the equilibrium distance h_0 between the two points is determined by minimizing the energy as $h_0=2^{1/6}\sigma=1.1225\sigma$ from $\frac{\partial V(h)}{\partial h} = 0$.

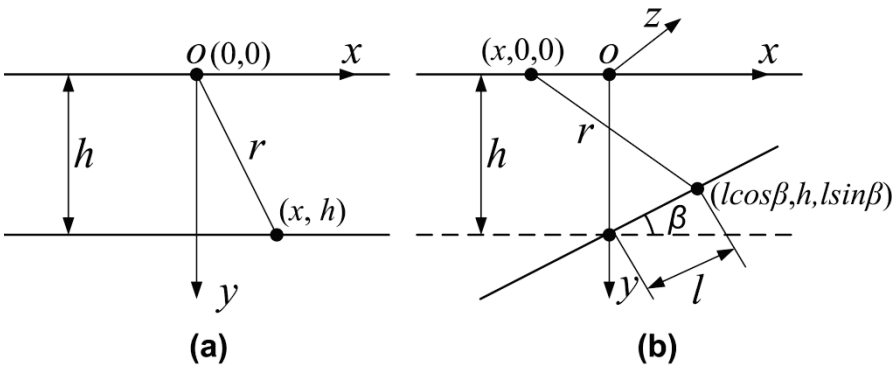

Fig. 2.2 The coordinate system and a schematic diagram of the two infinite parallel and two crossing lines: (a) two parallel lines; (b) two crossing lines.

We first study the two special cases which are the cohesive energy between two parallel and two crossing lines. Fig. 2.2 shows the schematic diagram of two parallel and two crossing infinite lines.

The cohesive energy per unit length between two parallel lines can be obtained

$$\phi_{line-line} = \rho_l^2 \int_{-\infty}^{\infty} V(r)\, dx, \tag{2}$$

where $r^2=x^2+h^2$, and ρ_1 is the line density (the number of atoms per unit length).

Substituting Eq. (1) into Eq. (2) gives

$$\phi_{line-line} = 4 \in \rho_l^2 \sigma^6 \left(\frac{63\pi}{256} \sigma^6 \frac{1}{h^{11}} - \frac{3\pi}{8} \frac{1}{h^5} \right), \tag{3}$$

From the energy minimum condition $\frac{\partial \phi_{line-line}}{\partial h} = 0$, the equilibrium distance h_0 can be obtained $h_0=1.0631\sigma$.

The total cohesive energy between two crossing lines can be obtained by

$$\phi_{cross-lines} = \rho_l^2 \int_{-\infty}^{\infty} V(r)\, dx \int_{-\infty}^{\infty} dl \text{ , } (0<\beta\leq\pi/2) \tag{4}$$

where $r^2 = \left(l\cos\beta - x\right)^2 + h^2 + \left(l\sin\beta\right)^2$, and β is the crossing angle in Fig. 2.2b.

Eq. (4) can be rewritten as

$$\phi_{cross-lines} = 4 \in \rho_l^2 \sigma^6 \frac{1}{\sin\beta} \left(\frac{63\pi}{256} \sigma^6 A_0 \frac{1}{h^{10}} - \frac{3\pi}{8} A_1 \frac{1}{h^4} \right), \tag{5}$$

where

$$A_0 = \frac{1}{128} \left(98 + \frac{36}{5} - \frac{2}{63} \right), \tag{6}$$

$$A_1 = \frac{4}{3}.$$

The equilibrium distance $h_0=1\sigma$ between two crossing lines is determined by the energy minimization $\frac{\partial \phi_{cross-lines}}{\partial h} = 0$.

2.3.2 Two infinite parallel graphene sheets

In this section, we provide a continuum model to establish an analytical expression for the distribution of the cohesive energy between two parallel graphene sheets, as shown in Fig. 2.3. We homogenize carbon atoms on the graphene and represent them by an area density ρ, where ρ is related to the equilibrium bond length of graphene prior to deformation (He et al., 2005; Jiang et al., 2006; Zheng et al., 2008). From the unit cells and bond lengths, the area density ρ can be expressed as $\rho = 4/\left[3\sqrt{3}b^2\right]$, where b=1.42 Å is the bond length of the graphene sheets.

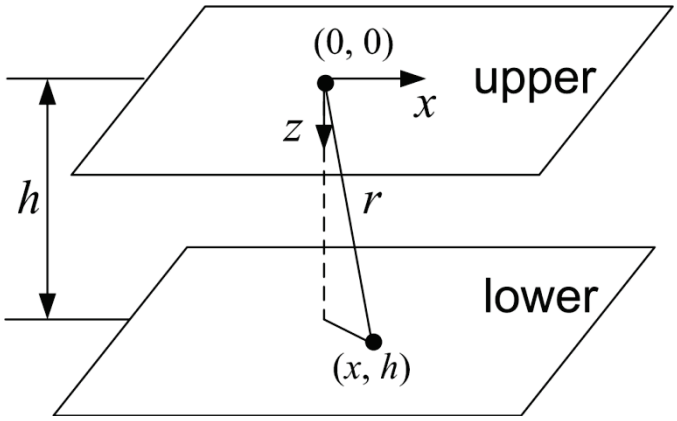

Fig. 2.3 The coordinate system and a schematic diagram of the two infinite graphene sheets.

The number of carbon atoms over an area dA on one sheet is ρdA. The distance between one point (0, 0) on the upper sheet and one point (x, z) ($x\geq 0$, $z=h$) on the lower sheet is $r^2= x^2+h^2$. For a CNT or graphene, $\in = 2.8437$ mev and σ=3.4 Å are adopted from the literature (Chang et al., 2007; Plimpton, 1995). The cohesive energy ϕ per unit area can be written as

$$\phi_{graphene-graphene} = \frac{\rho_l dA_l \int_{A_u} V(r)\rho_u dA_u}{dA_l} = 2\pi\rho_l\rho_u \int_0^\infty V(r)\, x dx\,, \tag{7}$$

where $r^2=h^2+x^2$, $\rho_l=\rho_u$ and $A_l=A_u$ are the lower and upper area densities and areas, respectively. If we define $\rho_l=\rho_u=\rho$, Eq. (7) can be given by

$$\phi_{graphene-graphene} = 4\pi\rho^2 \in \sigma^6 \left(\frac{\sigma^6}{5h^{10}} - \frac{1}{2h^4}\right), \tag{8}$$

The equilibrium distance $h_0=1\sigma$ is also determined by the energy minimization $\frac{\partial \phi_{graphene-graphene}}{\partial h}=0$.

From section 2.3.1, we find that the equilibrium distance between two crossing lines is identical to the distance of two graphene sheets, since the graphene sheet can be regarded as an array of lots of lines.

To show the validity of the present continuum model, the distribution of the analytical cohesive energy with distance by Eq. (8) for the graphene sheets is plotted in Fig. 2.4. The analytical results are in excellent agreement with the MD results. The minimum value of the cohesive energy in Fig. 2.4 from our MD simulation and Eq. (8) are both equal to 291 mJ/m^2 Å. The result is also in good agreement with the latest experimental result 310±30 mJ/m^2 (Koenig et al, 2011).

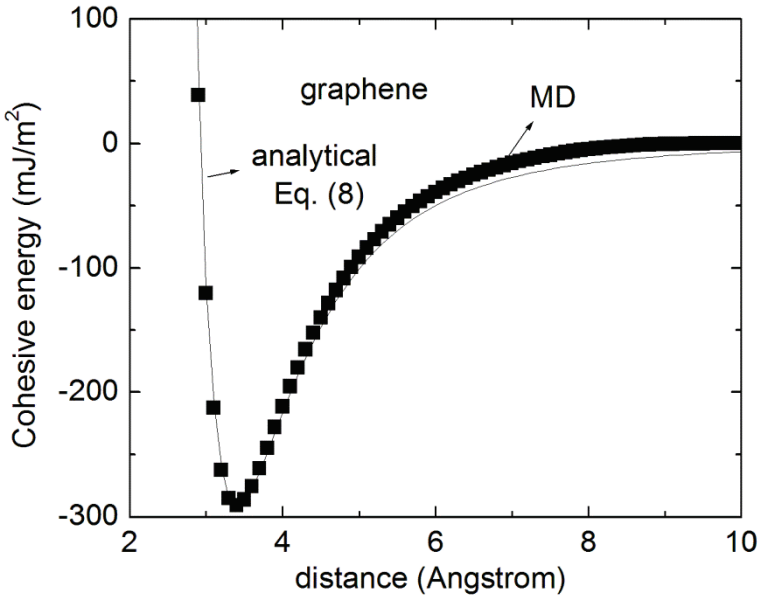

Fig. 2.4 The distribution of cohesive energy with distance between two graphene sheets.

Similarly, it is easy to show that the equilibrium distances between the point/graphene and the line/graphene (the line is parallel to the graphene sheet) are both 1σ. The relationship of the equilibrium distance can be written as follows: two points $h_0=1.1225\sigma$> two parallel lines

h_0=1.0631σ >two crossing lines h_0=1σ = point/graphene h_0= line/graphene h_0=graphene/graphene h_0=1σ.

2.3.3 One CNT parallel to one graphene sheet

In view of the importance of the cohesive energy between a CNT and a graphene sheet in the experiment, we further study the interaction between a CNT and an infinite graphene sheet, in which the CNT is parallel to the graphene sheet, as shown in Fig. 2.5. The distance from the central axis of the CNT to the sheet is h, and h=h'+r_1, where h' is the closest distance between the CNT and the sheet. The area density of the graphene and the CNT are both chosen as ρ. The difference of ρ between CNT and graphene increases with decreasing CNT radius. We homogenize carbon atoms on the CNT and represent them by an area density ρ, which may be slightly different from the area density of graphene due to the curvature effect in the CNT (He et al., 2005; Jiang et al., 2006). Fig. 2.5 shows the Cartesian coordinates (x, y, z), where z is along the central axis, and y is the direction normal to the graphene sheet. Without loss of generality we consider one point (r_1, θ, 0) on the upper CNT, and one point (x, h, z) in the graphene sheet, see Fig. 5. The distance between the two points can be expressed as r=[($r_1$cosθ-x)^2+($r_1$sinθ-h)^2+z^2]$^{1/2}$. The cohesive energy between the CNT and the graphene sheet can be obtained from V(h).

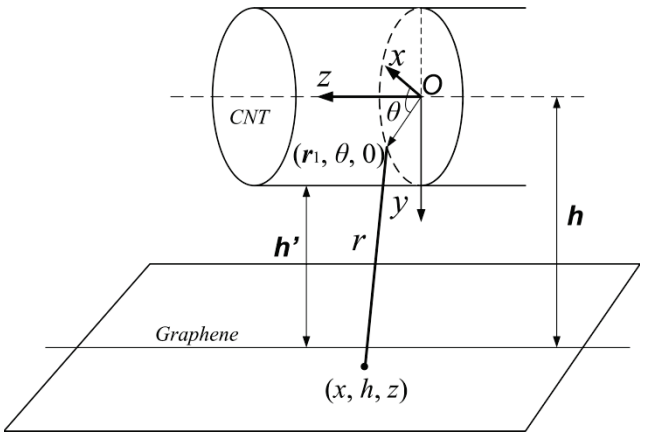

Fig. 2.5 The coordinate system and a schematic diagram of a carbon nanotube parallel to one infinite graphene sheet.

Unlike the analysis in section 2.3.1, the deformation for the CNT is nonuniform. We define the cohesive energy per unit length (along the central axis of the CNT) stored from the vdW interactions as

$$\phi_{CNT-graphene} = \rho^2 \int_0^{2\pi} r_1 d\theta \int_{-\infty}^{\infty} V(r)\, dz \int_{-\infty}^{\infty} dx\,, \tag{9}$$

where $r^2=(r_1\cos\theta-x)^2+(r_1\sin\theta-h)^2+z^2$.

Integrating Eq. (9) yields

$$\phi_{CNT-graphene} = \rho^2 r_1 \left(4 \in \sigma^{12} \frac{63\pi}{256} f_1 - 4 \in \sigma^6 \frac{3\pi}{8} f_2 \right). \tag{10}$$

where

$$f_1 = \frac{1}{128}\left(98 + \frac{36}{5} - \frac{2}{63}\right) T\,, \tag{11}$$

$$f_2 = \frac{4}{3} M\,. \tag{12}$$

T is expressed as

$$T = \frac{1}{9!} \frac{4T'}{\left(h^2 - r_1^2\right)^{9+\frac{1}{2}}} \left(\arctan \frac{-h + r_1}{\sqrt{h^2 - r_1^2}} - \arctan \frac{h + r_1}{\sqrt{h^2 - r_1^2}} \right), \tag{13}$$

where $T' = -2835\left(128h^9 + 2304 r_1^2 h^7 + 6048 r_1^4 h^5 + 3360 r_1^6 h^3 + 315 r_1^8 h\right)$.

M is given by

$$M = \frac{1}{3!} \frac{4M'}{\left(h^2 - r_1^2\right)^{3+\frac{1}{2}}} \left(\arctan \frac{-h + r_1}{\sqrt{h^2 - r_1^2}} - \arctan \frac{h + r_1}{\sqrt{h^2 - r_1^2}} \right), \tag{14}$$

where $h= h'+r_1$, $M' = -6h^3 - 9 r_1^2 h$.

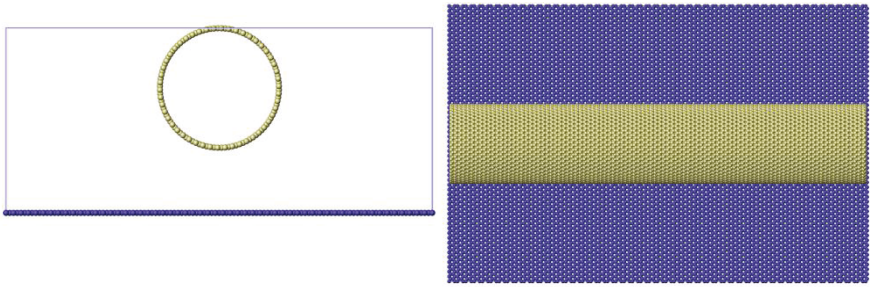

Fig. 2.6 One CNT (50, 0) parallel to one graphene sheet in our molecular dynamics simulation. (a) side view, (b) vertical view.

Fig. 2.6 shows a CNT (50, 0) parallel to a graphene sheet in our MD simulation. The free boundary condition is performed along the center axis of the CNTs. A single-walled CNT can be denoted by a chiral vector $\vec{R} = n_1\vec{a}_1 + n_2\vec{a}_2$ or equivalently, the radius r and chiral angle θ. $\vec{a}_1$ and $\vec{a}_2$ are the primitive lattice vectors in graphite lattices (Saito et al., 1998), $\vec{a}_1 = \vec{a}_2 = 2.46\,\text{Å}$. The radius r and chiral angle θ in terms of n_1 and n_2 are given by

$$r = \frac{|\vec{a}_1|}{2\pi}\sqrt{n_1^2 + n_1 n_2 + n_2^2}\ ,\ \theta = \arctan\frac{\sqrt{3}n_2}{2n_1 + n_2}\ . \tag{15}$$

Fig. 2.7 shows the cohesive energy with different diameters of CNTs between CNT/graphene using our analytical model and MD simulation. The cohesive energy increases with decreasing CNT radius. The analytical value from Eq. (10) is in good agreement with our MD results, in which the difference is less than 10%. The difference is mainly caused by the present LJ cutoff radius of 10.2 Å (or 3σ), while the cutoff radius is infinite in the analytical results. (the slight difference of the area density between CNT and graphene is also a possible reason.). It validates the accuracy of the continuum model in the description of the cohesive energy between a CNT and a graphene sheet.

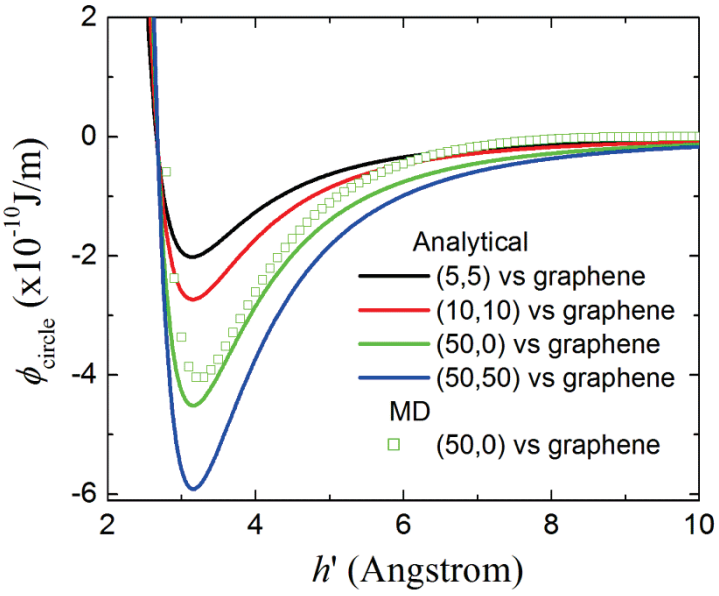

Fig. 2.7 The distribution of cohesive energy with different distance between one CNT and one graphene sheet using present analytical model and molecular dynamics simulation.

The equilibrium distance $h_0^{'}$ between the CNT and the graphene sheet can be determined by $\frac{\partial \phi_{CNT-graphene}}{\partial h'}=0$ from Eq. (10). Since the expression of $h_0^{'}/\sigma$ is very complicated, the fitting function can be provided

$$h_0'/\sigma = a_1\left(\frac{b_1}{(r_1+c_1)^{10}}-\frac{d_1}{(r_1+c_1)^4}\right)+e_1, \tag{16}$$

where a_1=10.64524, b_1=1592.5501, c_1=3.25323, d_1=0.59368 and e_1=0.9291.

The fitting results from Eq. (16) are shown in Fig. 2.8. The difference between the fitting results and the analytical results is smaller than 1%.

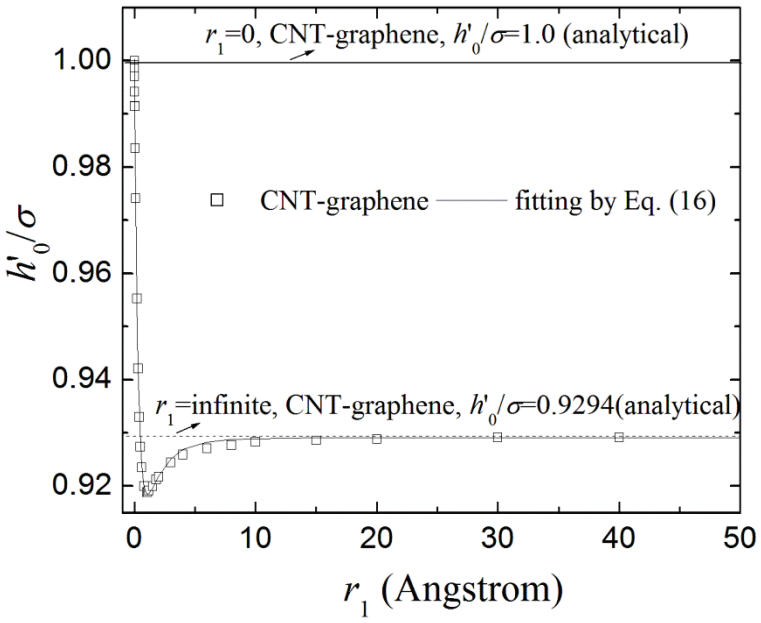

Fig. 2.8 The normalized equilibrium distance h_0'/σ between one CNT and one graphene sheet for different radii r_1.

Fig. 2.8 shows the normalized equilibrium distance h_0'/σ between the CNT and the graphene sheet for different radii r_1. The equilibrium distances decrease with increasing r_1 when r_1<1.2 Å, while they increase with increasing r_1 for r_1>1.2 Å. When r_1=0, h_0'/σ=1 for CNT/graphene tend to that between graphene/graphene. When r_1>10 Å, h_0'/σ tends to the corresponding constant 0.9294, respectively.

Since all the radii of CNTs are larger than 1.2 Å, the distance h_0'/σ between the CNT and the graphene sheet increases with increasing r_1 and then converges to a constant value of 0.9294.

2.3.4 One CNT parallel to one substrate

Next, we study the interaction between a CNT and an infinite substrate, in which the CNT is parallel to the substrate, as shown in Fig. 2.9. The distance from the central axis of the CNT to the substrate surface is h, and h=h'+r_1, where h' is the closest distance between CNT and substrate surface. The volume density of the substrate is ρ_m (the number of atoms per unit volume). Fig. 2.9 shows the Cartesian coordinates (x, y, z), where z is along the central axis, and y is the direction normal to the graphene sheet. Without loss of generality we consider one point (r_1, θ, 0) on the upper CNT, and one point (x, y, z) in Fig. 2.9. The distance between the two

points is $r=[(r_1\cos\theta-x)^2+(r_1\sin\theta-y)^2+z^2]^{1/2}$. The cohesive energy between the CNT and the graphene sheet can be obtained from $V(h)$.

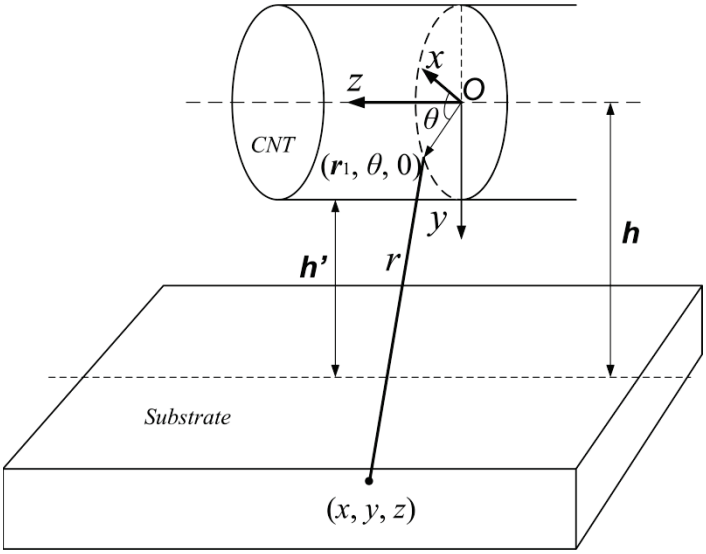

Fig. 2.9 The coordinate system and a schematic diagram of one CNT parallel to one infinite substrate.

We define the cohesive energy per unit length (along the central axis of the CNT) from the vdW interactions as

$$\phi_{CNT-substrate}=\rho dA_2\int_{V_1}V(r)\rho_m dV_1=\rho\rho_m dA_2\int_{-\infty}^{\infty}V(r)dz\int_{-\infty}^{\infty}dx\int_h^{\infty}dy\,, \tag{17}$$

$$\phi_{CNT-substrate}=\rho\rho_m\int_0^{2\pi}r_1 d\theta\int_{-\infty}^{\infty}V(r)dz\int_{-\infty}^{\infty}dx\int_h^{\infty}dy\,, \tag{18}$$

where $r^2=(r_1\cos\theta-x)^2+(r_1\sin\theta-y)^2+z^2$.

Using the LJ potential, we obtain

$$\phi_{CNT-substrate}=\rho\rho_m r_1\left(\frac{7\pi}{64}\in_m\sigma_m{}^{12}g_1-\frac{\pi}{2}\in_m\sigma_m^6 g_2\right), \tag{19}$$

where $\in_m$ is the depth between the carbon atom and the atom of the substrate, and σ_m is the equilibrium distance between carbon atom and the atom of the substrate; g_1 and g_2 can be written as

$$g_1 = \frac{1}{128}\left(98 + \frac{36}{5} - \frac{2}{63}\right)U \ . \tag{20}$$

$$g_2 = \frac{4}{3}W \ . \tag{21}$$

U is given by

$$U = \frac{1}{8!}\frac{4U'}{\left(h^2 - r_1^2\right)^{8+\frac{1}{2}}}\left(\arctan\frac{h + r_1}{\sqrt{h^2 - r_1^2}} - \arctan\frac{-h + r_1}{\sqrt{h^2 - r_1^2}}\right), \tag{22}$$

where $U' = 315\left(128h^8 + 1792r_1^2h^6 + 3360r_1^4h^4 + 1120r_1^6h^2 + 35r_1^8\right)$.

W is expressed as

$$W = \frac{1}{2!}\frac{4W'}{\left(h^2 - r_1^2\right)^{2+\frac{1}{2}}}\left(\arctan\frac{h + r_1}{\sqrt{h^2 - r_1^2}} - \arctan\frac{-h + r_1}{\sqrt{h^2 - r_1^2}}\right), \tag{23}$$

where $h = h' + r_1$ and $W' = 2h^2 + r_1^2$.

Eq. (19) can be used to characterize the cohesive energy between a CNT and a substrate. If the parameters ρ_m, $\in_m$ and σ_m are given, Eq. (19) can be solved directly for different substrates.

The equilibrium distance h_0 between the CNT and the graphene sheet can be determined by $\frac{\partial \phi_{CNT-substrate}}{\partial h'} = 0$ from Eq. (19). We also provide the fitting function of h_0'/σ as

$$h_0'/\sigma_m = a_2\left(\frac{b_2}{\left(r_1 + c_2\right)^9} - \frac{d_2}{\left(r_1 + c_2\right)^3}\right) + e_2, \tag{24}$$

where a_2=2.89208, b_2=600.08159, c_2=2.89826, d_2=0.37398 and e_2=0.783.

The fitting results from Eq. (24) are illustrated in Fig. 2.10 match the analytical results accurately.

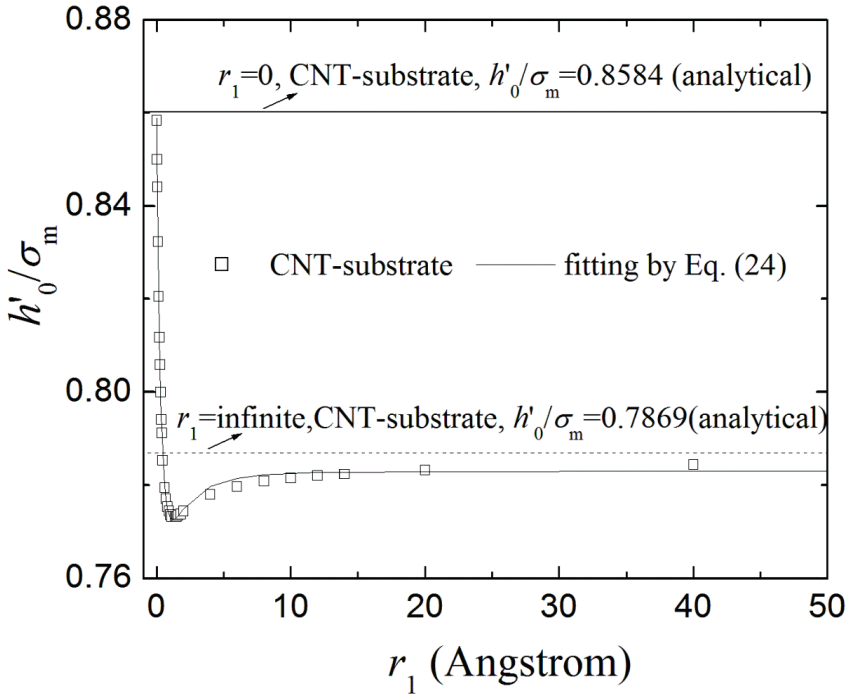

Fig. 2.10 The normalized equilibrium distance h_0'/σ between one CNT and a substrate for different radii r_1.

Fig. 2.10 shows the normalized equilibrium distance h_0'/σ between the CNT and the substrate for different radius r_1. The equilibrium distance for CNT/substrate decreases with increasing r_1 as r_1<1.4 Å, while it increases with increasing r_1 (r_1>1.4 Å). When r_1=0, h_0'/σ=0.8584 for CNT/substrate tends to line/substrate from Eq. (19). When r_1>10 Å, it tends to the corresponding two constants 0.8664. In practical applications, all the radii of CNT are larger than 1.2 Å. Hence, the distance h_0'/σ between the CNT and the graphene sheet increases with increasing r_1 and then tends to a constant of 0.8664.

2.4. Cohesive energy between two parallel CNTs and two crossing CNTs

2.4.1 Two parallel infinite CNTs

For the effective design of the nanoelectromechanical systems, the surface vdW forces play a key role on the mechanical behavior of the crossing CNTs, as shown in Fig. 1. To obtain the cohesive energy between two crossing infinite CNTs, we consider the two parallel infinite CNTs first. Fig. 11 shows the coordinate system and a schematic diagram of the two parallel CNTs.

The upper and lower CNT radii are r_1 and r_2, respectively. The closest distance between the two parallel CNTs edge is h.

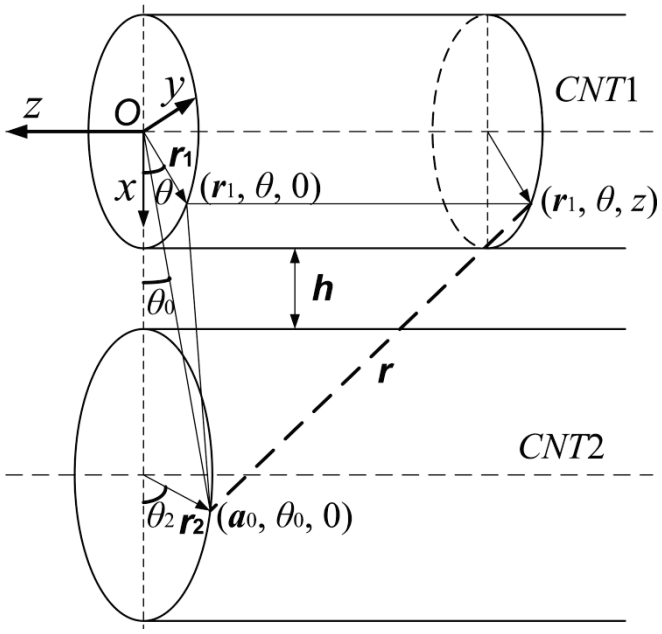

Fig. 2.11 The coordinate system and a schematic diagram of the two parallel infinite CNTs.

The cylindrical coordinates (r_1, θ, z) are used for the upper CNT, where z is the central axis of the CNT in Fig. 2.11. Considering the two parallel infinite CNTs, the cohesive energy per unit length along the z-direction should be the same. We assume the lower CNT circle on the z=0 plane. A point on the lower CNT circle is (a_0, θ_0, 0); r_2 is equal to the distance between the center point and the point on the lower CNT circle, and θ_2 denotes the angle between x axis and the direction along r_2 (see Fig. 2.11).

From the geometric relationship, we obtain

$$a_0 \cos\theta_0 = \left(r_1 + r_2 + h\right) + r_2 \cos\theta_2 , \tag{25}$$

$$a_0 \sin\theta_0 = r_2 \sin\theta_2 . \tag{26}$$

From Eq. (25) and Eq. (26), a_0 and θ_0 can be obtained

$$a_0 = \sqrt{\left(r_1 + r_2 + h\right)^2 + r_2^2 + 2\left(r_1 + r_2 + h\right) r_2 \cos\theta_2} , \tag{27}$$

$$\theta_0 = arc\cos\frac{\left(r_1+r_2+h\right)^2+a_0^2-r_2^2}{2\left(r_1+r_2+h\right)a_0}. \tag{28}$$

Let us define the energy per unit length along the z direction on the lower CNT from the vdW interactions as

$$\phi_{cicle} = \int_0^{2\pi}\rho r_2 d\theta_2 \int_{A_1} V(r)\rho dA_1 = \rho^2\int_0^{2\pi} r_2 d\theta_2 \int_{-\infty}^{\infty} V(r)dz\int_0^{2\pi} r_1 d\theta, \tag{29}$$

where the distance between the two points $r = \sqrt{\left(a_0\cos\theta_0 - r_1\cos\theta\right)^2+\left(a_0\sin\theta_0 - r_1\sin\theta\right)^2+z^2}$.

Submitting Eq. (27) and Eq. (28) into Eq. (29) gives

$$\phi_{cicle} = \pi\in\sigma^6\rho^2 r_1 r_2\left(\frac{63}{8}\sigma^6\int_0^{\pi}\frac{F_5\left[\frac{2\sqrt{a_0 r_1}}{r_1+a_0}\right]}{\left(r_1+a_0\right)^{11}}d\theta_2 - 12\int_0^{\pi}\frac{F_2\left[\frac{2\sqrt{a_0 r_1}}{r_1+a_0}\right]}{\left(r_1+a_0\right)^{5}}d\theta_2\right), \tag{30}$$

Defining $k = \frac{2\sqrt{a}}{1+a} = \frac{2\sqrt{a_0 r_1}}{r_1+a_0}$, we have

$$F_2[k] = \frac{1}{3\left(1-k^2\right)}\left[\left(\frac{4-2k^2}{1-k^2}\right)E(k) - K(k)\right], \tag{31}$$

$$F_5[k] = \frac{1}{315\left(1-k^2\right)^5}\left[\begin{array}{l}\left(128k^8-616k^6+1179k^4-1126k^2+563\right)E(k)\\ +\left(-64k^8+316k^6-624k^4+620k^2-248\right)K(k)\end{array}\right], \tag{32}$$

where the elliptic integrals are $E(k) = \int_0^{\frac{\pi}{2}}\left(1-k^2\sin^2 t\right)^{\frac{1}{2}}dt$, $K(k) = \int_0^{\frac{\pi}{2}}\frac{1}{\left(1-k^2\sin^2 t\right)^{\frac{1}{2}}}dt$.

Eq. (30) can be completely solved by Gaussian quadrature (Golub and Welsch, 1969). Fig. 2.12 shows the two parallel infinite CNTs in our MD simulation. Periodic boundary conditions are applied along the center axis of the CNTs.

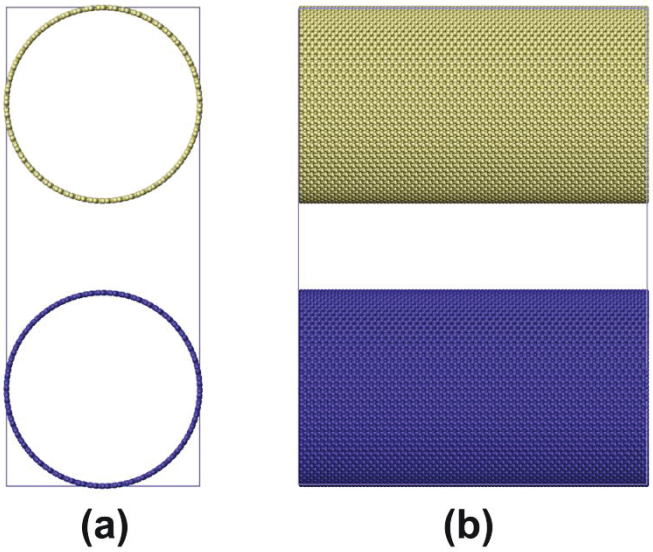

Fig. 2.12 The two parallel infinite CNTs of (50, 50) in our molecular dynamics simulation. (a) vertical view, (b) side view.

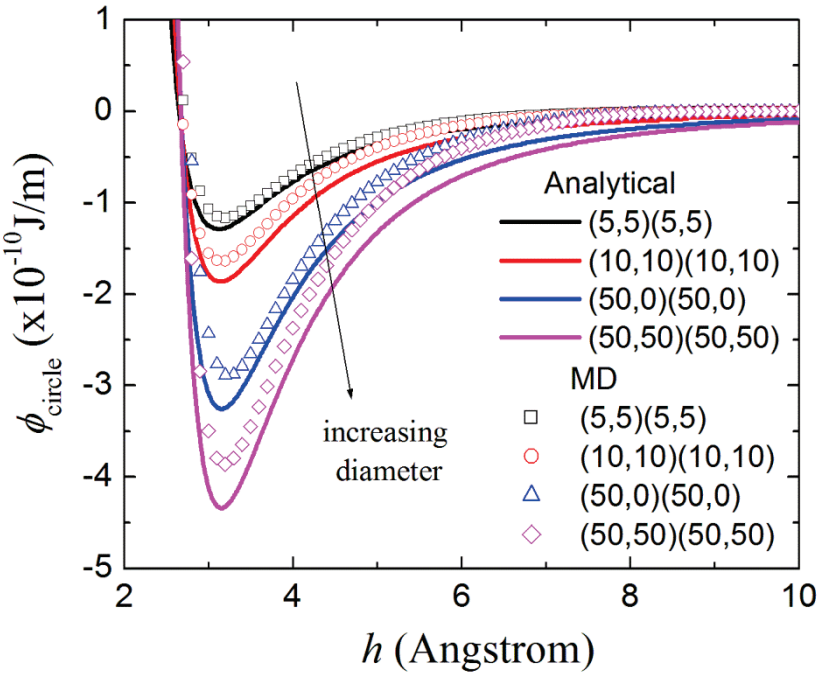

Fig. 2.13 The distribution of cohesive energy with different distance between two parallel infinite CNTs using present analytical model and molecular dynamics simulation.

Fig. 2.13 compares the cohesive energy for different distances between the two parallel infinite CNTs (where r_1=r_2) from our analytical model with results from MD simulations. The cohesive energy increases with decreasing CNT radius.

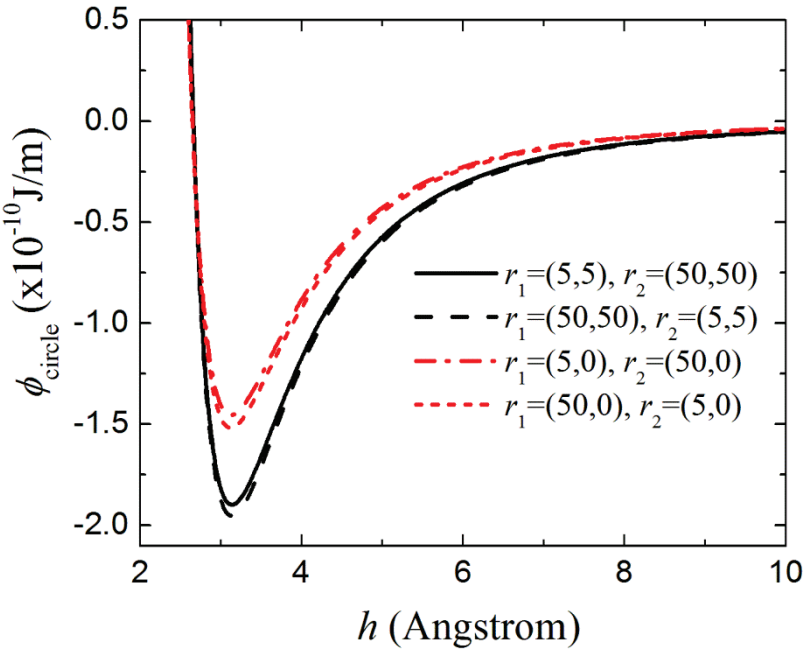

Fig. 2.14 The circle cohesive energy on the lower and upper CNTs with different distance between two parallel infinite CNTs using present analytical model.

Fig. 2.14 shows the cohesive energy for different distances between two parallel infinite CNTs (where $r_1 \neq r_2$) using our analytical model. The cohesive energy ϕ_{circle} on the circle of CNT radius r_1 as $r_1 \neq r_2$ is almost the same with that on the circle of CNT radius r_1' as $r_1' \neq r_2'$ (where $r_1'=r_2$ and $r_2'=r_1$). In other words, the total cohesive energy on the CNT of radius r_1 is the same with that on the radius r_2 between the two CNTs. The difference is less than 2% caused probably by integration errors. To reduce the difference, we perform the Gaussian quadrature on 100 sections [0, π/100], [π/100, 2π/100], [2π/100, 3π/100] …… [99π/100, 100π/100] and 10 Gaussian points in each section. The first fifth terms in the two elliptic integrals $E(k)$ and $K(k)$ are chosen in our calculations. Fig. 2.15 shows the distribution of the cohesive energy ϕ_{circle} between two parallel infinite CNTs with different radii using present analytical model. The cohesive energy ϕ_{circle} decreases with increasing CNT radius for a given distance h when $\phi_{circle}<0$, while, for $\phi_{circle}>0$, ϕ_{circle} increases with increasing CNT radius.

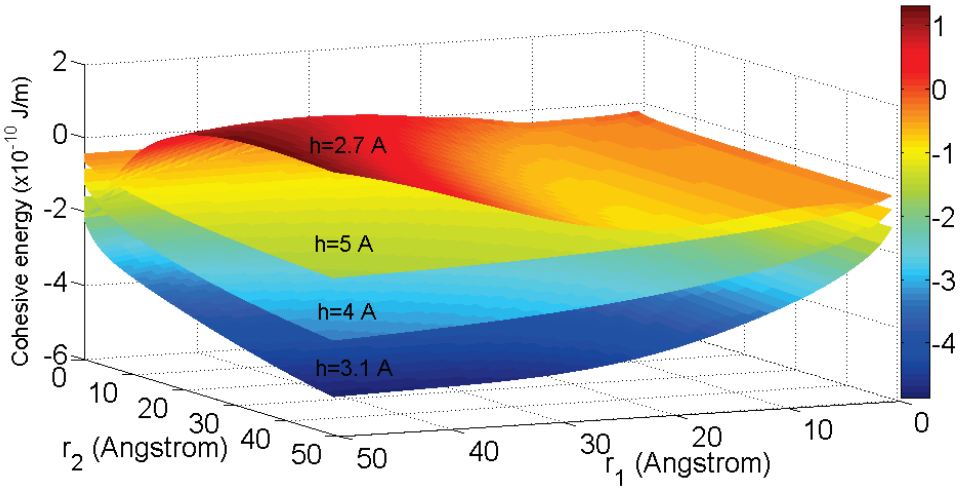

Fig. 2.15 The distribution of the cohesive energy between two parallel infinite CNTs with different radii using present analytical model.

The equilibrium distance h_0 is determined by $\frac{\partial \phi_{circle}}{\partial h} = 0$ from Eq. (30). For two parallel CNTs with r_1=r_2, the fitting function of the normalized equilibrium distance h_0/σ can be expressed as

$$h_0/\sigma = a_3\left(\frac{b_3}{(r_1+c_3)^{10}} - \frac{d_3}{(r_1+c_3)^4}\right) + e_3, \tag{33}$$

where a_3=20.80767, b_3=1968.22873, c_3=3.30743, d_3=0.71993 and e_3=0.9271.

Eq. (33) accurately characterizes the distribution of the equilibrium distances between two parallel infinite CNTs (the relative error is smaller than 1%), as shown in Fig. 2.16. We also find that the Eq. (16) of CNT/graphene in section 3.3 effectively describes the equilibrium distance between two parallel infinite CNTs for a given r_2=100 Å.

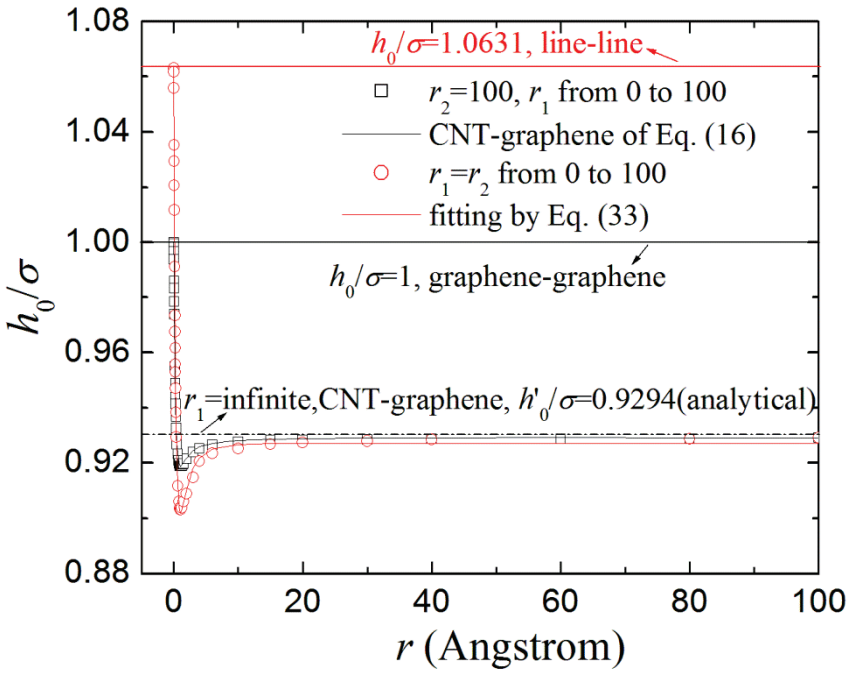

Fig. 2.16 The normalized equilibrium distance h_0/σ between two parallel infinite CNTs.

Fig. 2.16 shows the normalized equilibrium distance h_0/σ between two parallel infinite CNTs. When r_1=r_2, the normalized equilibrium distance decreases with increasing r_1 as r_1<1.2 Å, while they increase with increasing r_1 as r_1>1.2 Å. When r_1=r_2=0, the equilibrium distance from Eq. (30) tends to that of two parallel lines in Eq. (3). When r_1=r_2>10 Å, the equilibrium distance tends to that of the tube/graphene (r_1>10 Å in CNT/graphene).

For a given r_2=100 Å, the normalized equilibrium distance also decreases with increasing r_1 as r_1<1.2 Å, while it increases with increasing r_1 (r_1>1.2 Å). When r_1=0, the equilibrium distance approaches the distance of two graphene sheets. On the other hand, the equilibrium distance tends to that of tube/graphene for r_1>10 Å.

Since all the radii of CNT are larger than 1.2 Å, the h_0/σ between the CNT and the graphene sheet increases with increasing r_1 and then tends to a constant 0.9294.

2.4.2 Two crossing infinite CNTs

Last, we study the two crossing infinite CNTs, as shown in Fig. 2.17. The upper and lower CNT radii are r_1 and r_2, respectively. The crossing angle between the two center axes of the two crossing CNTs is denoted as β.

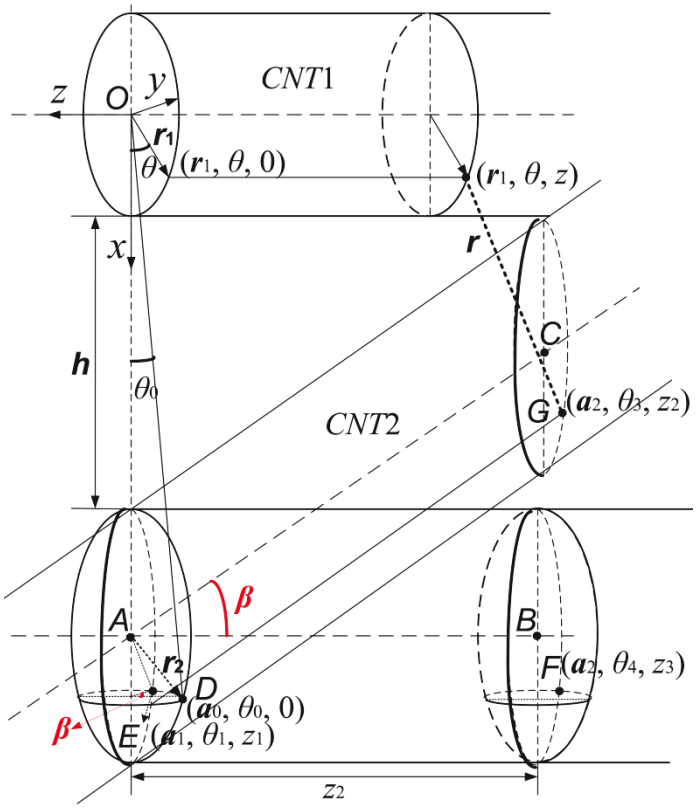

Fig. 2.17 The coordinate system and a schematic diagram of the two crossing infinite CNTs.

The cylindrical coordinates (r_1, θ, z) and the Cartesian coordinates (x, y, z) are both used for the upper CNT, where z is the central axis of the CNT. We assume the vertical line between the two center axes of the two crossing CNTs on the z=0 plane. The closest distance between the two parallel CNTs edge is h. For example, the point D on the lower CNT moves to the position of the point E after rotating the lower CNT. Then, the center point B moves to the position of the point C, and so on. Based on the geometric relationship, we obtain the coordinates of the points A, B, C, D, E, F and G in the Cartesian coordinates, i.e., A (r_1+r_2+h, 0, 0), B (r_1+r_2+h, 0, z_2), C (r_1+r_2+h, $z_2$sinβ, $z_2$cosβ), D ($a_0$cosθ_0, $a_0$sinθ_0, 0), E ($a_0$cosθ_0, $a_0$sin$\theta_0$cosβ, -$a_0$sin$\theta_0$sinβ), F ($a_0$cosθ_0, $a_0$sin$\theta_0$cosβ, z_2-$a_0$sin$\theta_0$sinβ), G ($a_0$cosθ_0, $a_0$sinθ0-$z_2$sinβ, $z_2$cosβ+$r_2$cos$\theta_2$sinβ), where a_0 and θ_0 are defined in Eq. (27) and Eq. (28).

The total cohesive energy of the two nanotubes due to the vdW force can be written as

$$\phi_{total}=\int_0^{2\pi}\rho r_2 d\theta_2\int_{-\infty}^{\infty}1dz_2\int_{A_1}V(r)\rho dA_1=\rho^2\int_0^{2\pi}r_2 d\theta_2\int_{-\infty}^{\infty}1dz_2\int_{-\infty}^{\infty}V(r)dz\int_0^{2\pi}r_1 d\theta\,,\ (0<\beta\leq\pi/2)\ (34)$$

where

$$r=\sqrt{\left(a_0\cos\theta_0-r_1\cos\theta\right)^2+\left[\left(a_0\sin\theta_0\cos\beta\text{-}z_2\sin\beta\right)-r_1\sin\theta\right]^2+\left[z-z_2\cos\beta-r_2\cos\theta_2\sin\beta\right]^2}\,.$$

The total cohesive energy ϕ_{total} can be integrated analytically to yielding

$$\phi_{total}=4\rho^2 r_1 r_2\in\sigma^6\frac{1}{\sin\beta}\left(\frac{63\pi}{128}\sigma^6\int_0^{\pi}\frac{A_0B_0S_0}{S_d}d\theta_2-\frac{3\pi}{4}\int_0^{\pi}\frac{A_1B_1T_1}{T_d}d\theta_2\right),\qquad(35)$$

where

$$S_0=362880a_0^9\cos^9\theta_0+6531840a_0^7\cos^7\theta_0r_1^2+17146080a_0^5\cos^5\theta_0r_1^4$$
$$+9525600a_0^3\cos^3\theta_0r_1^6+893025a_0\cos\theta_0r_1^8\quad,$$

$$A_0=-\frac{1}{128}\left(98+\frac{36}{5}-\frac{2}{63}\right),\ B_0=-\frac{2\pi}{9!},\ S_d=\left[\left(r_1+r_2+h+r_2\cos\theta_2\right)^2-r_1^2\right]^{\frac{19}{2}}.$$

$$T_1=6a_0^3\cos^3\theta_0+9a_0\cos\theta_0r_1^2,\ A_1=-\frac{4}{3},\ B_1=-\frac{2\pi}{3!},\ T_d=\left[\left(r_1+r_2+h+r_2\cos\theta_2\right)^2-r_1^2\right]^{\frac{7}{2}}.$$

Eq. (35) is solved by Gaussian quadrature.

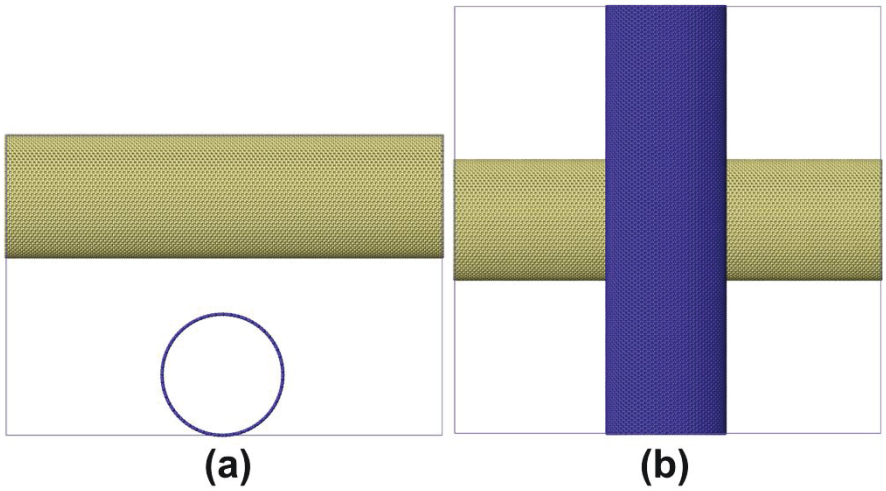

Fig. 2.18 The two crossing (β=90^0) infinite CNTs of (50, 50) in our molecular dynamics simulation.

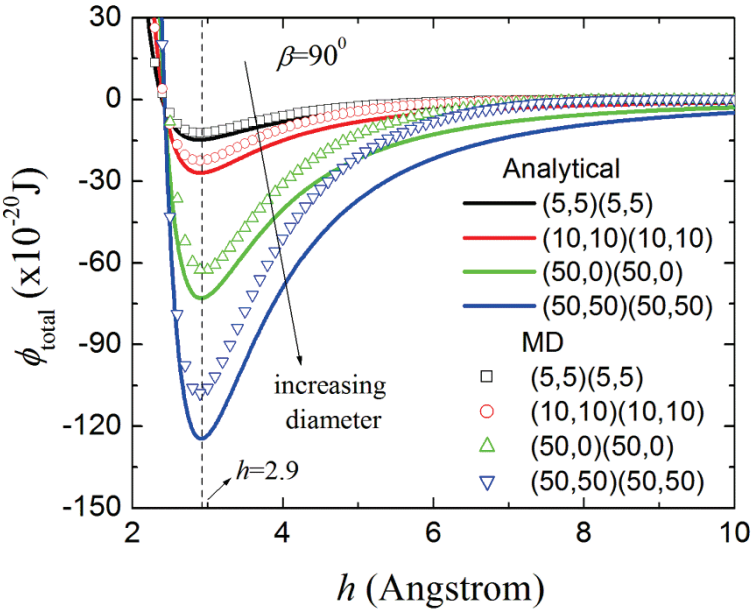

Fig. 2.19 The distribution of cohesive energy with different distance between two crossing infinite CNTs using present analytical model and molecular dynamics simulation.

To further validate the analytical results of Eq. (35), we carry out the MD simulation at β=90^0 (see Fig. 2.18). Fig. 2.19 shows the distribution of cohesive energy with different distance between two crossing infinite CNTs using our present analytical model and molecular dynamics simulations. The results from Eq. (35) agree well with results from the MD simulation. Fig. 2.20 shows the total energy on the lower and upper CNTs with different distances between two crossing infinite CNTs. We find that the two kinds of total energy are both the same. The results show that the present model is accurate to describe the cohesive energy between two crossing infinite CNTs.

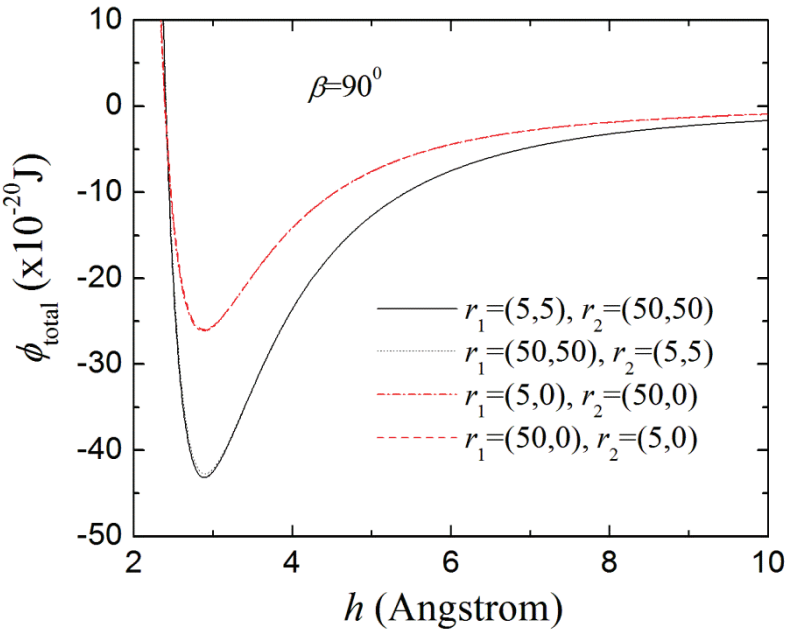

Fig. 2.20 The total cohesive energy on the lower and upper CNTs with different distance between two crossing infinite CNTs using present analytical model.

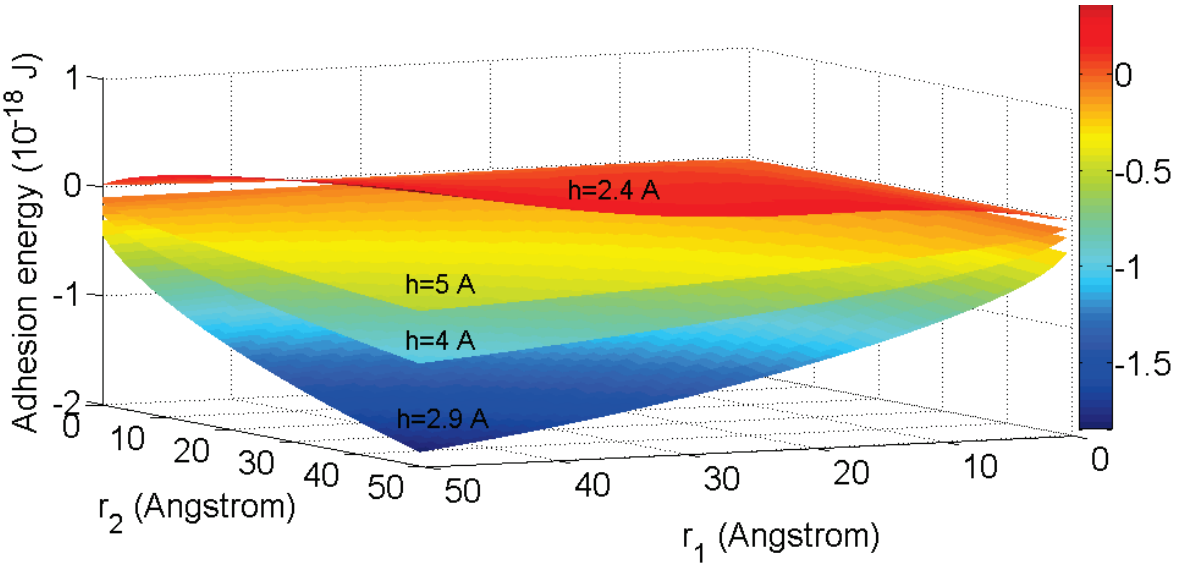

Fig. 2.21 The distribution of the cohesive energy between two crossing infinite CNTs for different radii using present analytical model.

The distribution of the cohesive energy ϕ_{total} between two crossing (β=90^0) infinite CNTs for different radii is illustrated in Fig. 2.21. The cohesive energy ϕ_{total} decreases with increasing

CNT radius for a given distance h when $\phi_{total}<0$, while ϕ_{circle} increases with increasing CNT radius when $\phi_{total}>0$.

We find that the equilibrium distance h_0 between two crossing CNTs is independent of the crossing angle β which is the same as for two crossing lines in section 2.3.1.

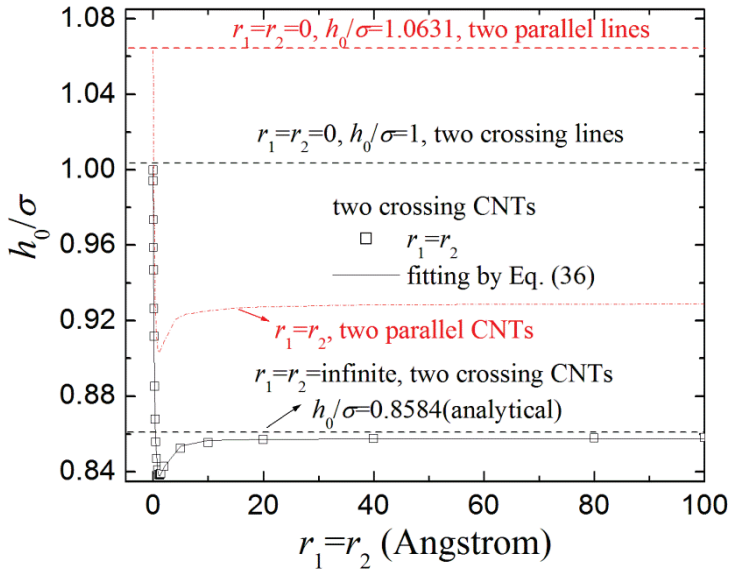

Fig. 2.22 The normalized equilibrium distance h_0/σ between two crossing infinite CNTs.

Fig. 2.22 shows the normalized equilibrium distance h_0/σ between two crossing infinite CNTs. When $r_1=r_2$, the normalized equilibrium distance decreases with increasing r_1 as $r_1<1.2$ Å, while it increases with increasing r_1 as $r_1>1.2$ Å. When $r_1=r_2=0$, the equilibrium distance from Eq. (35) tends to that of two crossing lines in Eq. (4). When $r_1=r_2>20$ Å, the equilibrium distance approaches 0.8584.

For two crossing CNTs with $r_1=r_2$, the fitting function of the normalized equilibrium distance h_0/σ is expressed as

$$h_0/\sigma = a_4\left(\frac{b_4}{(r_1+c_4)^9}-\frac{d_4}{(r_1+c_4)^3}\right)+e_4, \tag{36}$$

where a_4=3.72383, b_4=531.35085, c_4=2.73816, d_4=0.46527 and e_4=0.85742.

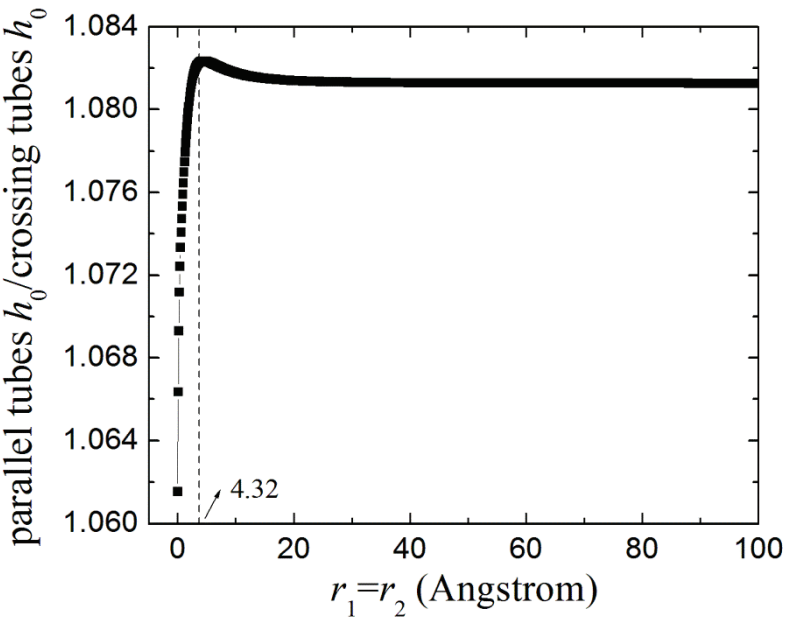

Fig. 2.23 The ratio between the equilibrium distances of the two parallel CNTs and those of the two crossing CNTs for different radii.

Fig. 2.23 shows the ratio between the equilibrium distances of the two parallel CNTs and those of the two crossing CNTs with different radii. They always higher than those between two crossing CNTs for different radii. The ratio increases with increasing r_1=r_2<4.32 Å, while they decreases with increasing r_1=r_2>1.2 Å. When r_1=r_2>20 Å, the ratio tends to a constant of 1.08127.

2.5 Concluding remarks

The surface van der Waals forces play a key role on the mechanical behavior of CNT/graphene, CNT/substrate and the two crossing CNTs. A clear understanding of the vdW interactions between two crossing CNTs or graphene sheets is crucial for their potential applications in the nanoelectromechanical systems and electronic devices.

In this paper, the cohesive energy and equilibrium distances for CNT/graphene, CNT/substrate and two crossing CNTs have been obtained by continuum modeling of the van der Waals interaction between them. Our calculations show that the cohesive energy and the equilibrium distances in the system strongly depend on their diameters, distance and crossing angles. The smaller diameters result in higher energy for a given distance and crossing angle between two crossing CNTs. The equilibrium distances always increase with increasing radius of the CNTs

and tend to the corresponding constants, while the equilibrium distances between two parallel infinite CNTs are always higher than those of two crossing CNTs and lower than that of two graphene sheets for a given radius. Compared with our molecular dynamics simulation, the analytical expressions are considerably effective to characterize the interaction between CNT/graphenes, CNT/substrate and two crossing CNTs. The obtained analytical solution can be further used to establish the cohesive law for the interactions and apply into finite element simulation (cohesive zone model) so that the interactions between the systems from nanoscale to micro/macroscale can be predicted well in the practical experiments. The analytical solution should also have great help for understanding the interaction between the nanostructures and substrates, and designing nanocomposites and nanoelectromechanical systems.

It should be noted that all the structures in the study (CNTs, graphene and substrates) are taken as rigid bodies. Actually, the CNTs and graphene might be seriously deformed when they contact with each other. The issue should be more complicated and can be further done in the next work.

Furthermore, it should be also noted that the chirality-dependent cohesive energy of the present systems is not considered in this paper, while the issue should be more accurate and useful in the practical application and will be further studied in the next work.

References:

Anantram, M.P., Leonard, F., 2006. Physics of carbon nanotube electronic devices. Rep. Prog. Phys. 69, 507-561.

Capaldi, F.M., Boyce, M.C., Rutledge, G.C., 2004. Molecular response of a glassy polymer to active deformation. Polymer 45, 1391.

Chang, T., Gao, H., 2003. Size-dependent elastic properties of a single-walled carbon nanotube via a molecular mechanics model. J. Mech. Phys. Solids 51, 1059-1074.

Chang, T., 2007. Torsional behavior of chiral single-walled carbon nanotubes is loading direction dependent. Appl. Phys. Lett. 90, 201910.

Chang, T., 2010. A molecular based anisotropic shell model for single-walled carbon nanotubes. J. Mech. Phys. Solids 58, 1422-1433.

Cranfor SW, Buehler MJ. Mechanical properties of graphyne. Carbon 2011;49:4111-21.

Golub, G.H., Welsch, J.H., 1969. Calculation of Gauss quadrature rules. Math. Comp. 23, 221-230.

Govindjee, S., Sackman, J.L., 1999. On the use of continuum mechanics to estimate the properties of nanotubes. Solid State Commun. 110, 227-230.

He, X.Q., Kitipornchai, S., Liew, K.M., 2005. Buckling analysis of multi-walled carbon nanotubes: a continuum model accounting for van der Waals interaction. J. Mech. Phys. Solids 53, 303-326.

Hernandez, E., Goze, C., Bernier, P., Rubio, A., 1998. Elastic properties of C and $B_xC_yN_z$ composite nanotubes. Phys. Rev. Lett. 80, 4502-4505.

Hertel, T., Walkup, R.E., Avouris, P. 1998. Deformation of carbon nanotubes by surface van der Waals forces. Phys. Rev. B 58, 13870.

Iijima, S., Brabec, C., Maiti, A., Bernholc, J., 1996. Structural flexibility of carbon nanotubes. J. Chem. Phys. 104, 2089-2092.

Jiang, J., Wang, J.S., Li B., 2009. Young's modulus of graphene: a molecular dynamics study. Phys. Rev. B 80, 113405.

Jiang, J., Zhao, J., Kun, Z., Rabczuk, T., 2012. Superior thermal conductivity and extremely high mechanical strength in polyethylene chains from ab initio calculation. J. Appl. Phys., 111, 124304.

Jiang, L., Guo, W., 2011. A molecular mechanics study on size-dependent elastic properties of single-walled boron nitride nanotubes. J. Mech. Phys. Solids 59, 1204-1213.

Jiang, L.Y., Huang, Y., Jiang, H., Ravichandran, G., Gao, H., Hwang, K.C., Liu, B. 2006. A cohesive law for carbon nanotube/polymer interface based on the van der Waals force. J. Mech. Phys. Solids 53, 2436-2452.

Kasti, N., 2007. Zigzag carbon nanotubes-Molecular/structural mechanics and finite element method. Int. J. Solids Struct. 44, 6914-6929.

Koening, S.P., Boddedi, N.G., Dunn, M.L., Bunch, J.S. 2011. Ultro-strong adhesion of graphene membranes. Nat. Nanotech. 6, 543-546.

Li, C.Y., Chou, T.W., 2003. A structural mechanics approach for the analysis of carbon nanotubes. Int. J. Solids Struct. 40, 2487-2499.

Li, C.Y., Chou, T.W., 2004. Elastic properties of single-walled carbon nanotubes in transverse directions. Phys. Rev. B 69, 073401.

Li, H., Guo, W., 2008. Transversely isotropic elastic properties of single-walled carbon nanotubes by a rectangular beam model for the C-C bonds. J. Appl. Phys. 103, 103501.

Lu, W.B., Wu, J., Jiang, L.Y., Huang, Y., Hwang, K.C., Liu, B., 2007. A cohesive law for multi-wall carbon nanotubes. Philos. Mag. 87, 2221-2232.

Lu, W.B., Wu, J., Song, J., Hwang, K.C., Jiang, L.Y., Huang, Y., 2008. A cohesive law for interfaces between multi-wall carbon nanotubes and polymers due to the van der Waals interactions. Comput. Methods Appl. Mech. Engrg. 197, 3261-3267.

Plimpton, S., 1995. Fast parallel algorithms for short-range molecular dynamics. J. Comput. Phys. 117, 1-19.

Ru, C.Q., 2000. Effect of van der Waals forces on axial buckling of a double-walled carbon nanotube. J. Appl. Phys. 87, 7227-7231.

Ru, C.Q., 2001. Axially compressed buckling of a doublewalled carbon nanotube embedded in an elastic medium. J. Mech. Phys. Solids 49, 1265-1279.

Saito, R., Dresselhaus, G., Dresselhaus, M.S., 1998. Physical properties of carbon nanotubes. Imperial college press, London.

Sanchez-Portal, D., Artacho, E., Soler, J.M., Rubio, A., Ordejon, P., 1999. Ab-initio structural, elastic, and vibrational properties of carbon nanotubes. Phys. Rev. B 59, 12678.

Shen, H.S., 2004. Postbuckling prediction of double-walled carbon nanotubes under hydrostatic pressure. Int. J. Solids and Struct. 41, 2643–2657.

Shepherd, J.E., 2006. Multiscale modeling of the deformation of semi-crystalline polymers. Ph. D thesis. Georgia Institute of Technology, USA.

To, C., 2006. Bending and shear moduli of single-walled carbon nanotubes. Finite Elem. Anal. Des. 42, 404-413.

Tserpes, K.I., Papanikos, P., 2005. Finite element modeling of single-walled carbon nanotubes. Composites B 36, 468-477.

Vaccarini, L., Goze, C., Henrard, L., Hernandez, E., Bernier, P., Rubio, A, 2000. Mechanical and electronic properties of carbon and boron-nitride nanotubes. Carbon 38, 1681-1690.

Waheed, N., 2005. Molecular simulation of crystal growth in alkane and polyethylene melts. Ph. D thesis. Cornell University, USA.

Wang, C.Y., Ru, C.Q., Mioduchowski, A., 2003. Axially compressed buckling of pressured multiwall carbon nanotubes. Int. J. Solids Struct. 40, 3893-3911.

Wang, C.Y., Zhang, Y.Y., Wang, C.M., Tan, V.B.C., 2007. Buckling of carbon nanotubes: Aliterature survey. J. Nanosci. Nanotech. 7, 4221-4247.

Wu, J., Hwang, K.C., Huang, Y., 2008. An atomistic-based finite-deformation shell theory for single-wall carbon nanotubes. J. Mech. Phys. Solids 56, 279-292.

Xia, J.R., Gama, B.A., Gillespie Jr., J.W., 2005. An analytical molecular structural mechanics model for the mechanical properties of carbon nanotubes. Int. J. Solids Struct. 42, 3075-3092.

Yakobson, B.I., Brabec, C.J., Bernholc, J., 1996. Nanomechanics of carbon tubes: instability beyond linear response. Phys. Rev. Lett. 76, 2511-2514.

Yoon, J., Ru, C.Q., Mioduchowski, A., 2003. Sound wave propagation in multiwall carbon nanotubes. J. Appl. Phys. 93, 4801-4806.

Zeng, Q., Wang, S., Yang, L., Wang, Z., Pei, T., Zhang, Z., Peng, L.M., Zhou, W., Liu, J., Zhou, W., Xie, S., 2012. Carbon nanotubes arrays based high-performance infrared photodetector [Invited]. Opt. Mat. Express 2, 839-848.

Zhang, Z., Guo, W., Tai, G., 2007. Coaxial nanocable: Carbon nanotube core sheathed with boron nitride nanotube. Appl. Phys. Lett. 90, 133103.

Zhang, Z., Guo, W., 2008. Energy-gap modulation of BN ribbons by transverse electric fields: First-priciples calculations. Phys. Rev. B 77, 075403.

Zhao, H., Min, K., Aluru, R., 2009. Size and chirality dependent elastic properties of graphene nanoribbons under uniaxial tension. Nano Lett., 9, 3012-3015.

Zhao, J., Nagao, S., Zhang, Z. 2010. Thermo-mechanical properties dependence on chain length in bulk polyethylene: coarse-grained molecular dynamics simulations. J. Mater. Res. 25, 537-544.

Zhao, J., Guo, W., Zhang, Z.L., Rabczuk, T., 2011. Size-dependent elastic properties of crystalline polymers via a molecular mechanics model. Appl. Phys. Lett. 99, 241902.

Zhao, J., Guo, W., Rabczuk, T., 2012. An analytical molecular mechanics model for the elastic properties of crystalline polyethylene. J. Appl. Phys. 112, 033516.

Zheng, Q.S., Jiang, B., Liu, S.P., Weng, Y.X., Lu, L., Xue, Q.K., Zhu, J., Jiang, Q., Wang, S., Peng, L.M., 2008. Self-retracting motion of graphite microflakes, Phys. Rev. Lett. 100, 067205.

Chapter 3

Novel coarse-grained potentials of single-walled carbon nanotubes*

Abstract

The novel coarse-grained (CG) potentials of single-walled carbon nanotubes (SWCNTs) are developed for studying static and dynamic behavior of CNT bundles and buckypaper. The explicit expressions of the CG stretching, bending and torsion potentials for the nanotubes are obtained by the stick-spiral and the beam models. Based on our analytical results of cohesive energy between two parallel and crossing SWCNTs from the van der Waals interactions, the non-bonded CG potentials between two different CG beads are completely established. Combination of the bonded and non-bonded terms makes the CG model accurately for large deformation of the complex CNT systems. Checking against full atom molecular dynamics calculations and our analytical results shows that the present CG potentials have high accuracy. The established CG potentials are used to study the mechanical properties of the CNT bundles and buckypaper efficiently at a minor fraction of the computational cost, which show great potential for designing micro- and nanomechanical devices and systems.

3.1 Introduction

Carbon nanotubes (CNTs) have attracted considerable interests due to their excellent mechanical, electronic, thermal, optical and structural properties, which enable them for many applications (Baughman et al., 2002). The mechanical properties of CNTs have been extensively studied by continuum modeling and atomistic simulations in the past decade (Odergard et al., 2002; Arroyo and Belytschko, 2002; Zhang et al., 2002; Chang and Gao, 2003; Li and Guo, 2008) since the properties could be important in the CNT-based devices. Atomistic-based methods such as classical molecular dynamics (MD) (Iijima et al., 1996; Yakobson et al., 1996), tight-binding MD (Hernandez et al., 1998; Zhao et al., 2009), and density functional theory (Sanchez-Portal et al., 1999; Zhang et al., 2007) have been used to study the mechanical properties of CNTs. However, compared with bottom-up approaches, top-down approaches may substantially reduce

* The work has been submitted on <<Journal of Mechanics and Physics of Solids>> in 2013.

the computational costs and are thus frequently used in related investigations. By equating the molecular potential energy of nano-materials to the mechanical strain energy of a representative continuum model, Odergard et al. (2002) obtained a relation between effective bending rigidity and molecular properties of a grapheme sheet. Chang and Gao (2003) established an analytical stick-spiral model (SSM) based on molecular mechanics method and for the first time derived closed-form expressions for the elastic properties of different SWCNTs. An improved model by Jiang and Guo (2011) was used to investigate the elastic properties of single-walled boron nitride nanotubes. Li and Chou (2003, 2004) presented a beam model for carbon-carbon bonds based on the molecular mechanics. By extending the two analytical methods to crystalline polymers (Zhao et al., 2010), we presented the SSM and beam model to investigate the size-dependent elastic properties of crystalline polyethylene (PE) (Zhao et al., 2011, 2012). From all of these works, we found the analytical methods are especially useful for linking molecular and continuum mechanics, since the mechanical properties can be directly connected by the closed-form expressions.

Recently, CNT networks feature outstanding mechanical performance and hierarchical structures and network topologies, which have been taken as a potential saving-energy material (Xie et al., 2011). In the synthesis of nanocomposites, the formation of the CNT bundles is a challenge to remain in understanding how to measure and predict the properties of such large systems (Ajayan and Banhart, 2002; Kis et al., 2004). On the other hand, the dispersion of CNTs within the matrics and their interfaces are of critical importance to establish efficient load-bearing performance for large-scale applications (Cranford et al., 2010). However, this problem has not been solved satisfactorily yet. Zhigilei et al. (2005) developed a mesoscopic model of individual SWCNTs by full atom molecular dynamics (MD) simulations with MFF potentials. The stretching, bending and torsion CG potentials of different SWCNTs were reported, while the non-bonded CG potentials were not considered in this work. Buehler and his group developed a mesoscale model to study the nanomechanical characterization of CNT buckypaper and bundle formation (Buehler, 2006; Cranford and Buehler, 2010; Cranford et al., 2010). Xu's group (Xie et al., 2011; Wang et al., 2012) and Li and Kröger (2012) detailed studied the mechanical properties of the two-dimensional and three-dimensional CNT networks based on the mesoscale model. However, the potentials of one kind of single-walled CNT (SWCNT) (5,5) were only

reported and the torsion potentials were neglected in their work. The non-bonded potentials between the two identical CG beads of two parallel (5,5) SWCNTs were only provided based on the full atom MD results (Buehler, 2006). Actually, the two parameters of their Lennard-Jones (LJ) potentials are obtained by fitting the adhesion energy at the equilibrium distance between two (5,5) CNTs, and the results are only effective under small deformation by comparison the full atom MD with the CG MD simulations. However, the large deformations frequently occur in the practical applications. In particular, the non-bonded CG potentials between two different parallel CNTs and two crossing CNTs have not been reported yet, which should be more important to study the mechanical properties of CNT bundles, buckypaper and networks.

Therefore, it is important to develop the non-bonded coarse-grained (CG) potentials between two different parallel and two different crossing SWCNTs. At the nanoscale, the weak van der Waals (vdW) interactions govern the structural organization and the mechanical properties of CNT bundles and networks (Cranford et al., 2010; Ru, 2000, 2001; Zhou et al., 2007). The interactions of individual CNTs in larger-scale structures often play a critical role in the mechanical characterization of CNT systems. How to provide accurate CG non-bonded potentials between two same CG beads (especially between two different CG beads) for two parallel CNTs and two crossing CNTs is a critical issue for obtaining reliable results from the CG MD simulations.

In this paper, the novel CG potentials of different SWCNTs are developed from a molecular mechanics model, in which the stretching, bending and torsion CG potentials are obtained based on the SSM and the beam model. In particular, the two different non-bonded CG potentials between two parallel and crossing CNTs are completely established based on the cohesive energy between the two CNTs from vdW interactions. Following the similar idea (Buehler, 2006), we further provide the first kind non-bonded CG model to obtain the two parameters of the non-bonded CG LJ potentials between two different CNTs, which is accurate enough when the displacement is close to the equilibrium distance between two parallel and two crossing CNTs. To obtain a CG model for large deformations, the second kind non-bonded CG model is further developed. We find the second kind CG model has high accuracy by checking against the full atom MD, CG MD simulations and the analytical results. The established CG potentials are

efficiently used to study the mechanical properties of the CNT bundles and buckypaper at a minor fraction of the computational cost, which should be also of great help for designing the corresponding nanomechanical devices and systems.

The paper is organized as follows: Section 3.2 shows the CG bond stretching, bending and torsion potentials of SWCNTs based on the stick-spiral and the beam models. In section 3.3, the non-bonded CG potentials between two parallel CNTs and their applications in different free vibrations and bundles are systematically investigated. Section 3.4 describes the non-bonded CG potentials between two crossing CNTs and their application for studying the mechanical properties of the buckypaper. In section 3.5, the effects of the equilibrium bond length and the staggered and non-staggered positions between the two CG beads on the CG potentials, and the advantages and limitations of the CG potentials are discussed. The paper is concluded in section 3.6.

3.2 Coarse-grained stretching, bending and torsion potentials of SWCNTs

For CNT bundles, buckypaper and networks, the vdW interactions between two CNTs have a great effect on their organization and mechanical properties. To reduce the computational cost, the CG model is developed in this paper so that the large-scale CNT bundles and networks can be studied based on the model (Buehler, 2006). Fig. 3.1 shows the full atom SWCNT and its CG beads, in which the mass center per unit length is always along the central axis of the CNT. All bond angles among the CG beads are always 180^0 (Buehler, 2006), while the equilibrium bond length (EBL) r_0 in the CG model can be determined later. The mass per CG bead is equal to $2\pi r r_0 \rho_{ge} m_c$, where r is the radius of the CNT, m_c is the mass of carbon atom, ρ_{ge} (approximate 0.3818 $Å^{-2}$) represents the area density of graphene which may be slightly different from the area density of graphene due to the curvature effect in the CNT (He et al., 2005; Jiang et al., 2006). Fig. 3.2 shows two different SWCNTs and their CG model, where r_1 and r_2 are the radii of the two SWCNTs, respectively.

In the framework of molecular dynamics, the total energy, U, of a CNT at small strains along the axial direction of CNT can be expressed as a sum of energies associated with the variance of bond length, U_b, and bond angle, U_θ, i.e., (Chang and Gao, 2003)

$$U = U_b + U_\theta = \frac{1}{2}\sum_i K_b \left(db_i\right)^2 + \frac{1}{2}\sum_j K_\theta \left(d\theta_j\right)^2 , \tag{1}$$

where db_i is the bond elongation of bond i and $d\theta_j$ is the variance of bond angle j, and K_b and K_θ are the related force constant.

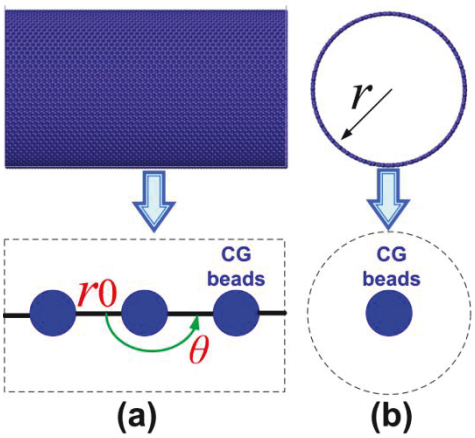

Fig. 3.1 The CG model for a SWCNT. (a) slide view; (b) front view.

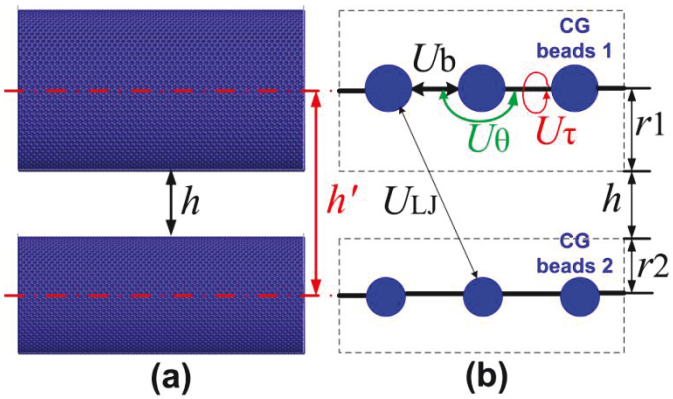

Fig. 3.2 The two parallel SWCNTs and their CG model. (a) full atom structure for two parallel SWCNTs; (b) CG model and CG potentials in (a).

Based on the SSM (Chang and Gao, 2003; Chang, 2010), the Young's modulus and shear modulus of a CNT can be expressed as

$$E = \frac{4\mu K_b t}{\sqrt{3}\left(\lambda + 3\mu\right)} , \tag{2}$$

$$G = \frac{\mu K_b t}{\sqrt{3}\left(\zeta + \eta\mu\right)} \ , \tag{3}$$

where $\mu = K_b/(K_\theta b^2)$ and t is the thickness of the CNT, and b=1.42 Å is the initial bond length between two carbons. The other parameters strongly depend on the chirality of the CNT and can be found in Appendix. In this paper, K_b=742 nN/nm and K_θ=1.42 nN nm is chosen for the continuum model 1 (Chang, 2010), and K_b=730 nN/nm and K_θ=1.35 nN nm is chosen for the continuum model 2 (Li and Guo, 2008).

For the CG model in Fig. 2, the total energy, U_{cg}, of a CNT can be expressed as a sum of energies associated with the variance of bond length, U_{cgb}, bond angle, $U_{cg\theta}$, and torsion angle, $U_{cg\tau}$, i.e., (Chang and Gao, 2005)

$$U_{cg} = U_{cgb} + U_{cg\theta} + U_{cg\tau} = \frac{1}{2}\sum_i K_{cgb}\left(db_{cgi}\right)^2 + \frac{1}{2}\sum_j K_{cg\theta}\left(d\theta_{cgj}\right)^2 + \frac{1}{2}\sum_k K_{cg\tau}\left(d\tau_{cgk}\right)^2 \ , \tag{4}$$

where db_{cgi} is the bond elongation of bond i, $d\theta_{cgj}$ is the variance of bond angle j and $d\tau_{cgk}$ is the variance of torsion angle k, and K_{cgb}, $K_{cg\theta}$ and $K_{cg\tau}$ are the related force constant.

From the beam model theory (Li and Chou, 2003; 2004), it is easy to obtain the equation based on the equilibrium energy between the SSM and beam model,

$$K_{cgb} = \frac{EA}{r_0} \ , \tag{5}$$

$$K_{cg\theta} = \frac{EI}{r_0} \ , \tag{6}$$

$$K_{cg\tau} = \frac{GJ}{r_0} \ , \tag{7}$$

where A is the cross section area of the CNT, I and J are the in-plane and out-of-plane moments of inertia, respectively. Zhigilei et al. (2005) reported the three force constants of the CG model by using full atom MD with MFF potential.

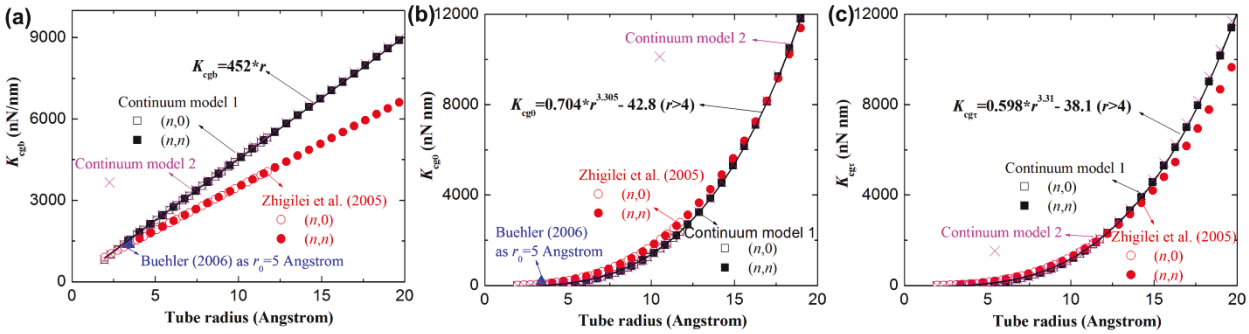

Fig. 3.3 The distribution of K_{cgb}, $K_{cg\theta}$ and $K_{cg\tau}$ with different radii CNTs using analytical model, full atom MD simulations. (a) K_{cgb}, (b) $K_{cg\theta}$, (c) $K_{cg\tau}$.

The three force constants distribution with CNT radius is plotted from our analytical results and Zhigilei et al.'s simulations in Fig. 3.3. From Fig. 3.3a, the K_{cgb} agrees well with each other for the small CNTs. Our analytical results are higher than Zhigilei et al.'s results for large radius since the two different potentials are used in our analytical model and Zhigilei et al.'s model. The other two constants $K_{cg\theta}$ and $K_{cg\tau}$ are reasonable by comparison with Zhigilei et al.'s results. Note that r_0 is chosen as 5 Å so that the non-bonded CG model is effective enough (detailed discussion is given later). Moreover, the Buehler's results based on r_0=5 Å are also plotted. We find that his K_{cgb}=1390 nN/nm for the (5,5) CNT agrees well with the other two results (analytical 1511 nN/nm and Zhigilei et al.'s 1370 nN/nm), while $K_{cg\theta}$=199 nN nm is higher than the other two results (analytical 22 nN nm and Zhigilei et al.'s 73 nN nm). To conveniently use our analytical model, the fitting functions of the three constants are also presented in Fig. 3.3.

The present CG stretching, bending and torsion potentials for CNTs are obtained by using the same method with Zhigilei et al's approach. It has been also validated that the CG model can reproduce well the dynamic behavior of individual CNTs predicted in atomistic simulations (Zhigilei et al., 2005). More complicated validation will be given later.

It should be noted that the Eq. (5), Eq. (6) and Eq. (7) are efficient enough under small deformation for individual SWCNT. Under large deformation, Chang's group (Geng and Chang, 2006) established a nonlinear stick-spiral model to describe the mechanical behavior of

SWCNTs based on a Morse type potential. The nonlinear model could be directly used to develop the nonlinear CG stretching, bending and torsion potentials.

3.3 Coarse-grained non-bonded potentials for two parallel SWCNTs and their applications

3.3.1 Coarse-grained non-bonded potentials for two parallel SWCNTs

3.3.1 .1 Cohesive energy between two parallel SWCNTs

The energy of the vdW interactions between the two carbons of CNTs (He et al., 2005) is given by

$$V(d) = 4 \in \left[\left(\frac{\sigma}{d} \right)^{12} - \left(\frac{\sigma}{d} \right)^{6} \right], \tag{8}$$

where d is the distance between the interacting atoms, $\in$ is the depth of the potential, σ is a parameter that is determined by the equilibrium distance ($\in$= 2.8437 mev and σ=3.4 Å are adopted from the literatures) (Yakobson, 1996; Chang, 2007).

To obtain the cohesive energy between two parallel SWCNTs, Fig. 2.11 shows the coordinate system and a schematic diagram of the two parallel infinite CNTs. The upper and lower CNT radii are r_1 and r_2, respectively. The closest distance between the two parallel CNTs edge is h.

The energy per unit length along the z direction on the lower CNT from the vdW interactions can be written as (Zhao et al., 2013a)

$$\phi_{cicle} = \pi \in \sigma^6 \rho^2 r_1 r_2 \left(\frac{63}{8} \sigma^6 \int_0^{\pi} \frac{F_5 \left\lfloor \frac{2\sqrt{a_0 r_1}}{r_1 + a_0} \right\rfloor}{(r_1 + a_0)^{11}} d\theta_2 - 12 \int_0^{\pi} \frac{F_2 \left\lfloor \frac{2\sqrt{a_0 r_1}}{r_1 + a_0} \right\rfloor}{(r_1 + a_0)^{5}} d\theta_2 \right), \tag{9}$$

where all the parameters can be seen in Eq. (29) of chapter 2.

Eq. (9) can be completely solved by Gaussian quadrature (Golub and Welsch, 1969). To show the validity of the present continuum model, the distribution of the analytical cohesive energy with distance by Eq. (9) for two different parallel CNTs is plotted in Fig. 3.4. The analytical

results are in excellent agreement with the full atom MD results (detailed process can be seen in our previous work (Zhao et al., 2013a)), in which the MD simulation is performed using LAMMPS (Plimpton, 1995) with the AIREBO potential and periodic boundary conditions are applied along the center axis of the CNTs (the LJ cutoff radius is chosen 60 Å which is an enough distance to get accurate results). It validates the accuracy of the continuum model of Eq. (9) in the description of the cohesive energy between two parallel CNTs.

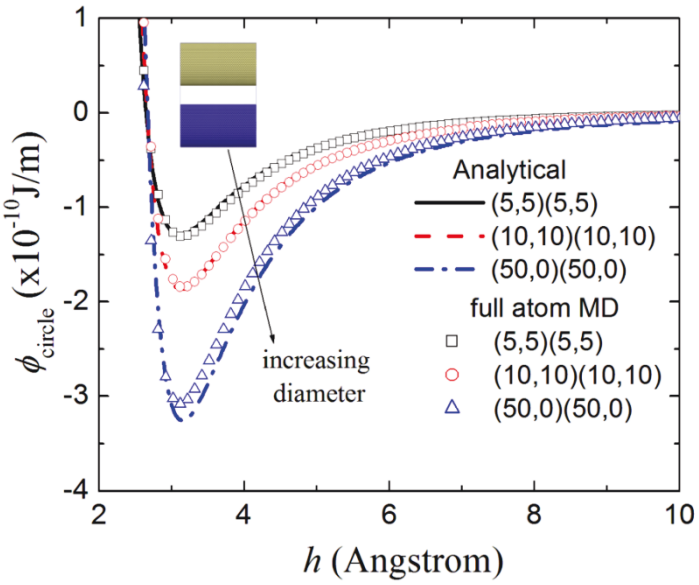

Fig. 3.4 The distribution of cohesive energy with different distance between two parallel SWCNTs using present analytical model and full atom molecular dynamics simulations.

3.3.1.2 Coarse-grained non-bonded potentials between two parallel SWCNTs

To obtain the non-bonded CG potentials, the two parallel CNTs can be taken as two rows of CG beads in Fig. 3.2. The two rows of CG beads can be further taken as two continuum lines in Fig. 3.5, in which the mass per unit length of line is equal to $2\pi r\rho_{ge}m_c$. A similar method was effectively used to study the crystalline polymers in our previous work (Zhao et al., 2011; Zhao et al., 2012).

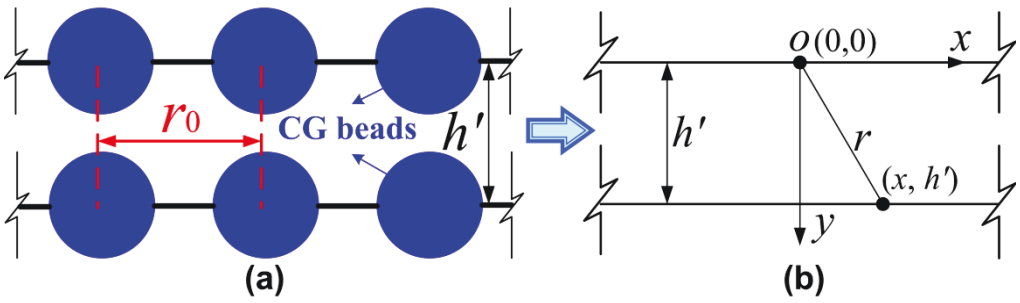

Fig. 3.5 The coordinate system and a schematic diagram of the two parallel CG beads chains and the first non-bonded CG model. (a) CG beads chains, (b) first non-bonded CG model.

If we assume that the vdW interaction between two CG beads is also the function of 6-12 LJ potential in Eq. (8), the cohesive energy per unit length between two parallel lines can be obtained

$$\phi_{line-line} = \rho_l^2 \int_{-\infty}^{\infty} V(d)\,dx, \tag{10}$$

where $d^2=x^2+h'^2$, and ρ_l is the line density ($\rho_l=1/r_0$, r_0 is the EBL of the CG model).

Substituting Eq. (8) into Eq. (10) gives

$$\phi_{cg\,6-12} = 4 \in_{6-12} \rho_l^2 \sigma_{6-12}{}^6 \left(\frac{63\pi}{256} \sigma_{6-12}{}^6 \frac{1}{h'^{11}} - \frac{3\pi}{8} \frac{1}{h'^5} \right), \tag{11}$$

where $\in_{6-12}$ is the depth and $\sigma_{6\text{-}12}$ is the dispersive parameter of the CG 6-12 LJ potential. From the energy minimum condition $\frac{\partial \phi_{cg\,6-12}}{\partial h'_{6-12}} = 0$, the equilibrium distance h_0' between the two lines can be given as $h_0'=1.0631\sigma_{6\text{-}12}$. Note that r_0 is chosen as 5 Å so that the continuum modeling of Eq. (11) is effective enough in Fig. 3.6 (detailed discussion is given later). Fig. 3.6a shows the adhesion energy (that is, the absolute minimum value of ϕ_{circle} in Eq. (9)) and the equilibrium distance h_0' (see Fig. 3.2 and Fig. 3.5) between two same CNTs from Eq. (9). The analytical results are in excellent agreement with those of full atom MD simulations. In view of $\sigma_{6\text{-}}$

$_{12}$=h_0'/1.0631, the values of $\sigma_{6\text{-}12}$ are plotted in Fig. 3.6c. Substituting $\sigma_{6\text{-}12}$=h_0'/1.0631 and $\phi_{cg6\text{-}12}$=minimum value of ϕ_{circle} into Eq. (11) gives the values of $\in_{6-12}$ in Fig. 3.6b.

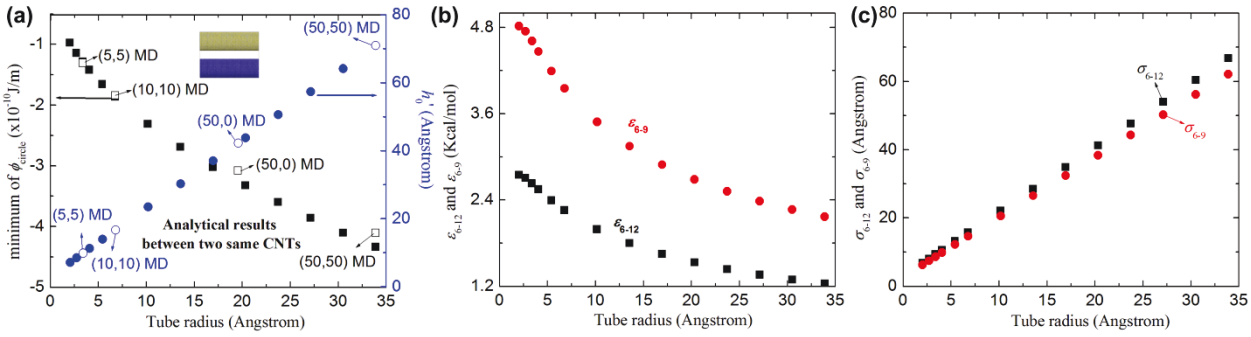

Fig. 3.6 The minimum of ϕ_{circle} and h_0' distribution with CNT radius from Eq. (7) and the two dispersive parameters of CG 6-12 and CG 6-9 LJ potentials by fitting the results. (a) The minimum of ϕ_{circle} and h_0' distribution with CNT radius from Eq. (7), (b) $\in_{6-12}$ and $\in_{6-9}$ of CG 6-12 and CG 6-9 LJ potentials, (c) $\sigma_{6\text{-}12}$ and $\sigma_{6\text{-}9}$ of CG 6-12 and CG 6-9 LJ potentials.

In our previous work and available published articles (Zhao et al., 2010; Nielsen et al., 2003), the 6-9 LJ potentials are mainly used to describe the vdW interactions between two CG beads for polymers and biomaterials. The 6-9 LJ potentials is expressed as

$$V(d) = 4 \in \left[\left(\frac{\sigma}{d} \right)^9 - \left(\frac{\sigma}{d} \right)^6 \right], \tag{12}$$

where all the parameters meanings are the same with those in Eq. (8).

Substituting Eq. (12) into Eq. (10) gives

$$\phi_{cg6-9} = 4 \in_{6-9} \rho_l^2 \sigma_{6-9}^6 \left(\frac{32}{35} \sigma_{6-9}^3 \frac{1}{h'^8} - \frac{3\pi}{8} \frac{1}{h'^5} \right), \tag{13}$$

where $\in_{6-9}$ is the depth and $\sigma_{6\text{-}9}$ is the dispersive parameter of the CG 6-9 LJ potential. From the energy minimum condition $\frac{\partial \phi_{cg6-9}}{\partial h'_{6-9}} = 0$, the equilibrium distance h_0' between the two lines can be

given as h_0'=1.0748$\sigma_{6\text{-}9}$. Similar to the CG 6-12 LJ potential fitting (r_0=5 Å), the two parameters of $\in_{6-9}$ and $\sigma_{6\text{-}9}$ can be obtained in Figs. 3.5b and c. It should be noted that all above results are only fitted by the minimum value of the cohesive energy and the corresponding equilibrium distance h_0'. Similar method can be found in previous work (Buehler, 2006). **Note that we define above CG 6-12 (and 6-9) non-bonded model as CG model1.**

In order to conveniently use the non-bonded CG potentials of the CG model1, all the values of minimum of ϕ_{circle}, h_0', $\in_{6-12}$ *and* $\in_{6-9}$, and $\sigma_{6\text{-}12}$ and $\sigma_{6\text{-}9}$ between two different SWCNTs are shown in Tables 3.1, 3.2, 3.3, 3.4, 3.5 and 3.6.

Table 3.1. The minimum of ϕ_{circle} from Eq. (9) (unit: 10^{-10} J/m).

CNT	(5,5)	(10,10)	(15,15)	(20,20)	(25,25)	(30,30)
(5,5)	-1.2888	-1.5127	-1.6348	-1.7127	-1.7668	-1.8066
(10,10)	-1.5127	-1.8642	-2.0557	-2.1838	-2.2760	-2.3455
(15,15)	-1.6348	-2.0557	-2.3128	-2.4821	-2.6070	-2.7031
(20,20)	-1.7127	-2.1838	-2.4821	-2.6914	-2.8448	-2.9645
(25,25)	-1.7668	-2.2760	-2.6070	-2.8448	-3.0238	-3.1660
(30,30)	-1.8066	-2.3455	-2.7031	-2.9645	-3.1660	-3.3238

Table 3.2. The h_0' of CG model1 from Eq. (9) (unit: Å).

CNT	(5,5)	(10,10)	(15,15)	(20,20)	(25,25)	(30,30)
(5,5)	9.9114	13.3120	16.7127	20.1034	23.4941	26.8847
(10,10)	13.3020	16.7027	20.1034	23.4941	26.8847	30.2754
(15,15)	16.7027	20.1034	23.4941	26.8847	30.2754	33.6661
(20,20)	20.0934	23.4941	26.8847	30.2754	33.6661	37.0568
(25,25)	23.4841	26.8847	30.2754	33.6661	37.0568	40.4474
(30,30)	26.8747	30.2754	33.6661	37.0568	40.4474	43.8381

Table 3.3. The $\varepsilon_{6\text{-}12}$ values of the CG 6-12 LJ potential of CG model1 for r_0=5 Å (unit: Kcal/mol).

CNT	(5,5)	(10,10)	(15,15)	(20,20)	(25,25)	(30,30)
(5,5)	2.6280	2.2966	1.9770	1.7219	1.5199	1.3581
(10,10)	2.2984	2.2558	2.0667	1.8786	1.7110	1.5658
(15,15)	1.9782	2.0667	1.9896	1.8659	1.7403	1.6228
(20,20)	1.7227	1.8786	1.8659	1.7967	1.7078	1.6168
(25,25)	1.5205	1.7110	1.7403	1.7078	1.6492	1.5820
(30,30)	1.3586	1.5658	1.6228	1.6168	1.5820	1.5324

Table 3.4. The $\sigma_{6\text{-}12}$ values of the CG 6-12 LJ potential of CG model1 for r_0=5 Å (unit: Å).

CNT	(5,5)	(10,10)	(15,15)	(20,20)	(25,25)	(30,30)
(5,5)	9.3231	12.5219	15.7207	18.9101	22.0996	25.2890
(10,10)	12.5125	15.7113	18.9101	22.0996	25.2890	28.4784
(15,15)	15.7113	18.9101	22.0996	25.2890	28.4784	31.6678
(20,20)	18.9007	22.0996	25.2890	28.4784	31.6678	34.8573
(25,25)	22.0902	25.2890	28.4784	31.6678	34.8573	38.0467
(30,30)	25.2796	28.4784	31.6678	34.8573	38.0467	41.2361

Table 3.5. The $\varepsilon_{6\text{-}9}$ values of the CG 6-9 LJ potential of CG model1 for r_0=5 Å (unit: Kcal/mol).

CNT	(5,5)	(10,10)	(15,15)	(20,20)	(25,25)	(30,30)
(5,5)	4.0824	3.5676	3.0710	2.6747	2.3610	2.1097
(10,10)	3.5703	3.5041	3.2104	2.9183	2.6579	2.4323
(15,15)	3.0729	3.2104	3.0906	2.8986	2.7035	2.5208
(20,20)	2.6761	2.9183	2.8986	2.7910	2.6529	2.5116
(25,25)	2.3620	2.6579	2.7035	2.6529	2.5618	2.4575
(30,30)	2.1105	2.4323	2.5208	2.5116	2.4575	2.3804

Table 3.6. The $\sigma_{6\text{-}9}$ values of the CG 6-9 LJ potential of CG model1 for r_0=5 Å (unit: Å).

CNT	(5,5)	(10,10)	(15,15)	(20,20)	(25,25)	(30,30)
(5,5)	9.2213	12.3852	15.5492	18.7038	21.8584	25.0130
(10,10)	12.3759	15.5399	18.7038	21.8584	25.0130	28.1676
(15,15)	15.5399	18.7038	21.8584	25.0130	28.1676	31.3222
(20,20)	18.6945	21.8584	25.0130	28.1676	31.3222	34.4769
(25,25)	21.8491	25.0130	28.1676	31.3222	34.4769	37.6315
(30,30)	25.0037	28.1676	31.3222	34.4769	37.6315	40.7861

To check the accuracy of the CG potentials, Fig. 3.7 shows the distribution of the cohesive energy with h' using our analytical model, full atom MD and CG MD simulations. The cohesive energy of CG 6-12 LJ and 6-9 LJ MD results which is close to the equilibrium distance are in good agreement with the analytical and full MD results, while the difference sharply increases with increasing or decreasing h'. In other words, all above CG 6-12 and 6-9 LJ fitting parameters are effective when the CG MD structures are subjected to very small deformation (the two chains of CG MD structures are built in the inset of Fig. 3.7).

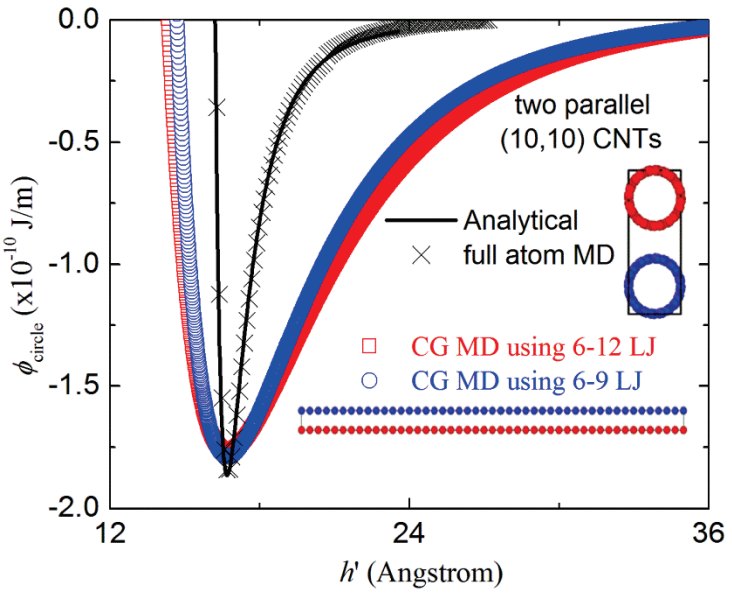

Fig. 3.7 The distribution of the cohesive energy between two parallel (10,10) CNTs using analytical model, full atom MD and CG MD simulations.

In order to obtain more accurate non-bonded CG potentials which can be used to describe the large deformation, we can use the second CG 6-12 and 6-9 LJ functions of Eq. (11) and Eq. (12) (h' is replaced by h) to fit the ϕ_{circle}-h (like Fig. 3.4) curves, as shown in Fig. 3.8. **Note that we define this kind CG 6-12 (and 6-9) non-bonded model as CG model2.**

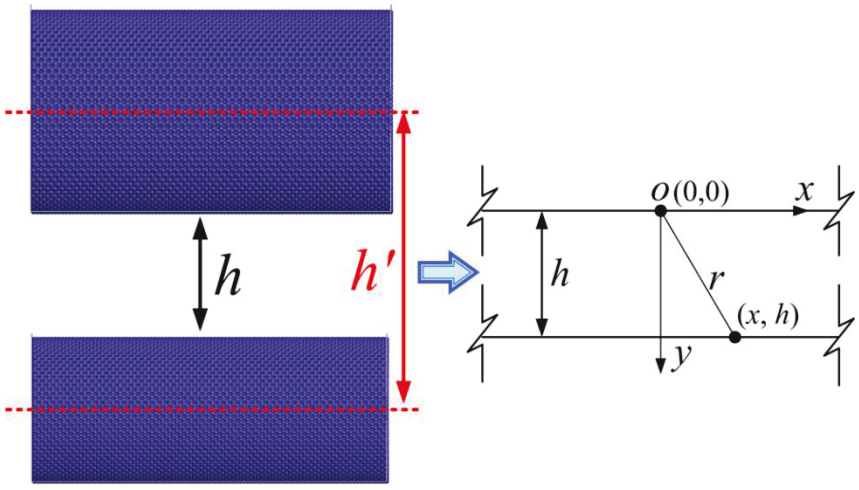

Fig. 3.8 The second CG non-bonded two continuum lines model for two parallel SWCNTs.

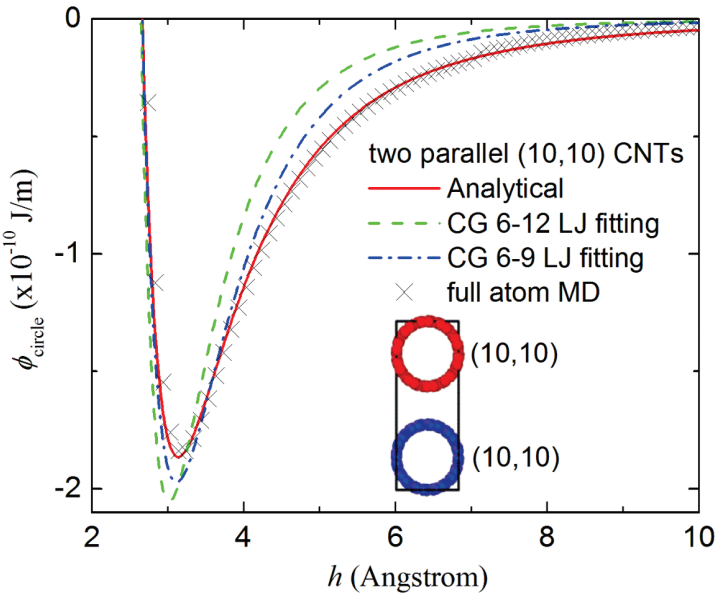

Fig. 3.9 The cohesive energy distribution with different distance between two (10,10) CNTs using analytical model, full atom molecular dynamics simulation and the second CG 6-12 LJ potential of Eq. (18) and 6-9 LJ potential of Eq. (20) fitting.

From Fig. 3.9, we find that the fitting results from 6-9 LJ potential are better than those from 6-12 LJ potential by comparison with our analytical and full atom MD results. The two parameters $\in$ and σ of the two CG LJ potentials strongly depend on the radii of the two CNTs, in which the EBL r_0 has also a large effect on $\in$.

To determine the two parameters, we assume $\in_{6-12}$ *and* $\in_{6-9}$ from 1 to 10 Å, and then the ten kinds of $\in_{6-12}$ *and* $\in_{6-9}$ and the corresponding $\sigma_{6\text{-}12}$ and $\sigma_{6\text{-}9}$ are obtained by fitting the analytical results of (5,5) CNTs. The CG MD simulations are performed based on the obtained parameters of the two 6-12 and 6-9 LJ potentials, as shown in Fig. 3.10. The results are both accurate when the EBL r_0 is not more than 5 Å, and the accuracy sharply decreases with increasing r_0 (r_0>5 Å). As r_0=10 Å, the minimum cohesive energy is almost two times lower than that of $r_0 \leq 5$ Å. Therefore, the EBL r_0 is better chosen as 5 Å to reduce the computational costs and keep the accuracy.

From the above analysis, the continuum line model is effective only as $r_0 \leq 5$ Å, while the discrete model (Buehler, 2006) should be used to fit the analytical results when r_0>5 Å in which the fitting process will be more difficult and complicated. It should be noted that the non-staggered position between two CG beads is only considered here.

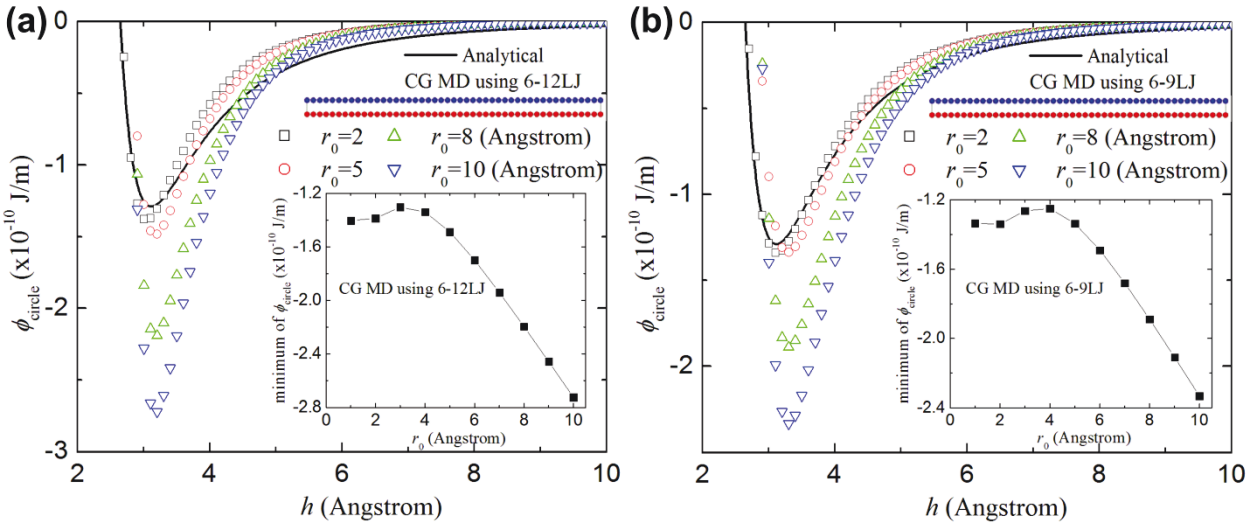

Fig. 3.10 The cohesive energy distribution with different distance between two (5,5) CNTs using analytical model and CG MD simulation with different LJ potentials for different r_0. (a) CG 6-12 LJ potential, (b) CG 6-9 LJ potential.

As shown in Figs. 3.11a and b, we find that the values of $\in_{6-12}$ *and* $\in_{6-9}$ increase with increasing CNT radius, while $\sigma_{6\text{-}12}$ and $\sigma_{6\text{-}9}$ increase with increasing radius and tends to a constant for CG 6-12 LJ and 6-9 LJ potentials. The equilibrium distance h_0 between two parallel SWCNTs is plotted in Fig. 3.11c. The values of CG 6-9 LJ potentials are closer to the analytical results than those of CG 6-12 LJ potentials. To conveniently use the CG non-bonded potentials, all the values of $\in_{6-12}$ *and* $\in_{6-9}$ and $\sigma_{6\text{-}12}$ and $\sigma_{6\text{-}9}$ between two different SWCNTs are shown in Table 3.7, 3.8, 3.9 and 3.10.

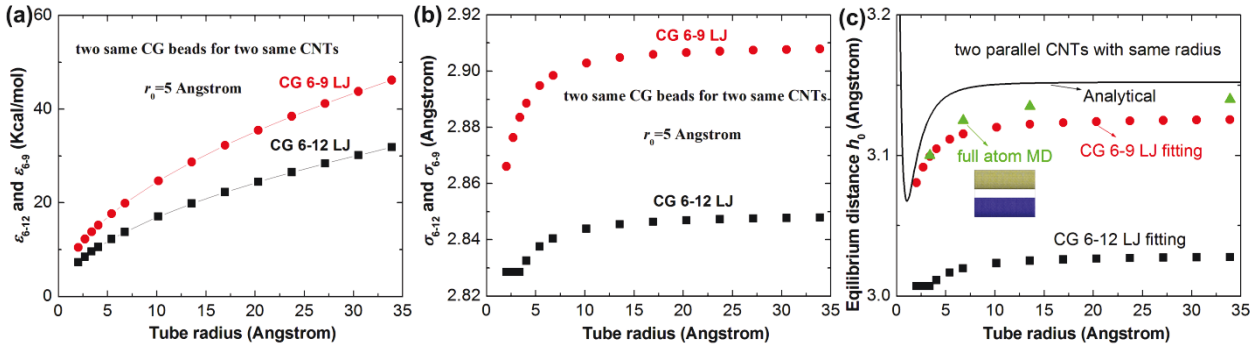

Fig. 3.11 The distribution of ε, σ and h_0 with different radii CNTs for two same parallel CNTs using analytical model, full atom MD simulations and two LJ potentials fitting. (a) $\varepsilon_{6\text{-}12}$ and $\varepsilon_{6\text{-}9}$, (b) $\sigma_{6\text{-}12}$ and $\sigma_{6\text{-}9}$, (c) h_0.

Table 3.7. The $\varepsilon_{6\text{-}12}$ values of the CG 6-12 LJ potential of CG model2 for r_0=5 Å (unit: Kcal/mol).

CNT	(5,5)	(10,10)	(15,15)	(20,20)	(25,25)	(30,30)
(5,5)	9.570	11.189	12.094	12.689	13.094	13.379
(10,10)	11.189	13.737	15.141	16.093	16.760	17.284
(15,15)	12.094	15.141	17.022	18.260	19.165	19.879
(20,20)	12.689	16.093	18.260	19.807	20.926	21.807
(25,25)	13.094	16.760	19.165	20.926	22.236	23.283
(30,30)	13.379	17.284	19.879	21.807	23.283	24.450

Table 3.8. The $\sigma_{6\text{-}12}$ values of the CG 6-12 LJ potential of CG model2 for r_0=5 Å (unit: Å).

CNT	(5,5)	(10,10)	(15,15)	(20,20)	(25,25)	(30,30)
(5,5)	2.829	2.835	2.836	2.837	2.837	2.837
(10,10)	2.835	2.840	2.842	2.843	2.843	2.844
(15,15)	2.836	2.842	2.844	2.845	2.845	2.845
(20,20)	2.837	2.843	2.845	2.845	2.846	2.846
(25,25)	2.837	2.843	2.845	2.846	2.846	2.847
(30,30)	2.837	2.844	2.845	2.846	2.847	2.847

Table 3.9. The $\varepsilon_{6\text{-}9}$ values of the CG 6-12 LJ potential of CG model2 for r_0=5 Å (unit: Kcal/mol).

CNT	(5,5)	(10,10)	(15,15)	(20,20)	(25,25)	(30,30)
(5,5)	13.784	16.165	17.474	18.331	18.926	19.355
(10,10)	16.165	19.879	21.926	23.283	24.283	25.045
(15,15)	17.474	21.926	24.664	26.473	27.806	28.830
(20,20)	18.331	23.283	26.473	28.711	30.330	31.615
(25,25)	18.926	24.283	27.806	30.330	32.258	33.758
(30,30)	19.355	25.045	28.830	31.615	33.758	35.496

Table 3.10. The $\sigma_{6\text{-}9}$ values of the CG 6-12 LJ potential of CG model2 for r_0=5 Å (unit: Å).

CNT	(5,5)	(10,10)	(15,15)	(20,20)	(25,25)	(30,30)
(5,5)	2.884	2.891	2.893	2.894	2.895	2.895
(10,10)	2.891	2.898	2.901	2.902	2.902	2.903
(15,15)	2.893	2.901	2.903	2.904	2.904	2.905
(20,20)	2.894	2.902	2.904	2.905	2.905	2.906
(25,25)	2.895	2.902	2.904	2.905	2.906	2.906
(30,30)	2.895	2.903	2.905	2.906	2.906	2.907

Note that one should use the second kind non-bonded CG model (CG model2) carefully. For three-dimensional CNT bundles, the real box length l_0' should be equal to l_0*(1.0631$\sigma_{6\text{-}12}$+r_1+r_2)/(1.0631$\sigma_{6\text{-}12}$) and l_1*(1.0748$\sigma_{6\text{-}9}$+r_1+r_2)/(1.0748$\sigma_{6\text{-}9}$) if the box length is l_0 and l_1 after minimization using our two CG 6-12 and 6-9 LJ potentials, respectively. In the other words, the practical density is $[(1.0631\sigma_{6\text{-}12}+r_1+r_2)/(1.0631\sigma_{6\text{-}12})]^3$ and $[(1.0748\sigma_{6\text{-}9}+r_1+r_2)/(1.0748\sigma_{6\text{-}9})]^3$ times of that from our second two CG non-bonded potentials, respectively, while the total energy

is same with that from full atom MD simulation and doesn't need modification. Although the appropriate postprocessing should be further accomplished, the two CG LJ potentials are highly accurate to describe the mechanical behavior under large deformation.

3.3.2 Mechanical stability and adhesion of two parallel (5,5) SWCNTs

To validate the present CG potentials, we consider that two parallel (5,5) SWCNTs are moved toward each other in which the ends on the same one side of the two parallel CNTs are fixed in Fig. 3.12. The Young's modulus E=962 GPa and the bending stiffness EI=3.95×10^{-26} J m of the (5,5) CNT are obtained by full atom MD calculations with AIREBO potential (the thickness t of the CNT is chosen 3.4 Å here) (see Figs. 3.13a and b), in which the present Young's modulus agrees well with the available value 1.03±0.06 TPa (Sanchez-Portal, 1999) and the present bending stiffness is very close to the available value 3.84 ×10^{-26} J m (Zhou et al., 2007). U_{tension} is the total energy per unit volume of the CNT and ε is the tensile strain in Fig. 3.13a. U_{bending} is the bending energy per unit length and κ is the 1/r, in which r is the curvature radius and the (5,5) CNT length is equal to 11.6 nm since the boundary effect could be neglected in Fig. 3.13b (Zhao et al., 2009; Zhao et al., 2013a). Detailed MD process is the same with previous work (Cao and Chen, 2006; Zhao et al., 2013b).

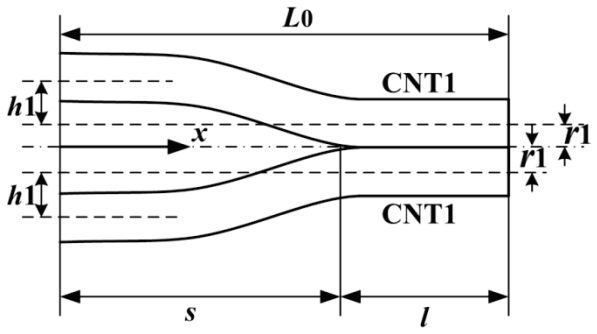

Fig. 3.12 The geometry of two same parallel SWCNTs.

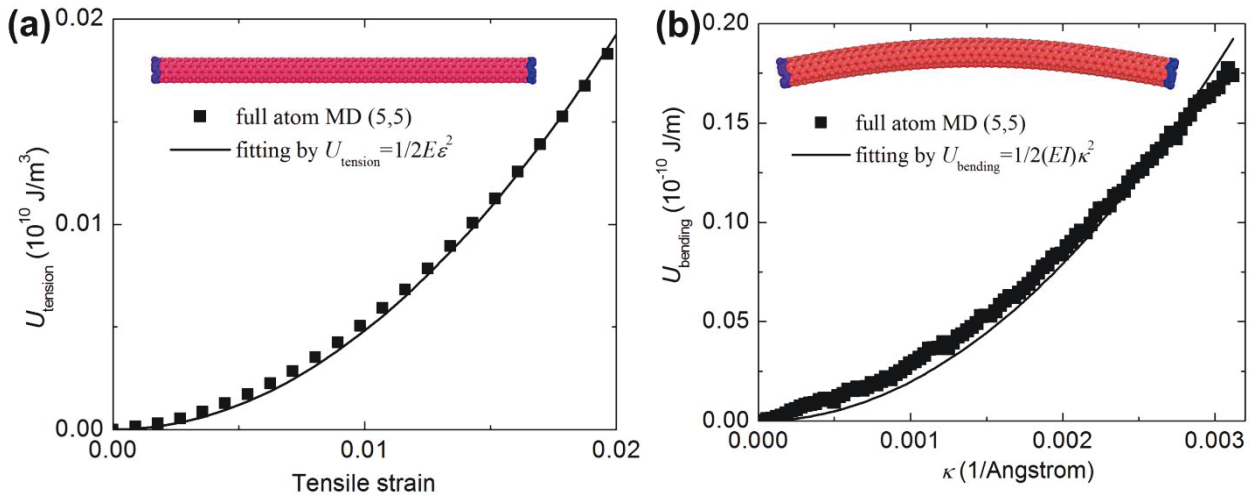

Fig. 3.13 The Young's modulus and bending stiffness of (5,5) SWCNT using full atom MD simulations.

In order to validate the effectivity of present CG model, some assumptions are proposed to simplify the problem. (1) The two (5,5) CNTs are taken as two cantilever beams and the shear deformation is neglected. (2) The closest distance between the adherent components of the two CNTs is taken as zero or a constant d (which does not influence the results). (3) The radii of CNTs and the displacement between the two CNTs are both far less than the length L_0, that is to say, $L_0=s+l$ in Fig. 3.12. The total energy is composed of elastic energy and adhesion energy

$$U_T = 2U_{CNT1} - \gamma\left(L_0 - s\right), \tag{14}$$

where U_{CNT1} and γ are elastic energy of CNT1 and binding energy per unit length, respectively.

In view of the equilibrium of system, the total energy should be a minimum value. The critical value of s can be obtained by $\frac{dU_T}{ds}=0$, that is given

$$s^{critical} = \left(\frac{36EIh^2}{\gamma}\right)^{1/4}, \tag{15}$$

where E and I are the Young's modulus and the moment of inertial for the two CNTs, and EI is the bending stiffness.

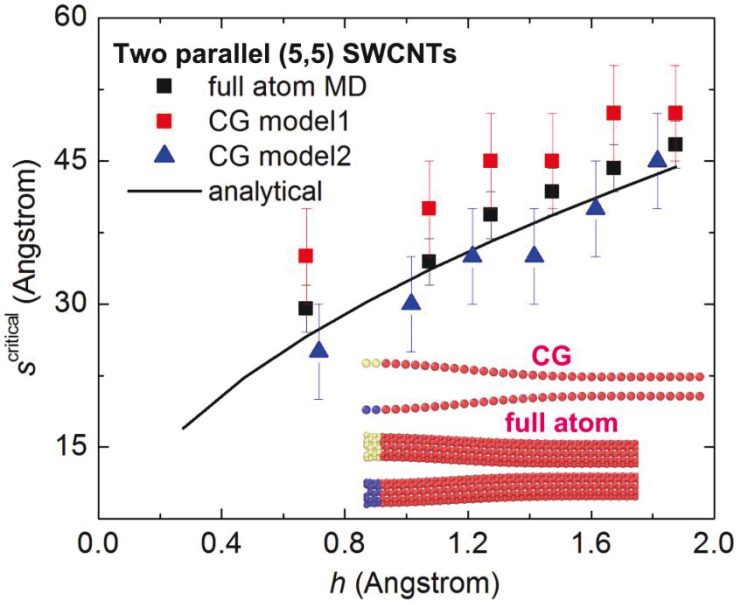

Fig. 3.14 The distribution of $s^{critical}$ with the distance h by comparison with our analytical results, full atom MD and two CG MD calculations.

Fig. 3.14 shows the distribution of $s^{critical}$ with the distance h by comparison with our analytical results, full atom MD and CG MD calculations. The parameters of the two CG non-bonded potentials for two (5,5) CNTs are used in Fig. 3.14, in which the non-bonded potential parameters of CG model1 is chosen from Table 3.3 and Table 3.4, and the non-bonded potential parameters of CG model2 is chosen from Table 3.7 and Table 3.8. The harmonic potentials K_{cgb} =2006 Kcal/(mol Å^2) and $K_{cg\theta}$=11370 Kcal/mol can be easily obtained from Eq. (5) and Eq. (6) based on full atom MD results. Since the torsion effect is very small in this example, we neglect the torsion potential here (Cranford and Buehler, 2010).

The present full atom MD results and the CG MD results with CG model2 are both in good agreement with those of analytical results, while all the values of $s^{critical}$ by the CG model1 calculations are always higher than the present analytical results. From Fig. 3.7, we know that the attractive force ($\partial\phi_{circle}/\partial h$) of the non-bonded potentials in CG model1 is always higher than that of the full atom MD results and analytical results although all γ of them are the same, which leads to the lower $s^{critical}$ in the full atom MD results, CG model2 and analytical results for the same h, while the higher $s^{critical}$ in the CG model1.

From above analysis, the present CG model2 is more effective to apply to describe the adhesion behavior of two CNTs, which should be also used to describe the mechanical behavior of the CNT bundles and networks.

3.3.3 Free vibrations of two parallel (5,5) SWCNTs after tension, bending and moving

To further validate the present CG potentials, we study the free vibrations of two parallel (5,5) SWCNTs after tension, bending and moving using full atom MD and CG MD simulations, respectively. The above harmonic potentials K_{cgb} =2006 Kcal/(mol Å^2), $K_{cg\theta}$=11370 Kcal/mol and 6-12 LJ potential $\varepsilon_{6\text{-}12}$=9.57 Kcal/mol and $\sigma_{6\text{-}12}$=2.829 (see Tables 3.7 and 3.8) are only adopted in our CG MD simulations since the torsion angle is only weakly coupled to other independent variables through the torsion-stretching coupling term (Zhigilei et al., 2005).

3.3.3.1 Free tension vibration

Two parallel 170 Å long (5,5) CNTs are adopted to study the free tension vibration in Fig. 3.15, in which 2800 carbon atoms are included in the two CNTs. After the energy minimization of the two parallel CNTs, the vibration is generated by creating a local strain of 2% beginning of the simulations and allowing the left end (10 Å long part) of the systems to evolve freely at later time, while the right end (10 Å long part) is fixed. Two same long CG models are used to do the same simulation, in which only 68 CG beads are contained in the CG models. From Fig. 3.15a and Fig. 3.15b, the vibration frequency of the potential energy and kinetic energy by full atom MD simulations is in good agreements with that by CG MD simulations (the CG average frequency is 0.71 THz and the full atom average frequency is 0.69 THz), and the difference increases with increasing time (The maximum relative error is less than 5% as t<5 ps and less than 10% as t<10 ps). The probable reason is that the other different modal (more atoms or beads result in more freedoms) could be stimulated with increasing time in the two MD simulations, which leads to the increasing difference. The insets in Fig. 3.15a and Fig. 3.15b represents the potential energy per atom and kinetic energy per atom at t=0.82 ps (The time is at the first peak point of the kinetic energy or the first valley point of the potential energy).

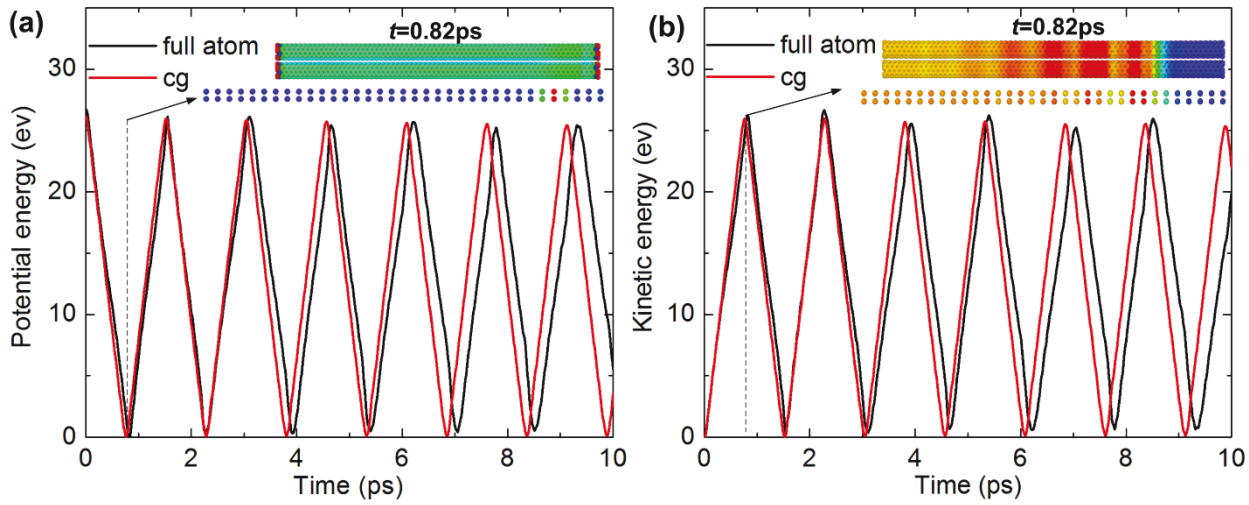

Fig. 3.15 Time dependence of the potential energy and kinetic energy of two parallel (5,5) CNTs in full atom MD and CG MD simulations under tension. (a) potential energy distribution with time; (b) kinetic energy distribution with time.

3.3.3.2 Free bending vibration

The above two parallel 170 Å long (5,5) CNTs are also adopted to study the free bending vibration in Fig. 3.16. After the energy minimization of the two parallel CNTs, the vibration is generated by creating a local bending strain of κ=0.002 (1/Å) beginning of the simulations and allowing the two ends (left and right ends) of the systems to evolve freely at later time. Two same long CG models are used to do the same simulation. From Fig. 3.16a and Fig. 3.16b, the vibration frequency of the potential energy and kinetic energy by full atom MD simulations is reasonable with that by CG MD simulations (the CG average frequency is 0.072 THz and the full atom average frequency is 0.081 THz, and the maximum relative error is less than 12%. The reason of the difference is the same with section 3.3.3.1). The insets in Fig. 3.16a and Fig. 3.16b represents the potential energy per atom and kinetic energy per atom at t=33.33 ps (The time is at the first peak point of the kinetic energy or the first valley point of the potential energy in full atom MD simulations).

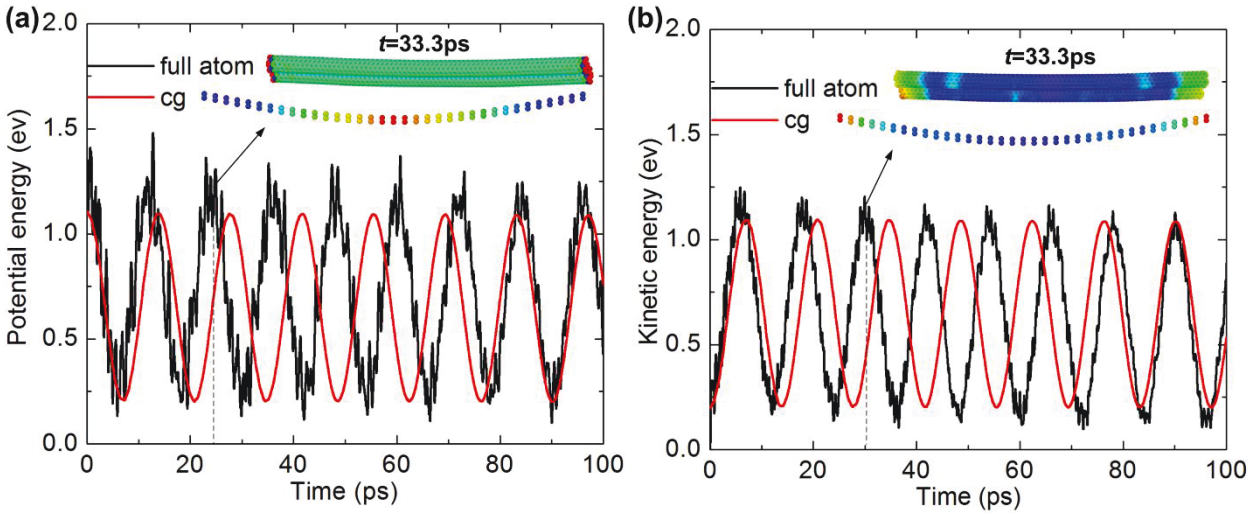

Fig. 3.16 Time dependence of the potential energy and kinetic energy of two parallel (5,5) CNTs in full atom MD and CG MD simulations after bending. (a) potential energy distribution with time; (b) kinetic energy distribution with time.

3.3.3.3 Free vibration after moving a middle part of one CNT between two parallel (5,5) CNTs

The above two parallel 170 Å long (5,5) CNTs are adopted to further study the free vibration after moving a middle part of one CNT between two parallel CNTs (see Fig. 3.17). First, the two parallel CNTs are fixed a given distance and the whole lower CNT is completely fixed, and then the total energy of the two parallel CNTs is minimized by conjugate-gradient algorithm. Afterwards, the left and right 10 Å long ends of the upper CNT are fixed and the middle 5 Å part of the upper CNT is moved 0.01 Å along upper direction, in which the middle part move 0.001 Å at each time step (time step is chosen as 0.1 fs here) based on the displacement-control method (the structure is optimized for each displacement increment (Zhao et al., 2013b)). Finally, the vibration is generated by allowing the middle part of the upper CNT to evolve freely at later time, while the two left and right ends of the upper CNT is always fixed and the whole lower CNT is always fixed. Two same long CG models are used to do the same simulation, in which only 68 CG beads are contained in the CG models and only one CG bead on the upper CG chain is totally moved 0.01 Å. From Fig. 3.17, the vibration frequency by full atom MD simulations agrees very well with those by CG MD simulations when the distance between the two CNTs is the equilibrium distance h_0 (From Fig. 3.11c, CG MD h_0=3.01 Å and full atom MD h_0=3.12 Å) or is higher than 10 Å, while the difference of the frequency between the two MD simulations is

high in the range of $h_0<h<10$ Å (see Fig. 3.17). From the inset in Fig. 3.17, we can find that some middle part of the upper CNT is adherent with the lower CNT as h=5 Å before the vibration is generated. The phenomenon can be explained from section 3.2 and the system is more stable in this adherent condition. The frequency is highly affected by the bending structure (see inset of Fig. 3.17) which has a large deformation, so the difference of the frequency between the two MD simulations should be higher than that in $h=h_0$. With increasing h (h is higher than 10 Å), the cohesive force effect sharply decreases and the difference of the frequency should also decrease.

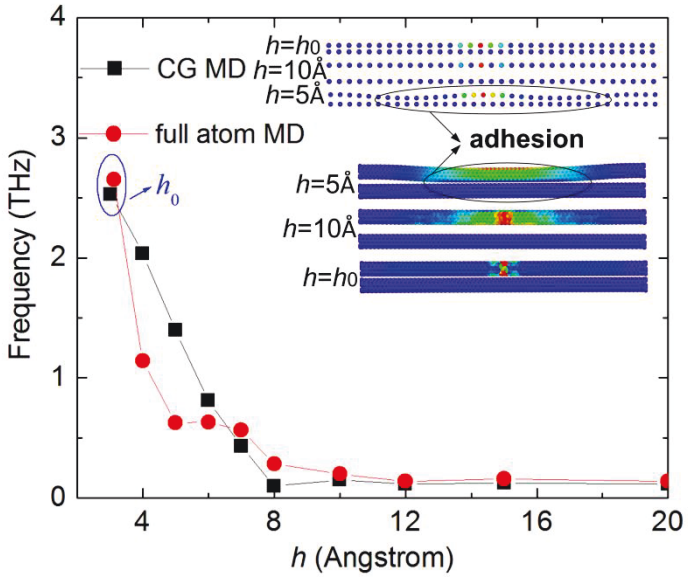

Fig. 3.17 The vibration after moving a middle part of one CNT between two parallel (5,5) CNTs between two parallel (5,5) CNTs by full atom MD and CG MD simulations (The inset represents the kinetic energy distribution for different distance between the two CNTs).

All the free vibration in section 3.3.3 validates that the present CG potentials are effective to describe the dynamics behavior of CNT bundles.

3.3.4 The mechanical behavior of CNT bundles

In this section, we study the mechanical behavior of (5,5) CNT bundles under tension and all the potentials are the same with those in section 3.3.4. First, we calculate the distribution of potential energy with tensile strain and bending angle for one and two (5,5) CNTs using full atom MD and CG MD simulations in Fig. 3.18. From Fig. 3.18a, the difference of the potential energy using the two MD methods is very small when tensile strain is less than 4%, while the

difference increases with increasing tensile strain. The reason is that the Young's modulus of the CNT is obtained by fitting potential-(tensile strain) curve in the range of 2% (see Fig. 3.13a). With the increase of the tensile strain, the nonlinear behavior of full atom MD results should be occurred, which leads to the increasing difference with CG MD results. Second, the bending behavior of one and two (5,5) CNTs using the two MD calculations is plotted in Fig. 3.18b. The difference is also small and similar with the difference between the fitting results and full atom MD results in Fig. 3.13b.

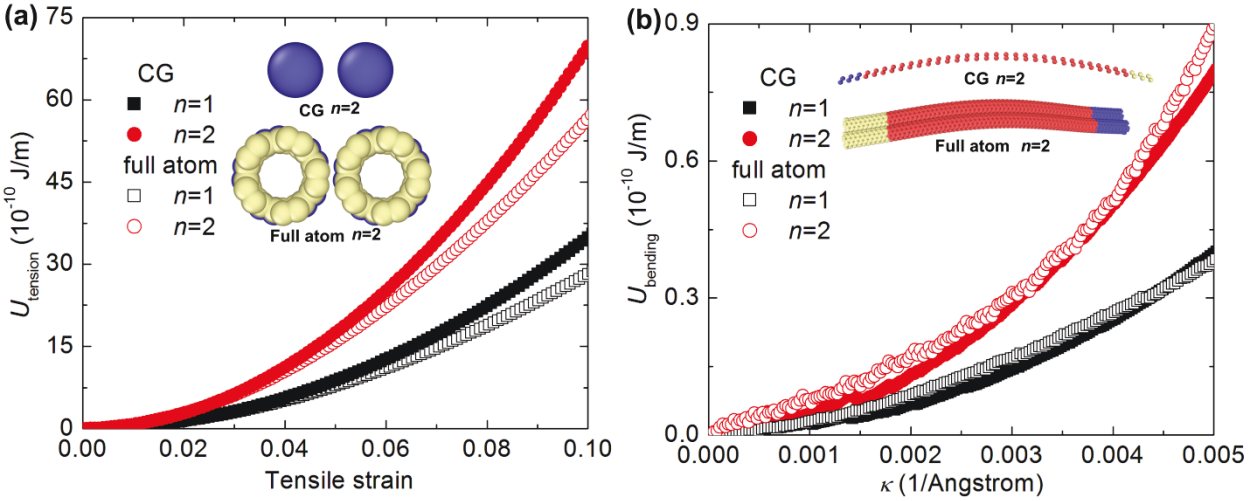

Fig. 3.18 The distribution of the potential energy with tensile strain and bending angle for one and two parallel (5,5) SWCNT using full atom MD and CG MD simulations. (a) under tension; (b) under bending.

To show the advantage of the present CG model, we study the mechanical behavior of more CNT bundles under tension in Fig. 3.19. Fig. 3.19a shows the distribution of the potential energy with tensile strain for n=4 and n=6 using full atom MD and CG MD calculations. The different between the two MD methods is still small in small deformation, while the CG beads are only about 1/40 times of full carbon atoms. Fig. 3.19b shows the mechanical behavior of different CNT bundles using CG MD simulations. The CG beads of n=36 are only 1692 in Fig. 3.19b, while the same bundles of full atom model are about 68800 carbon atoms. Therefore, the computational cost using CG model is less than 1/40 times of full atom model. Note that the comparison is just for (5,5) CNT bundles. For large diameter CNT, the computational cost is much less than 1/40 (which can be given by the function $1/(2\pi r r_0 \rho_{ge})$).

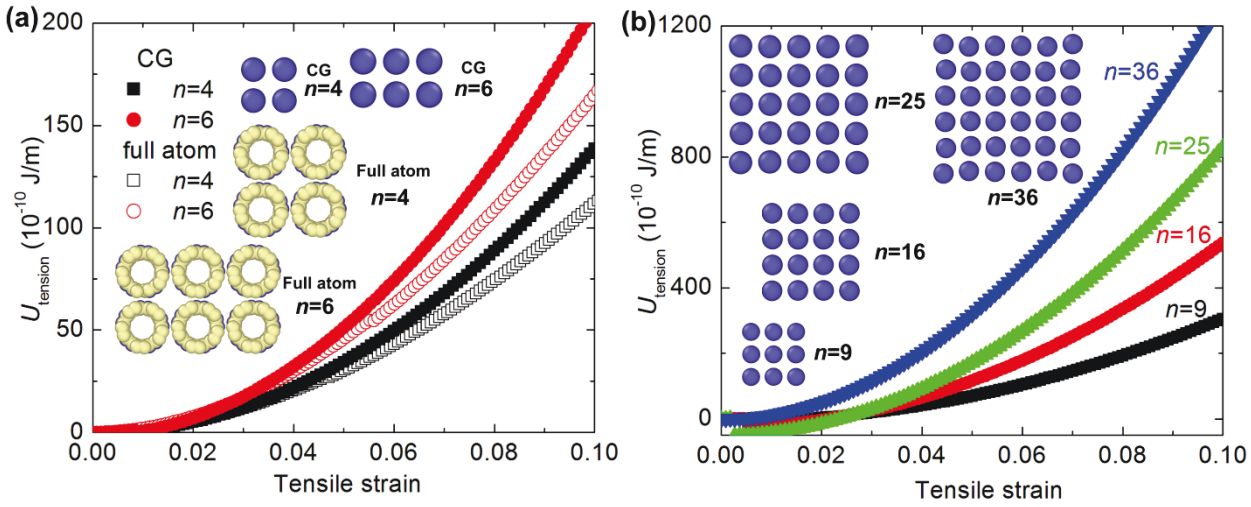

Fig. 3.19 The distribution of the potential energy with tensile strain for (5,5) CNT bundles using full atom MD and CG MD simulations. (a) n=4 and n=6 using full atom MD and CG MD simulations; (b) n=9, n=16, n=25 and n=36 using CG MD simulations.

It should be noted that the negative potential energy is occurred somewhere for small strain as n=9, 16 and 25 in Fig. 3.19b. To further analyze the reason, we plot the potential energy per atom of different CNT bundles under tension in Fig. 3.20 (r_0=5 Å). The strain=0 represents the structures after energy minimization before deformation. The structures of n=9, 16 and 25 after energy minimization always keep parallel although the structures are all at the local energy minimization, while the CG linear chains are all staggered among each other as n=36. It means that the initial structures of strain=0 at n=9, 16 and 25 are not stable. Under small tensile strain, the CG linear chains tend to stagger among each other in advance so that the structures become most stable (in other words, the minimum energy position), which leads to the negative potential energy in the range of the strain.

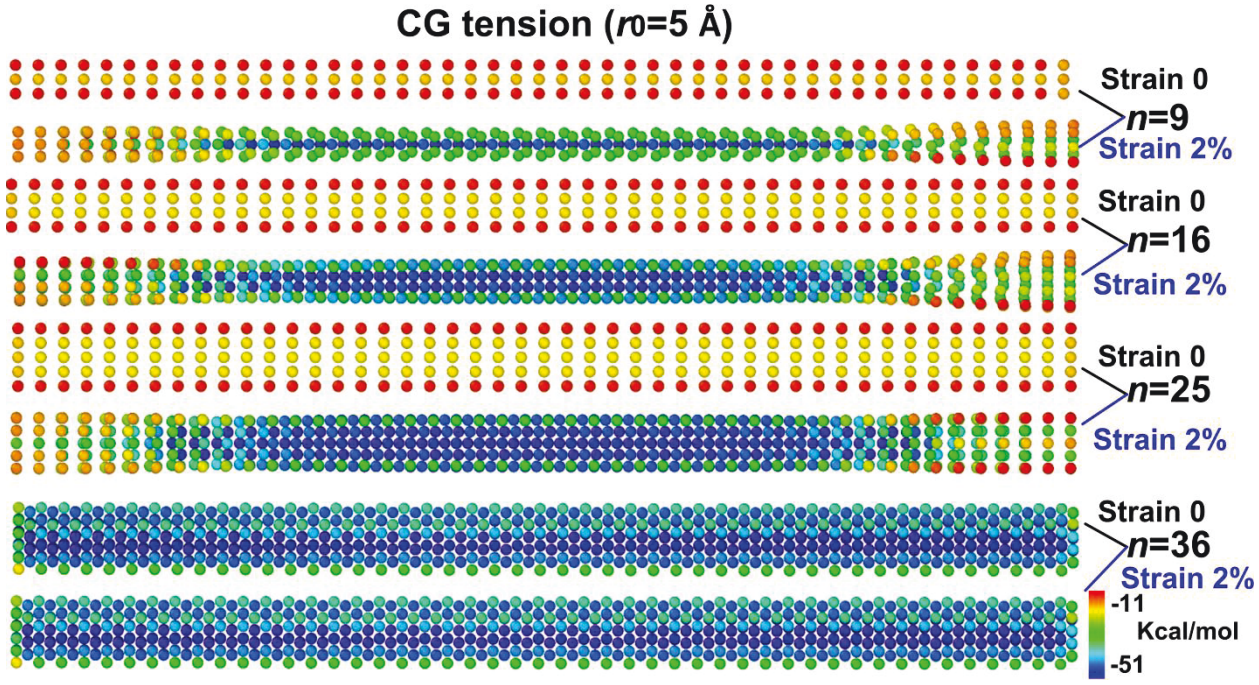

Fig. 3.20 The distribution of the potential energy per atom with tensile strain for (5,5) CNT bundles using CG MD simulations (r_0=5 Å).

To show the difference between the two positions, Fig. 3.21 shows the cohesive energy distribution with distance between two parallel (5,5) CNTs using analytical model and CG MD simulations for different r_0 and two positions. For r_0=5 Å, the minimum cohesive energy and the equilibrium distance h_0 at the staggered position are about two times and 2/3 time lower than those at the non-staggered position, respectively. The difference between the two positions decreases with decreasing r_0. As r_0=2 Å, the cohesive energy and equilibrium distance almost don't change with the two positions. Therefore, r_0=2 Å have to be adopted so that the vdW interactions doesn't change with the positions. In the other hand, all the parameters of the harmonic potentials have to be modified if r_0=2 Å in this paper. Detailed modifications of the parameters can be seen in the discussion of section 3.5.

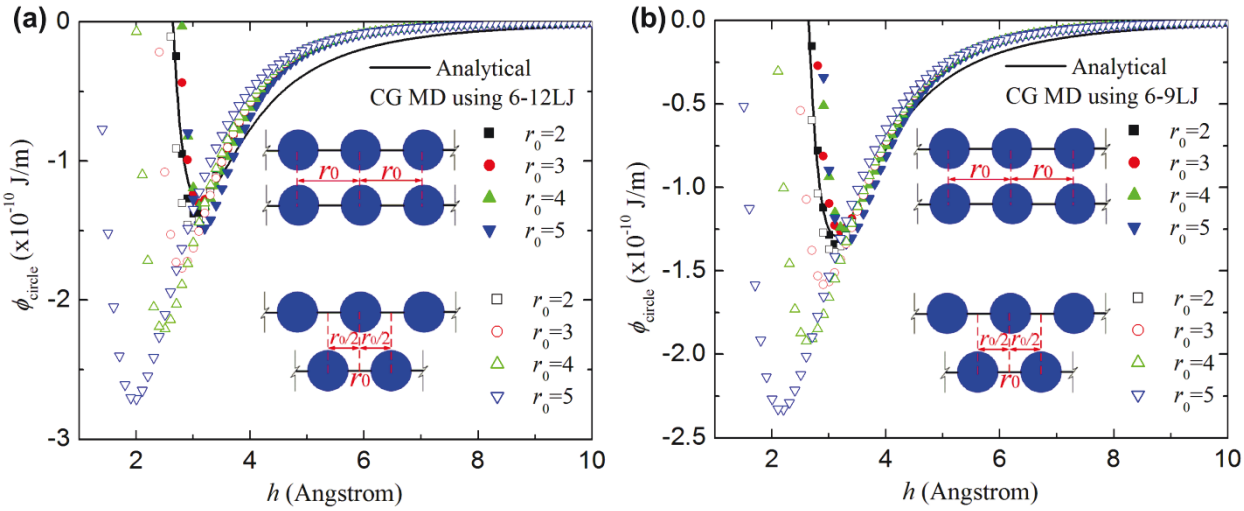

Fig. 3.21 The cohesive energy distribution with different distance between two (5,5) CNTs using analytical model and CG MD simulation with different LJ potentials for different r_0 and two positions (all units of r_0 are Å). (a) CG 6-12 LJ potential, (b) CG 6-9 LJ potential.

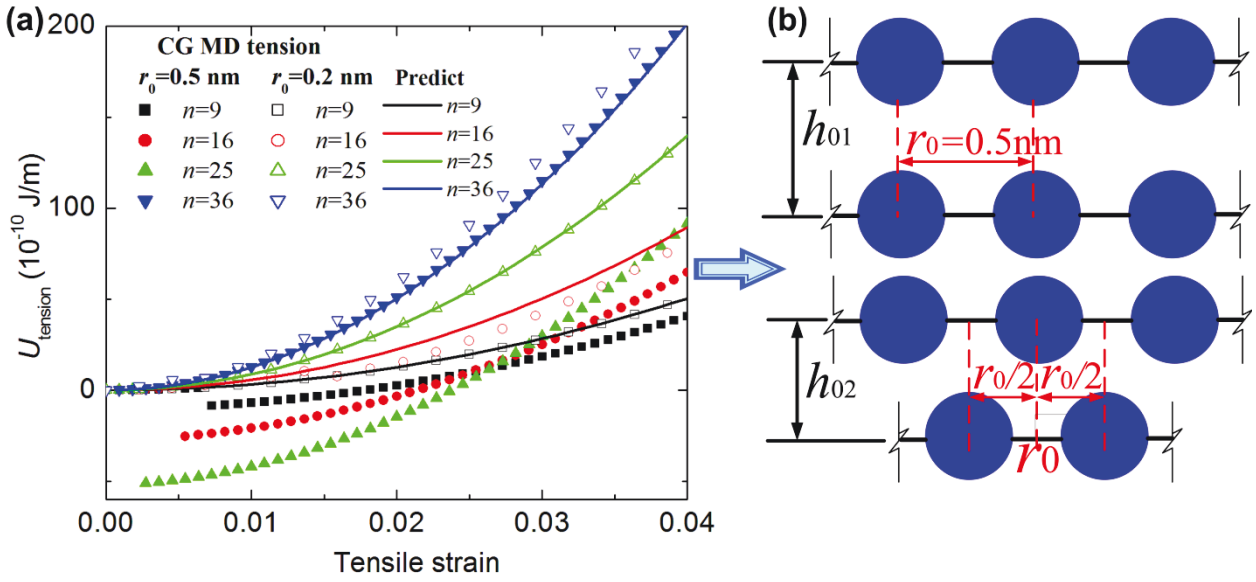

Fig. 3.22 The cohesive energy distribution with different distance between two (5,5) CNTs using analytical model and CG MD simulation with different LJ potentials for different r_0 and two positions. (a) CG 6-12 LJ potential, (b) CG 6-9 LJ potential.

To compare the difference of mechanical behavior between r_0=2 Å and r_0=5 Å, we further calculate the mechanical behavior under tension for different CNT bundles using the CG MD model in Fig 3.22. The harmonic potentials of (5,5) CNT for the CG model with r_0=2 Å should

be given as K_{cgb} =5015 Kcal/(mol Å^2), $K_{cg\theta}$=28425 Kcal/mol and 6-12 LJ potential $\varepsilon_{6\text{-}12}$=1.5313 Kcal/mol and $\sigma_{6\text{-}12}$=2.829 Å. The predicted results in Fig. 3.22 are obtained by U_{tension}= (U_{tension}/oneCNT)×n, where $U_{tension} \Big/ oneCNT = \frac{1}{2} EA\varepsilon^2 = 3495\varepsilon^2$ (10^{-10} J/m), and E and A are the Young's modulus and the cross section area of the CNT (see section 3.3). We find that the CG model with r_0=2 Å agrees well with the predicted results and no negative potential energy is occurred in the tensile process. Furthermore, the equilibrium distance h_{01} at staggered position is always less than that at non-staggered position h_{02} as r_0>2 Å in Fig. 3.21 and Fig. 3.22b, which results in the large difference of the cross section area of the CNT bundles. That is to say, the incorrect Young's moduli of the CNT bundles are obtained for large r_0. Since the two staggered and non-staggered positions as r_0=2 Å doesn't change the cohesive energy and the equilibrium distance (see Fig. 3.21), the CG beads don't need adjust their positions under tension. Therefore, no negative energy as r_0=2 Å is occurred in Fig. 3.22. To further show the detailed process, Fig. 3.23 shows the potential energy per atom of different CNT bundles under tension using CG MD simulation (r_0=2 Å). The structures always keep consistency under tension and the distribution of the energy is very uniform along the length of the CNTs, while the non-uniform distribution of the energy can be clearly seen in Fig. 3.20. The potential energy and cross section area only slightly change for r_0=2 Å at the two staggered and non-staggered positions (see n=25 in Fig. 3.23).

Therefore, it should be noted that most accurate mechanical properties of CNT bundles (especially for large n) can be obtained if r_0=2 Å is used in the CG model.

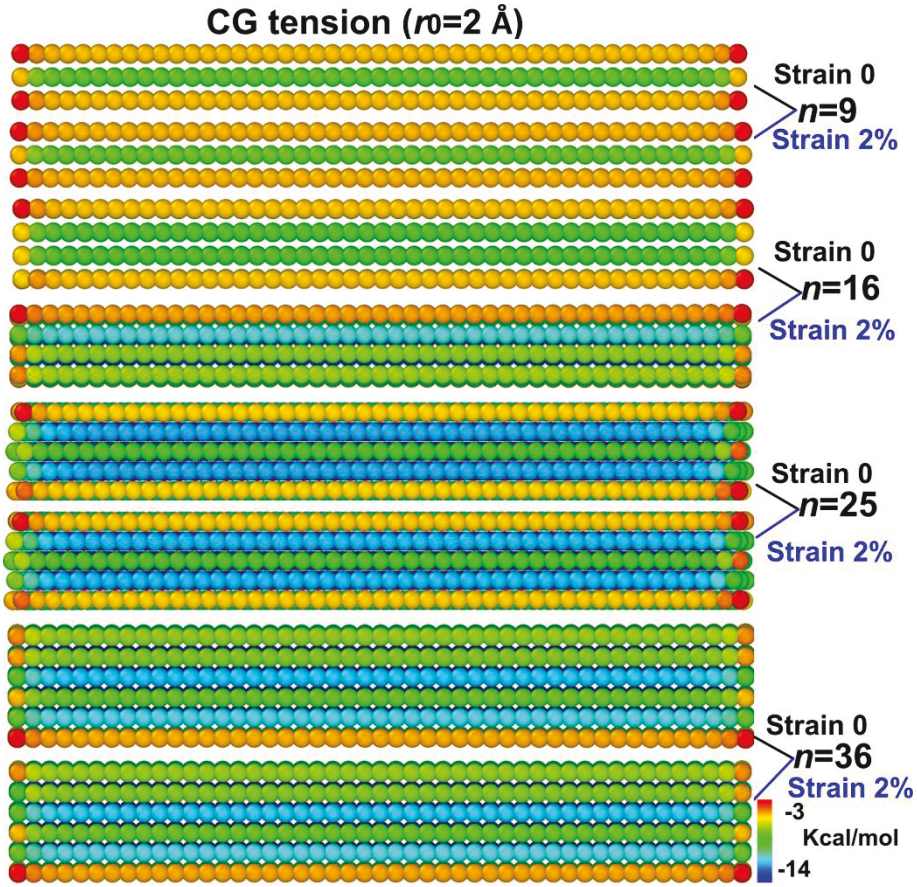

Fig. 3.23 The distribution of the potential energy per atom with tensile strain for (5,5) CNT bundles using CG MD simulations (r_0=2 Å).

3.4 The non-bonded potentials for two crossing SWCNTs and their applications

3.4.1 The non-bonded potentials for two crossing SWCNTs

From above sections, the non-bonded CG potentials are developed by fitting the cohesive energy between two parallel SWCNTs, in which all harmonic potentials are obtained and used to study the different mechanical behavior of the CNT bundles.

In order to clearly understand the mechanical behavior of the CNT buckypaper and networks, it is necessary and important to give the non-bonded CG potentials between two crossing CNTs. This section will study whether the obtained non-bonded CG potentials between two parallel CNTs are also effective between two crossing CNTs or not.

3.4.1.1 Cohesive energy between two crossing SWCNTs

The cylindrical coordinates (r_1, θ, z) and the Cartesian coordinates (x, y, z) are both used on the upper CNT, where z is the central axis of the CNT in Fig. 2.17.

The total cohesive energy on the two nanotubes due to the vdWs force can be written as (Zhao et al., 2013a)

$$\phi_{total} = 4\rho^2 r_1 r_2 \in \sigma^6 \frac{1}{\sin\beta}\left(\frac{63\pi}{128}\sigma^6 \int_0^{\pi} \frac{A_0 B_0 S_0}{S_d} d\theta_2 - \frac{3\pi}{4}\int_0^{\pi} \frac{A_1 B_1 T_1}{T_d} d\theta_2\right), \tag{16}$$

where all parameters can be seen in Eq. (35) of chapter 2.

To validate the analytical results from Eq. (16), the distribution of the analytical cohesive energy with distance by Eq. (16) for different two crossing CNTs is plotted in Fig. 3.24. The analytical results are in excellent agreement with the full atom MD results (detailed process can be seen in our previous work (Zhao et al., 2013a) (the LJ cutoff radius is chosen 60 Å which is an enough distance to get accurate results). It validates the accuracy of the continuum model of Eq. (16) in the description of the cohesive energy between two parallel CNTs.

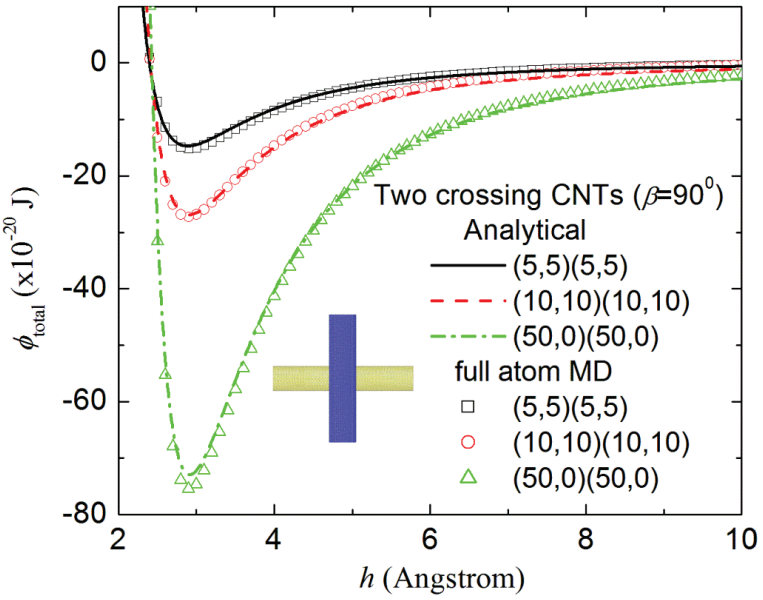

Fig. 3.24 The distribution of cohesive energy with different distance between two crossing SWCNTs (β=90^0) using present analytical model and full atom molecular dynamics simulations.

It should be noted that the unit (J) of the total energy in Eq. (16) is for two crossing CNTs, while the unit (J/m) of the energy per length in Eq. (14) is for two parallel CNTs.

3.4.1.2 Coarse-grained non-bonded potentials between two crossing SWCNTs

Similar with section 3.2, the non-bonded CG potentials for two crossing CNTs can be fitted the cohesive energy function of two crossing lines. For two crossing lines in Fig. 3.25, the total cohesive energy between the two crossing lines can be obtained by

$$\phi_{cross-lines} = \rho_l^2 \int_{-\infty}^{\infty} dx \int_{-\infty}^{\infty} V(r)\, dl \text{ , } (0<\beta\leq\pi/2) \tag{17}$$

where $r^2 = (l\cos\beta - x)^2 + h^2 + (l\sin\beta)^2$, and β is the crossing angle in Fig. 3.25.

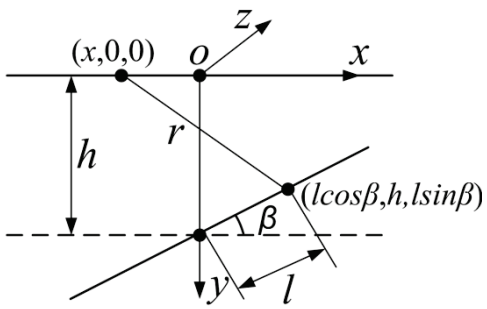

Fig. 3.25 The coordinate system and a schematic diagram of the two infinite crossing lines: (a) two parallel lines; (b) two crossing lines.

If vdW interaction between two CG beads is the function of 6-12 LJ potential, then the total cohesive energy can be given by substituting Eq. (8) into Eq. (17)

$$\phi_{cross6-12} = 4 \in_{6-12} \rho_l^2 \sigma_{6-12}^6 \frac{1}{\sin\beta}\left(\frac{63\pi}{256}\frac{1}{128}\left(98+\frac{36}{5}-\frac{2}{63}\right)\sigma_{6-12}^6 \frac{1}{h^{10}} - \frac{\pi}{2}\frac{1}{h^4}\right). \tag{18}$$

If vdW interaction between two CG beads is the function of 6-9 LJ potential, then the total cohesive energy can be given by substituting Eq. (12) into Eq. (17)

$$\phi_{cross6-9} = 4 \in_{6-9} \rho_l^2 \sigma_{6-9}^6 \frac{1}{\sin\beta}\left(\frac{2\pi}{7}\sigma_{6-9}^3 \frac{1}{h^7} - \frac{\pi}{2}\frac{1}{h^4}\right). \quad (19)$$

From the energy minimum condition $\frac{\partial \phi_{cg6-12}}{\partial h} = 0$ and $\frac{\partial \phi_{cg6-9}}{\partial h} = 0$, the equilibrium distance h_0 between the two crossing lines can be given as $h_0=\sigma_{6\text{-}12}$ and $h_0=\sigma_{6\text{-}9}$, respectively. If we use the same equilibrium CG model1 in Fig. 3.5 (see section 3.3.1) to fit the minimum cohesive energy of Eq. (16), then the value h of Eq. (18) and Eq. (19) should be replaced by h' (see Fig. 3.2 and Fig. 3.4). Similar with Fig. 3.7, the distribution of the cohesive energy between two crossing (10,10) CNTs using analytical model, full atom MD and CG MD simulations is plotted in Fig. 3.26. It should be noted that r_0=5 Å at non-staggered position of the two CG beads are considered in the CG MD simulations of Fig. 3.26. We can find that both above CG 6-12 and 6-9 LJ models are only effective at the distance which is close to the equilibrium distance.

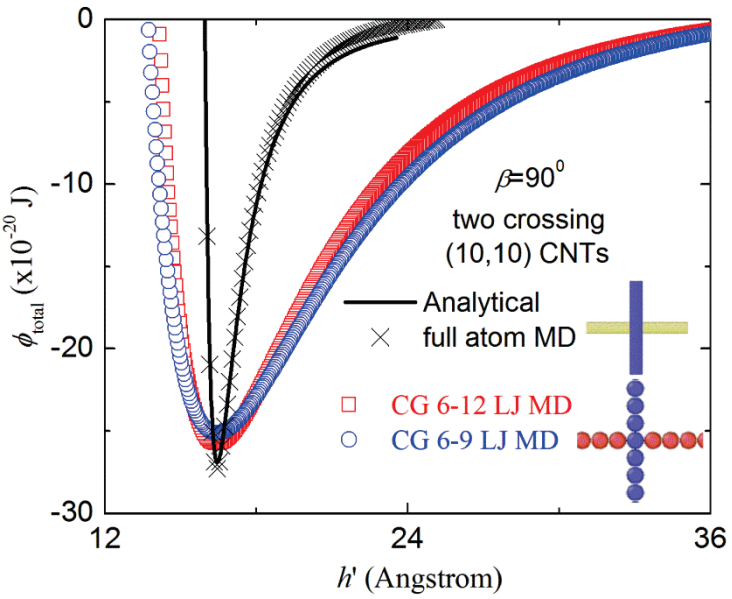

Fig. 3.26 The distribution of the cohesive energy between two crossing (10,10) CNTs (β=90^0) using analytical model, full atom MD and CG MD simulations.

To conveniently use the non-bonded CG potentials, all the values of minimum of ϕ_{total}, h_0', $\in_{6-12}$ *and* $\in_{6-9}$, $\sigma_{6\text{-}12}$ and $\sigma_{6\text{-}9}$ between two different crossing SWCNTs are shown in Tables 3.11, 3.12, 3.13 and 3.14. The values of corresponding $\sigma_{6\text{-}12}$ and $\sigma_{6\text{-}9}$ are the same with h_0' in Table 12.

Table 3.11. The minimum of ϕ_{total} from Eq. (16) (unit: 10^{-20} J).

CNT	(5,5)	(10,10)	(15,15)	(20,20)	(25,25)	(30,30)
(5,5)	-14.6945	-19.8647	-23.9351	-27.4189	-30.5140	-33.3266
(10,10)	-19.8647	-26.8694	-32.3796	-37.0931	-41.2797	-45.0838
(15,15)	-23.9351	-32.3796	-39.0245	-44.7078	-49.7554	-54.3415
(20,20)	-27.4189	-37.0931	-44.7078	-51.2209	-57.0052	-62.2603
(25,25)	-30.5140	-41.2797	-49.7554	-57.0052	-63.4436	-69.2931
(30,30)	-33.3266	-45.0838	-54.3415	-62.2603	-69.2931	-75.6824

Table 3.12. The h_0' from Eq. (16) (unit: Å).

CNT	(5,5)	(10,10)	(15,15)	(20,20)	(25,25)	(30,30)
(5,5)	9.6684	16.4607	19.8534	23.2441	26.6357	26.8847
(10,10)	13.0680	16.4667	19.8604	23.2521	26.6437	30.0344
(15,15)	16.4607	19.8604	23.2541	26.6457	30.0374	33.4281
(20,20)	19.8534	23.2521	26.6457	30.0374	33.4291	36.8198
(25,25)	23.2441	26.6437	30.0374	33.4291	36.8198	40.2114
(30,30)	26.6357	30.0344	33.4281	36.8198	40.2114	43.6021

Table 3.13. The $\varepsilon_{6\text{-}12}$ values of the CG 6-12 LJ potential of CG model1 for r_0=5 Å (unit: Kcal/mol).

CNT	(5,5)	(10,10)	(15,15)	(20,20)	(25,25)	(30,30)
(5,5)	1.5115	0.7049	0.5839	0.4880	0.4136	0.4433
(10,10)	1.1185	0.9528	0.7893	0.6597	0.5591	0.4806
(15,15)	0.8494	0.7893	0.6939	0.6055	0.5302	0.4676
(20,20)	0.6689	0.6597	0.6055	0.5459	0.4905	0.4416
(25,25)	0.5430	0.5591	0.5302	0.4905	0.4500	0.4121
(30,30)	0.4517	0.4806	0.4676	0.4416	0.4121	0.3828

Table 3.14. The $\varepsilon_{6\text{-}9}$ values of the CG 6-9 LJ potential of CG model1 for r_0=5 Å (unit: Kcal/mol).

CNT	(5,5)	(10,10)	(15,15)	(20,20)	(25,25)	(30,30)
(5,5)	2.1006	0.9797	0.8115	0.6781	0.5747	0.6161
(10,10)	1.5544	1.3242	1.0970	0.9168	0.7770	0.6678
(15,15)	1.1804	1.0970	0.9644	0.8414	0.7369	0.6498
(20,20)	0.9296	0.9168	0.8414	0.7586	0.6817	0.6137
(25,25)	0.7547	0.7770	0.7369	0.6817	0.6253	0.5726
(30,30)	0.6277	0.6678	0.6498	0.6137	0.5726	0.5320

Based on the same equilibrium CG model2 of Fig. 3.7, Fig. 3.27 shows the CG model2 fitting results from Eq. (26) and Eq. (27). We can also find that the fitting results from 6-9 LJ potential are also better than those from 6-12 LJ potential by comparison with our analytical and full atom MD results.

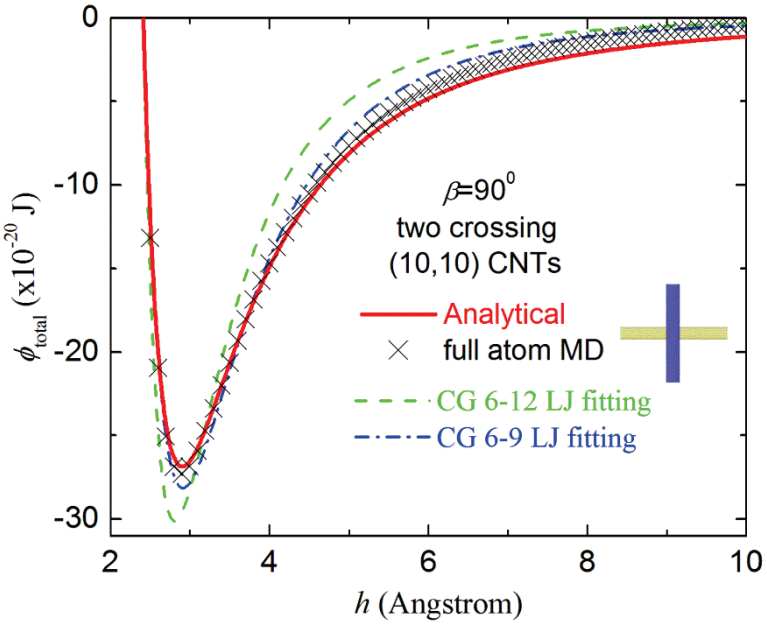

Fig. 3.27 The distribution of the cohesive energy between two crossing (10,10) CNTs (β=90^0) using analytical model, full atom MD and the second CG 6-12 LJ potential of Eq. (18) and 6-9 LJ potential of Eq. (27) fitting.

To conveniently use the CG non-bonded potentials, all the values of minimum of h_0, $\in_{6-12}$ *and* $\in_{6-9}$ between two different crossing SWCNTs are shown in Tables 3.15, 3.16 and 3.17. The values of corresponding $\sigma_{6\text{-}12}$ and $\sigma_{6\text{-}9}$ are the same with h_0 in Table 3.15.

Table 3.15. The h_0 of CG model2 from Eq. (18) (unit: Å).

CNT	(5,5)	(10,10)	(15,15)	(20,20)	(25,25)	(30,30)
(5,5)	2.812	2.830	2.832	2.833	2.837	2.838
(10,10)	2.830	2.840	2.846	2.847	2.848	2.848
(15,15)	2.832	2.846	2.848	2.853	2.854	2.854
(20,20)	2.833	2.847	2.853	2.854	2.855	2.855
(25,25)	2.837	2.848	2.854	2.855	2.855	2.856
(30,30)	2.838	2.848	2.854	2.855	2.856	2.856

Table 3.16. The $\varepsilon_{6\text{-}12}$ values of the CG 6-12 LJ potential of CG model2 for r_0=5 Å (unit: Kcal/mol).

CNT	(5,5)	(10,10)	(15,15)	(20,20)	(25,25)	(30,30)
(5,5)	20.330	27.111	32.565	37.245	41.309	45.093
(10,10)	27.111	36.339	43.552	49.814	55.384	60.451
(15,15)	32.565	43.552	52.334	59.712	66.392	72.468
(20,20)	37.245	49.814	59.712	68.307	75.951	82.903
(25,25)	41.309	55.384	66.392	75.951	84.452	92.183
(30,30)	45.093	60.451	72.468	82.903	92.183	100.623

Table 3.17. The $\varepsilon_{6\text{-}9}$ values of the CG 6-9 LJ potential of CG model2 for r_0=5 Å (unit: Kcal/mol).

CNT	(5,5)	(10,10)	(15,15)	(20,20)	(25,25)	(30,30)
(5,5)	24.563	32.905	39.503	45.168	50.177	54.721
(10,10)	32.905	44.080	52.933	60.526	67.283	73.431
(15,15)	39.503	52.933	63.571	72.695	80.813	88.198
(20,20)	45.168	60.526	72.695	83.132	92.418	100.865
(25,25)	50.177	67.283	80.813	92.418	102.744	112.136
(30,30)	54.721	73.431	88.198	100.865	112.136	122.387

To show the difference between the two positions (staggered and non-staggered) of the two CG beads, Fig. 3.28 shows the cohesive energy distribution with distance between two parallel (10,10) CNTs using analytical model and CG MD simulations for different r_0 and their two positions. For r_0=5Å, the minimum cohesive energy at the staggered position is two times lower than that at the non-staggered position, while the equilibrium distance h_0 at the staggered position decreases to 0. Therefore, these results have a large effect on the density of the buckypaper and newworks (see section 4.2). As r_0=2 Å, the cohesive energy and the equilibrium distance h_0 almost doesn't change with the positions. Therefore, r_0=2 Å have to be adopted so that the vdW interactions doesn't change with the positions. In the other hand, all the parameter of the harmonic potentials have to be modified if r_0=2 Å in this paper. Detailed modifications of the parameters can be seen in the discussion of section 3.5. **It should be noted that all the parameters of the non-bonded CG potentials between two crossing CNTs are independent of the crossing angle β from Eq. (16), Eq. (18) and Eq. (19).**

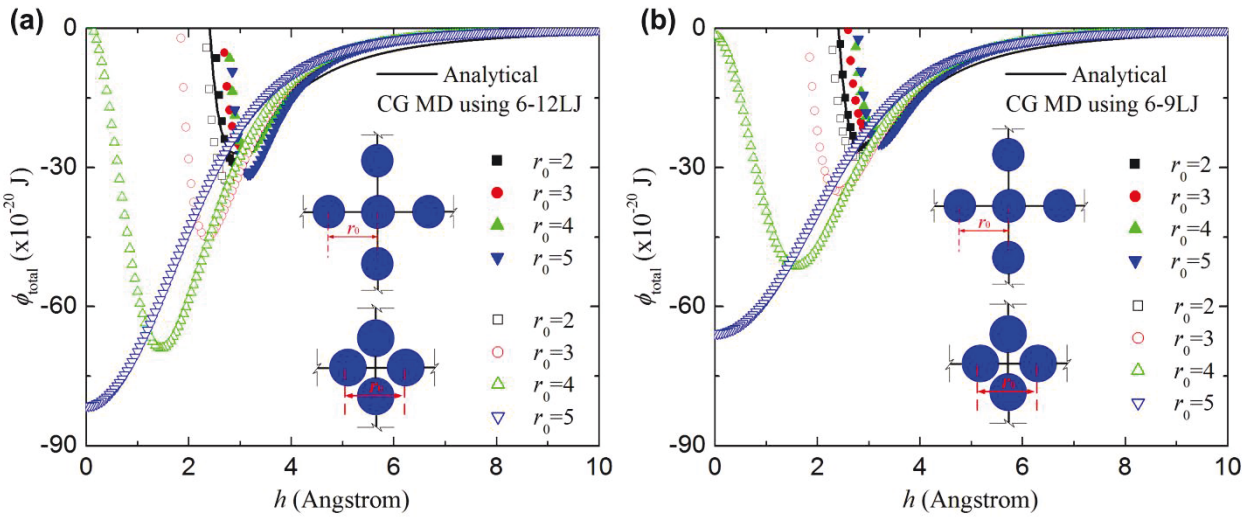

Fig. 3.28 The cohesive energy distribution with different distance between two crossing (10,10) CNTs using analytical model and CG MD simulation with different LJ potentials for different r_0 and two positions (all units of r_0 are Å). (a) CG 6-12 LJ potential, (b) CG 6-9 LJ potential.

3.4.2 Mechanical properties of buckypaper

In this section, we study the mechanical properties of buckypaper based on our non-bonded CG model. All potentials functions and their parameters of (5,5) CNT buckypaper are adopted in Table 3.18.

Table 3.18. The potential functions and their parameters.

Type of potential	Form	Parameters
Stretching	$E=\frac{1}{2}k_b\left(r_b-r_0\right)^2$	k_b=5015 kcal/mol Å^2; r_0=2 Å
Bending	$E=\frac{1}{2}k_\theta\left(\theta-\theta_0\right)^2$	k_0=28425 kcal/mol; θ_0=180^0
Non-bonded	$E=4\varepsilon\left[\left(\frac{\sigma}{r}\right)^{12}-\left(\frac{\sigma}{r}\right)^{6}\right]$	ε=0.2418 kcal/mol; σ=9.668 Å; r_c=10 Å (truncation radius)

3.4.2.1 Computational methods

To generate the initial amorphous buckypaper structure, we use the semi-crystalline lattice method (Faulon, 2001), which utilize the face-centered cubic (*fcc*) diamond structure as a template to carbon backbones of entangled buckypaper. Linear chains are generated by the random walk process on the diamond lattice without explicit bias or guidance, except for one-step-forward collision-check to avoid obvious self-crossing. Instead, simple backtracking along the last several growth steps are used in case of both intra- and intermolecular crossing, and retry random walk until the chain reaches the required chain length. The generated chains of carbons are then replaced with CG beads, so that each CG bead represents the mass center of the section of EBL r_0=2 Å CNTs. The detailed process is similar with generated linear polymers and was described in our previous work (Zhao et al., 2010). The total number of CG beads in the initial structure is kept constant 10000. Twenty CG chains and 500 CG beads per chain are contained in the buckypaper. The generated initial structure (see Fig. 3.29a, in which the blue beads represent the end beads and the red beads represent the middle beads on the chains) is annealed for 2 ns until the pressure and energy of the system is stable, keeping both the temperature T=500 K and the pressure P=1 atm (the time step Δt=1 fs) in the NPT ensemble controlled by the Nose-Hoover's thermostat (Nose, 1984; Hoover, 1985). Then, the system is cooled down to T= 300 K with the cooling rate of 0.2 K/ps in the NPT ensemble. The system is then kept at constant T=300 K and P=1 atm in the NPT ensemble for 2 ns (The box size is about 31.9×31.9×31.9 nm^3, see Figs. 3.29b and d). The uniaxial tension and compression tests (along x direction) are performed to obtain the stress–strain response with strain rate 1×10^{-10} s^{-1} (Capaldi, 2004) in the NPT ensemble (see Figs. 3.29c and e). To obtain the shear properties of the buckypaper, the above equilibrium structure in the NPT ensemble (before tension and compression) is kept at T=300 K in the NVT ensemble for 1 ns. Then the shear tests (along xy direction) are performed to obtain the stress–strain response with strain rate 1×10^{-10} s^{-1} (Capaldi, 2004) in the NVT ensemble (see Figs. 3.29c and f). Note that the distribution of atomic strain ε_{xx} and ε_{xy} per atom is shown in Figs. 3.29e and f. Periodic boundary conditions are applied in all three directions. All the MD simulations are performed using LAMMPS software (Plimpton, 1995) and some figures in Fig. 3.29 are plotted by OVITO software (Stukowski, 2010).

3.4.2.2 Computational results and discussion

First, the bulk density of the buckypaper at 300 K and 1 atm after above annealing process is obtained about 0.09 g/cm^3, which is lower than 0.28 g/cm^3 from Xie et al. (2011) since the two dimensional structure and r_0=10 Å are only considered in their work. Actually, the two dimensional structure has a large limitation and will lose much information (For example, the equilibrium distance h_0 between two crossing CG chains is zero in their work), while the real equilibrium distance h_0 between two crossing (5,5) CNTs are about 9.67 Å (see Table 3.12). The reason leads to the Xie et al.'s higher density.

The stress-strain curves under uniaxial tension and compression as well as pure shear are plotted in Fig. 3.29c. The Young's modulus (E=5.06±0.15 GPa) and shear modulus (G=3.34±0.06 GPa) are calculated by fitting the linear section of the curves in the range of strain 0.6%, which is almost 5 times higher than those of amorphous linear bulk polyethylene (Capaldi, 2004). The ultimate strength is around 60 MPa and 37 MPa under tension and shear, respectively. The corresponding ultimate strains are both about 2% under tension and shear, which are much lower than those of bulk polyethylene (Capaldi, 2004). Note that the ultimate strength/strain is defined as the peak stress and the corresponding peak strain in the stress-strain curves. Although the elastic properties of amorphous buckypaper are much higher than amorphous linear bulk polyethylene, the buckypaper is more brittle than the polyethylene.

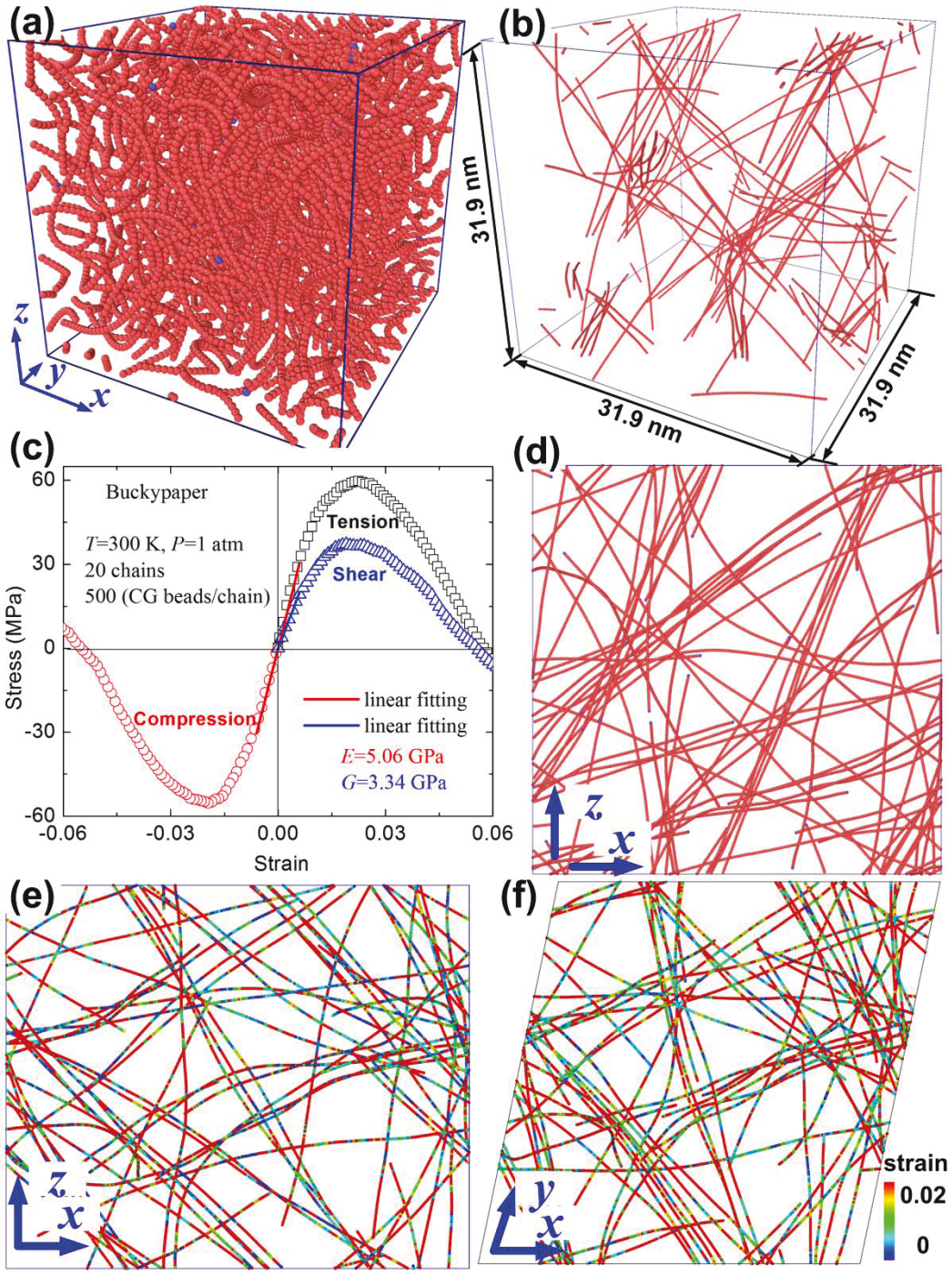

Fig. 3.29 The mechanical properties of the (5,5) CNT buckypaper using CG MD simulations. (a) the initial structure after energy minimization, (b) the equilibrium structure at 300 K and 1 atm after annealing process, (c) the strain-stress curves under uniaxial tension and compression as well as shear, (d) side view in *xoz* plane of (b), (e) the distribution of the atomic strain ε_{xx} per atom under tension, (f) the distribution of the atomic strain ε_{xy} per atom under shear.

The probable reason is that the bond angle among the carbons in bulk polyethylene is about 110^0 (Capaldi, 2004; Zhao et al., 2010) and the stretching potentials between two carbons are lower than those of our CG beads (Capaldi, 2004), so the entanglements in the bulk polyethylene is higher than those in the buckypaper.

It is well known that the vdW interactions play a significant role in the mechanical properties of the buckypaper, so how to determine an accurate cohesive energy between two CG beads is a critical issue for obtaining reliable properties of the buckypaper from the CG MD simulations.

3.5 Discussion

3.5.1 Minimum cohesive energy and equilibrium distance between two parallel and crossing SWCNTs

From Eq. (9) and Eq. (16), we find that the functions of the cohesive energy between two parallel CNTs and two crossing CNTs are quite different since the two issues are different and the units of the cohesive energy are also different.

From our previous work (Zhao et al., 2013a), the normalized equilibrium distance h_0/σ between two parallel CNTs and two crossing CNTs from Eq. (9) and Eq. (16) is plotted in Fig. 3.30. The equilibrium distances between two parallel CNTs are always different with those between two crossing CNTs.

As $r_1=r_2\rightarrow\infty$ for two parallel CNTs and two crossing CNTs, the normalized equilibrium distances h_0/σ are 0.9294 and 0.8584, respectively, which are both different with $h_0/\sigma=1$ of two graphene sheets (Zhao et al., 2013a). In other words, when two CNTs radii tend to infinite, the equilibrium distances between two parallel CNTs or two crossing CNTs are never up to that between two graphene sheets. Actually, $r_1=r_2\rightarrow\infty$ in Eq. (9) and Eq. (16) is a mathematical non-continuous point. Similar phenomena are also occurred in other cases: For example, if the crossing angle β tends to 0 between two crossing lines in Eq. (11), the equilibrium distance between the two crossing lines can be never up to the equilibrium distance between the two parallel lines in Eq. (18). In other words, the point at $\beta=0$ should be moved from Eq. (18). With the crossing angle decreasing to zero, the equilibrium distance between two crossing lines (crossing angle is not zero) is jumped from 1σ to 1.0631σ. Similarly, the crossing angle $\beta=0$ is

also a non-continuous point in the cohesive energy of Eq. (16). Therefore, the cohesive energy and the equilibrium distance between two parallel CNTs and two crossing CNTs are non-continuous, which leads to our non-bonded CG potentials are different in the two conditions.

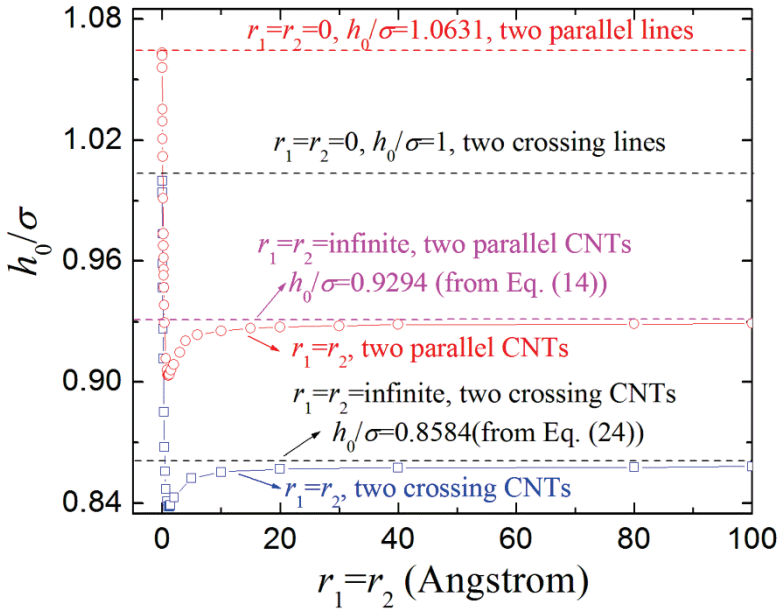

Fig. 3.30 The normalized equilibrium distance h_0/σ between two parallel CNTs and two crossing CNTs.

It should be noted that the two conditions don't like the double-walled CNTs. For double-walled CNTs, if the radii tend to infinity in double-walled CNTs, the equilibrium distance between the two CNTs should be same with that between two graphene sheets, because the cohesive energy per unit area distribution is uniform around CNTs. However, for two parallel CNTs and two crossing CNTs, the cohesive energy distribution is still non-uniform since the curvature still has effect on the energy distribution. Although the difference of the equilibrium distance is not large (normally smaller than 10% for two parallel CNTs, smaller than 15% for two crossing CNTs), it should be very important in other fields (eg. nuclear industry, aeronautics and astronautics, precision machining, etc.).

Therefore, it should be noted that the non-bonded CG potential parameters between two parallel CNTs and two crossing CNTs should be different. In other words, the non-bonded CG potentials for CNT bundles should be different with those for CNT buckypaper or networks.

3.5.2 The equilibrium bond length r_0 between two CG beads

From Fig. 3.9 and Fig. 3.22, the CG model2 is accurate enough as EBL $r_0 \leq 5$ Å by comparison with the analytical and full atom MD results when the two CG beads between the two CNTs are non-staggered with each other. From Fig. 3.21 and Fig. 3.27, the CG model2 is only accurate enough as $r_0 \leq 2$ Å when the two CG beads between the two CNTs are staggered with each other. The difference of the cohesive energy between the CG MD and the analytical results increases with increasing r_0. From Fig. 3.22, the EBL r_0 has a large effect on the mechanical behavior of CNT bundles. Therefore, it is necessary and important to provide all the CG potential parameters of r_0=2 Å. All non-bonded CG potentials between two parallel CNTs are given in Tables 3.19 and 3.20, in which the values of $\sigma_{6\text{-}12}$ and $\sigma_{6\text{-}9}$ are the same with those in Table 3.8 and 3.10, respectively. All non-bonded CG potentials between two crossing CNTs are given in Tables 21 and 22, in which the values of $\sigma_{6\text{-}12}$ and $\sigma_{6\text{-}9}$ are the same with h_0 in Table 3.15. It is easy to find that the values of $\varepsilon_{6\text{-}12}$ and $\varepsilon_{6\text{-}9}$ for r_0=2 Å are both as 4/25 times as those for r_0=5 Å, while $\sigma_{6\text{-}12}$ and $\sigma_{6\text{-}9}$ for r_0=2 Å are the same with those for r_0=5 Å.

Table 3.19. The $\varepsilon_{6\text{-}12}$ values of the CG 6-12 LJ potential of CG model2 for two parallel CNTs as r_0=2 Å (unit: Kcal/mol).

CNT	5	10	15	20	25	30
5	1.531	1.790	1.935	2.030	2.095	2.141
10	1.790	2.198	2.423	2.575	2.682	2.765
15	1.935	2.423	2.724	2.922	3.066	3.181
20	2.030	2.575	2.922	3.169	3.348	3.489
25	2.095	2.682	3.066	3.348	3.558	3.725
30	2.141	2.765	3.181	3.489	3.725	3.912

Table 3.20. The $\varepsilon_{6\text{-}9}$ values of the CG 6-9 LJ potential of CG model2 for two parallel CNTs as r_0=2 Å (unit: Kcal/mol).

CNT	5	10	15	20	25	30
5	2.205	2.586	2.796	2.933	3.028	3.097
10	2.586	3.181	3.508	3.725	3.885	4.007
15	2.796	3.508	3.946	4.236	4.449	4.613
20	2.933	3.725	4.236	4.594	4.853	5.058
25	3.028	3.885	4.449	4.853	5.161	5.401
30	3.097	4.007	4.613	5.058	5.401	5.679

Table 3.21. The $\varepsilon_{6\text{-}12}$ values of the CG 6-12 LJ potential of CG model2 for two crossing CNTs as r_0=2 Å (unit: Kcal/mol).

CNT	(5,5)	(10,10)	(15,15)	(20,20)	(25,25)	(30,30)
(5,5)	3.253	4.338	5.210	5.959	6.609	7.215
(10,10)	4.338	5.814	6.968	7.970	8.861	9.672
(15,15)	5.210	6.968	8.373	9.554	10.623	11.595
(20,20)	5.959	7.970	9.554	10.929	12.152	13.264
(25,25)	6.609	8.861	10.623	12.152	13.512	14.749
(30,30)	7.215	9.672	11.595	13.264	14.749	16.100

Table 3.22. The $\varepsilon_{6\text{-}9}$ values of the CG 6-9 LJ potential of CG model2 for two crossing CNTs as r_0=2 Å (unit: Kcal/mol).

CNT	(5,5)	(10,10)	(15,15)	(20,20)	(25,25)	(30,30)
(5,5)	3.930	5.265	6.321	7.227	8.028	8.755
(10,10)	5.265	7.053	8.469	9.684	10.765	11.749
(15,15)	6.321	8.469	10.171	11.631	12.930	14.112
(20,20)	7.227	9.684	11.631	13.301	14.787	16.138
(25,25)	8.028	10.765	12.930	14.787	16.439	17.942
(30,30)	8.755	11.749	14.112	16.138	17.942	19.582

Moreover, the parameters K_{cgb}, $K_{cg\theta}$ and $K_{cg\tau}$ of stretching, bending and torsion potentials in Fig. 3.11 for r_0=2 Å should be replaced as 2.5 times as those of r_0=5 Å. That is to say, K_{cgb}=1130r (unit: nN/nm), $K_{cg\theta}$=2.5×(0.704$r^{3.305}$-42.8)(r>4 Å) (unit: nN nm) and $K_{cg\tau}$=2.5×(0.598$r^{3.31}$-38.1)(r>4 Å) (unit: nN nm) from Fig. 3.11, respectively, in which r is the CNT radius (unit: Å).

3.5.3 The advantages and limitations of the present CG models

It is well known that the computational cost using our CG models is much less than that of full atom MD simulations. From section 3.5, the 36 numbers (5,5) CNTs are about 68800 carbon atoms (23 nm long per CNT), while only 1692 CG beads and 4230 CG beads are used in the CG MD simulations (r_0=5 Å and r_0=2 Å). From section 3.4.2, the 10000 CG beads are used in the buckypaper, while around 160000 carbons in the full atom MD simulations (r_0=2 Å). For large diameter CNT, the number of CG beads per CNT are only as $1/(2\pi r r_0 \rho_{ge})$ times as those of full atoms. The CG models can be used to study the mechanical properties of even microscale CNT bundles. Since the CG bead mass is $2\pi r r_0 \rho_{ge} m_c$, the time scale in the CG MD simulations can also be used as 10 times as that of full atom MD simulations (Nielsen et al., 2003). Therefore, the CG model can used to study the microscale and large time scale results, which are the large limitations of full atom MD simulations.

The limitation of the CG model is that the stretching, bending and torsion potentials from Eq. (5), Eq. (6) and Eq. (7) are obtained by fitting the mechanical behavior under small deformation, so the nonlinear behavior of the CNT bundles and networks by present CG model should be only the qualitative results. Under large deformation, Chang's group (Geng and Chang, 2006) established a nonlinear stick-spiral model to describe the mechanical behavior of SWCNTs based on a Morse type potential (Arroyo and Belytschko, 2002). The nonlinear model could be directly used to obtain our CG nonlinear stretching, bending and torsion potentials.

Note that one should use the second CG non-bonded model carefully. For three-dimensional CNT bundles, the real box length l_0' should be equal to l_0*$(1.0631\sigma_{6\text{-}12}+r_1+r_2)/(1.0631\sigma_{6\text{-}12})$ using CG 6-12 LJ potential and l_1*$(1.0748\sigma_{6\text{-}9}+r_1+r_2)/(1.0748\sigma_{6\text{-}9})$ if the box length is l_0 and l_1 after minimization using our two CG 6-12 and 6-9 LJ potentials between two parallel CNTs, respectively. In the other words, the practical density is $[(1.0631\sigma_{6\text{-}12}+r_1+r_2)/(1.0631\sigma_{6\text{-}12})]^3$ and $[(1.0748\sigma_{6\text{-}9}+r_1+r_2)/(1.0748\sigma_{6\text{-}9})]^3$ times of that from our second two CG non-bond potentials, respectively, while the total energy is same with that from full atom MD simulation and doesn't need modification.

For three-dimensional CNT buckypaper, the real box length l_0' should be equal to l_0*($\sigma_{6\text{-}12}$+r_1+r_2)/($\sigma_{6\text{-}12}$) using CG 6-12 LJ potential and l_1*($\sigma_{6\text{-}9}$+r_1+r_2)/($\sigma_{6\text{-}9}$) if the box length is l_0 and l_1 after minimization using our two CG 6-12 and 6-9 LJ potentials for two crossing CNTs, respectively. In the other words, the practical density is $[(\sigma_{6\text{-}12}+r_1+r_2)/(\sigma_{6\text{-}12})]^3$ and $[(\sigma_{6\text{-}9}+r_1+r_2)/(\sigma_{6\text{-}9})]^3$ times of that from our second two CG non-bond potentials, respectively, while the total energy is same with that from full atom MD simulation and doesn't need modification. Although the appropriate postprocessing should be further accomplished, the two CG LJ potentials are highly accurate to describe the mechanical behavior under large deformation.

If one uses the CG model1 in CNT bundles and CNT buckypaper as shown in Fig. 3.8 and Fig. 3.25 which don't need any postprocessing although the non-bonded potentials are only accurate enough at the position close to the equilibrium distance, then the parameters of the potentials as r_0=5 Å can be used from Tables 3.3, 3.4, 3.5 and 3.6 for CNT bundles and from Tables 3.12, 3.13 and 3.14 for CNT buckypaper and networks. For r_0=2 Å, the parameters of the potentials are shown in Tables 3.23, 3.24, 3.25 and 3.26, while the corresponding equilibrium distances don't change.

Table 3.23. The $\varepsilon_{6\text{-}12}$ values of the CG 6-12 LJ potential of CG model1 for two parallel CNTs as r_0=2 Å from Table 3 (unit: Kcal/mol).

CNT	(5,5)	(10,10)	(15,15)	(20,20)	(25,25)	(30,30)
(5,5)	0.4205	0.3675	0.3163	0.2755	0.2432	0.2173
(10,10)	0.3677	0.3609	0.3307	0.3006	0.2738	0.2505
(15,15)	0.3165	0.3307	0.3183	0.2986	0.2785	0.2596
(20,20)	0.2756	0.3006	0.2986	0.2875	0.2733	0.2587
(25,25)	0.2433	0.2738	0.2785	0.2733	0.2639	0.2531
(30,30)	0.2174	0.2505	0.2596	0.2587	0.2531	0.2452

Table 3.24. The $\varepsilon_{6\text{-}9}$ values of the CG 6-9 LJ potential of CG model1 for two parallel CNTs as r_0=2 Å from Table 5 (unit: Kcal/mol).

CNT	(5,5)	(10,10)	(15,15)	(20,20)	(25,25)	(30,30)
(5,5)	0.6532	0.5708	0.4914	0.4280	0.3778	0.3376
(10,10)	0.5712	0.5607	0.5137	0.4669	0.4253	0.3892
(15,15)	0.4917	0.5137	0.4945	0.4638	0.4326	0.4033
(20,20)	0.4282	0.4669	0.4638	0.4466	0.4245	0.4019
(25,25)	0.3779	0.4253	0.4326	0.4245	0.4099	0.3932
(30,30)	0.3377	0.3892	0.4033	0.4019	0.3932	0.3809

Table 3.25. The $\varepsilon_{6\text{-}12}$ values of the CG 6-12 LJ potential of CG model1 for two crossing CNTs as r_0=2 Å from Table 16 (unit: Kcal/mol).

CNT	(5,5)	(10,10)	(15,15)	(20,20)	(25,25)	(30,30)
(5,5)	0.2418	0.1128	0.0934	0.0781	0.0662	0.0709
(10,10)	0.1790	0.1524	0.1263	0.1055	0.0895	0.0769
(15,15)	0.1359	0.1263	0.1110	0.0969	0.0848	0.0748
(20,20)	0.1070	0.1055	0.0969	0.0873	0.0785	0.0707
(25,25)	0.0869	0.0895	0.0848	0.0785	0.0720	0.0659
(30,30)	0.0723	0.0769	0.0748	0.0707	0.0659	0.0612

Table 3.26. The $\varepsilon_{6\text{-}9}$ values of the CG 6-9 LJ potential of CG model1 for two crossing CNTs as r_0=2 Å from Table 17 (unit: Kcal/mol).

CNT	(5,5)	(10,10)	(15,15)	(20,20)	(25,25)	(30,30)
(5,5)	0.3361	0.1567	0.1298	0.1085	0.0920	0.0986
(10,10)	0.2487	0.2119	0.1755	0.1467	0.1243	0.1069
(15,15)	0.1889	0.1755	0.1543	0.1346	0.1179	0.1040
(20,20)	0.1487	0.1467	0.1346	0.1214	0.1091	0.0982
(25,25)	0.1208	0.1243	0.1179	0.1091	0.1001	0.0916
(30,30)	0.1004	0.1069	0.1040	0.0982	0.0916	0.0851

Since the parameters of the non-bonded CG potentials between two parallel and crossing CNTs are different, so we should use the non-bonded CG potentials between two parallel CNTs in CNT bundles and use the potentials between two crossing CNTs in CNT buckypaper and networks.

3.6 Concluding remarks

In summary, the CG potentials for SWCNT systems are developed from molecular mechanics models. The explicit expressions of the CG stretching, bending and torsion potentials of SWCNTs are obtained based on the stick-spiral and the beam models. Based on our analytical results of cohesive energy between two parallel and crossing SWCNTs, the non-bonded CG potentials between different CG beads are systematically analyzed. The effect of the equilibrium bond length (EBL) r_0 of the two CG beads and the influence of the position between the CG beads on the CG potentials are both detailedly discussed. We find that the cohesive energy and equilibrium distance of EBL r_0=5 Å is only accurate enough for the non-staggered position between two CG beads, while the energy and distance of r_0=2 Å are always accurate enough for non-staggered and staggered position between two CG beads. Checking against full atom molecular dynamics calculations and our analytical results shows that the present CG potentials have high accuracy.

The two non-bonded CG models of r_0=2 Å are developed in this paper. The non-bonded parameters of the first model are obtained by fitting the minimum cohesive energy and the corresponding equilibrium distance, which are effective at the distance which is close to the equilibrium distance between two CG beads. The advantage of the model is that no postprocessing should be performed. The non-bonded parameters of the second model are obtained by fitting the total cohesive energy-distance curves, which are effective at any distance between two CG beads, while some postprocessing have to be performed.

It should be noted that the parameters of the obtained non-bonded CG potentials between two parallel and crossing CNTs are different, so we have to use the non-bonded CG potentials between two parallel CNTs in CNT bundles and use the potentials between two crossing CNTs in CNT buckypaper and networks.

The established CG potentials are efficiently used to study the mechanical properties of CNT bundles and CNT buckypaper at a minor fraction of the computational cost, which should be of great help for further designing the corresponding nanomechanical devices and systems.

Appendix

The parameters of λ, ζ and η of the Eq. (17) and Eq. (18) in the text are given as (Chang, 2010)

$$\lambda=\frac{5-3\cos(\pi/n)}{14-2\cos(\pi/n)},\zeta=\frac{1}{6\cos^2(\pi/2n)},\eta=\frac{\left[1+2\cos(\pi/2n)\right]^2}{9\cos^2(\pi/2n)} \quad \text{, for the } (n,0) \text{ CNTs.} \tag{A1}$$

$$\lambda=\frac{7-\cos(\pi/n)}{34+2\cos(\pi/n)},\zeta=\frac{4-\cos^2(\pi/2n)}{2\left[1+2\cos(\pi/2n)\right]^2},\eta=\frac{\left[2+\cos(\pi/2n)\right]^2}{\left[1+2\cos(\pi/2n)\right]^2} \quad \text{, for the } (n,n) \text{ CNTs.} \tag{A2}$$

The detailed information for different chirality can be seen in the literatures (Chang and Gao, 2003; Chang et al., 2005; Chang, 2010).

References

Ajayan, P.M., Banhart, F., 2002. Strong bundles. Nat. Mater. 3, 135-136.

Baughman, R.H., Zakhidov, A.A, de Heer, W.A., 2002. Carbon nanotubes-the route toward applications. Science 297, 787-792.

Arroyo, M., Belytschko, T., 2002. Large deformation atomistic-based continuum analysis of carbon nanotubes. AIAA-2002-1317.

Buehler, M.J., 2006. Mesoscale modeling of mechanics of carbon nanotubes: self-assembly, self-folding, and fracture. J. Mater. Res. 21, 2855-2869.

Capaldi, F.M., Boyce, M.C., Rutledge, G.C., 2004. Molecular response of a glassy polymer to active deformation. Polymer 45, 139-1399.

Carnford, S., Buehler, M.J., 2010. In silico assembly and nanomechanical characterization of carbon nanotube buckypaper. Nanotechnology 21, 265706.

Carnford, S., Yao, H., Ortiz, C., Buehler, M.J., 2010. A single degree of freedom 'lollipop' model for carbon nanotube bundle formation. J. Mech. Phys. Solids 58, 409-427.

Chang, T., Gao, H., 2003. Size-dependent elastic properties of a single-walled carbon nanotube via a molecular mechanics model. J. Mech. Phys. Solids 51, 1059-1074.

Chang, T., Geng, J., Guo, X.., 2005. Chirality- and size-dependent elastic properties of single-walled carbon nanotubes. Appl. Phy. Lett. 87, 251929.

Chang, T., 2007. Torsional behavior of chiral single-walled carbon nanotubes is loading direction dependent. Appl. Phys. Lett. 90, 201910.

Chang, T. 2010. A molecular based anisotropic shell model for single-walled carbon nanotubes. J. Mech. Phys. Solids 58, 1422-1433.

Faulon, J.L. 2001. Stochastic generator of chemical structure. (4) Building polymeric systems with specified properties. J. Comput. Chem. 22, 580-590.

Geng, J., Chang, T., 2006. Nonlinear stick-spiral model predicting mechanical behavior of single-walled carbon

nanotubes. Phy. Rev. B 74, 245428.

Golub, G.H., Welsch, J.H., 1969. Calculation of Gauss quadrature rules. Math Comp 23, 221-230.

He, X.Q., Kitipornchai, S., Liew, K.M., 2005. Buckling analysis of multi-walled carbon nanotubes: a continuum model accounting for van der Waals interaction. J. Mech. Phys. Solids 53, 303-326.

Hernandez, E., Goze, C., Bernier, P., Rubio, A., 1998. Elastic properties of C and $B_xC_yN_z$ composite nanotubes. Phys. Rev. Lett. 80, 4502-4505.

Hoover, W.G., 1985. Canonical dynamics: Equilibrium phase-space distributions. Phys. Rev. A 31, 1695-1697.

Iijima, S., Brabec, C., Maiti, A., Bernholc, J., 1996. Structural flexibility of carbon nanotubes. J. Chem. Phys. 104, 2089-2092.

Jiang, L., Guo, W., 2011. A molecular mechanics study on size-dependent elastic properties of single-walled boron nitride nanotubes. J. Mech. Phys. Solids 59, 1204-1213.

Jiang, L.Y., Huang, Y., Jiang, H., Ravichandran, G., Gao, H., Hwang, K.C., Liu, B., 2006. A cohesive law for carbon nanotube/polymer interface based on the van der Waals force. J. Mech. Phys. Solids 53, 2436-2452.

Kis, A., Csanyi, G., Salvetat, J.P., Lee, T.N., Couteau, E., Kulik, A.J., Benoit, W., Brugger, J., Forro, L., 2004. Reinforcement of single-walled carbon nanotube bundles by intertube bridging. Nat. Mater. 3, 153-157.

Li, C.Y., Chou, T.W., 2003. A structural mechanics approach for the analysis of carbon nanotubes. Int. J. Solids Struct., 40, 2487-2499.

Li, C.Y., Chou, T.W., 2004. Elastic properties of single-walled carbon nanotubes in transverse directions. Phys. Rev. B 69, 073401.

Li, H., Guo, W., 2008. Transversely isotropic elastic properties of single-walled carbon nanotubes by a rectangular beam model for the C-C bonds. J. Appl. Phys. 103, 103501.

Li, Y., Kröger, M. 2012. Viscoelasticity of carbon nanotube buckypaper: zipping-unzipping mechanism and entanglement effects. Soft Matter 8, 7822-7830.

Nielsen, S., Lopez, C.F., Srinivas, G., Klein, M.L. 2003. A coarse grain model for n-alkanes parameterized from surface tension data. J. Chem. Phys. 119, 7043-7049.

Nose, S., 1984. A unified formulation of the constant temperature molecular dynamics methods. J. Chem. Phys. 81, 511.

Odegard, G.M., Gates, T.S., Nicholson, L.M., Wise, K.E., 2002. Equivalent-continuum modeling with application to carbon nanotubes. NASA/TM-2002-211454.

Plimpton, S., 1995. Fast parallel algorithms for short-range molecular dynamics. J. Comput. Phys. 117, 1-19.

Ru, C.Q., 2000. Effect of van der Waals forces on axial buckling of a double-walled carbon nanotube. J. Appl. Phys. 87, 7227-31.

Ru, C.Q., 2001. Axially compressed buckling of a doublewalled carbon nanotube embedded in an elastic medium. J. Mech. Phys. Solids 49, 1265-1279.

Sanchez-Portal D, Artacho E, Soler JM, Rubio A, Ordejon P., 1999. Ab-initio structural, elastic, and vibrational properties of carbon nanotubes. Phys. Rev. B 59, 12678.

Stukowski, A., 2010. Visualization and analysis of atomistic simulation data with OVITO- the Open Visualization

Tool. Modelling Simul. Mater. Sci. Eng. 18, 015012.

Wang, C., Xie, B., Liu, Y., Xu, Z., 2012. Mechanotunable microstructures of carbon nanotube networks. ACS Macro Lett. 2012, 1, 1176−1179.

Xie, B., Liu, Y., Ding, Y., Zheng, Q., Xu, Z., 2011. Mechanics of carbon nanotube networks: microstrutural evolution and optimal design. Soft Matter 7, 10039-10047.

Yakobson, B.I., Brabec, C.J., Bernholc, J., 1996. Nanomechanics of carbon tubes: instability beyond linear response. Phys. Rev. Lett. 76, 2511-2514.

Yang, C., Xie, B., Liu, Y., Xu, Z., 2012. Mechanotunable microstructures of carbon nanotube networks. ACS Macro Lett. 1, 1176-1179.

Zhang, P., Huang, Y., Geubelle, P.H., Klein, P.A., Hwang, K.C., 2002. The elastic modulus of single-wall carbon nanotubes: a continuum analysis incorporating interatomic potentials. Int. J. Solids Struct. 39, 3893-3906.

Zhang, Z., Guo, W., Tai, G., 2007. Coaxial nanocable: Carbon nanotube core sheathed with boron nitride nanotube. Appl. Phys. Lett. 90, 133103.

Zhao H, Min K, Aluru R., 2009. Size and chirality dependent elastic properties of graphene nanoribbons under uniaxial tension. Nano Lett. 9, 3012-3015.

Zhao, J., Nagao, S., Zhang, Z.L., 2010. Thermo-mechanical properties dependence on chain length in bulk polyethylene: Coarse-grained molecular dynamics simulations, J. Mater. Res. 25, 537-544.

Zhao, J., Guo, W., Zhang, Z.L., Rabczuk, T., 2011. Size-dependent elastic properties of crystalline polymers via a molecular mechanics model. Appl Phys Lett 99, 241902.

Zhao, J., Guo, W., Rabczuk, T., 2012. An analytical molecular mechanics model for the elastic properties of crystalline polyethylene. J. Appl. Phys. 112, 033516.

Zhao, J., Jiang, J.W., Jia, Y., Guo, W., Rabczuk, T., 2013a. A theoretical analysis of cohesive energy between carbon nanotubes, graphene and substrates. Carbon 57, 108-119.

Zhao, J., Wang, L., Jiang, J.W., Wang, Z., Guo, W., Rabczuk, T., 2013b. A comparative study of two molecular mechanics models based on harmonic potentials. Journal of Applied Physics, 113, 063509.

Zhigilei, L., Wei, C., Srivastava, D., 2005. Mesoscopic model for dynamics simulations of carbon nanotubes. Phy. Rev. B 71, 165417.

Zhou, W., Huang, Y., Liu, B., K.C. Hwang., Zuo, J.M., Buehler, M.J., Gao, H., 2007. Self-folding of single- and multiscale carbon nanotubes. Appl. Phys. Lett. 90, 073107.

Chapter 4

Binding energy and mechanical stability of two parallel and two crossing carbon nanotubes*

Abstract

The binding energy between two parallel (and two crossing) single-walled (and multi-walled) carbon nanotubes (CNTs) is obtained by continuum modeling of the van der Waals interaction between them. The dependence of the binding energy on their diameters, number of walls and crossing angles is systematically analyzed. The critical length for the mechanical stability and adhesion of the CNTs has been determined by the function of E_iI_i, h and γ, where E_iI_i, h and γ are the CNTs bending stiffness, distance and binding energy between them. Checking against full atom molecular dynamics calculations show that the continuum solution has high accuracy. The established analytical solutions should be of great help for designing nanoelectromechanical devices.

4.1 Introduction

The unique mechanical, electrical, thermal and optical properties of carbon nanotubes (CNTs) enable them highly potential and ideal candidates for multifarious applications (Iijima, 1991; Baughman et al., 2002; Modi et al., 2003). CNT exists in several structures forms such as single-walled CNTs (SWCNTs), multi-walled CNTs (MWCNTs), bundles and networks (Ajayan and Banhart, 2002; Bronikowski, 2006). The mechanical properties of SWCNTs and MWCNTs have been extensively studied in previous work (Yakobson et al., 1996; Chang and Gao, 2003; Li and Chou, 2003; Li and Guo, 2008). Recently, the CNT networks have been taken as a potential saving-energy material (Xie et al., 2011), while the CNT bundles have potential applications in nanocomposites materials. In the synthesis of CNT bundles and networks, their formation is a challenge to remain in understanding how to measure and predict the properties of such large systems (Ajayan and Banhart, 2002; Kis et al., 2004). At the nanoscale, the weak van der Waals (vdW) interactions govern the structural organization and the mechanical properties of CNT

* The work will be submitted.

bundles and networks (Ru, 2000, 2001; Zhou et al., 2007; Cranford et al., 2010). Therefore, a clear understanding of the vdW interactions in these systems is crucial for their potential applications in the nanoelectromechanical systems and electronic devices. The self-folding of SWCNTs, MWCNTs, multilayer graphene sheets have been investigated and the bundle pattern formation has also been studied in previous work (Zhou et al., 2007; Cranford et al., 2009; Geblinger et al., 2008). However, all their binding energies were used from full atom molecular dynamics simulation or experimental results. Girifalco et al. (Girifalco et al., 2000) obtained the cohesive energy between two parallel and same radii SWCNTs using atomistic models.

In this letter, the binding energy between two parallel (and two crossing) SWCNTs (and MWCNTs) is obtained from a continuum model based on the Lennard-Jones (LJ) potential. The analytical expressions are validated by comparing with our full atom molecular dynamics (MD) simulations. The critical length for the mechanical stability and adhesion of the two CNTs has been also determined.

4.2 Results and discussion

Fig. 4.1 shows the two parallel CNTs (Fig. 4.1b) and two crossing CNTs (Fig. 4.1c) under adherent conditions, in which the two CNT radii could be different. To determine the critical and stable length where the two CNTs do not contact together, an analytical model is presented in this paper and the corresponding geometry of the problem is plotted in Fig. 4.1. Some assumptions are proposed to simplify the problem: 1) The two CNTs are taken as two cantilever beams and the shear deformation is neglected. 2) The closest distance between the adherent components of the two CNTs is taken as zero (or a constant d which does not influence the results). 3) The radii of CNTs and the displacement between the two CNTs are both far less than the length L, that is to say, L approximately equals to $s+l$ under adherent condition.

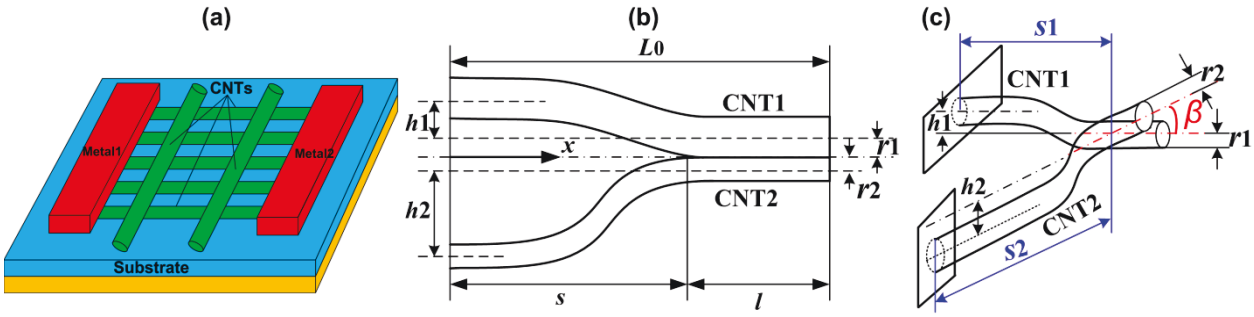

Fig. 4.1 Schematic diagrams showing the fabrication process of CNTs electronic devices and the geometry of two parallel and two crossing CNTs under adherent conditions. (a) The fabrication process of CNTs electronic devices (Zhao et al., 2013), (b) two parallel CNTs, (c) two crossing CNTs.

As shown in Fig. 4.1b, the total energy is composed of elastic energy and adhesion energy.

$$U_T = U_{CNT1} + U_{CNT2} - \gamma(L-s), \tag{1}$$

where U_{CNT1}, U_{CNT2} and γ are elastic energy of CNT1 and CNT2 as well as binding energy per unit length, respectively.

Based on the present boundary condition, the total energy of Eq. (1) can be expressed

$$U_T = \frac{6\left(E_1 I_1 h_1^2 + E_2 I_2 h_2^2\right)}{s^3} - \gamma(L-s), \tag{2}$$

where E_1 and E_2 are the Young's moduli of CNT1 and CNT2, and I_1 and I_2 are the moment of inertia of CNT1 and CNT2.

For a SWCNT, the bending stiffness of the beam is (Timoshenko and Maccullough, 1935)

$$EI = \frac{\pi E}{4}\left[r^4 - (r-t)^4\right], \tag{3}$$

where r and t (0.34 nm is chosen here) are the radius and the thickness of the SWCNT.

For a MWCNT, the bending stiffness of the beam is (Pantano et al., 2003, 2004)

$$(EI)_{MW} = (EI)_{inner}\, m\left[1 + \frac{3(m-1)}{2}\frac{\sigma}{r_{inner}} + \frac{(m-1)(2m-1)}{2}\frac{\sigma^2}{r_{inner}^2} + \frac{m(m-1)^2}{4}\frac{\sigma^3}{r_{inner}^3}\right], \tag{4}$$

where $(EI)_{\text{inner}}$ and r_{inner} are the bending stiffness and radius of the innermost wall, respectively, m is the number of walls, and σ=0.34 nm is the interwall spacing.

In view of the equilibrium of system, the total energy should be a minimum value. The critical value of s can be obtained by $\frac{dU_T}{ds}=0$, that is given

$$L_0^{critical}=\left(\frac{18\left(E_1I_1h_1^2+E_2I_2h_2^2\right)}{\gamma}\right)^{1/4}. \tag{5}$$

If E_1=E_2=E and I_1=I_2=I (that is, CNT1=CNT2), then h_1=h_2=h and Eq. (5) can be written as

$$L_0^{critical}=\left(\frac{36EIh^2}{\gamma}\right)^{1/4}. \tag{6}$$

For two crossing CNTs, the stability length of the CNTs can be obtained from

$$U_T=U_{CNT1}+U_{CNT2}-\gamma_{crossing}\geq 0, \tag{7}$$

where γ_{crossing} is the absolute minimum of the cohesive energy between two crossing CNTs at the equilibrium distance. If we assume the s_1 and s_2 of the two crossing CNTs are both same, we can obtain the stability length from Eq. (2) and Eq. (7),

$$L_0^{stability}=\left(\frac{6\left(E_1I_1h_1^2+E_2I_2h_2^2\right)}{\gamma_{crossing}}\right)^{1/3}, \tag{8}$$

If E_1=E_2=E and I_1=I_2=I (that is, CNT1=CNT2), then h_1=h_2=h and Eq. (8) can be written as

$$L_0^{stability}=\left(\frac{12EIh^2}{\gamma_{crossing}}\right)^{1/3}. \tag{9}$$

From Eq. (5) and Eq. (9), how to determine γ and γ_{crossing} between two parallel CNTs and two crossing CNTs is a crucial issue in this work.

For two parallel SWCNTs, the cohesive energy per unit length has been obtained (Zhao et al., 2013) as

$$\phi_{cicle} = \pi \in \sigma^6 \rho^2 r_1 r_2 \left(\frac{63}{8}\sigma^6 \int_0^{\pi} \frac{F_5\left[\frac{2\sqrt{a_0 r_1}}{r_1 + a_0}\right]}{\left(r_1 + a_0\right)^{11}} d\theta_2 - 12\int_0^{\pi} \frac{F_2\left[\frac{2\sqrt{a_0 r_1}}{r_1 + a_0}\right]}{\left(r_1 + a_0\right)^{5}} d\theta_2 \right), \tag{10}$$

where $\in$ and σ are the depth and the equilibrium distance of the LJ potential between two carbon atoms ($\in = 2.8437\,\text{mev}$ and σ=3.4 Å are adopted from the literatures) (Yakobson, 1996; Chang, 2007), and ρ is the area density CNTs, and r_1 and r_2 are the radii of the two CNTs, and $a_0 = \sqrt{\left(r_1 + r_2 + h\right)^2 + r_2^2 + 2\left(r_1 + r_2 + h\right) r_2 \cos\theta_2}$, and F_5 and F_2 could be found in our previous work (Zhao et al., 2013). The binding energy γ per unit length is the absolute minimum of ϕ_{circle} at equilibrium distance between the two SWCNTs.

For two crossing SWCNTs, the total cohesive energy has been obtained (Zhao et al., 2013) as

$$\phi_{total} = 4\rho^2 r_1 r_2 \in \sigma^6 \frac{1}{\sin\beta}\left(\frac{63\pi}{128}\sigma^6 \int_0^{\pi} \frac{A_0 B_0 S_0}{S_d} d\theta_2 - \frac{3\pi}{4}\int_0^{\pi} \frac{A_1 B_1 T_1}{T_d} d\theta_2 \right), (0<\beta\leq\pi/2) \tag{11}$$

where
$$S_0 = 362880 a_0^9 \cos^9\theta_0 + 6531840 a_0^7 \cos^7\theta_0 r_1^2 + 17146080 a_0^5 \cos^5\theta_0 r_1^4 + 9525600 a_0^3 \cos^3\theta_0 r_1^6 + 893025 a_0 \cos\theta_0 r_1^8 ,$$

$$A_0 = -\frac{1}{128}\left(98 + \frac{36}{5} - \frac{2}{63}\right),\ B_0 = -\frac{2\pi}{9!},\ S_d = \left[\left(r_1 + r_2 + h + r_2\cos\theta_2\right)^2 - r_1^2\right]^{\frac{19}{2}}.$$

$$T_1 = 6a_0^3\cos^3\theta_0 + 9a_0\cos\theta_0 r_1^2 \quad , \quad A_1 = -\frac{4}{3} \quad , \quad B_1 = -\frac{2\pi}{3!} \quad , \quad T_d = \left[\left(r_1 + r_2 + h + r_2\cos\theta_2\right)^2 - r_1^2\right]^{\frac{7}{2}} \quad ,$$

$\theta_0 = arc\cos\frac{\left(r_1 + r_2 + h\right)^2 + a_0^2 - r_2^2}{2\left(r_1 + r_2 + h\right)a_0}$, and β is the crossing angle between the two center axes of the two crossing CNTs (Zhao et al., 2013). The binding energy γ_{crossing} is the absolute minimum of ϕ_{total} at equilibrium distance between the two SWCNTs.

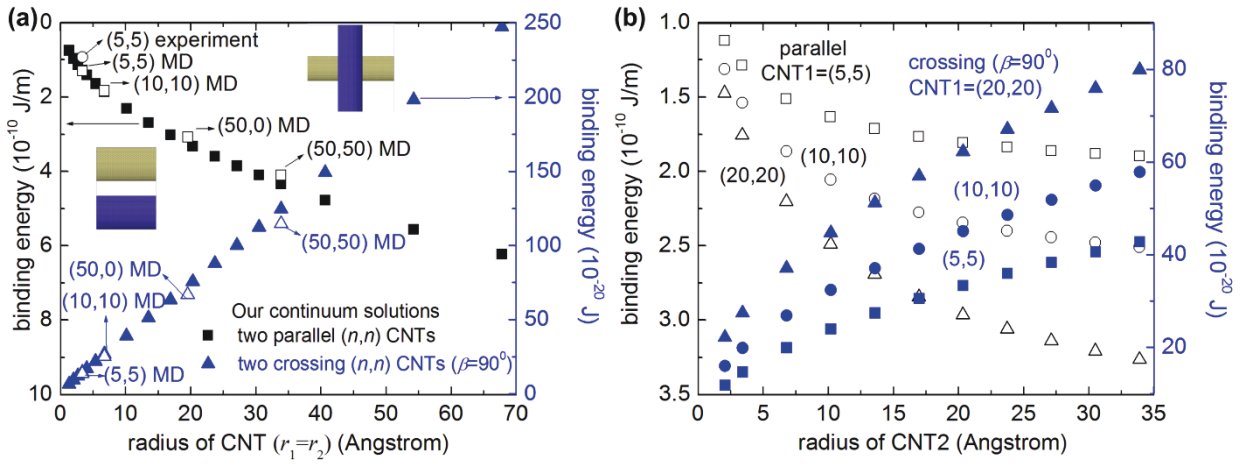

Fig. 4.2 The binding energy distribution with CNT radius between two parallel SWCNTs and two crossing SWCNTs. (a) two same radii SWCNTs, (b) two different radii SWCNTs.

Fig. 4.2a shows the binding energy distribution with CNT radius between two same parallel SWCNTs and two same crossing SWCNTs using Eq. (10), Eq. (11) and full atom MD simulations, in which the MD simulation is performed using LAMMPS (Plimpton, 1995) with the AIREBO potential and periodic boundary conditions are applied along the center axis of the CNTs (the LJ cutoff radius is chosen 60 Å which is an enough distance to get accurate results). The analytical results are in good agreements with those from our full atom MD simulations. Fig. 4.2b shows the analytical binding energy between two different parallel SWCNTs and two different crossing SWCNTs.

Fig. 4.3 shows a SWCNT parallel to a MWCNT. We assume that the distance between any two neighbor CNTs in the MWCNT is 3.4 Å. Based on Eq. (10) and Eq. (11), the cohesive energy between the *i*th CNT in the MWCNT and a SWCNT should be easily obtained as

$$\phi_{i0} = \pi \in \sigma^6 \rho^2 r_0 r_i \left(\frac{63}{8}\sigma^6 \int_0^{\pi} \frac{F_5\left[\frac{2\sqrt{a_0 r_0}}{r_0 + a_0}\right]}{\left(r_0 + a_0\right)^{11}} d\theta_2 - 12 \int_0^{\pi} \frac{F_2\left[\frac{2\sqrt{a_0 r_0}}{r_0 + a_0}\right]}{\left(r_0 + a_0\right)^{5}} d\theta_2 \right), \tag{12}$$

where $a_0 = \sqrt{\left[r_0 + r_i + \left(3.4(i-1) + h_1\right)\right]^2 + r_i^2 + 2\left(r_0 + r_i + \left(3.4(i-1) + h_1\right)\right) r_i \cos\theta_2}$, h_1 is the distance between the SWCNT and the outmost CNT in the MWCNT (see Fig. 4.3).

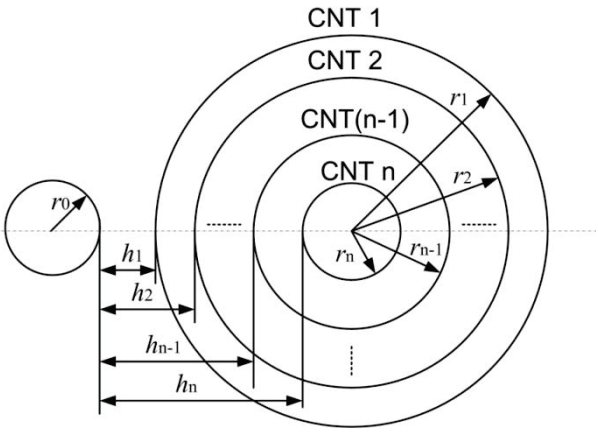

Fig. 4.3 A schematic diagram of a single-walled carbon nanotube parallel a multi-walled carbon nanotubes.

The total cohesive energy from Eq. (12) should be given as

$$\phi_{MW-SW} = \pi \in \sigma^6 \rho^2 r_0 \sum_{1\le i\le n} r_i \left(\frac{63}{8}\sigma^6 \int_0^{\pi} \frac{F_5\left[\frac{2\sqrt{a_0 r_0}}{r_0 + a_0}\right]}{\left(r_0 + a_0\right)^{11}} d\theta_2 - 12\int_0^{\pi} \frac{F_2\left[\frac{2\sqrt{a_0 r_0}}{r_0 + a_0}\right]}{\left(r_0 + a_0\right)^{5}} d\theta_2 \right), \quad (13)$$

where a_0 is the same that in Eq. (11).

Similarly, the total energy between two parallel MWCNTs can be obtained

$$\phi_{MW-MWparallel} = \pi \in \sigma^6 \rho^2 \sum_{1\le i\le m} \sum_{1\le i\le n} r_i r_j \left(\frac{63}{8}\sigma^6 \int_0^{\pi} \frac{F_5\left[\frac{2\sqrt{a_0 r_j}}{r_j + a_0}\right]}{\left(r_j + a_0\right)^{11}} d\theta_2 - 12\int_0^{\pi} \frac{F_2\left[\frac{2\sqrt{a_0 r_j}}{r_j + a_0}\right]}{\left(r_j + a_0\right)^{5}} d\theta_2 \right), \quad (14)$$

where $a_0 = \sqrt{\left[r_j + r_i + \left(3.4\left(i + j - 2\right) + 2h_1\right)\right]^2 + r_i^2 + 2\left(r_j + r_i + \left(3.4\left(i + j - 2\right) + 2h_1\right)\right) r_i \cos\theta_2}$, m is the number of the walls in the other MWCNT.

Similarly, the total energy between two crossing MWCNTs can be obtained

$$\phi_{MW-MWcross} = 4\rho^2 \in \sigma^6 \frac{1}{\sin\beta} \sum_{1\le i\le m} \sum_{1\le i\le n} r_i r_j \left(\frac{63\pi}{128} \sigma^6 \int_0^{\pi} \frac{A_0 B_0 S_0}{S_d} d\theta_2 - \frac{3\pi}{4} \int_0^{\pi} \frac{A_1 B_1 T_1}{T_d} d\theta_2 \right), \quad (15)$$

where $\theta_0 = arc\cos \dfrac{\left(r_i + r_j + \left(3.4\left(i+j-2\right)+2h_1\right)\right)^2 + a_0^2 - r_j^2}{2\left(r_i + r_j + \left(3.4\left(i+j-2\right)+2h_1\right)\right)a_0}$

,

$$S_0 = 362880a_0^9 \cos^9\theta_0 + 6531840a_0^7 \cos^7\theta_0 r_i^2 + 17146080a_0^5 \cos^5\theta_0 r_i^4 + 9525600a_0^3 \cos^3\theta_0 r_i^6 + 893025a_0 \cos\theta_0 r_i^8$$

,

$S_d = \left[\left(r_i + r_j + \left(3.4\left(i+j-2\right)+2h_1\right) + r_j\cos\theta_2\right)^2 - r_i^2 \right]^{\frac{19}{2}}$, $T_1 = 6a_0^3\cos^3\theta_0 + 9a_0\cos\theta_0 r_i^2$,

$T_d = \left[\left(r_i + r_j + \left(3.4\left(i+j-2\right)+2h_1\right) + r_j\cos\theta_2\right)^2 - r_i^2 \right]^{\frac{7}{2}}$, a_0 is the same with that in Eq. (14), and the other parameters are the same with those in Eq. (11).

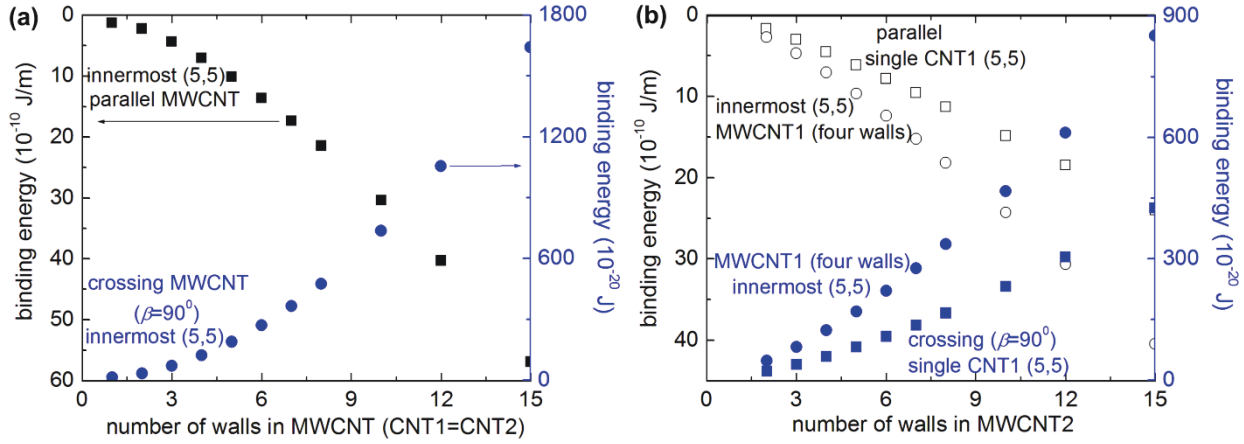

Fig. 4.4 The binding energy distribution with CNT radius between two parallel MWCNTs and two crossing MWCNTs. (a) two same radii MWCNTs, (b) two different radii MWCNTs.

Fig. 4.4 shows the binding energy between two parallel MWCNTs and two crossing MWCNTs, in which the innermost CNT is the (5,5) CNT. The binding energy nonlinearly increases with increasing number of walls.

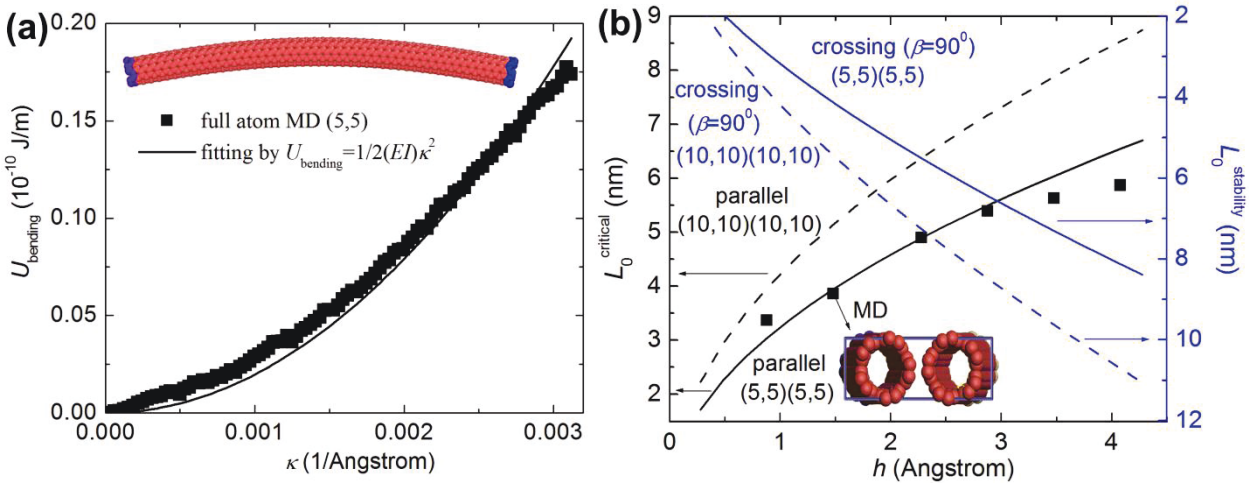

Fig. 4.5 (a) The bending stiffness of a (5,5) CNT by full atom MD simulation, (b) The critical length and stable length for two parallel SWCNTs and two crossing SWCNTs based on our analytical results and full atom MD simulations.

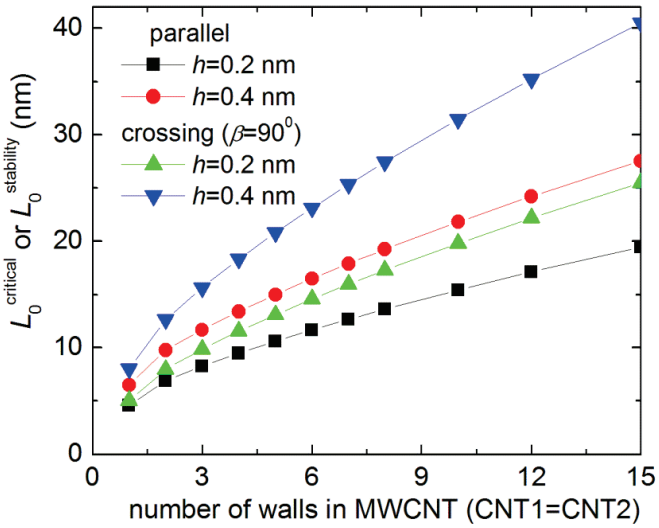

Fig. 4.6 The critical length and stable length with number of walls for two parallel MWCNTs and two crossing MWCNTs based on our analytical results.

Fig. 4.5 shows the critical length and stable length for two parallel SWCNTs and two crossing SWCNTs based on our analytical results and full atom MD simulations. The bending stiffness EI=3.95×10^{-26} J m of the (5,5) CNT is obtained by our MD results with AIREBO potential (see Fig. 4.5a), which is close to the available value 3.84 ×10^{-26} J m from previous work (Zhou et al., 2007). $U_{bending}$ is the bending energy per unit length and κ is the 1/r, in which r is the curvature

radius and the (5,5) CNT length is equal to 11.6 nm in Fig. 4.5a (Zhao et al., 2013). We find that the present analytical results are in good agreement with those from MD simulations for two parallel (5,5) CNTs in Fig. 4.5b. Fig. 4.6 shows the critical length and stable length for two parallel MWCNTs and two crossing MWCNTs based on our analytical results. For a given distance (the distance between the two outmost CNTs in the two MWCNTs (Fig. 4.1)), the critical length and stable length both nonlinearly increase with increasing number of walls.

4.3 Conclusion

In summary, the binding energy between two parallel (and two crossing) single-walled (and multi-walled) carbon nanotubes (CNTs) is obtained by continuum modeling of the vdW interactions between them. The dependence of the binding energy on their diameters, number of walls and crossing angles is systematically analyzed. The critical length for the mechanical stability and adhesion of the CNTs has been determined by the function of E_iI_i, h and γ, where E_iI_i, h and γ are the CNTs bending stiffness, distance and binding energy between them. Checking against full atom molecular dynamics calculations show that the continuum solution has high accuracy. The established analytical solutions should be of great help for designing nanoelectromechanical devices.

References:

Ajayan, P.M., Banhart, F., 2002. Strong bundles. Nat. Mater. 3, 135-136.

Baughman, R.H., Zakhidov, A.A, de Heer, W.A., 2002. Carbon nanotubes-the route toward applications. Science 297, 787-792.

Bronikowski, M., 2006. CVD growth of carbon nanotube bundle arrays. Carbon 44, 2822-2832.

Chang, T., Gao, H., 2003. Size-dependent elastic properties of a single-walled carbon nanotube via a molecular mechanics model. J. Mech. Phys. Solids 51, 1059-1074.

Chen, B., Gao, M., Zuo, J.M., Qu, S., Liu, B., Huang, Y., 2003. Binding energy of parallel carbon nanotubes. Appl. Phys. Lett. 83, 3570-3571.

Cranford, S. Sen, D., Buehler, M.J., 2009. Meso-origami: folding multilayer graphene sheets. Appl. Phys. Lett. 95, 123121.

Cranford, S., Yao, H., Ortiz, C., Buehler, M.J., 2010. A single degree of freedom 'lollipop' model for carbon nanotube bundle formation. J. Mech. Phys. Solids 58, 409-427.

Geblinger, N. Ismach, A., Joselevich, E., 2008. Self-organized nanotube serpentines. Nat. Nanotechnol. 3, 195-200.

Girifalco, L.A., Hodak, M., Lee, R., 2000. Carbon nanotubes, buckyballs, ropes, and a universal graphitic potential. Phys. Rev. B 62, 13104-13110.

Iijima, S., 1991. Helical microtubules of graphitic carbon. Nature 354, 56-58.

Kis, A., Csanyi, G., Salvetat, J.P., Lee, T.N., Couteau, E., Kulik, A.J., Benoit, W., Brugger, J., Forro, L., 2004. Reinforcement of single-walled carbon nanotube bundles by intertube bridging. Nat. Mater. 3, 153-157.

Li, C.Y., Chou, T.W., 2003. A structural mechanics approach for the analysis of carbon nanotubes. Int. J. Solids Struct., 40, 2487-2499.

Li, H., Guo, W., 2008. Transversely isotropic elastic properties of single-walled carbon nanotubes by a rectangular beam model for the C-C bonds. J. Appl. Phys. 103, 103501.

Modi, A., Koratkar, N., Lass, E., Wei, B.Q., Ajayan, P.M., 2003. Miniaturized gas ionization snsors using carbon nanotubes. Nature 424, 171-174.

Pantano, A., Boyce, M.C., Parks, D.M., 2003. Nonlinear structural mechanics based modeling of carbon nanotube deformation. Phys. Rev. Lett. 91, 145504.

Pantano, A., Parks, D.M., Boyce, M.C., 2004. Mechanics of deformation of single and multi-wall carbon nanotubes. J. Mech. Phys. Solids 52, 789-821.

Ru CQ. Effect of van der Waals forces on axial buckling of a double-walled carbon nanotube. J Appl Phys 2000;87:7227-31.

Ru, C.Q., 2001. Axially compressed buckling of a doublewalled carbon nanotube embedded in an elastic medium. J. Mech. Phys. Solids 49, 1265-1279.

Timoshenko, S., Maccullough, G.H., Elements of Strength of Materials (Van Nostrand, New York, 1935)

Xie, B., Liu, Y., Ding, Y., Zheng, Q., Xu, Z., 2011. Mechanics of carbon nanotube networks: microstrutural evolution and optimal design. Soft Matter 7, 10039-10047.

Yakobson, B.I., Brabec, C.J., Bernholc, J., 1996. Nanomechanics of carbon tubes: instability beyond linear response. Phys. Rev. Lett. 76, 2511-2514.

Zhao, J., Jiang, J.W., Jia, Y., Guo, W., Rabczuk, T., 2013. A theoretical analysis of cohesive energy between carbon nanotubes, graphene and substrates. Carbon, accept.

Zhou, W., Huang, Y., Liu, B., Hwang, K.C., Zuo, J.M., Buehler, M.J., Gao, H., 2007. Self-folding of single- and multiwall carbon nanotubes. Appl. Phys. Lett. 90, 073107.

Chapter 5

Size-dependent elastic properties of crystalline polymers via a molecular mechanics model*

Abstract

An analytical molecular mechanics model is developed to obtain the size-dependent elastic properties of crystalline polyethylene. An effective "stick-spiral" model is adopted in the polymer chain. Explicit equations are derived from the Lennard-Jones potential function for the van der Waals force between any two polymer chains. By using the derived formulas, the nine size-dependent elastic constants are investigated systematically. The present analytical results are in reasonable agreement with those from present united-atom molecular dynamics simulations. The established analytical model provides an efficient route for mechanical characterization of crystalline polymers and related materials toward nanoelectromechanical applications.

5.1 Introduction

Crystalline polyethylene (PE) is increasingly used in modern industry as structural materials due to its important mechanical and physical properties. Despite its importance and the studies of available molecular dynamics (MD) simulations and constitutive models (Karasawa et al., 1991; Zhao et al., 2010; Nikolov et al., 2002), the link between molecular and continuum descriptions of its mechanical properties is still not well established. In order to overcome limitations of atomistic simulations and continuum models, a "stick-spiral" model (Chang and Gao, 2003) based on interatomic potentials has been effectively developed for different nanotubes (Chang et al., 2005; Jiang and Guo, 2011). However, the van der Waals (vdW) interactions have a crucial effect on the elastic properties in crystalline PE (Fig. 5.1), while the vdW interactions can be neglected in the "stick-spiral" model (Chang and Gao, 2003; Jiang and Guo, 2011) in view of the small deformation in a single-walled nanotube. To extend the analytical model to more complicated polymers, we present an improved model to investigate the size-dependent elastic properties of crystalline PE.

* The work has been published on <<Applied Physics Letters>> 99, 241902 (2011).

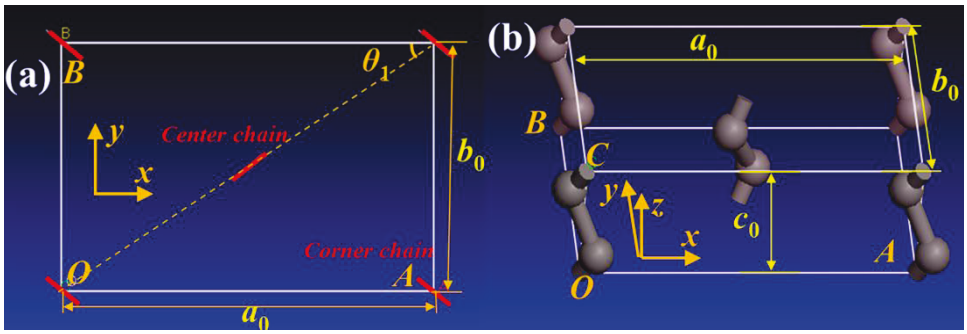

Fig. 5.1 Geometry of a single crystalline PE and corresponding coordinates. (a) each polymer chain's position view in *xoy* plane, (b) three-dimensional structure.

In this letter, we use the "stick-spiral" model to simulate united-atom (UA) CH_2-CH_2 bonds stretching, angle bending potentials along the polymer chain (or *z* direction), while the vdW force between any two polymer chains can be directly calculated (Ru, 2001; He et al., 2005; Lu et al., 2009) based on the Lennard-Jones (LJ) pair potential functions.

2. Results and discussion

In the framework of molecular dynamics, the total energy, U, of a crystalline PE at small strains along *z* direction can be expressed as a sum of energies associated with the variance of bond length, U_b, and bond angle, U_θ, i.e., (Chang and Gao, 2003)

$$U = U_b + U_\theta = \frac{1}{2}\sum_i K_b \left(db_i\right)^2 + \frac{1}{2}\sum_j K_\theta \left(d\theta_j\right)^2 , \tag{1}$$

where db_i is the bond elongation of bond i and $d\theta_j$ is the variance of bond angle j, and K_b and K_θ are the related force constant.

To obtain the equilibrium equations of the structure along *z* direction under tension, we adopt the "stick-spiral" model developed by Chang and Gao (2003). As shown in Fig. 5.2, force equilibrium of bond extension and moment equilibrium lead to

$$\begin{cases} f\sin\left(\dfrac{\alpha}{2}\right) = K_b db \\ f\cos\left(\dfrac{\alpha}{2}\right)\dfrac{b}{2} = K_\theta d\alpha \end{cases}, \tag{2}$$

where f is the external force in z direction on one polymer chain.

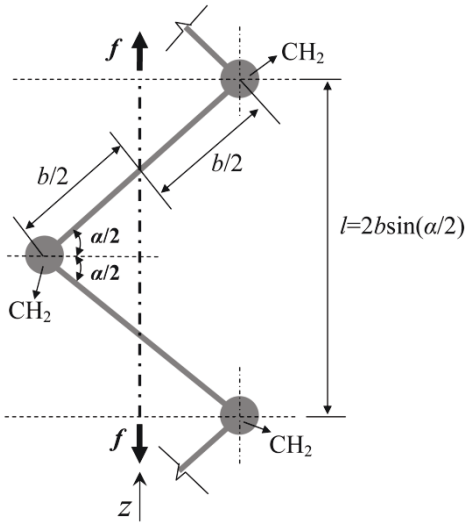

Fig. 5.2 Schematic illustration of polymer chain under z tension.

We define the z direction strain as

$$\varepsilon_z = \frac{d\left(2b\sin\frac{\alpha}{2}\right)}{2b\sin\frac{\alpha}{2}} = db\left(\frac{1}{b} + \frac{b\cos^2\frac{\alpha}{2}K_b}{4K_\theta \sin^2\frac{\alpha}{2}}\right), \tag{3}$$

Assuming the structural parameters of every cell remain constant with different-sized structures in Fig. 5.1, we can obtain the size-dependent elastic properties of crystalline PE. From Eq. (2) and Eq. (3), the elastic property of C_{33} can be written as[1]

$$C_{33} = \frac{\sigma_z}{\varepsilon_z} = \frac{\left[(m+1)(n+1)+mn\right]f}{mna_0b_0\varepsilon_z} = \frac{\left[\left(1+\frac{1}{n}\right)\left(1+\frac{1}{m}\right)+1\right]4K_\theta K_b b\sin\frac{\alpha}{2}}{a_0b_0\left(4K_\theta\sin^2\frac{\alpha}{2}+K_b b^2\cos^2\frac{\alpha}{2}\right)}, \tag{4}$$

where a_0 and b_0 denote the cell length, m and n are the number of cells along the x- and y-direction, respectively.

We find that the result of C_{33} in one cell wire (m=1, n=1 and periodic boundary in z direction) is about 2.5 times higher than that of in bulk PE ($m\to\infty$, $n\to\infty$), while C_{33} is independent of the

thickness in z direction. The constants α=109.5°, K_b=700 Kcal/mol.Å^2 and K_θ=120 Kcal/mol (Waheed, 2005; Shepherd, 2006) are adopted here and in the latter UA MD simulations.

To model vdW interaction between any two chains of crystalline PE, the LJ pair potential U_{LJ} is adopted as (He et al., 2005) $U_{LJ} = 4 \in \left[\left(\frac{\sigma}{r} \right)^{12} - \left(\frac{\sigma}{r} \right)^{6} \right]$, where r is the distance between the interacting atoms, $\in$ the depth of the potential, and σ a parameter that is determined by the equilibrium distance. Here, we use the avaliable LJ potential's parameters of σ=4.01 Å and $\in$ =0.112 Kcal/mol (Waheed, 2005; Shepherd, 2006).

The vdW force F_{vdW} can be obtained from taking the derivative of the LJ pair potential $F_{vdw}(r) = -\frac{dU_{LJ}}{dr} = 24\frac{\in}{\sigma}\left[2\left(\frac{\sigma}{r} \right)^{13} - \left(\frac{\sigma}{r} \right)^{7} \right]$. It should be noted that the negative value of the vdW force represents the attractive force of an approaching pair of atoms from a certain distance whereas the positive value represents the repulsive force between a pair of atoms.

The vdW force exerted on any bead (CH_2) of a polymer chain can be estimated by summing all forces between the bead and all beads on the other chains. To simplify the calculations, we consider the chain as a straight continuum stick (He et al., 2005) and note that each bead corresponds to the length of $l/2=b\sin(\alpha/2)=c_0/2$ (c_0 is the cell length along z-direction) in Fig. 5.1b. Thus, the integration of F_{vdW} over the entire chain leads to an analytical representation for the initial force contribution f_{ij} caused by the vdW interaction

$$
\begin{aligned}
f_{ij}(L, r_0) = 2Lp_{ij} &= \frac{2L}{(c_0/2)}\left(\int_{-L}^{L} 24\frac{\in}{\sigma}\left[2\left(\frac{\sigma}{r} \right)^{13} - \left(\frac{\sigma}{r} \right)^{7} \right]\frac{1}{(c_0/2)}\cos\theta dz \right) \\
&= \frac{2L}{(c_0/2)^2}\left[\left(\frac{48 \in \sigma^{12}}{r_0^{12}} \int_{\arctan(-L/r_0)}^{\arctan(L/r_0)} \cos^{12}\theta d\theta \right) - \left(\frac{24 \in \sigma^{6}}{r_0^{6}} \int_{\arctan(-L/r_0)}^{\arctan(L/r_0)} \cos^{6}\theta d\theta \right) \right],
\end{aligned}
\tag{5}
$$

where $\cos\theta=r_0/r$, $z=r\sin\theta$, L is the length along z direction, r_0 is the initial displacement between two polymer chains, p_{ij} is the force per unit length of a chain. Because the distributions of the vdW force F_{vdW} and its gradient dF_{vdW}/dr between two polymer beads are both close to zero when r_0>8.5 Å, we only consider the vdW interaction with the initial displacement r_0<8.5 Å.

In view of the crystalline PE in the PNAM space group, the nine independent elastic constants C_{11}, C_{12}=C_{21}, C_{13}=C_{31}, C_{22}, C_{23}=C_{32}, C_{33}, C_{44}, C_{55} and C_{66} should be in the elastic matrix (Karasawa et al., 1991). The four kinds of positions change between two polymer chains are plotted in Fig. 5.3 under the six direction strains, respectively.

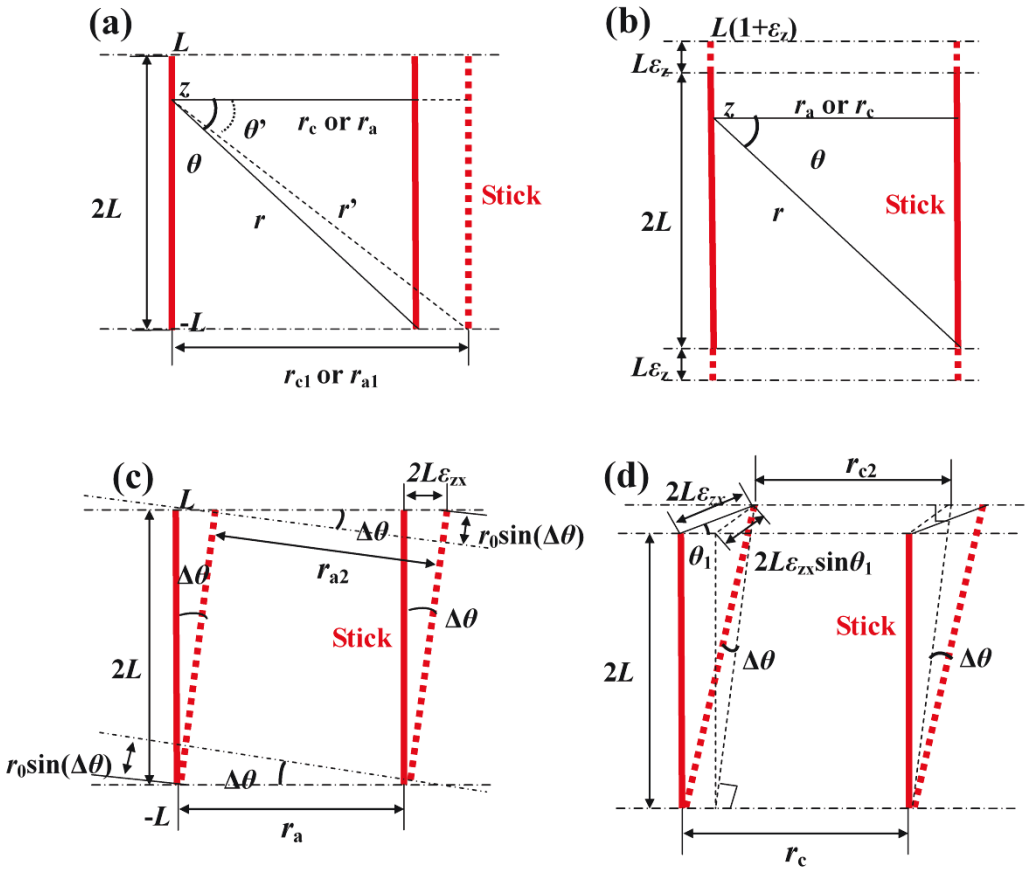

Fig. 5.3 Schematic illustration of the position change between two "sticks" in one PE cell after deformation. (a) under *x* or *y* tension or *yx* shear, (b) under *z* tension, (c) any two corner sticks under *zx* or *zy* shear, (d) between corner and center sticks under *zx* or *zy* shear.

When the strain in the *x*-direction is ε_x (see Fig. 5.3a), the C_{11} and C_{12} can be expressed as

$$\begin{cases} C_{11}=\dfrac{\sigma_x}{\varepsilon_x}=\dfrac{4\left[f_{ij}\left(L,r_c\right)\cos\theta_1-f_{ij}\left(L,r_{c1}\right)\cos\theta_1'\right]+2\left[f_{ij}\left(L,r_a\right)-f_{ij}\left(L,r_{a1}\right)\right]}{2Lb_0\varepsilon_x} \\ C_{21}=\dfrac{\sigma_y}{\varepsilon_x}=\dfrac{4\left[f_{ij}\left(L,r_c\right)\sin\theta_1-f_{ij}\left(L,r_{c1}\right)\sin\theta_1'\right]}{2L\left(1+\varepsilon_x\right)a_0\varepsilon_x} \end{cases}, \tag{6}$$

where $r_c = \frac{\sqrt{a_0^2 + b_0^2}}{2}, r_{c1} = \frac{\sqrt{\left(1+\varepsilon_x\right)^2 a_0^2 + b_0^2}}{2}, r_a = a_0, r_{a1} = \left(1+\varepsilon_x\right)a_0, \cos\theta_1 = \frac{a_0}{\sqrt{a_0^2 + b_0^2}}$,

$\cos\theta_1' = \frac{\left(1+\varepsilon_x\right)a_0}{\sqrt{\left(1+\varepsilon_x^2\right)a_0^2 + b_0^2}}$, θ_1 is the angle in Fig. 1a.

When the strain in the *y*-direction is ε_y or in the *xy*-direction is ε_{xy}, the C_{22}, C_{12} and C_{66} can be easily obtained in the elastic matrix in view of the similar position change between two chains in Fig. 3a. The average values of C_{21} and C_{12} are shown in Table I (see C_{12}). For the strain in the *z*-direction ε_z in Fig. 5.3b, the $C_{13}=\sigma_x/\varepsilon_z$ and $C_{23}=\sigma_y/\varepsilon_z$ are easily obtained from Eq. (1).

When the strain in the *zx*-direction is ε_{zx} (see Fig. 5.3c and d), the C_{44} can be expressed as

$$C_{55} = \frac{\sigma_{zx}}{\varepsilon_{zx}} = \frac{4\left[f_{ij}\left(l, r_c\right)\cos\theta_1 - f_{ij}\left(l', r_{c2}\right)\eta\right] + 2\left[f_{ij}\left(l, r_a\right) - f_{ij}\left(l_1', r_{a2}\right)\cos\left(\Delta\theta\right)\right] + 2F_{stick}}{a_0 b_0 \varepsilon_{zx}}, \quad (7)$$

where $l=c_0$, $l' = l\sqrt{1+\varepsilon_{zx}^2} - \frac{\varepsilon_{zx}\cos\theta_1}{\sqrt{1+\varepsilon_{zx}^2}} r_c$, $r_{c2} = \frac{\sqrt{1+\varepsilon_{zx}^2\sin\theta_1^2}}{\sqrt{1+\varepsilon_{zx}^2}} r_c$,

$\eta = \frac{\sqrt{1+\varepsilon_{zx}^2\sin\theta_1^2}}{\sqrt{1+\varepsilon_{zx}^2}}\cos\theta_1 - \frac{\varepsilon_{zx}\cos\theta_1}{\sqrt{1+\varepsilon_{zx}^2}}\frac{\varepsilon_{zx}\sin\theta_1}{\sqrt{1+\varepsilon_{zx}^2\sin\theta_1^2}}\sin\theta_1$, $l_1' = l\sqrt{1+\varepsilon_{zx}^2} - \frac{1}{\sqrt{1+\varepsilon_{zx}^2}} r_a$,

$r_{a2} = \frac{1}{\sqrt{1+\varepsilon_{zx}^2}} r_a$, $\cos\left(\Delta\theta\right) = \frac{1}{\sqrt{1+\varepsilon_{zx}^2}}$, $F_{stick} = \left(\sqrt{1+\varepsilon_{zx}^2} - 1\right)\frac{4K_\theta K_b b \sin\frac{\alpha}{2}}{\left(4K_\theta \sin^2\frac{\alpha}{2} + K_b b^2 \cos^2\frac{\alpha}{2}\right)}\frac{\varepsilon_{zx}}{\sqrt{1+\varepsilon_{zx}^2}}$.

The method under *zy* shear is similar to that of under *zx* shear, in which the force increment along *y* direction can be obtained by replacing θ_1 with 90°-θ_1.

To validate the present analytical model, the Karasawa et al.'s MC PE (Karasawa et al., 1991) of supercell (2×2×2) structure is built from Materials Studio (MS) (version 5.0) (Avitabile et al., 1975) as the initial UA structure. Afterwards, the nine independent elastic constants are calculated through the MD simulations (Plimpton, 1998) in 0 K under periodic boundary condition based on the Ray and Moody's method.

TABLE 5.1 Nine elastic constants (GPa) of present analytical model, united-atom molecular dynamics results and Karasawa et al.'s all-atom molecular dynamics calculations for bulk PE.

Elactic constants	C11	C12	C22	C33	C23	C13	C44	C55	C66
Anal. pure LJ	14.52	6.89	2.92	/	0.72	1.28	0.02	0.03	7.53
Anal. all potential	14.50	6.97	2.83	195.08	0.70	1.27	0.03	0.04	7.57
MD pure LJ	15.3±0.3	7.1±0.4	4.9±1.4	0.9±0.4	0.3±0.2	0.5±0.3	0.6±0.2	1.1±0.2	6.5±0.3
MD all potential	15.6±0.5	7.0±0.4	5.1±1.2	200±0.6	1.61±1.0	3.03±2.0	5.58±0.3	5.97±0.3	6.48±0.5
Karasawa MC (1991)	13.9	7.9	13.5	237.9	4.8	2.3	5.4	3.0	5.9

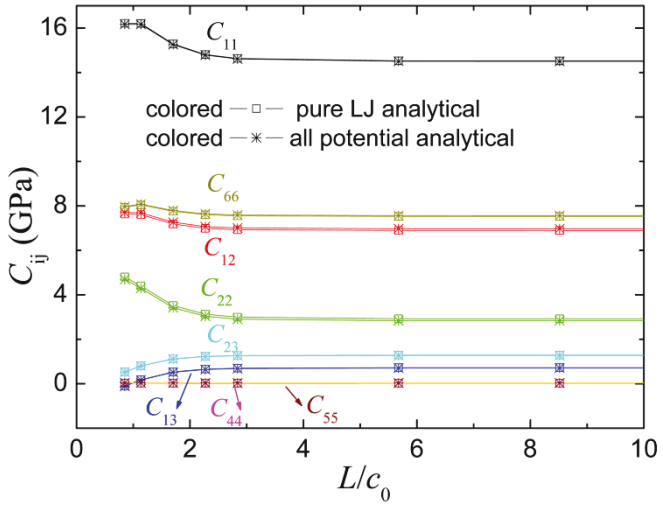

Fig. 5.4 Eight size-dependent elastic constants with different thickness along *z* direction using the present analytical model.

We find that the most elastic constants using the present UA MD simulations of all potentials (include all bond, angle and LJ potentials) are very different with those of Karasawa et al.'s all-atom MD calculations (Karasawa et al., 1991) in Table I. The possible reason is that the present analytical model is based on the UA potentials, in which the torsion potential, out-of-plane bending potentials and coulomb interactions are neglected. Therefore, we should compare present analytical model with UA MD simulations. Compared with the two UA MD results using all potentials and the pure LJ potential in Table 5.1, we find that the difference of the values of C_{23}, C_{33}, C_{13}, C_{44} and C_{55} are large. It indicates that the bond and angle potentials have a large effect on these elastic constants. The present analytical result C_{33}=195 GPa is in excellent agreement with the value of C_{33}=200±0.6 GPa using all potentials' UA MD simulations. The

analytical values of C_{11}, C_{12}, C_{23}, C_{13} and C_{66} are also in good agreement with those of this UA MD method, while the difference of C_{44} and C_{55} are very large. It indicates that the present analytical model is effective to predict the most elastic constants, while it has limitations to predict C_{44} and C_{55}. One possible reason is that the shear and torsion properties of the "stick" in the present analytical model are neglected; another reason is that the present simplified straight stick has a little effect on the predictions of the elastic constants.

To understand the size-dependent elastic properties of PE, the effect of the polymer thickness along the z-direction on the elastic constants is further studied in Fig. 5.4, in which the periodic boundary is only adopted along the x- and y-directions. The elastic constants of C_{11}, C_{12}, C_{22} and C_{66} increase with decreasing thickness, while C_{13} and C_{23} decrease with decreasing it. The values of C_{44} and C_{55} are both independent of it. The results mean that the change tendency of the size-dependent elastic constants is not in accordance with one another, which strongly depends on the lattice direction. When $L/c_0>10$, all of the elastic constants are close to the corresponding constants in Fig. 5.4, respectively.

5.3 Concluding remarks

In summary, on the basis of the molecular mechanics approach, we present an analytical model to obtain the size-dependent elastic properties of crystalline PE. We obtain a set of closed-form expressions for nine size-dependent elastic constants of crystalline PE. Compared with the present united-atom molecular dynamics calculations, we find that the present analytical model can be used to effectively simulate the van der Waals interactions between any two polymer chains. This work is an new effort to establish analytical models of molecular mechanics for crystalline polymers, and is helpful for further analytical studies of elastic properties of other crystalline polymers.

References

Avitabile, G., Napolitano, N., Pirozzi, B., Rouse, K.D., Thomas, M.W., Willis, B.T.M., 1975. Low temperature crystal structure of polyethylene: Results from a neutron diffraction study and from potential energy calculations. J. Polymer Sci., Polym. Lett. Ed. **13**, 351-355.

Chang, T., Gao, H., 2003. Size-dependent elastic properties of a single-walled carbon nanotube via a molecular mechanics model. J. Mech. Phys. Solids 51, 1059-1074.

Chang, T., Geng, J., Guo, X., 2005. Chirality- and size-dependent elastic properties of single-walled carbon nanotubes. Appl. Phys. Lett. 87, 251929.

He, X.Q., Kitipornchai, S., Liew, K.M., 2005. Buckling analysis of multi-walled carbon nanotubes: a continuum model accounting for van der Waals interaction. J. Mech. Phys. Solids 53, 303-326.

Jiang, L., Guo, W., 2011. A molecular mechanics study on size-dependent elastic properties of single-walled boron nitride nanotubes. J. Mech. Phys. Solids 59, 1204-1213.

Karasawa, N., Dasgupta, S., Goddard III, W.A., 1991. Mechanical properties and force field parameters for polyethylene crystal. J. Phys. Chem. 95, 2260-2272.

Li, H., Guo, W., 2008. Transversely isotropic elastic properties of single-walled carbon nanotubes by a rectangular beam model for the C-C bonds. J. Appl. Phys. 103, 103501.

Lu, W.B., Liu, B., Wu, J., Xiao, J., Hwang, K.C., Fu, S.Y., Huang, Y., 2009. Continuum modeling of van der Waals interactions between carbon nanotube walls. Appl. Phys. Lett. 94, 101917.

Nikolov, S., Doghri, I., Pierard, O., Zealouk, L., Goldberg, A., 2002. Multi-scale constitutive modeling of the small deformations of semi-crystalline polymers. J. Mech. Phys. Solids 50, 2275-2302.

Plimpton, S., 1995. Fast parallel algorithms for short-range molecular dynamics. J. Comput. Phys. 117, 1-19.

Ray, J.R., Moody, M.C., 1985. Molecular dynamics calculation of elastic constants for a crystalline system in equilibrium. Phys. Rev. B 32, 733-735.

Ru, C.Q., 2001. Axially compressed buckling of a doublewalled carbon nanotube embedded in an elastic medium. J. Mech. Phys. Solids 49, 1265-1279.

Shepherd, J.E., 2006. Multiscale modeling of the deformation of semi-crystalline polymers. Ph. D thesis. Georgia Institute of Technology, USA.

Waheed, N., 2005. Molecular simulation of crystal growth in alkane and polyethylene melts. Ph. D thesis. Cornell University, USA.

Zhao, J., Nagao, S., Zhang, Z.L., 2010. Thermo-mechanicyal properties dependence on chain length in bulk polyethylene: Coarse-grained molecular dynamics simulations, J. Mater. Res., 25, 537-544.

Chapter 6

A comparative study of two molecular mechanics models based on the harmonic potentials*

Abstract

We show that the two molecular mechanics models, the stick-spiral and the beam models, predict considerably different mechanical properties of materials based on energy equivalence. The difference between the two models is independent of the materials since all parameters of the beam model are obtained from the harmonic potentials. We demonstrate this difference for finite width graphene nanoribbons and a single polyethylene chain comparing results of the molecular dynamics (MD) simulations with harmonic potentials and the finite element method with the beam model. We also find that the difference strongly depends on the loading modes, chirality and width of the graphene nanoribbons, and it increases with decreasing width of the nanoribbons under pure bending condition. The maximum difference of the predicted mechanical properties using the two models can exceed 300% in different loading modes. Comparing the two models with the MD results of AIREBO potential, we find that the stick-spiral model overestimates and the beam model underestimates the mechanical properties in narrow armchair graphene nanoribbons under pure bending condition.

6.1 Introduction

Harmonic potentials have been extentively used to investigate the mechanical and physical properties of various materials in molecular mechanics models, such as carbon nanotubes (CNTs), boron nitride nanotubes (BNTs), graphene sheets and polymers (Chopra et al., 1995; Chang and Gao, 2003; Li and Chou, 2003; Zhao et al., 2010; Zhao et al., 2011; Jiang and Guo, 2011). Atomistic-based methods such as classical MD (Iijima et al., 1996; Yakobson et al., 1996), tight-binding MD (Hernandez et al., 1998; Zhao et al., 2009a), and density functional theory (Sanchez-Portal et al., 1999; Zhang et al., 2007; Zhang and Guo, 2008) have been used to study

* The work has been published on <<Journal of Applied Physics>> 113, 063509 (2013).

the mechanical properties of CNTs, BNTs and nanoribbons. However, compared with bottom-up approaches, top-down approaches may substantially reduce the computational costs and are thus frequently used in related investigations. Recently, the molecular dynamics (MD) simulation with harmonic potentials coupling finite element (FE) method have been more and more applied to multiscale modeling in order to characterize the mechanical behavior of the different materials from nanoscale to microscale/macroscale (Badia et al., 2007; Di Matteo et al., 2007; Bian and Wang, 2011), so the predictive ability based on the harmonic potentials has special importance.

Some typical continuum models based on the harmonic potentials have been developed and broadly used to clarify the elastic properties of the graphene sheets, CNTs and BNTs (Hernandez et al., 1998; Vaccarini et al., 2000; Ru, 2001; Chang and Gao, 2003; Li and Chou, 2003). Three kinds of models are usually employed: 1). Shell models have been used to capture the buckling characterizes of CNTs (Yakobson et al., 1996; Ru, 2000; Ru, 2001; He et al., 2005; Wang et al., 2007; Wu et al., 2008). The applicability and limitations of shell models have been extensively discussed (Wang, 2004; Peng et al., 2008; Zhang et al., 2009). Chang (2010) developed an anisotropic shell model to investigate mechanical behavior of single-walled CNTs, in which the model can be used to effectively describe the chirality effect on mechanical properties. 2). The beam model was developed by Li and Chou (2003, 2004). They assume that the beam elements have circular cross sections and are always subjected to pure tension, pure bending, and pure torsion. The theory was further improved (Tserpes and Papanikos, 2005; Xia et al., 2005; To, 2006; Kasti, 2007; Jiang et al., 2009) and extended to calculate the five independent size- and chirality-dependent elastic moduli of single-walled CNTs using equivalent beam elements with rectangular section (Li and Guo 2008). 3). The “stick-spiral” model (SSM) was developed by Chang and Gao (2003). An improved model by Jiang and Guo (2011) was used to investigate the elastic properties of single-walled boron nitride nanotubes. By extending the two analytical methods to crystalline polymers (Zhao et al., 2010), we presented the SSM to investigate the size-dependent elastic properties of crystalline polyethylene (PE) (Zhao et al., 2011). Based on the united-atom MD simulations, we further verified the effectivity of the SSM in the crystalline polymers directly (Capaldi et al., 2004; Zhao et al., 2011). In this work, we utilized a united atom approximation in which the methyl groups (CH2) are represented by a single “atom” or unit, and the effect of the hydrogen atoms on the polymer’s configuration is accounted for in the potentials

(Waheed, 2005; Shepherd, 2006). Subsequently, we extended the beam-spring model to obtain the elastic properties of crystalline PE (Zhao et al., 2012).

Kasti (2007) found that the beam bending stiffness (BBS) (EI/b, where E is the Young's modulus, b is the beam length and I is the moment of inertia of the beam (see section 6.2)) is equal to the bond bending stiffness (K_θ, which is the bond angle bending force constant (see section 6.2)) in zigzag CNTs, while the BBS beam bending stiffness is only half of the bond bending stiffness K_θ in graphene nanoribbons. This discovery was verified in the zigzag CNT and graphene sheet based on energy equivalence.

Although the SSM and the beam models have been effectively used to describe the elastic properties of CNTs, BNTs and graphene sheets (Li and Chou, 2003, 2004; Kasti, 2007; Li and Guo 2008; Jiang and Guo, 2011), the difference of their prediction ability has never been systematically studied.

In this paper, we study the mechanical properties of the finite width graphene nanoribbons under different loading conditions using the two models. First, we consider the SSM under difference loading conditions. Then, the BBS of the graphene nanoribbons is derived from the energy equivalence between the two models. We show that the BBS strongly depends on the loading modes and the chirality in the finite width graphene nanoribbons. The closed-form expressions of the bending stiffness are derived under uniform tension, pure shear, pure bending, loading force, coupling force and bending conditions. Moreover, the BBS of the beam model under different loading conditions is systematically studied in the graphene nanoribbons using the MD simulation with present harmonic potentials (Chang and Gao, 2003) and the FE simulation. Finally, the results of the MD simulation with harmonic potentials and the FE method are compared with those of the MD results with AIREBO potential.

The paper is organized as follows: Section 6.2 describes the SSM and the beam model in armchair and zigzag graphene nanoribbons for different loading conditions. In Section 6.3, both models are validated by comparison to MD simulations and FE results. Moreover, a single PE chain under different loading conditions is investigated. The comparison of the two models with

MD simulations using the AIREBO potential is discussed in section 6.4. The paper is concluded in section 6.5.

6.2 The stick-spiral and beam models in graphene nanoribbons

In the framework of molecular mechanics, the total energy, U, of graphene at small strains can be expressed as a sum of energies associated with the varying bond length, U_b, and bond angle, U_θ, i.e., (Chang and Gao, 2003)

$$U = U_b + U_\theta = \frac{1}{2}\sum_i K_b \left(db_i\right)^2 + \frac{1}{2}\sum_j K_\theta \left(d\theta_j\right)^2 \ , \tag{1}$$

where db_i is the elongation of bond i and $d\theta_j$ is the variance of the bond angle j. K_b and K_θ are the corresponding force constants.

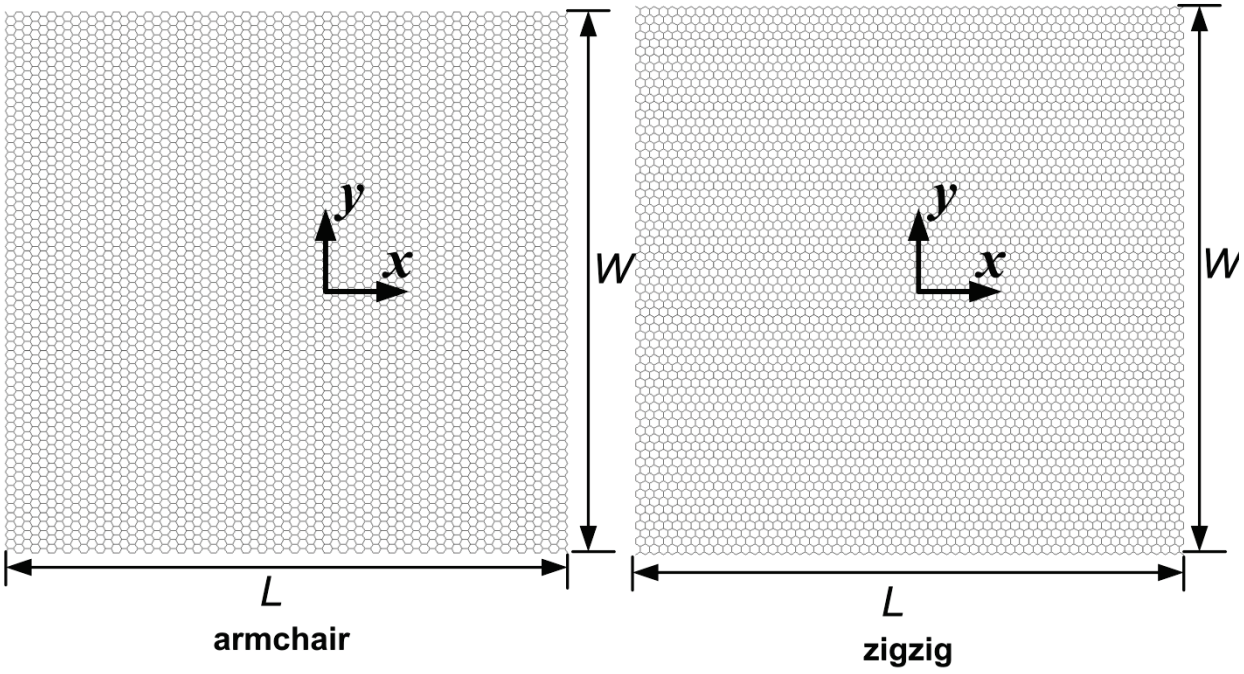

Fig. 6.1 The beam structures of the armchair and the zigzag graphene nanoribbons in the FE method based on the beam elements (L/W=1, L=14.7 nm).

To elucidate the difference between the SSM and the beam model, we analyze the relation of the two models in armchair and zigzag graphene nanoribbons (see Fig. 6.1) under different loading conditions.

6.2.1 The comparison between stick-spiral and beam models under the coupling force and moment

Most researchers calculated the elastic properties of CNTs and graphene nanoribbons under different loading conditions with beam models using a constant BBS ($EI/b=K_\theta$ or $EI/b=0.5K_\theta$) (Li and Chou, 2003, 2004; Kasti, 2007; Li and Guo 2008); E, I and b are the Young's modulus, the moment of inertia and the initial bond length of the beam. Based on the energy equivalence between the SSM and the beam models, we find that the BBS in armchair and zigzag graphene nanoribbons under uniaxial tension and pure shear is $EI/b=0.5K_\theta$. For the finite width armchair graphene sheet under coupling loading force F and moment M ($\alpha=\beta$ and $b_1=b_2=a=b$ here), the BBS EI/b should be employed, see Fig. 6.2. It should be noted that only the in-plane bending is considered in this paper.

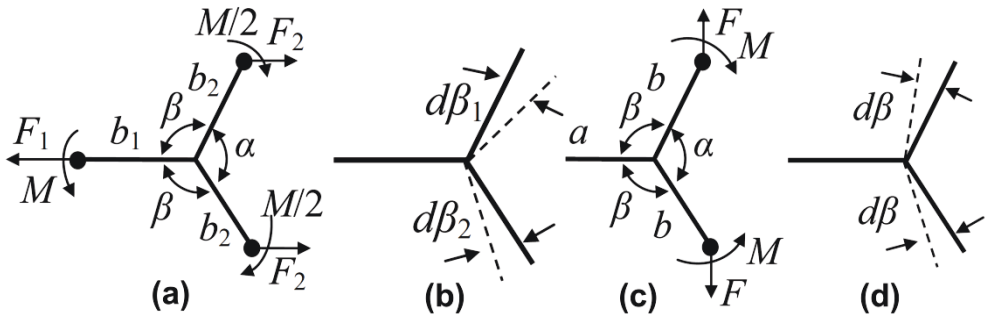

Fig. 6.2. (a) One cell of a finite width armchair graphene sheet under coupling loading force F and moment M, (b) angle increment of (a) for the stick-spiral model, (c) one cell of a finite width zigzag graphene sheet under coupling loading force F and moment M, (d) angle increment of (c) for the stick-spiral model.

For the SSM, the force and the moment equilibrium lead to

$$\begin{cases} F_1 = K_b db_1 \\ F_2 \cos\left(\dfrac{\alpha}{2}\right) = K_b db_2 \\ M = K_\theta \left(d\beta_1 + d\beta_2\right) \\ \dfrac{M}{2} + F_2 \sin\left(\dfrac{\alpha}{2}\right) b = K_\theta d\beta_1 + K_\theta \left(d\beta_1 - d\beta_2\right), \\ \dfrac{M}{2} - F_2 \sin\left(\dfrac{\alpha}{2}\right) b = K_\theta d\beta_2 - K_\theta \left(d\beta_1 - d\beta_2\right) \end{cases} \tag{2}$$

where $b_1=b_2=b$, $F_1=2F_2$, $d\beta_1$ and $d\beta_2$ are the angle increments.

The total energy of the stick U_T can be written as

$$\begin{aligned} U_T &= U_b + U_\theta \\ &= \frac{1}{2}K_b\left(db_1\right)^2 + 2\times\frac{1}{2}K_b\left(db_2\right)^2 + 2\times\left(\frac{1}{2}K_\theta\left(d\beta_1\right)^2 + \frac{1}{2}K_\theta\left(d\beta_2\right)^2 + \frac{1}{2}K_\theta\left(d\beta_1 - d\beta_2\right)^2\right) \\ &= \frac{1}{2}K_b\left(db_1\right)^2 + K_b\left(db_2\right)^2 + 2K_\theta\left(d\beta_1\right)^2 + 2K_\theta\left(d\beta_2\right)^2 - 2K_\theta d\beta_1 d\beta_2 \end{aligned} \quad (3)$$

The total energy of the beam model U_{Tbeam} can be written as

$$\begin{aligned} U_{Tbeam} &= U_{Fbeam} + U_{Mbeam} \\ &= \int_0^b \frac{\left(F_1\cos\left(\frac{\alpha}{2}\right)\right)^2}{2EA}dx_b + 2\int_0^b \frac{\left(F_2\cos\left(\frac{\alpha}{2}\right)\right)^2}{2EA}dx_b + \int_0^b \frac{\left(\frac{M}{2} - F_2\sin\left(\frac{\alpha}{2}\right)x_b\right)^2}{2EI}dx_b \\ &+ \int_0^b \frac{\left(\frac{M}{2} + F_2\sin\left(\frac{\alpha}{2}\right)x_b\right)^2}{2EI}dx_b + \int_0^b \frac{M^2}{2EI}dx_b \\ &= \frac{\left(F_1\cos\left(\frac{\alpha}{2}\right)\right)^2 b}{2EA} + \frac{\left(F_2\cos\left(\frac{\alpha}{2}\right)\right)^2 b}{EA} + \frac{3M^2 b}{4EI} + \frac{\left(F_2\sin\left(\frac{\alpha}{2}\right)\right)^2 b^3}{3EI} \end{aligned} \quad (4)$$

where x_b is the local coordinate systems along the beam, A is the cross section area of the beam, and U_{Fbeam} and U_{Mbeam} are the strain energy from the force and moment, respectively.

Let $U_{\mathrm{Tbeam}}=U_{\mathrm{T}}$, then the BBS can be obtained from Eq. (2)-Eq. (4)

$$\frac{EI}{b} = K_\theta\frac{9+4\left(\frac{N}{M}\right)^2}{6+8\left(\frac{N}{M}\right)^2}, \quad (5)$$

where $N=1/2F_1\sin(\alpha/2)b$.

Similarly, we obtain the value of EI/b when the beam model of the finite width zigzag nanoribbons in Fig. 6.1b is under the coupling force and moment (see Figs. 6.2 c and d):

$$\frac{EI}{b}=\frac{K_\theta}{2}\frac{\left(F\cos\frac{\alpha}{2}b\right)^2+3M^2-3MF\cos\frac{\alpha}{2}b}{\left(M-F\cos\left(\frac{\alpha}{2}\right)b\right)^2}=\frac{K_\theta}{2}\frac{3+\left(\frac{N}{M}\right)^2-3\left(\frac{N}{M}\right)}{\left(1-\frac{N}{M}\right)^2}, \tag{6}$$

where $N=F\cos(\alpha/2)b$.

Comparing Eq. (5) with Eq. (6), the distributions of the BBS in the zigzag graphene nanoribbons are different to those in the armchair nanoribbons. Therefore, it is not suitable to use the same EI/b to calculate the corresponding mechanical properties under coupling loading force and moment in the finite width armchair and zigzag graphene nanoribbons.

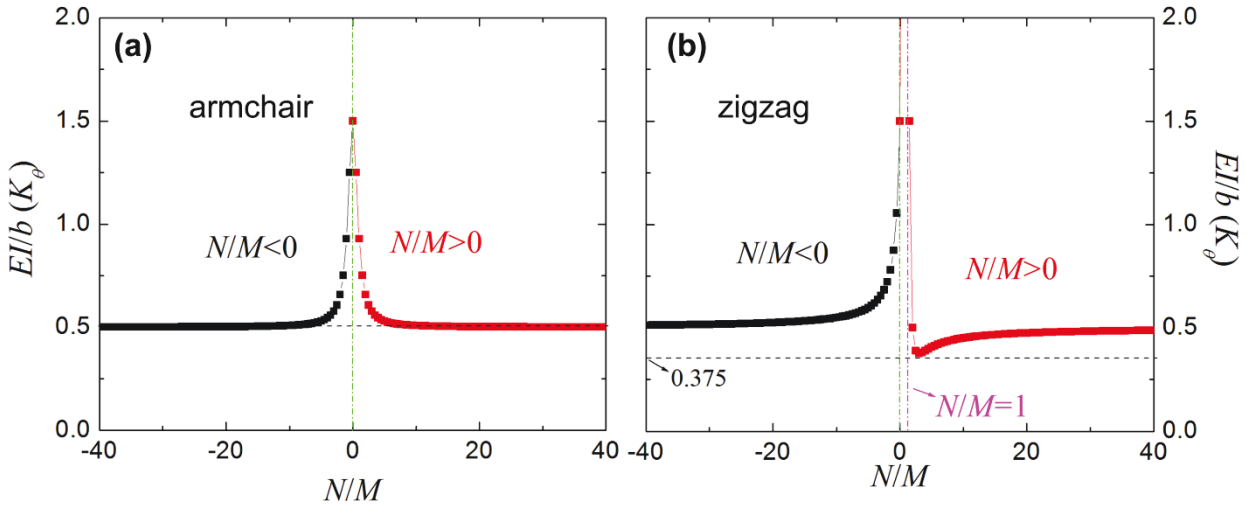

Fig. 6.3. The distribution of beam bending stiffness with N/M under coupling loading force F and moment M in the finite width graphene nanoribbons, (a) armchair, (b) zigzag.

The distribution of the BBS versus N/M in Eq. (5) is plotted in Fig. 6.3a. We find that the BBS strongly depends on the loading condition and is in the range of $0.5K_\theta \le EI/b \le 1.5K_\theta$ for the different loading conditions in the finite width armchair graphene nanoribbons. When $N/M=0$, Eq. (5) is degenerated into $EI/b=1.5K_\theta$ under pure moment M condition. When $N/M\to\infty$ (or $-\infty$), Eq. (5) is degenerated into $EI/b=0.5K_\theta$ under loading force F condition.

The distribution of the BBS versus N/M for the zigzag graphene nanoribbons is plotted in Fig. 6.3b. It also strongly depends on the loading condition. When $N/M=0$, $EI/b=1.5K_\theta$; when

$N/M \to \infty$ (or $-\infty$), $EI/b = 0.5K_{\theta;}$ when $N/M \to 1$, $EI/b \to \infty$; when $N/M \to 3$, $EI/b \to 0.375K_{\theta}$ (the minimum).

In summary, the BBS of the SSM and the beam model differs and depends on the chirality and loading condition.

6.2.2. The value of surface Young's modulus from stick-spiral and beam models

In this section, we will compare the value of surface Young's modulus Y_s ($E=Y_s/t=\sigma_s/(\varepsilon t)$ obtained from the SSM and the beam model; E and t denote the Young's modulus and thickness of the graphene sheet, and σ_s is the surface stress which is equal to the stress multiplied by the thickness t of the graphene sheet (Chang and Gao, 2003). Moreover, we derive the expressions of Y_s under uniaxial tension in armchair and zigzag nanoribbons.

For the zigzag graphene sheet in Fig. 6.1b under a uniform tensile stress f along x direction (Chang and Gao, 2003), we define the strain as

$$\varepsilon = \frac{d\left(2b\sin\frac{\alpha}{2}\right)}{2b\sin\frac{\alpha}{2}} = db\left(\frac{1}{b} + \frac{b\cos^2\frac{\alpha}{2}K_b}{6K_\theta \sin^2\frac{\alpha}{2}}\right), \tag{7}$$

The surface Young's modulus Y_s can be derived by the SSM (Chang and Gao, 2003)

$$Y_s = \frac{F}{\left(b+\frac{b}{2}\right)\varepsilon} = \frac{6K_\theta K_b b\sin\frac{\alpha}{2}}{\frac{3}{2}b\left(6K_\theta \sin^2\frac{\alpha}{2} + K_b b^2\cos^2\frac{\alpha}{2}\right)} = \frac{8\sqrt{3}K_\theta K_b}{18K_\theta + K_b b^2}, \tag{8}$$

where $F=3/2fb$ (Li and Guo, 2008).

For the beam model, the elastic strain energy of the structure should be equal to the external work.

$$U_{work} = \frac{1}{2}F\Delta L = \frac{F^2 L}{2E'A'} = \frac{\left(\frac{3}{2}fb\right)^2 L}{2E'A'}, \tag{9}$$

$$U_{Tbeam} = \frac{\left(3fb\cos\left(\frac{\alpha}{2}\right)\sin\left(\frac{\alpha}{2}\right)\right)^2 b}{EA} + \frac{9\left(f\cos^2\left(\frac{\alpha}{2}\right)\right)^2 b^5}{192EI}. \quad (10)$$

where $L=2b\sin(\alpha/2)$, $E'=E=Y_s/t$ and $A'=1.5b$ in one cell of graphene sheets (Chang and Gao, 2003; Li and Guo, 2008). Defining $EA/b=K_b$, and using Eq. (5), Eq. (6) and $U_{work}=U_{Tbeam}$, we obtain Y_s

$$Y_s = \frac{6K_\theta K_b b\sin\frac{\alpha}{2}}{\frac{3}{2}b\left(6K_\theta\sin^2\frac{\alpha}{2}+K_b b^2\cos^2\frac{\alpha}{2}\right)} = \frac{8\sqrt{3}K_\theta K_b}{18K_\theta + K_b b^2}. \quad (11)$$

Note that Eq. (8) for the SSM and Eq. (11) of the beam model are identical.

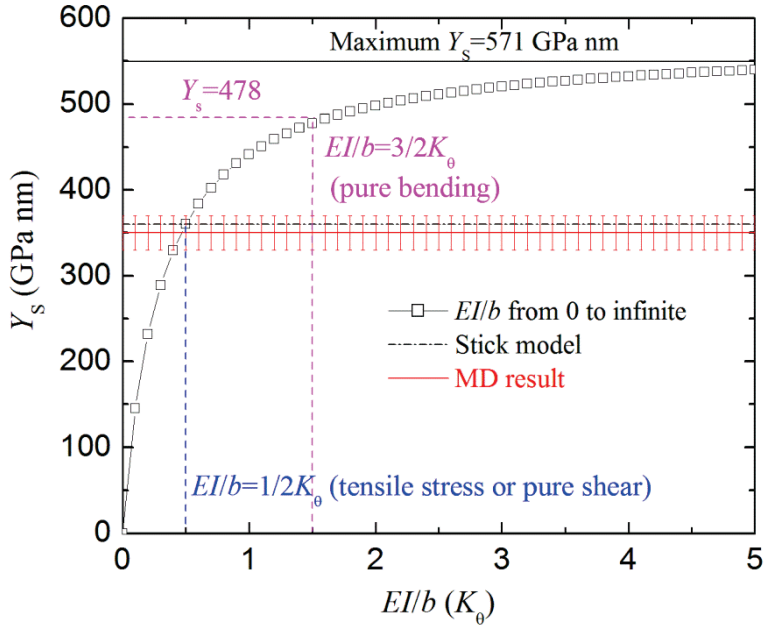

Fig. 6.4. The value of Y_s from two models and different beam bending stiffness EI/b in the finite width graphene nanoribbons.

We now compare the results of the two models with results from MD simulation. The value of Y_s from the two models with different EI/b is plotted in Fig. 6.4. When K_b=742 nN/nm, K_θ=1.42 nN nm and α=120° (Chang and Gao, 2003), the value of Y_s is equal to 360 GPa nm in Eq. (8) and Eq. (11) which is in very good agreement with the MD result Y_s=350±20 GPa nm from Sanchez-Portal et al. (1999) and Van Lier et al. (2000). The results for Y_s depending on the BBS are also

plotted in Fig. 6.4. The values of Y_s range from 321 GPa nm to 571 GPa nm under coupling force and moment. Those results are quite different to the MD result, when we use the BBS of the zigzag graphene sheet in Eq. (6). For example, the value of Y_s (478 GPa nm) is about 1.33 times of the MD result using $EI/b=1.5K_\theta$ under pure bending condition ($N/M\rightarrow 0$). The value of Y_s (360 GPa nm) is identical with MD result for $EI/b=0.5K_\theta$ under loading force ($N/M\rightarrow\infty$ or $-\infty$) or uniaxial tension conditions. When $N/M\rightarrow 1$ in Eq. (6), $EI/b\rightarrow\infty$ leads to the maximum Y_s=571 GP nm which is about 1.59 times of the MD result. When $N/M\rightarrow 3$ in Eq. (6) (see Fig. 6.3b), $EI/b=0.375K_\theta$ leads to the minimum Y_s=321 GP nm which is about 0.89 time of the MD result. Therefore, it is crucial to give an exact force analysis in the structures so that the correct EI/b can be obtained.

3. The validation using molecular dynamics simulation with harmonic potentials and finite element method

3.1 Molecular dynamics simulation with harmonic potentials

In this section, we present the results of FE and MD simulations with harmonic potentials. For the MD simulation, we keep the length L=14.7nm and the ratio L/W=1~60 in the armchair and L/W=1~52 in zigzag nanoribbons (see Fig. 6.5 and Fig. 6.6). Displacements are added at the left (green) and right (red) end layers. All MD simulations are performed using LAMMPS (Plimpton, 1995).

For uniaxial tension or pure shear, simulations are done at 0 K and all atoms in the two end layers move 0.3 Å along the x- or y-direction at each time step, respectively, and every 0.5 bending degree at each time step for pure bending except for armchair L/W=60 (every 0.15 bending degree at each time in view of the large fluctuation). Afterwards, the structure is optimized for each displacement increment and the optimized structure is taken as the initial geometry for the next calculations. The energy minimization is performed using the conjugate-gradient method. A tolerance of relative energies between minimization iterations is set at 0.0 with a force tolerance of 10^{-8} to ensure a sufficiently minimized system.

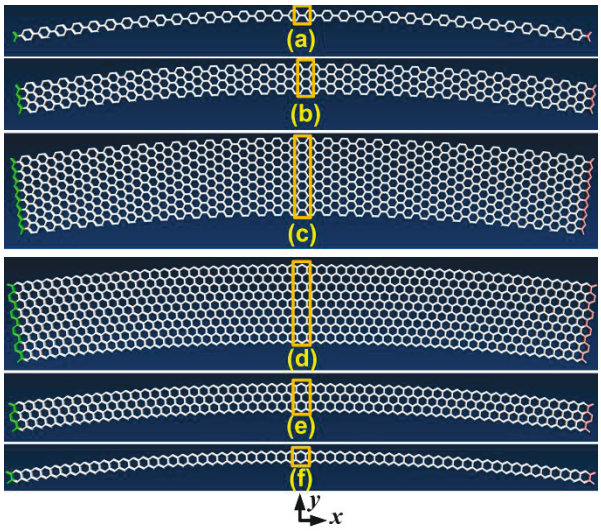

Fig. 6.5 Finite width armchair and zigzag graphite nanoribbons under pure bending at bending angle=15 degree, (a) armchair L/W=60, (b) armchair L/W=20, (c) armchair L/W=7.5, (d) zigzag L/W=52, (e) zigzag L/W=20.8, (f) zigzag L/W=7.4.

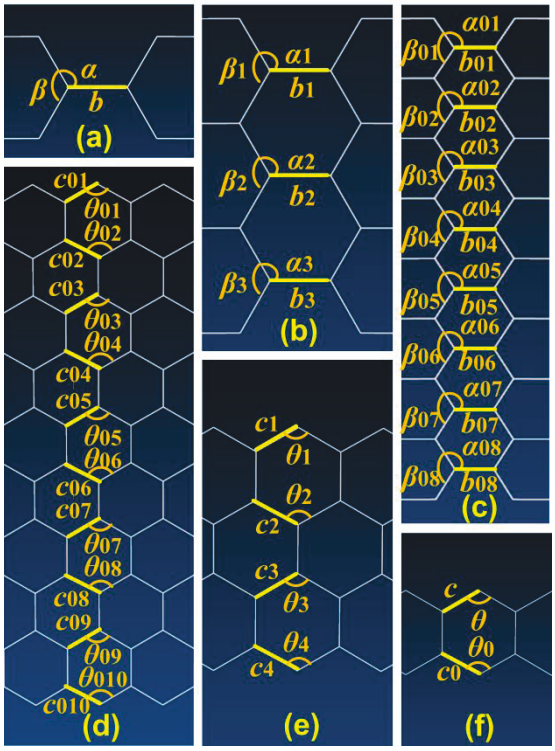

Fig. 6.6 The zoomed-in view of the graphene nanoribbons in Fig. 6.5, (a) a zoomed-in view of Fig. 6.5a, (b) a zoomed-in view of Fig. 6.5b, (c) a zoomed-in view of Fig. 6.5c, (d) a zoomed-in view of Fig. 6.5d, (e) a zoomed-in view of Fig. 6.5e, (f) a zoomed-in view of Fig. 6.5f.

To model the bending deformation, rigid body translation is applied to the atoms in both end layers of the graphene sheets (see the green and red parts in Fig. 6.5), such that both end sections remain straight and are kept perpendicular to the deformed axis in each displacement increment (Iijima et al., 1996; Cao and Chen, 2006). The length of the middle line along the deformed axis in the graphene sheet remains unchanged and its curvature is uniform throughout the deformation.

First, we consider the armchair and zigzag graphene nanoribbons under uniaxial tension. The harmonic bond and angle potentials parameters K_b=742nN/nm and K_θ=1.42 nN nm are adopted from Chang and Gao (Chang and Gao, 2003). The Lennard-Jones (LJ) pair potential U_{LJ} between carbon and carbon is adopted as $U_{LJ} = 4 \in \left[\left(\frac{\sigma}{r} \right)^{12} - \left(\frac{\sigma}{r} \right)^{6} \right]$ (Chang, 2007; Li and Guo, 2008), where r is the distance between the interacting atoms, $\in$ the depth of the potential, and σ a parameter that is determined by the equilibrium distance. We use σ=3.407 Å and $\in$ =4.7483×11.8^{-22} J (Kolmogorov et al., 2004; Vodenitcharova and Zhang, 2004; He et al., 2005; Chang, 2007).

In our MD simulations, the stress method and energy method are both used to calculate the Young's modulus and shear modulus. For the stress method, the stress on the surface of graphene sheet can be given by the component of the virial stress (Zhao et al., 2010)

$$\sigma_{ij} = -\frac{1}{V}\left(\sum_{i}^{N_{carbon}} m v_i v_i + \sum_{i=1, j<i}^{N_{carbon}} r_{ij} \frac{\partial U_{ij}}{\partial r_{ij}} \right), \tag{12}$$

where V is the current volume of the graphene sheet, m_i is the mass of atom i, v_i is the velocity, r_{ij} is the displacement vector between the atoms i and j, and U_{ij} is the potential energy between atoms i and j.

The idea for the energy method is that the increment of the total energy should be equal to the external work (Zhao et al., 2009b). The equation can be written as

$$\begin{cases} \sigma_c = \dfrac{1}{V_0}\dfrac{\partial U}{\partial \varepsilon} \\ M = \dfrac{1}{V_0}\dfrac{\partial U}{\partial \phi} \end{cases}, \tag{13}$$

where U and ε are the total energy increment and tensile strain, σ_c and M are the tensile stress and bending moment on the left or right regions in Fig. 6.5, and V_0 and ϕ are the initial volume and bending angle.

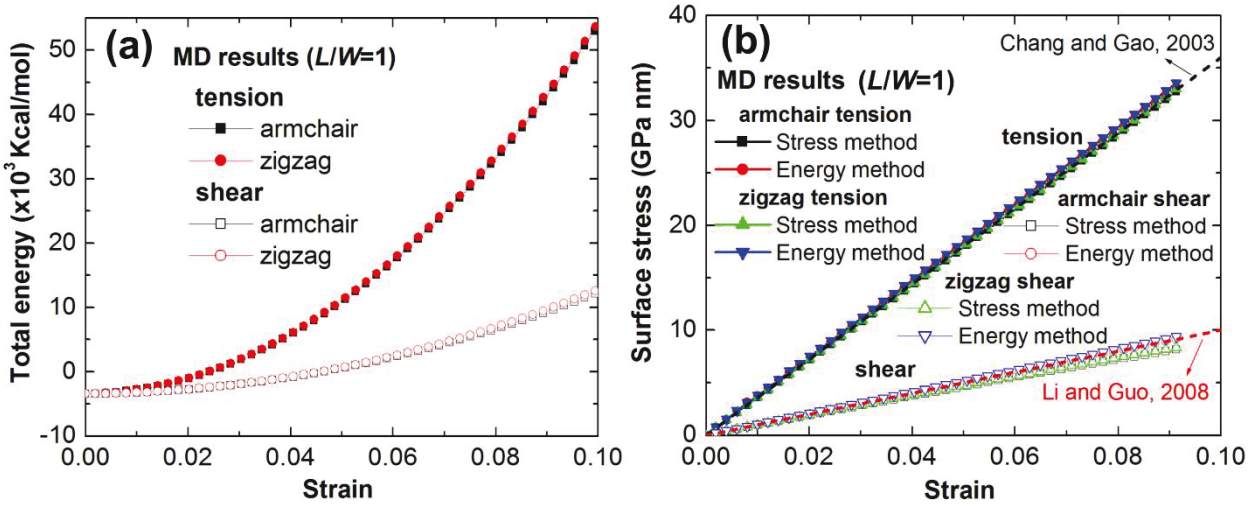

Fig. 6.7 (a) The total energy-strain and (b) the surface stress-strain curves of the armchair and the zigzag graphene sheet under uniaxial tension and pure shear in Fig. 1a and b.

The total energy for different tensile and shear strains is plotted in Fig. 6.7a. The surface tensile or shear stresses obtained from Eq. (13) are plotted in Fig. 6.7b. Note that the surface stress is the stress multiplied by the thickness t of the graphene sheet. Defining the surface tensile stress and the surface shear stress as σ_s and τ_s, the surface Young's modulus Y_s and shear modulus G is expressed as $Y_s=\sigma_s/\varepsilon$ and $G=\tau_s/\gamma$, where ε and γ are the tensile strain and shear strain. Fig. 6.7b shows that the difference of the surface stress-strain curves between the armchair and zigzag nanoribbons is very small. Those observations agree well with the results in the literature (Chang and Gao, 2003; Kasti, 2007; Li and Guo, 2008). Fig. 6.7b also shows that the surface stress-strain curves of the stress method are in very good agreement with those of the energy method. Our MD results agree with those of the available analytical models (see Fig. 6.7b)

(Chang and Gao, 2003; Li and Guo, 2008). The energy method is adopted to obtain all MD results in the following text.

6.3.2 Finite element method based on the beam model

The FE beam structures of graphene sheets can be easily built from the coordinates of the graphene MD models (Fig. 6.5).

We adopt the stiffness $EA/b=K_b$ and $EI/b=0.5K_\theta$ with Young's modulus E=9.18~14.77TPa and Poisson's ratio v=0~0.4 from Li and Guo (2008). All the present FE calculations are performed using the commercial ANSYS 12.0 package with 2-node BEAM188 element.

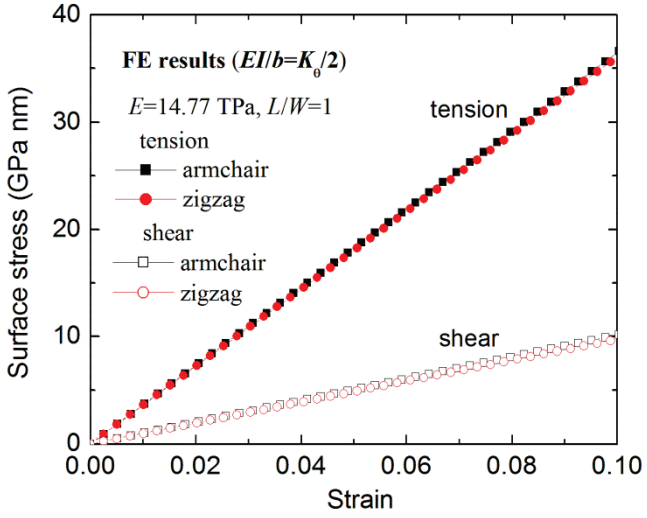

Fig. 6.8 The surface tensile and shear stress-strain curves of FE method in Fig. 1.

The surface stress-strain curves along different directions for E=14.77TPa, v=0.1 and $EI/b=0.5K_\theta$ are plotted in Fig. 6.8. The difference of the stress-strain curves between the armchair and zigzag graphene nanoribbons are very small, which agrees well with the observations from Li and Guo (2008) and Sakhaee-Pour (2009).

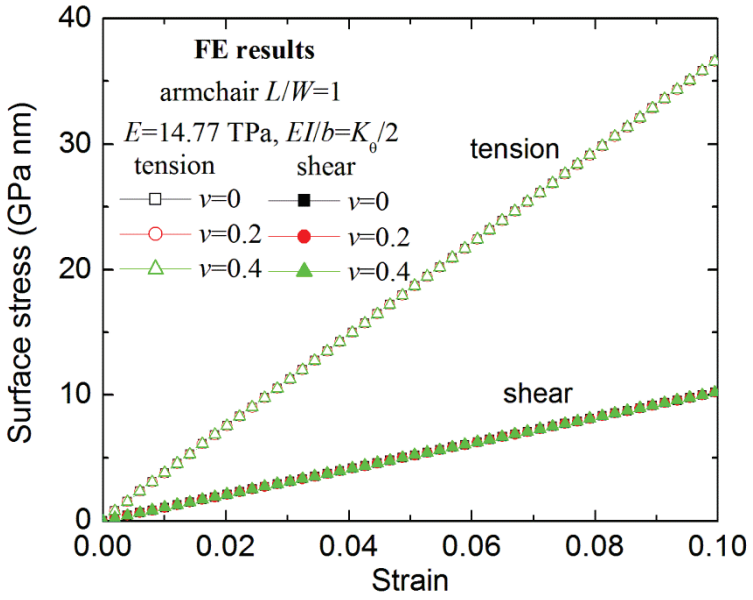

Fig. 6.9 The surface stress-strain curves of the FE method in Fig. 1a.

In view of so small difference, we only study the effect of the Poisson's ratio v on the stress-strain curves for the armchair sheet in Fig. 6.9. The surface stress-strain curves don't change with v at all in Fig. 6.9, which means that the Young's modulus and shear modulus of graphene sheet are both independent of Poisson's ratio v of the beam. Therefore, there is no limitation to use Poisson's ratio v (as v=0~0.4) of the beam element so that we can obtain the same Young's modulus and shear modulus. The Poisson's ratio v=0.1 are adopted in the following FE results.

As shown in Fig. 6.10, the effect of the beam Young's modulus on the surface stress-strain curves is also very small. Li and Guo's results are between the present two curves although K_b=723nN/nm and K_θ=1.36 nN nm is chosen in their literature (Li and Guo, 2008).

Since the Poisson's ratio v and the Young's modulus E of the beam model have almost no effect on the elastic properties of the graphene nanoribbons, we choose E=14.77TPa and v=0.1 in all the following FE calculations.

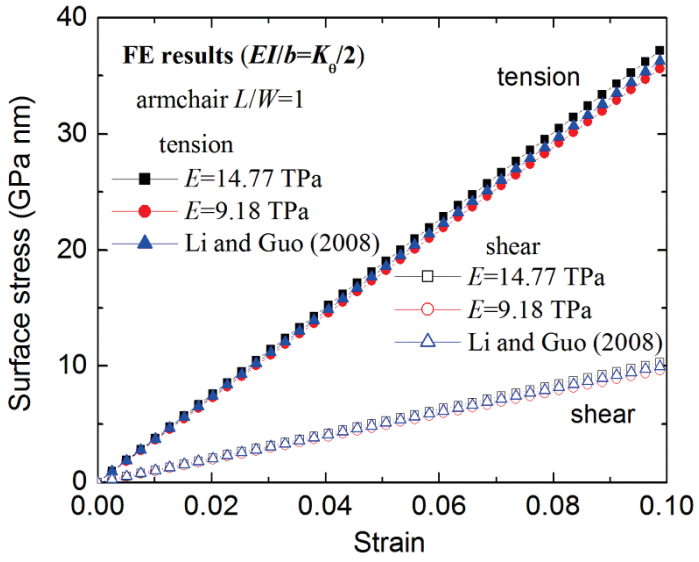

Fig. 6.10 The surface tensile and shear stress-strain curves of the FE method with different beam Young's modulus in Fig. 6.1b along *x*-direction tension and *xy*-direction shear.

6.3.3 Results and discussion

Fig. 6.11a plots the surface tensile stress ratios between the MD simulations with harmonic potentials and FE results based on the beam model under uniaxial tension. All the ratios are close to 1 for different L/W in the armchair and the zigzag graphene nanoribbons. It means that the BBS, $EI/b=0.5K_\theta$ is correct to describe the elastic properties of graphene nanoribbons under tension and shear, which validates our analytical results in section 6.2.1. Figs. 6.11b and c show that the bending moment ratios between the MD and FE results for the BBS of $EI/b=0.5K_\theta$. The ratios M_{MD}/M_{FE} increase with decreasing width W in both armchair and zigzag nanoribbons. The maximum ratios reach values up to 2.5 in the armchair nanoribbons and 1.25 in the zigzag nanoribbons. It indicates that the loading-mode dependent BBS in the armchair nanoribbons is more pronounced than the BBS in the zigzag nanoribbons.

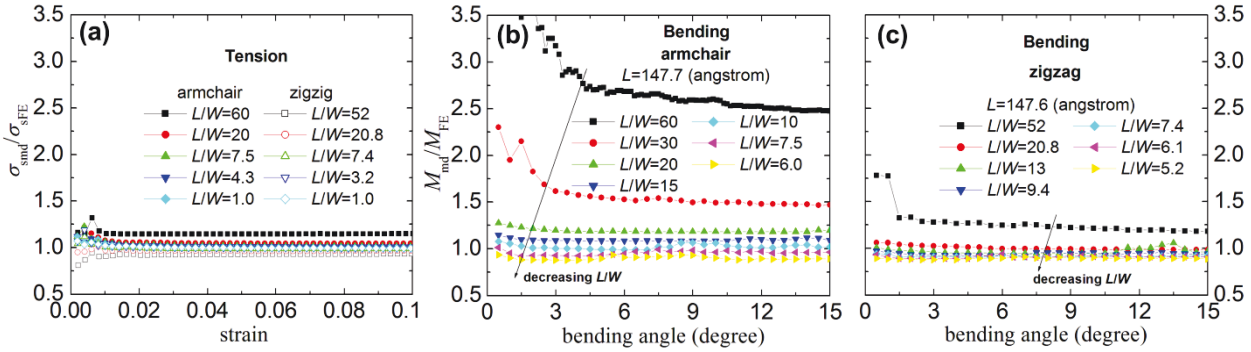

Fig. 6.11 The surface tensile stress ratios and bending moment ratios between MD and FE results in finite width armchair and zigzag graphene nanoribbons, (a) the surface tensile ratios in the armchair and the zigzag nanoribbons, (b) bending moment ratios in the armchair nanoribbons, (c) bending moment ratios in the zigzag nanoribbons.

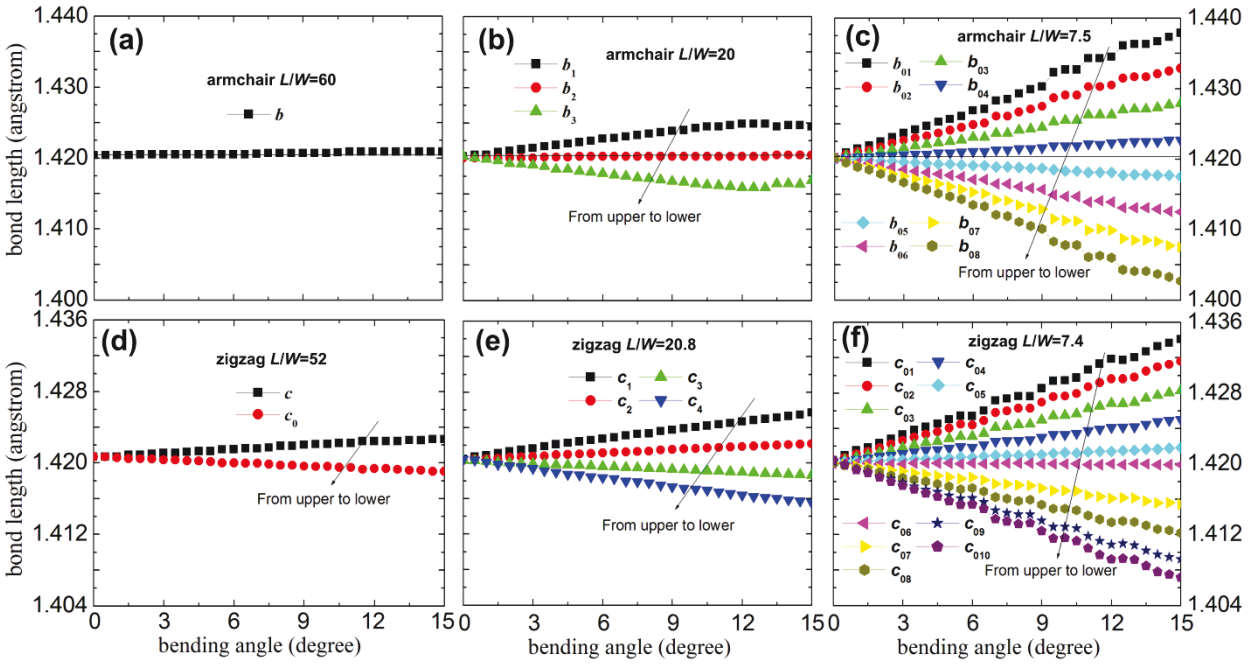

Fig. 6.12 Bond length distributions of the armchair and zigzag graphene nanoribbons with different bending angles in Fig. 6.5, (a) armchair L/W=60, (b) armchair L/W=20, (c) armchair L/W=7.5, (d) zigzag L/W=52, (e) zigzag L/W=20.8, (f) zigzag L/W=7.4.

We futher study the change of the corresponding bonds and angles in the armchair and zigzag graphene nanoribbons with different bending angles. The distributions of the bond length and the bond angles in the upper and lower regions are symmetric with regard to the middle line along the deformed axis. For the narrow sheets in Figs. 6.12a, d and Figs. 6.13a, d, the bond length and the angles change weakly with increasing bending angle. With increasing width, the bond length

and the bond angles from the middle line to the free surface along the undeformed axis increase sharply with increasing bending angle, as shown in Figs. 6.12c, f and Figs. 6.13c, f.

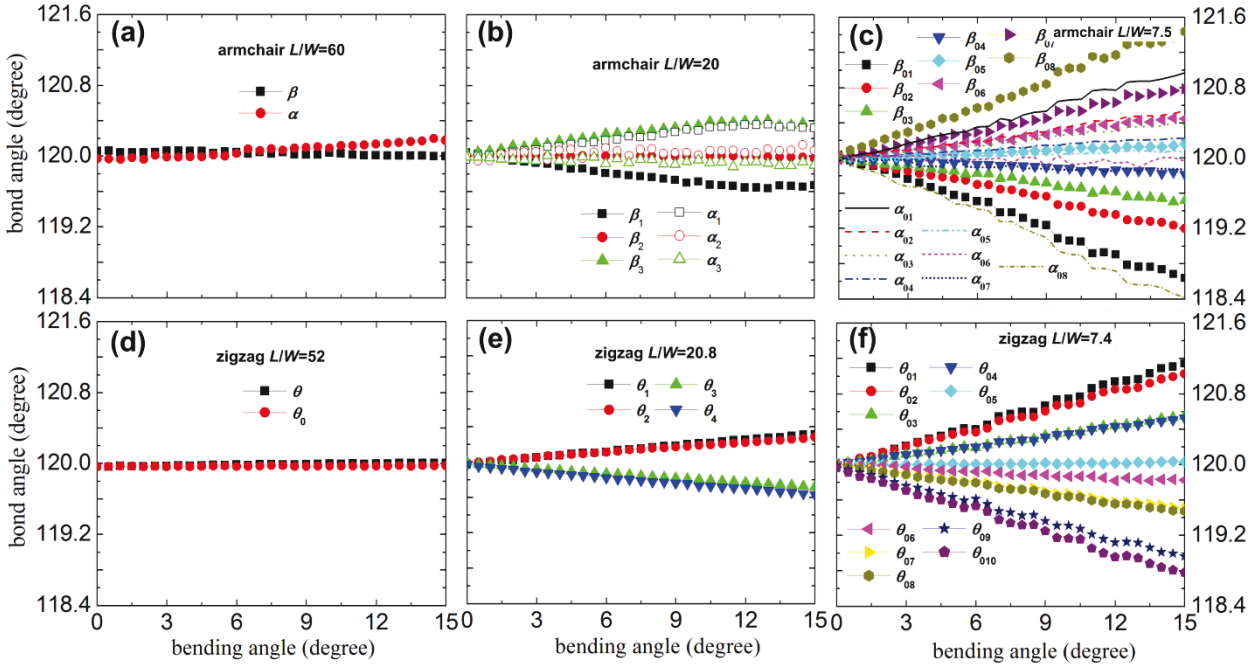

Fig. 6.13 Angle distributions of armchair and zigzag graphene nanoribbons with different bending angles in Fig. 5, (a) armchair L/W=60, (b) armchair L/W=20, (c) armchair L/W=7.5, (d) zigzag L/W=52, (e) zigzag L/W=20.8, (f) zigzag L/W=7.4.

For all sheets, the bond length and the bond angles in the middle regions change weakly, while the bond length in the upper and the lower regions is sharply elongated and shortened, respectively. Fig. 6.13d indicates that all the bond length change considerably in the narrow zigzag sheet, while the bond length does not change in the narrow armchair sheet. From the armchair sheets in Fig. 6.5, we find that the bonds b_k (k=1, 2, 3, 01, 02, ···,08) are parellel to the deformed axial. When the armchair sheets are under pure bending, the bonds b_k in the middle parts of the sheets are always under pure bending. Therefore, the ratio $m=N_b/N_{tc}$ increases with decreasing width, where N_b is the number of the bonds subjected to bending and N_{tc} is the number of the bonds subjected to tension/compression in the sheets. However, all of the bonds c_l (l=0, 1, 2, 3, 01, 02, ···, 09, 010) in the zigzag sheets are not parallel to the deformed aixal. The ratio in the zigzag sheets is always less than that in the armchair sheets for the same value of L/W.

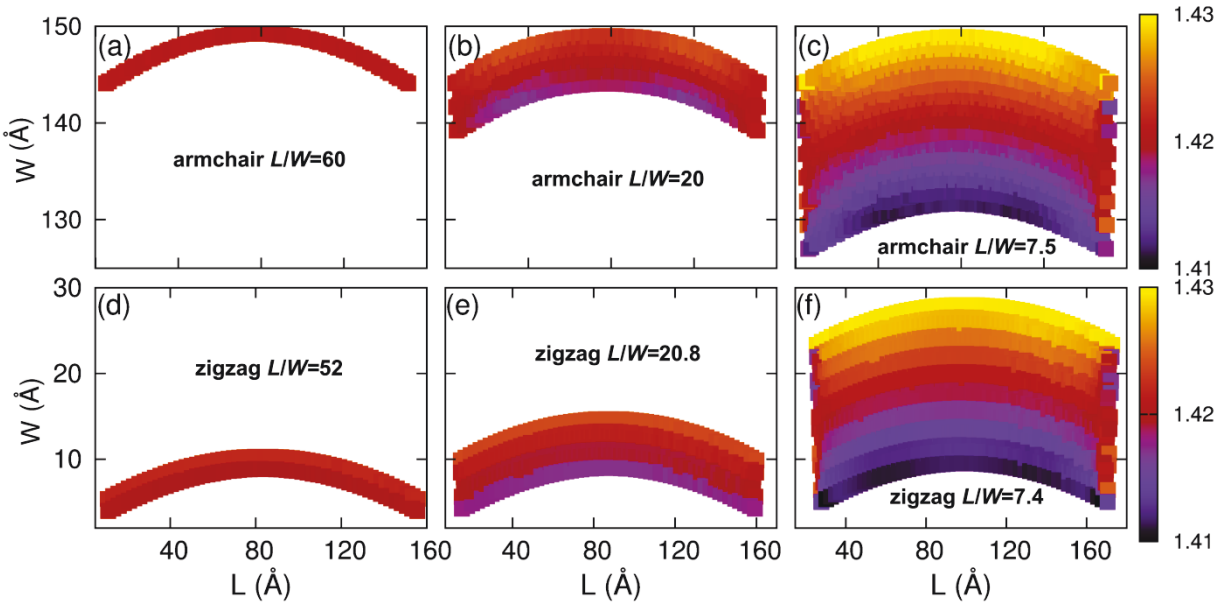

Fig. 6.14 The spatial distributions of the bond length in armchair and zigzag graphene nanoribbons at the bending angle 15 degree, (a) armchair *L*/*W*=60, (b) armchair *L*/*W*=20, (c) armchair *L*/*W*=7.5, (d) zigzag *L*/*W*=52, (e) zigzag *L*/*W*=20.8, (f) zigzag *L*/*W*=7.4.

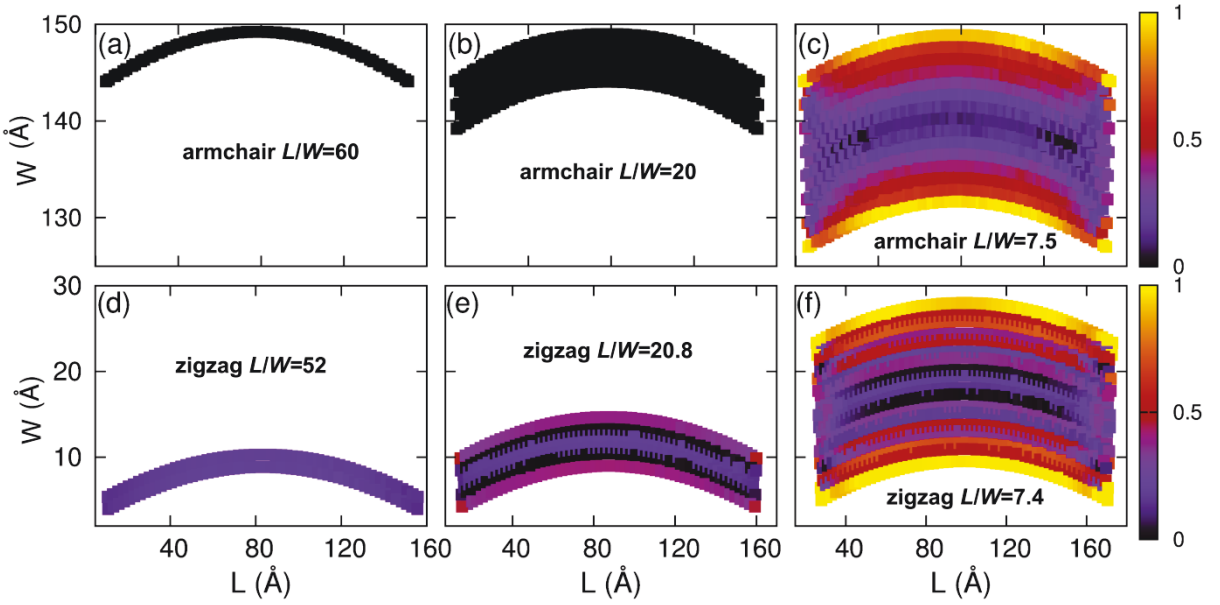

Fig. 6.15 The spatial distributions of the average angle increment in armchair and zigzag graphene nanoribbons at the bending angle 15 degree, (a) armchair *L*/*W*=60, (b) armchair *L*/*W*=20, (c) armchair *L*/*W*=7.5, (d) zigzag *L*/*W*=52, (e) zigzag *L*/*W*=20.8, (f) zigzag *L*/*W*=7.4.

It is the main reason that the bending moment ratios in the armchair sheets (see Figs. 6.11b and c) are larger than those in the zigzag sheets. The loading-mode dependent BBS of the armchair nanoribbons is more pronounced than that of the zigzag nanoribbons.

Fig. 6.14 and Fig. 6.15 show the spatial distributions of the bond length and the average angle variation in different armchair and zigzag graphene nanoribbons for a bending angle of 15 degree. The average angle variation of atom i is calculated by

$$\Delta\theta_i = \frac{1}{3}\sum_{i=1}^{3}|\theta_i - \theta_0|, \tag{14}$$

where θ_i (i=1,2,3) are the three angles around the atom i at a given bending angle, and θ_0 is the initial angle of 120 degrees.

The bond length and the average angle variation change weakly in the middle regions and sharply in the upper and lower regions. It indicates that the middle regions of all graphene nanoribbons are always subjected to bending, while the upper and lower regions are mainly under tension or compression, respectively. With increasing width, tension and compression dominate the bending properties of the graphene nanoribbons (see Figs. 6.14c and f or Figs. 6.15c and f). Conversely, with decreasing width, bending or coupling tension/compression-bending dominate the bending properties of the nanoribbons (see Figs. 6.14a and d or Figs. 6.15a and d). From our analysis in section 6.2.1, the BBS EI/b=0.5K_θ should be used in uniaxial tension/compression/shear, while BBS EI/b=1.5K_θ in pure bending should be used for considerably narrow graphene nanoribbons. Therefore, it is reasonable to adopt the BBS 0.5$K_\theta \le EI/b \le$ 1.5K_θ and 0.375$K_\theta \le EI/b$ in the finite width armchair sheets and zigzag sheets under pure bending in Figs. 6.3a and b, respectively.

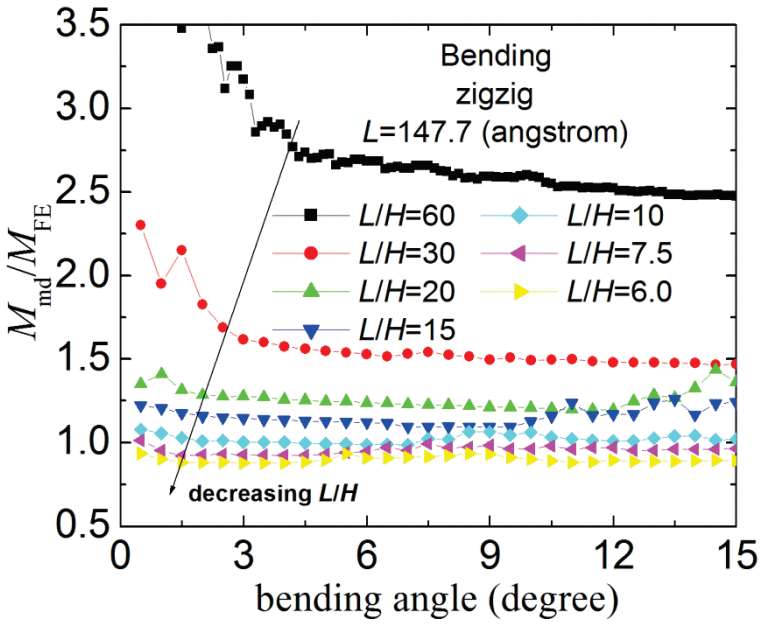

Fig. 6.16 Bending moment ratios between MD and FE results for graphene nanoribbons with different EI/b.

Fig. 6.16 illustrates the bending moment ratios for graphene nanoribbons for different BBS EI/b. The ratio is close to 1 when $EI/b=1.5K_\theta$ is used in our FE calculation with $L/W=60$ in Fig. 6.5a, which perfectly validates our analytical result in section 6.2.1. Furthermore, $EI/b=K_\theta$ can be used to describe the elastic properties in $L/W=30$ (armchair) and $L/W=52$ (zigzag) graphene nanoribbons considering the domination of the coupling tensile/compressive-bending mode.

The BBS $EI/b=0.5K_\theta$ of the beam models describe the elastic properties well under uniaxial tension or pure shear. However, the BBS strongly depends on the width and the chirality of the graphene nanoribbons under pure bending or tensile-bending modes. When the width of the armchair graphene sheets becomes small enough ($L/W=60$), $EI/b=1.5K_\theta$ describes the bending behavior excellently under pure bending. With increasing width, $0.5K_\theta \le EI/b \le 1.5K_\theta$ and $0.375K_\theta \le EI/b$ should be used to effectively describe the mechanical behavior in armchair and zigzag sheets, respectively.

In view of the extremely narrow structure of a single polyethylene PE chain, we further analyzed the elastic properties of the PE chain under different loading conditions too.

6.3.4 The two models in a single polyethylene chain

In this section, we study one PE chain under coupling loading force f and moment m, see Fig. 6.17a. In analogy to our analysis in section 6.2.1, the value of the BBS EI/b of the PE can be written as

$$\frac{EI}{b}=\frac{K_{p\theta}}{3}\frac{3m^2+\left(f\cos\frac{\theta}{2}b\right)^2-3mf\cos\frac{\theta}{2}b}{\left(m-f\cos\frac{\theta}{2}b\right)^2}=\frac{K_{p\theta}}{3}\frac{3+\left(\frac{n}{m}\right)^2-3\left(\frac{n}{m}\right)}{\left(1-\frac{n}{m}\right)^2}, \tag{15}$$

where $n=f\cos(\alpha/2)b$, b and θ are the initial bond length and angle of the PE chain, respectively, and $K_{p\theta}$ is the bond bending stiffness of PE (Zhao et al., 2011).

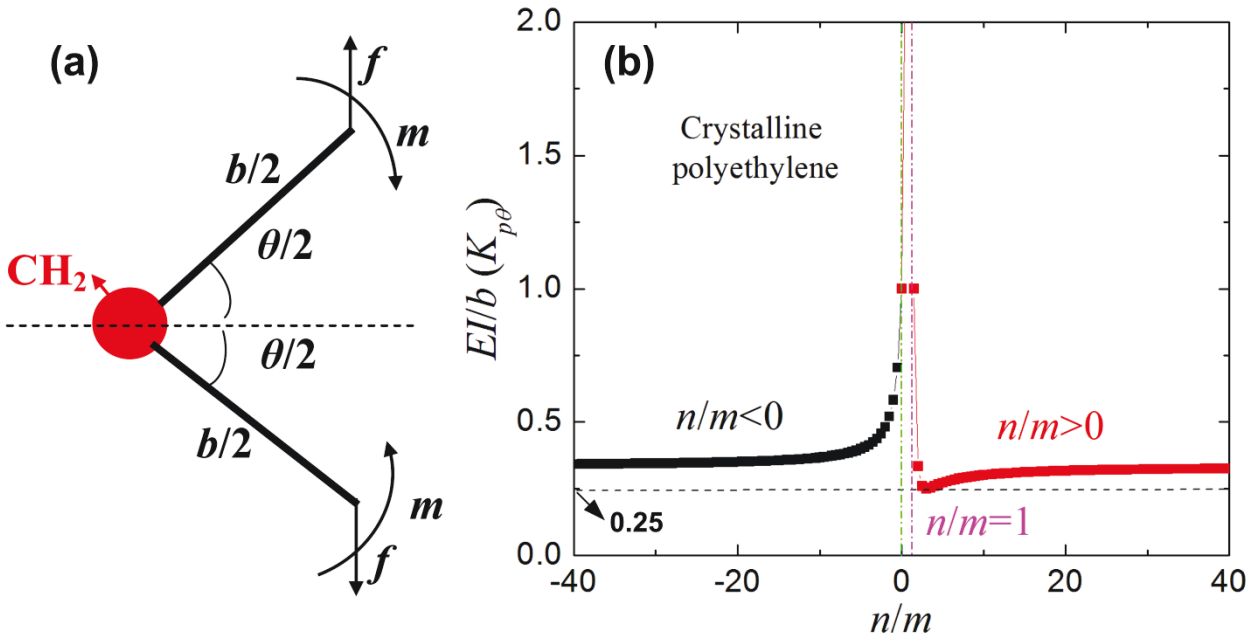

Fig. 6.17. (a) One cell of a crystalline polyethylene chain under coupling loading force f and moment m, (b) the distribution of beam bending stiffness with n/m.

Eq. (15) and Eq. (6) differ only in the coefficients. The distribution of the bending stiffness in Eq. (15) over n/m is shown in Fig. 6.17b. The bending stiffness EI/b is larger than $0.25K_\theta$ for the different loading conditions. When $n/m=0$, Eq. (15) is degenerated into $EI/b=K_\theta$ under pure

moment m condition. When $n/m \to \infty$ (or $-\infty$), Eq. (15) is degenerated into $EI/b=K_\theta/3$ under loading force F condition. As $n/m \to 1$, Eq. (15) leads to $EI/b \to \infty$. The minimum $EI/b=0.25K_\theta$ is obtained for $n/m \to 3$.

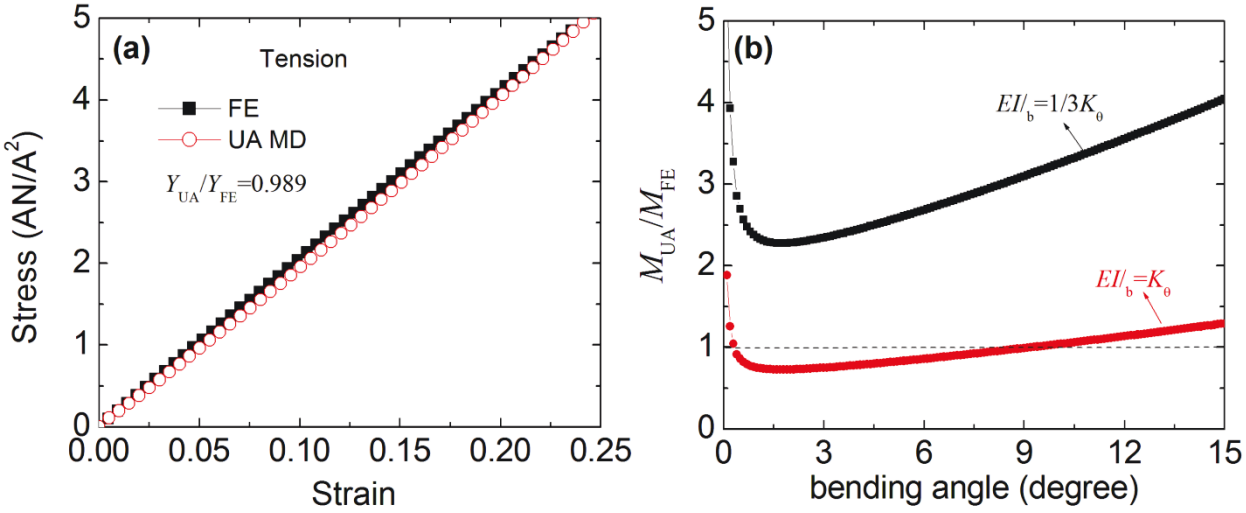

Fig. 6.18. (a) One cell of a crystalline polyethylene chain under coupling loading force f and moment m, (b) the distribution of beam bending stiffness with n/m.

To further validate the analytical results, we carried out the united-atom MD simulation and FE simulation in Fig. 6.18. The PE chain consists of 19 united-atom beads with a length L=2.28 nm. In the united atom approximation, the methyl groups (CH_2) are represented by a single "atom" and the effect of the hydrogen atoms on the polymer's configuration is accounted for in the potentials (Waheed, 2005; Shepherd, 2006; Zhao et al., 2011). The parameters of the harmonic potentials are K_b=700 Kcal/mol Å^2, K_θ=120 Kcal/mol, b=1.53 Å, θ=109.5°. The LJ pair potential (see section 6.3.1) with $\in$=0.112 Kcal/mol and σ=4.01 Å is adopted (Waheed, 2005; Shepherd, 2006; Zhao et al., 2011).

Fig. 6.18a compares the tensile stress-strain curves of the united-atom model with the FE model. The Young's moduli Y_{UA} for both models are in excellent agreement. A cross sectional area of 17.3 Å^2 is adopted in the FE model which is equal to the average area of one PE chain in crystalline PE (Henry and Chen, 2008; Zhao et al., 2011; Jiang et al., 2012). The Young's moduli Y_{UA}=190.4 GPa and Y_{FE}=192.6 GPa are obtained by fitting the data in the range of 10% tensile stress-strain curves in Fig. 6.18a. Those results are in good agreement with the analytical value

195.1 GPa of crystalline PE in our previous work (Zhao et al., 2011). The distribution of the bending moment ratios between the united-atom and FE models for $EI/b=1/3K_\theta$ and $EI/b=K_\theta$ versus bending angles are plotted in Fig. 6.18b. The bending moment ratios between those models at $EI/b=1/3K_\theta$ are always higher than 2.28, while the ratios are close to 1 when $EI/b=K_\theta$. The result effectively validates Eq. (15) under tension and pure bending conditions.

The above analysis shows that the difference between the stick-spiral and the beam models is independent of the materials because all the parameters of the beam model are obtained from the harmonic potential.

Moreover, one has to be taken when the beam model is employed for the crystalline (or amorphous) polymers or other biopolymers (Zhao et al., 2010; Zhao et al., 2011; Zhao et al., 2012; Zheng and Sept, 2008), as their structures are composed of many single molecular chains and there are only weak van der Waals and coulomb interactions (Zhao et al., 2011) between two chains. It is possible to observe more pronounced difference between the MD and FE results in large deformation under uniaxial tension and pure bending (see Fig. 6.18b) if one uses a same constant $EI/b=1/3K_\theta$.

Despite of the difference between the SSM and the beam model, it is not clear yet which model is better suitable to predict the elastic properties of carbon nanotubes and graphene sheets.

Therefore, we carried out additional MD simulation with the AIREBO potential (Plimpton, 1995), which is commonly used to obtain the mechanical properties of graphene nanoribbons (Zhao et al., 2009a).

6.4 The comparison of the two models with molecular dynamics simulation of AIREBO potential

We adopt the setup from section 6.3.1 but use the AIREBO potential in this section (Zhao et al., 2009a). The total energy increments with the harmonic potentials and the AIREBO potential under uniaxial tension and pure bending are plotted in Fig. 6.19 and Fig. 6.20, respectively. Higher values are obtained for the harmonic potentials.

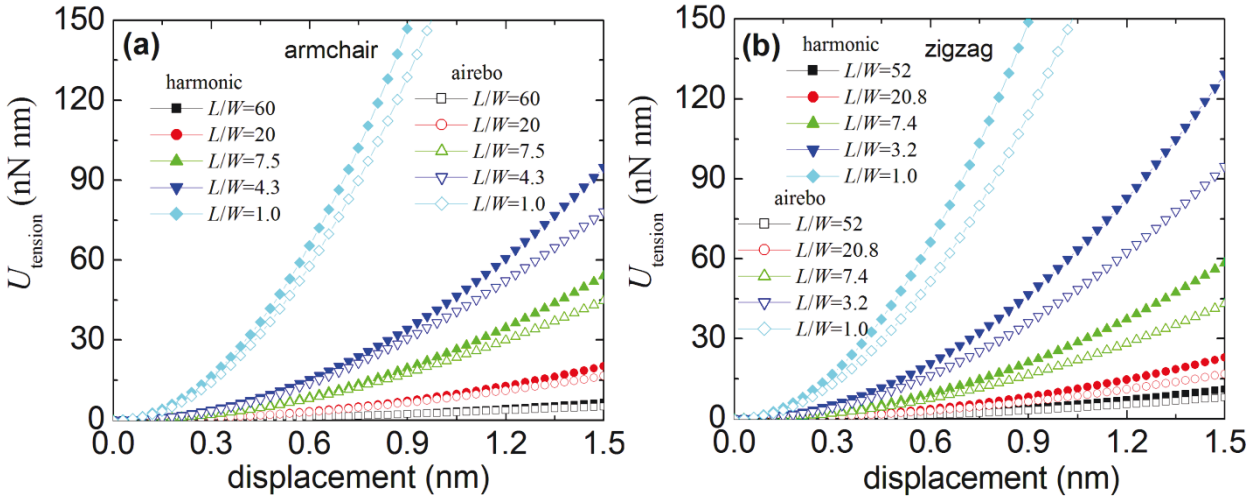

Fig. 6.19 Total energy increment with present harmonic potentials and AIREBO potential in armchair and zigzag graphene nanoribbons under tension.

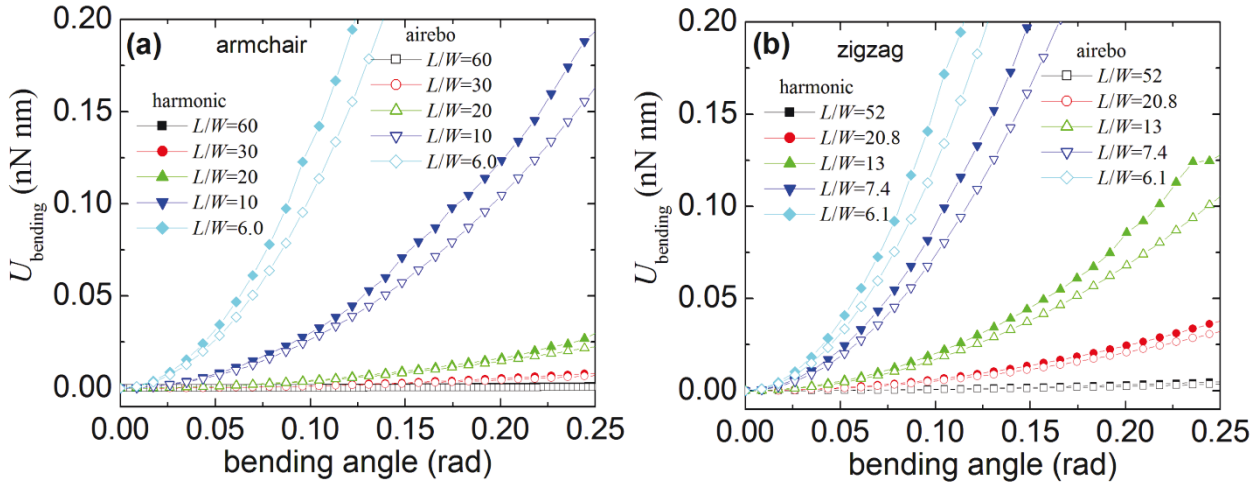

Fig. 6.20 Total energy increment with present harmonic potentials and AIREBO potential in armchair and zigzag graphene nanoribbons under pure bending.

Fig. 6.21 shows the elastic properties of the different models, *C*A, *C*H and *C*FE are the stretching stiffness (the bending stiffness of a total nanoribbon) of the AIREBO, the harmonic and the FE results, respectively, and *D*A, *D*H and *D*FE are the bending stiffness (in-plane bending stiffness of each nanoribbon) of the AIREBO, the harmonic and the FE results, respectively. For all the FE results, we used $EI/b=0.5K\theta$. Modeling each nanoribbon as a beam under small deformation condition, the stretching stiffness C and bending stiffness D per unit volume from Eq. (13) can be written as

$$C = Y_g = 2U_{tension} \Big/ \left(V_0 \varepsilon^2\right), \text{ under uniaxial tension,} \tag{16}$$

$$D = 2U_{bending} \Big/ \left(V_0 \theta^2\right), \text{ under pure bending,} \tag{17}$$

where U_{tension} and U_{bending} are the total tension energy increment and the bending energy increment, V_0 is the initial volume, Y_g is the Young's modulus, ε is the tensile strain and θ is the bending angle of each graphene nanoribbon.

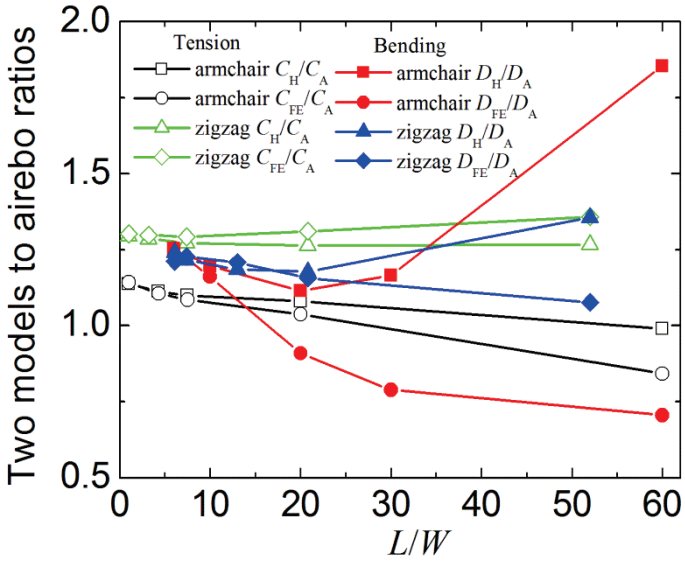

Fig. 6.21 Distribution of the two models to AIREBO ratios with L/W.

From Eq. (16) and Eq. (17), the stiffnesses C and D for different L/W can be obtained by fitting the data in Fig. 6.19 and Fig. 6.20, in which the data in the range of 0~6% tensile strain and 0~10 degrees of bending angle are used in the fitting procedure. Fig. 6.21 shows that the values of CH/CA are about 1.26~1.3 and 0.99~1.1 in different width zigzag and armchair graphene nanoribbons. The values of CFE/CA (about 1.29~1.35 and 0.84~1.14 in zigzag and armchair nanoribbons) are similar to those of CH/CA.

Under pure bending condition, DH/DA (from 1.18~1.24) and DFE/DA (from 1.16~1.22) are almost identical in the finite width zigzag nanoribbons except for L/W=52 (DH/DA=1.36, DFE/DA=1.08). All values of DH/DA and DFE/DA are very close to the values of CH/CA and CFE/CA besides the value of DFE/DA at L/W=52 which is a little lower. In other words, the

BBS in the zigzag nanoribbons is insensitive to different loading modes except for the ultra-narrow nanoribbon with L/W=52. A similar phenomenon can be observed from Fig. 6.11.

For the armchair nanoribbons, the results of DH/DA (1.11~1.85) and DFE/DA (0.7~1.25) are much higher and lower than those of CH/CA (0.99~1.1) and CFE/CA (0.84~1.14) with increasing L/W, respectively. Hence, the SSM overestimates the values, while the beam model underestimates the values. Therefore, we suggest to choose the average value between the SSM and beam models in the narrow graphene nanoribbons under pure bending. Above analysis indicates that the loading-mode dependent BBS in the armchair nanoribbons is more pronounced than that in the zigzag nanoribbons.

6.5 Concluding remarks

We extensive studied the difference between the stick-spiral and beam models in the finite width armchair and zigzag graphene nanoribbons and the single PE chain. Based on the total energy equilibrium in the two models, the closed-form expressions of the BBS are derived under uniform tension, pure shear, pure bending, loading force, coupling force and bending conditions.

By comparisons of the two models, we found that the BBS of the beam model strongly depends on the loading modes in narrow graphene nanoribbons. Based on the MD simulations with harmonic potentials and FE results, the BBS EI/b=0.5$K\theta$ of the beam model can be used to describe the elastic properties well under uniaxial tension or pure shear. Under pure bending or coupling tensile-bending modes, the BBS depends on the width and chirality of the graphene nanoribbons. When the width of the armchair graphene sheets becomes small enough, EI/b=1.5$K\theta$ can be used to describe the bending behavior effectively under pure bending. With increasing width, 0.5$K\theta \le EI/b \le$1.5$K\theta$ and 0.375$K\theta \le EI/b$ should be used to model the mechanical behavior in the armchair and the zigzag sheets, respectively. For a single PE chain, similar phenomena can be found, in which 1/3$K\theta \le EI/b \le K\theta$ under different loading conditions.

We also found that the difference of the stick-spiral and the beam models exists and they are independent of the materials because all parameters of the beam model are obtained from the harmonic potentials. For the narrow graphene nanoribbons or a single PE chain, the maximum

difference can exceed 300% in different loading modes, while the difference is completely concealed in higher width nanoribbons.

Therefore, the beam model should be used carefully to model crystalline polymers and biomaterials in view of van der Waals and coulomb interactions between any two chains. It is possible to obtain more pronounced difference between the MD results with harmonic potentials and FE results in large deformation under uniaxial tension and pure bending if one uses the same constant $EI/b=1/3K\theta$ in a single PE chain or $EI/b=0.5K\theta$ in narrow armchair graphene nanoribbons, respectively.

When the results of the MD models with harmonic potentials and the FE calculation based on the beam model are compared with those of the MD results with the AIREBO potential, the SSM overestimates and the beam model underestimates the values of the armchair nanoribbons under pure bending condition, respectively.

References:

Badia, S., Bochev, P., Lehoucq, R., Parks, M. L., Fish, J., Nuggehally, M., Gunzburger M., 2007. A force-based blending model for atomistic-to-continuum coupling. Int. J. Multiscale Comput. Eng. 5, 387–406.

Bian, J.J, Wang, G.F., 2012. A multi-scale approach of amorphous polymer from coarse grain to finite element. Comput. Mater. Sci. 57, 8-13.

Capaldi, F.M., Boyce, M.C., Rutledge, G.C., 2004. Molecular response of a glassy polymer to active deformation. Polymer 45, 1391.

Chang, T., Gao, H., 2003. Size-dependent elastic properties of a single-walled carbon nanotube via a molecular mechanics model. J. Mech. Phys. Solids 51, 1059-1074.

Chang, T., Geng, J., Guo, X., 2005. Chirality- and size-dependent elastic properties of single-walled carbon nanotubes. Appl. Phys. Lett. 87, 251929.

Chang, T., 2007. Torsional behavior of chiral single-walled carbon nanotubes is loading direction dependent. Appl. Phys. Lett. 90, 201910.

Chang, T., 2010. A molecular based anisotropic shell model for single-walled carbon nanotubes. J. Mech. Phys. Solids 58, 1422-1433.

Chopra, N.G., Luyken, R.J., Cherrey, K., Crespi, V.H., Cohen, M.L., Louie, S.G., Zettl, A., 1995. Boron nitride nanotubes. Science 269, 966-967.

Cao, G., Chen, X., 2006. Bulking of single-walled carbon nanotubes upon bending: Molecular dynamics simulations and finite element method. Phys. Rev. B 73, 155435.

Di Matteo, A., Müller-Plathe, F., Milano, G., 2007. From Mesoscale back to Atomistic Models: A Fast Reverse-Mapping Procedure for Vinyl Polymer Chains. J. Phys. Chem. B 111, 2765-2773.

Hageman, J.C.L., Meier, R.J., Heinemann, M., Groot, R.A., 1997. Young's modulus of crystalline polyethylene from ab initio molecular dynamics. Macromolecules 30, 5953-5957.

He, X.Q., Kitipornchai, S., Liew, K.M., 2005. Buckling analysis of multi-walled carbon nanotubes: a continuum model accounting for van der Waals interaction. J. Mech. Phys. Solids 53, 303-326.

He, X.Q., Kitipornchai, S., Wang, C.M., Liew, K.M., 2005. Modeling of van der Waals force for infinitesimal deformation of multi-walled carbon nanotubes treated as cylindrical shells. Int. J. Solids Struct. 42, 6032~6047.

Hernandez, E., Goze, C., Bernier, P., Rubio, A., 1998. Elastic properties of C and $B_xC_yN_z$ composite nanotubes. Phys. Rev. Lett. 80, 4502-4505.

Henry, A., Chen, G., 2008. High thermal conductivity of single polyethylene chains using molecular dynamics simulations. Phys. Rev. Lett. 101, 235502.

Iijima, S., Brabec, C., Maiti, A., Bernholc, J., 1996. Structural flexibility of carbon nanotubes. J. Chem. Phys. 104, 2089-2092.

Jiang, J., Wang, J.S., Li B., 2009. Young's modulus of graphene: a molecular dynamics study. Phys. Rev. B 80, 113405.

Jiang, J., Zhao, J., Kun, Z., Rabczuk, T., 2012. Superior thermal conductivity and extremely high mechanical strength in polyethylene chains from ab initio calculation. J. Appl. Phys., 111, 124304.

Jiang, L., Guo, W., 2011. A molecular mechanics study on size-dependent elastic properties of single-walled boron nitride nanotubes. J. Mech. Phys. Solids 59, 1204-1213.

Kasti, N., 2007. Zigzag carbon nanotubes-Molecular/structural mechanics and finite element method. Int. J. Solids Struct. 44, 6914-6929.

Kolmogorov, A.N., Crespi, V.H., Schleier-Smith, M.H., Ellenbogen, J.C., 2004. Nanotube-Substrate Interactions: Distinguishing Carbon Nanotubes by the Helical Angle. Phys. Rev. Lett. 92, 085503.

Li, C.Y., Chou, T.W., 2003. A structural mechanics approach for the analysis of carbon nanotubes. Int. J. Solids Struct. 40, 2487-2499.

Li, C.Y., Chou, T.W., 2004. Elastic properties of single-walled carbon nanotubes in transverse directions. Phys. Rev. B 69, 073401.

Li, H., Guo, W., 2006. Finite element model with equivalent beam elements of single-walled carbon nanotubes. Acta Mech. Sin. 38, 488-495.

Li, H., Guo, W., 2008. Transversely isotropic elastic properties of single-walled carbon nanotubes by a rectangular beam model for the C-C bonds. , J. Appl. Phys. 103, 103501.

Peng, J., Wu, J., Hwang, K.C., Song, J., Huang, Y., 2008. Can a single-wall carbon nanotube be modeled as a thin shell? J. Mech. Phys. Solids 56, 2213-2224.

Plimpton, S., 1995. Fast parallel algorithms for short-range molecular dynamics. J. Comput. Phys. 117, 1-19.

Ru, C.Q., 2000. Effect of van der Waals forces on axial buckling of a double-walled carbon nanotube. J. Appl. Phys. 87, 7227-7231.

Ru, C.Q., 2001. Axially compressed buckling of a doublewalled carbon nanotube embedded in an elastic medium. J. Mech. Phys. Solids 49, 1265-1279.

Sakhaee-Pour, A., 2009. Elastic properties of single-layered graphene sheet. Solid State Commu. 14, 91-95.

Sanchez-Portal, D., Artacho, E., Soler, J.M., Rubio, A., Ordejon, P., 1999. Ab-initio structural, elastic, and vibrational properties of carbon nanotubes. Phys. Rev. B 59, 12678.

Shepherd, J.E., 2006. Multiscale modeling of the deformation of semi-crystalline polymers. Ph. D thesis. Georgia Institute of Technology, USA.

To, C., 2006. Bending and shear moduli of single-walled carbon nanotubes. Finite Elem. Anal. Des. 42, 404-413.

Tserpes, K.I., Papanikos, P., 2005. Finite element modeling of single-walled carbon nanotubes. Composites B 36, 468-477.

Vaccarini, L., Goze, C., Henrard, L., Hernandez, E., Bernier, P., Rubio, A, 2000. Mechanical and electronic properties of carbon and boron-nitride nanotubes. Carbon 38, 1681-1690.

Vodenitcharova, L., Zhang L.C, 2004. Mechanism of bending with kinking of a single-walled carbon nanotube. Phys. Rev. B 69, 115410.

Waheed, N., 2005. Molecular simulation of crystal growth in alkane and polyethylene melts. Ph. D thesis. Cornell University, USA.

Wang, C.Y., Ru, C.Q., Mioduchowski, A., 2004. Applicability and limitations of simplified elastic shell equations for carbon nanotubes. J. Appl. Mech. ASME. 71, 622-631.

Wang, C.Y., Zhang, Y.Y., Wang, C.M., Tan, V.B.C., 2007. Buckling of carbon nanotubes: Aliterature survey. J. Nanosci. Nanotech. 7, 4221-4247.

Wu, J., Hwang, K.C., Huang, Y., 2008. An atomistic-based finite-deformation shell theory for single-wall carbon nanotubes. J. Mech. Phys. Solids 56, 279-292.

Xia, J.R., Gama, B.A., Gillespie Jr., J.W., 2005. An analytical molecular structural mechanics model for the mechanical properties of carbon nanotubes. Int. J. Solids Struct. 42, 3075-3092.

Yakobson, B.I., Brabec, C.J., Bernholc, J., 1996. Nanomechanics of carbon tubes: instability beyond linear response. Phys. Rev. Lett. 76, 2511-2514.

Zhang , Y.Y., Wang, C.M, Duan, W.H., Xiang, Y., Zong, Z., 2009. Assessment of continuum mechanics models in predicting buckling strains of single-walled carbon nanotubes. Nanotechnology 20, 395707.

Zhang, Z., Guo, W., Tai, G., 2007. Coaxial nanocable: Carbon nanotube core sheathed with boron nitride nanotube. Appl. Phys. Lett. 90, 133103.

Zhang, Z., Guo, W., 2008. Energy-gap modulation of BN ribbons by transverse electric fields: First-priciples calculations. Phys. Rev. B 77, 075403.

Zhao, H., Min, K., Aluru, R., 2009a. Size and chirality dependent elastic properties of graphene nanoribbons under uniaxial tension. Nano Lett., 9, 3012-3015.

Zhao, J., Zhou, B., Liu, B.G., Guo, W., 2009b. Elasticity of single-crystal calcite by first-principles calculations. J. Comput. Theor. Nanosci. 6, 1181-1188.

Zhao, J., Nagao, S., Zhang, Z.L., 2010. Thermo-mechanicyal properties dependence on chain length in bulk polyethylene: Coarse-grained molecular dynamics simulations, J. Mater. Res., 25, 537-544.

Zhao, J., Guo, W., Zhang, Z.L., Rabczuk, T., 2011. Size-dependent elastic properties of crystalline polymers via a molecular mechanics model. Appl. Phys. Lett. 99, 241902.

Zhao, J., Guo, W., Rabczuk, T., 2012. An analytical molecular mechanics model for the elastic properties of crystalline polyethylene. J. Appl. Phys. doi: 10.1063/1.4745035.

Zheng, X, Sept, D., 2008. Molecular modeling of the cytoskeleton. Methods Cell Biol. 84, 893-910.

Chapter 7

The tensile and shear failure behavior dependence on chain length and temperature in amorphous polymers*

Abstract

The tensile and shear failure behavior dependence on chain length and temperature in amorphous polymers are scrutinized using molecular dynamics simulations. A wide range chain length of alkane is tested under tension and shear with various temperatures. We find that the broken rate (the broken bond number to all polymer chain number ratios) under tension and shear increases with increasing chain length and temperature. For a given chain length and temperature, the broken rates under shear are always higher than those under tension at a same large strain. For a given chain length, the tensile and shear stresses decrease with increasing temperature. We propose three typical fracture mechanisms to effectively elucidate the ductile fracture response based on the predominance of chain scission process.

7.1 Introduction

Amorphous polymers are one of the most fundamental polymer molecular shapes that have widely been investigated by many researchers due to the important physical and chemical properties (Boyd et al., 1994; Pant et al., 1993). Glass forming polymers ($T<T_g$, T_g is the glass-transition temperature) are of great industrial importance and scientific interest. Their unique mechanical properties arise from the connectivity and random-walk-like structure of the constituent chains (Shepherd, 2006). At very small strains, the response is elastic. At slightly larger strains, yielding occurs when intermolecular barriers to segmental rearrangements are overcome. Following yield, the material may exhibit strain softening, a reduction in stress to a level corresponding to plastic flow. At higher strains, the stress increases as the chain molecules orient, in a process known as strain hardening. Strain hardening suppresses strain localization (crazing, necking, shear banding) and is critical in determining material properties such as toughness and wear resistance (Hoy et al., 2007; Hoy et al., 2008). In the other hand, the yield

* The work has been published on <<13th international conference of fracture>> in 2013.

point of the polymers disappears after $T>T_g$. Recently, we have found that the chain length (CL) and temperature have a large effect on the thermomechanical properties of linear polymers (Zhao et al., 2010a; Zhao et al., 2010b; Zhao et al., 2011) based on united-atom (UA) and coarse-grained (CG) molecular dynamics (MD) simulations. Since the UA and CG potentials limitations, the effect of the CL and temperature on the failure behavior is not understood well yet. Especially, the failure behavior under shear has been scarcely reported in previous work. Therefore, understanding the molecular origins of macroscopic fracture behavior such as fracture energy is a fundamental scientific challenge (Hoy et al., 2007).

In this paper, the tensile and shear failure behavior dependence on CL and temperature in linear polymers are scrutinized using MD simulations. A wide range chain length of alkane is tested under tension and shear with various temperatures. The fracture mechanism is proposed based on the detailed analysis of the fracture response.

7.2 Simulations details

The bulk structure of linear polymers can be modeled using the semicrystalline lattice method (Faulon, 2001), which utilizes the face-centered cubic (*fcc*) diamond structure as a template to carbon backbones of entangled polymers. The detailed process was detailedly described in our previous work (Kremer and Grest, 1990). The total number of beads in the initial structure is kept constant 180000 from CL=9 to CL=1200, in which the number of chains changes accordingly from 20000 (CL=9) to 150 (CL=1200). Since our aim does not simulate a specific polymer, we use a bead-spring polymer model derived from the one suggested by Kremer and Grest (1990). A finitely extendable nonlinear elastic (FENE) backbond potential is applied along the polymer chain

$$U\left(r\right)=-\frac{k}{2}R_0^2\ln\left[1-\left(\frac{r}{R_0}\right)^2\right], \tag{1}$$

where k=30 and R_0=1.5 to guarantee a certain stiffness of the bonds while avoiding high frequency modes (which would require a rather small time step for the integration) and chain crossing (Bennemann et al., 1998). The beads interact through a truncated Lennard-Jones (LJ) potential of the form

$$\begin{cases} U_{LJ}(r) = 4 \in \left[\left(\frac{\sigma}{r} \right)^{12} - \left(\frac{\sigma}{r} \right)^{6} - \left(\frac{\sigma}{r_c} \right)^{12} + \left(\frac{\sigma}{r_c} \right)^{6} \right], r < r_c = 1.5\sigma, \\ U_{LJ}(r) = 0, r > r_c \end{cases} \quad (2)$$

where ε and σ are the characteristic energy and distance parameters that define the shape of the energy distance curve, while r_c is the cutoff distance for the potential. The LJ potential provides a smooth transition to zero values at the cutoff distance. In this work, we adopt the reduced units formalism and all physical quantities are expressed as multiples of m (bead mass), ε, σ and k_b (Boltzmann constant) while these parameters are set equal to one in our computation (Panico et al., 2010). The bond is broken as r>1.15σ and the corresponding interaction is shut off, while a non-bonded LJ interaction is introduced between the two beads.

Each generated initial three-dimensional structure is annealed for 1×10^6 steps until the pressure and energy of the system is stable, keeping both the temperature T=1.3ε/k_b and the pressure P=1 (the time step dt=0.002) in the *NPT* ensemble controlled by the Nose-Hoover's thermostat (Nose, 1984). Then, the system is cooled down to be the given temperature by the same *NPT* ensemble and the density of the system is monitored while cooling step-wise at an effective rate of 1/(1×10^6 steps). The system is then kept at the constant temperature (the given temperature) for 1×10^6 steps in the same *NPT* ensemble. The obtained structures are subjected to the uniaxial tension and compression and performed to obtain stress–strain response with different CL and temperature in the non-equilibrium MD simulations (Capaldi et al., 2004). Periodic boundary conditions are applied in all directions. All the MD simulations have been performed using LAMMPS software (Plimpton, 1995).

7.3 Results and discussion

7.3.1 Failure behavior under uniaxial tension

Fig. 7.1 shows the stress-strain curves with different CL for two different temperature T=0.1 and T=0.3. The typical process (elastic, yielding, softening and hardening) is displayed in Fig. 7.1, while the hardening process is not evident when CL≤18 and the difference among the nonlinear parts of the stress-strain curves is also not large when CL≤144. The main reason is that

the density and entanglement of short CL is lower than those of longer chain, which results in that the bond number per unit volume in short CL is lower than those in longer CL. So the required external work for the shorter CL is lower than that for the longer CL. That is to say, the stiffness of the shorter CL is lower than that of longer CL. Since the density almost tends to a constant when CL≥140 (Zhao et al., 2010a), the effect is not evident in the range of CL≥140. Fig. 7.2 shows bond broken rate (the number of broken bond / the number of total chains) with different tensile strain for different CL and two temperatures T=0.1 and T=0.3, in which the broke rate increases with increasing CL.

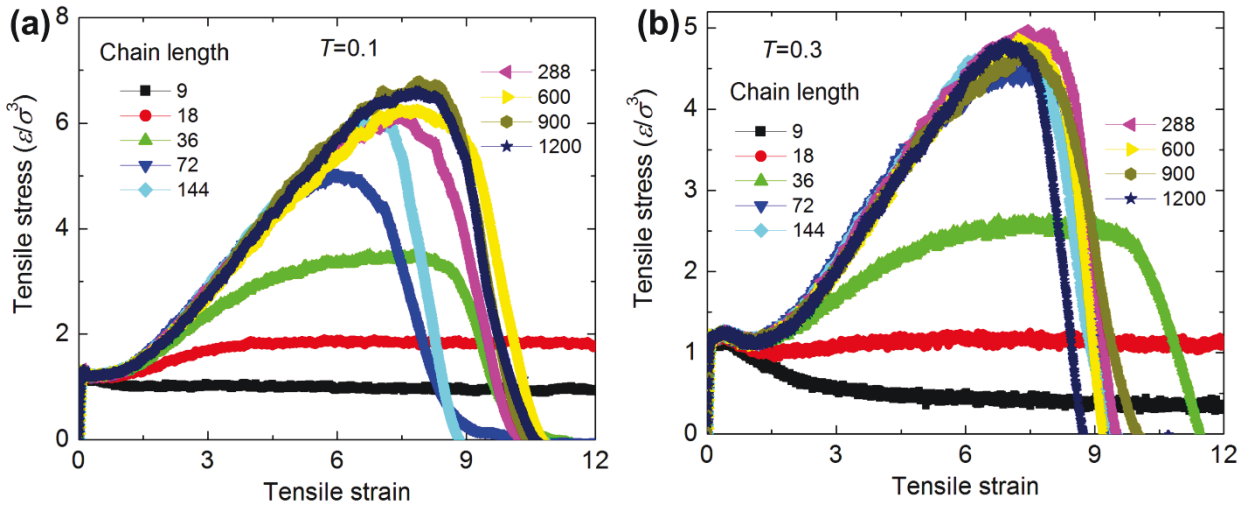

Fig. 7.1 The tensile stress-strain curves with different chain length for two different temperatures. (a) T=0.1; (b) T=0.3.

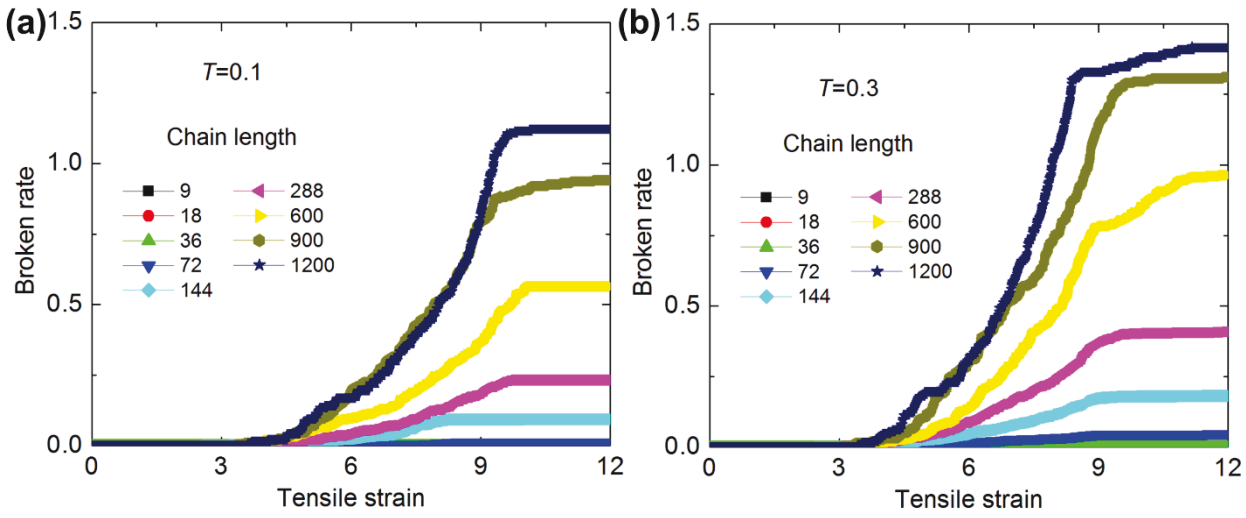

Fig. 7.2 The broken rate-strain curves with different chain length for two different temperatures. (a) T=0.1; (b) T=0.3.

We also find that the first broken bond is occurred at strain>3 and the stress is still hardening with increasing strain by comparison with Fig. 7.1 and Fig. 7.2. After strain>9, the stress decreases and the number of the total broken bonds tends to a constant. Fig. 7.3 shows the stress-strain curves and broken rate for CL=288 with different temperature. The stress decreases and the broken rate increases with increasing temperature for same strain. For high temperature (T=0.5 and 0.7), the number of broken bond always increases with increasing strain even if the strain is higher than 12. The possible reason is that the temperature is higher than the glass-transition temperature T_g=0.35 (here) when T=0.5 and 0.7, in which the creep and high-elastic property is more evident in the high temperature and the yield point disappears. To interpret these MD simulations and obtain insight into the difference in fracture behavior of different CL and temperature, we plot the atomic strain distribution in the deformed configuration of the polymer models in Fig. 7.4 and Fig. 7.5. The ultimate fracture strain increases with increasing temperature in Fig. 7.4, which gives a good explanation of the above analysis. In Fig. 7.5, no void or atomic strain concentration for CL=18 can be found even at strain=12, which validates no broken bond in Fig. 7.2a. The ultimate fracture strain almost increases with increasing CL when CL≥72, which is also validated from Fig. 7.2a.

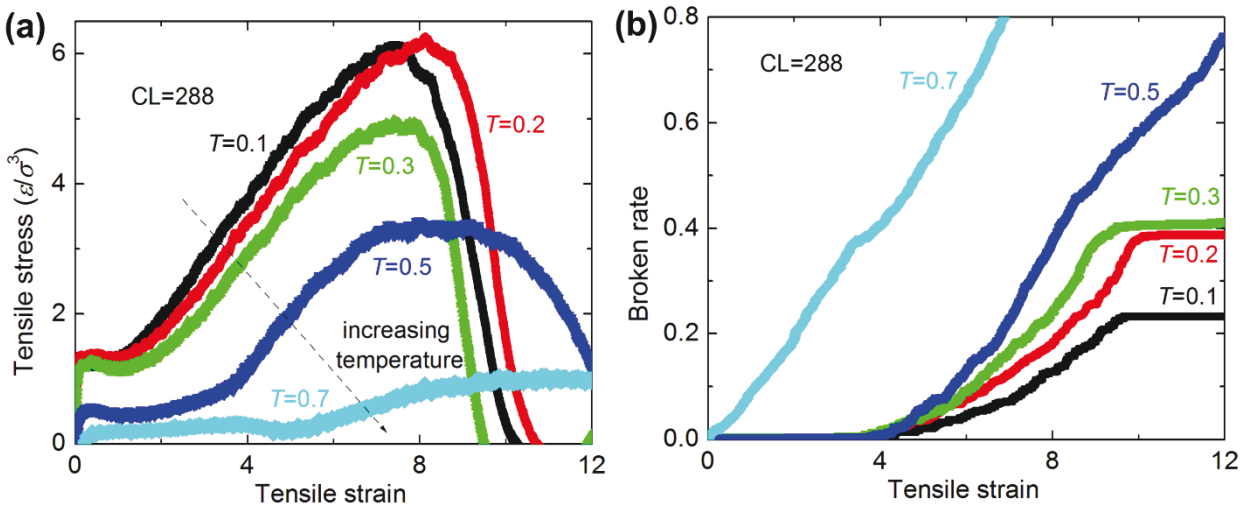

Fig. 7.3 The tensile stress-strain and broken rate-strain curves with different temperature for CL=288. (a) Stress-strain curves; (b) Broken rate-strain curves.

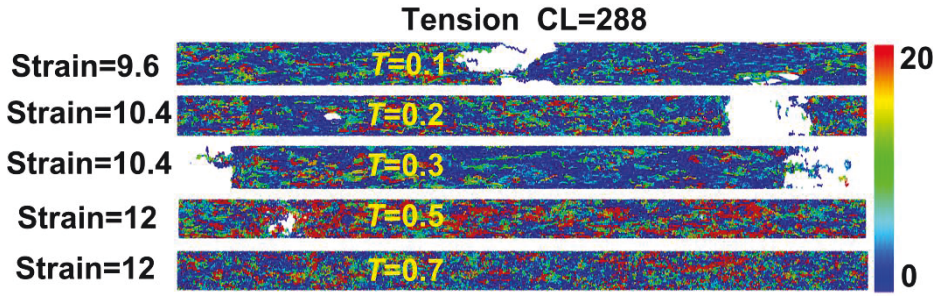

Fig. 7.4 The atomic strain (along the tensile direction) distribution for CL=288 at different temperature.

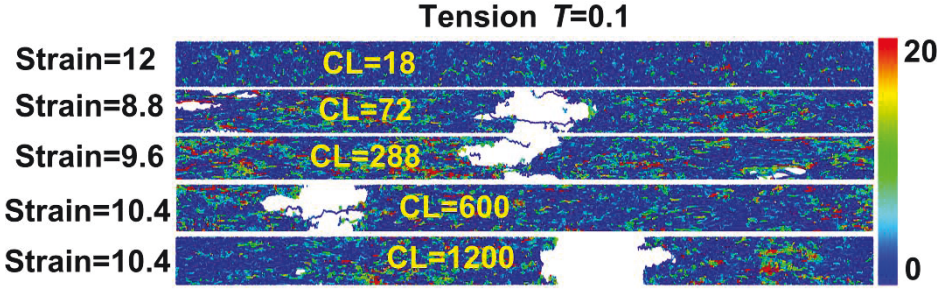

Fig. 7.5 The atomic strain (along the tensile direction) distribution for different CL at T=0.1.

Three typical mechanisms of the fracture behavior under uniaxial tension are plotted in Fig. 7.6. Fig. 7.6a represents the covalent bond broken phenomenon, which requires very high external loading (about 15000 MPa for linear polymers). Fig. 7.6b represents the polymer chain slipping with each other (about 5000 MPa). Fig. 7.6c represents the separation between any two polymer chains, which is mainly dominated by van der Waals interactions (about 100 MPa). For short CL, the fracture behavior is mainly determined by the chain slipping and separation. For longer CL, the fracture behavior is dominated by the competition between the chain slipping and bond broken mechanisms, in which the bond broken mechanism increases with increasing CL since the entanglement density increases with increasing CL. For very long CL, the bond broken mechanism mainly dominates the fracture behavior. The three mechanisms provide a good explanation of the MD results from Fig. 7.1 to Fig. 7.5.

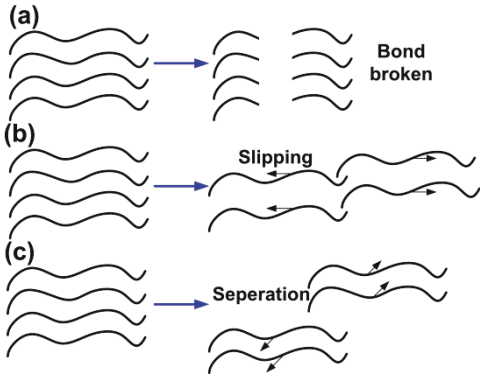

Fig. 7.6 Three typical mechanisms of microstructural evolution under uniaxial tension in linear polymers.

7.3.2 Failure behavior under shear

Fig. 7.7 shows the shear stress-strain curves with different CL for two different temperatures T=0.1 and T=0.3. The typical process (elastic, yielding, softening and hardening) is also displayed in Fig. 7.7. Unlike tension, the hardening process is also evident even for very short CL. The stress strength (the peak point of the stress) and strain strength (the strain at the stress strength point) both increase with increasing CL when CL≤144. The possible reason is that the polymer chains mainly keep the slipping process even in the hardening stage under shear, while the polymer chains are mainly stretching process after elastic stage under tension.

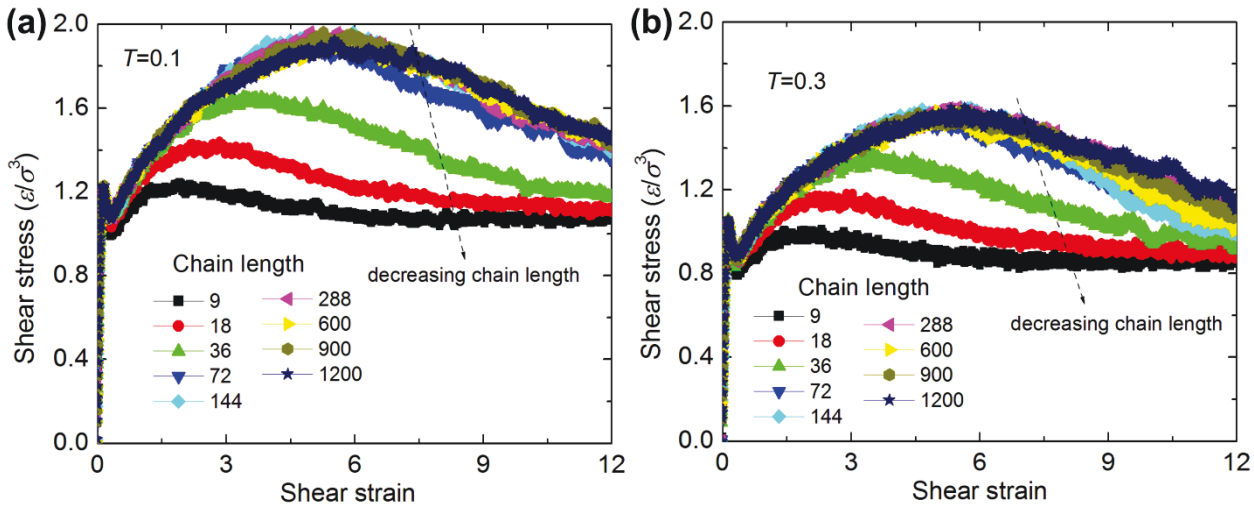

Fig. 7.7 The shear stress-strain curves with different chain length for two different temperatures. (a) T=0.1; (b) T=0.3.

Fig. 7.8 shows the corresponding broken rate with different CL for two different temperatures of Fig. 7.7. Similar to tension, the shear broken rate also increases with increasing CL. Unlike tension, the broke rate always increases with increasing shear strain even strain>12. Fig. 7.9 shows the ratio of tensile broken rate to shear broken rate with different strain. The ratio is always smaller than 1. In other words, for a given chain length and temperature, the broken rates under shear are always higher than those under tension for a same large strain. The possible reason is that the slipping and separation process mainly dominate the forward stage of the fracture behavior under shear, while the coupling slipping and broken mechanisms determine the fracture behavior under uniaxial tension. The r_c=1.5 of LJ potential is higher than the broken distance of r_{broken}=1.15 (see section 7.2), which leads to the higher ultimate fracture strain (that is, the structure is broken as two parts) under shear.

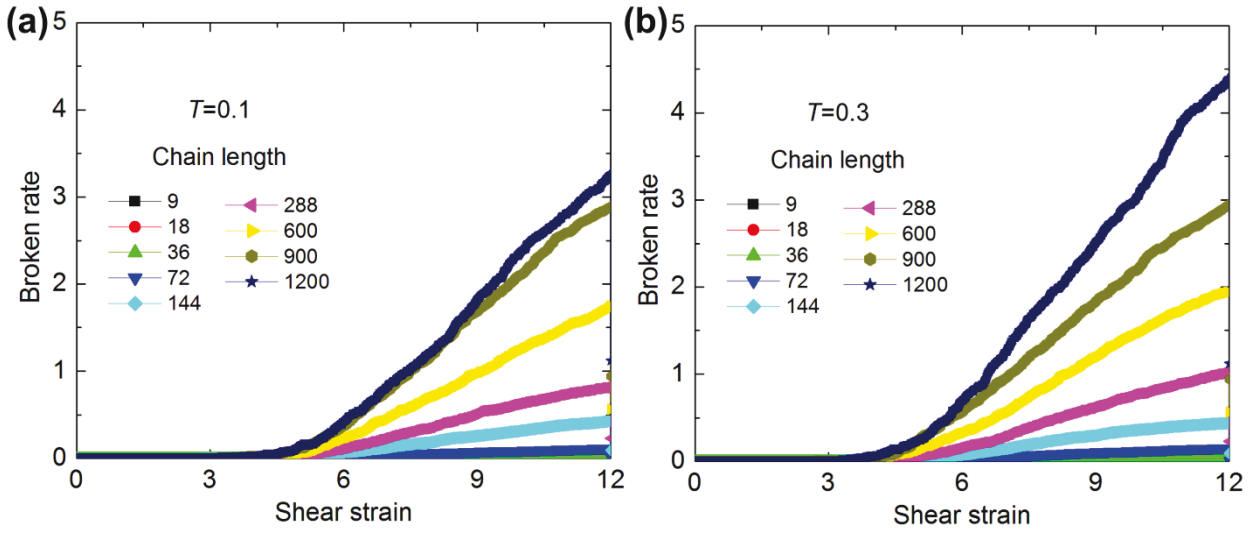

Fig. 7.8 The shear broken rate-strain curves with different chain length for two different temperature. (a) T=0.1; (b) T=0.3.

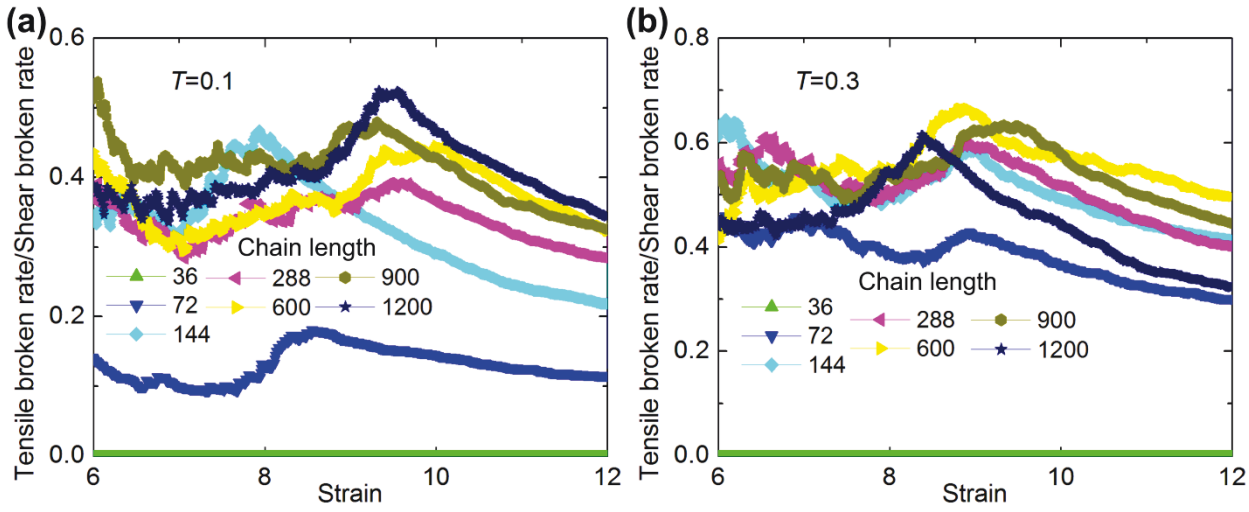

Fig. 7.9 The tensile broken rate/shear broken rate with different chain length for different temperature. (a) T=0.1; (b) T=0.3.

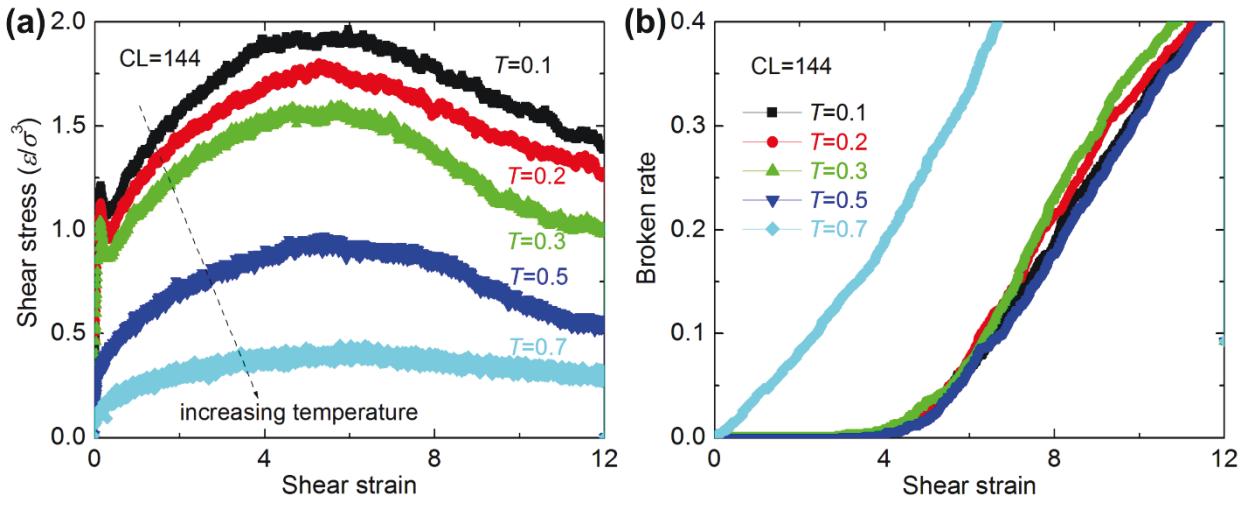

Fig. 7.10 The shear stress-strain and broken rate-strain curves with different temperature for CL=144. (a) Stress-strain curves; (b) Broken rate-strain curves.

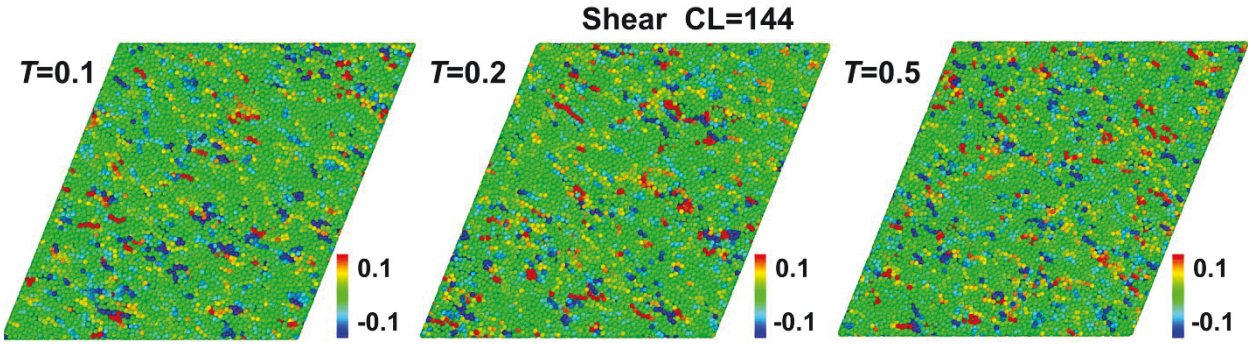

Fig. 7.11 The atomic strain (along the shear direction) distribution for CL=144 at different temperature under shear strain=58%.

Fig. 7.10 shows the shear stress-strain curves and broken rate for CL=144 with different temperature. The shear stress decreases with increasing temperature for same strain. For high temperature (T=0.5 and 0.7), no evident yield point can be also seen in Fig. 7.10a, which is same with tension. The difference of shear broken rate for different temperature is not large as T<0.7. To further understand the response, we plot the atomic strain (along the shear direction) distribution under shear strain (58%) for different temperatures and CL in the deformed

configuration of the polymer models in Fig. 7.11 and Fig. 7.12. For CL=144 under same shear strain, the difference of the atomic strain distribution with different temperature is not evident in Fig. 7.11. For T=0.1, the atomic strain concentration increases with increasing CL in Fig. 7.12. The possible reason is that more entanglements are in large CL, which leads to the atomic stress concentration at these positions.

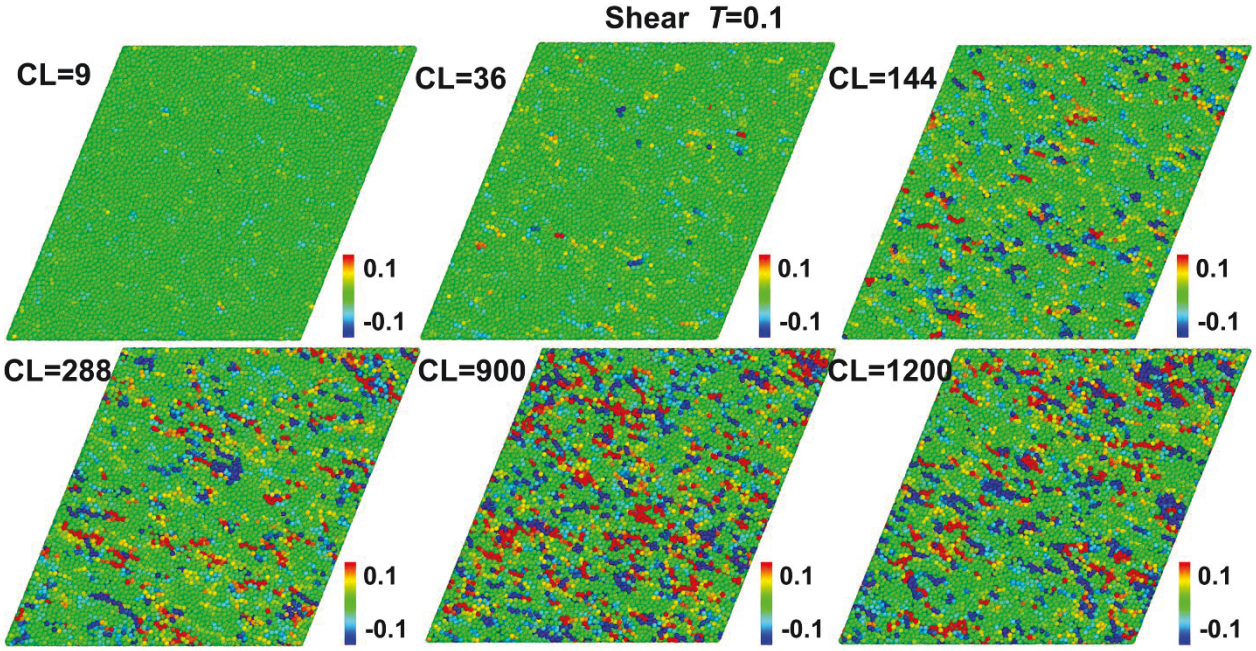

Fig. 7.12 The atomic strain (along the shear direction) distribution for different CL under shear strain=58% at T=0.1.

From above analysis, the ultimate fracture strain increases with increasing temperature under uniaxial tension. Under uniaxial tension, the fracture behavior is mainly determined by the chain slipping and separation for short CL. For longer CL, the fracture behavior is dominated by the competition between the chain slipping and bond broken mechanisms, in which the bond broken mechanism increases with increasing CL since the entanglement density increases with increasing CL. For very long CL, the bond broken mechanism mainly dominates the fracture behavior. Under shear, the atomic strain concentration increases with increasing CL for a given temperature. The shear broken rate is always higher than that under tension for same CL in the same large strain. The possible reason is that the slipping and separation process mainly dominate the forward stage of the fracture behavior under shear, while the coupling slipping and broken mechanisms determine the fracture behavior under uniaxial tension. The r_c=1.5 of LJ

potential is higher than the broken distance of r_{broken}=1.15 (see section 7.2), which leads to the higher ultimate fracture strain (that is, the structure is broken as two parts) under shear.

7.4 Concluding remarks

In summary, the tensile and shear failure behavior dependence on chain length and temperature in linear polymers are investigated using molecular dynamics simulations. A wide range chain length of alkane is tested under tension and shear with various temperatures. We find that the broken rate (the broken bond number to all polymer chain number ratios) under tension and shear increases with increasing chain length and temperature. For a given chain length and temperature, the broken rates under shear are always higher than those under tension at a same large strain. For a given chain length, the tensile and shear stresses decrease with increasing temperature. Under uniaxial tension, the fracture behavior is mainly determined by the chain slipping and separation for short CL. For longer CL, the fracture behavior is dominated by the competition between the chain slipping and bond broken mechanisms, in which the bond broken mechanism increases with increasing CL. For very long CL, the bond broken mechanism mainly dominates the fracture behavior. The slipping and separation process mainly dominate the forward stage of the fracture behavior under shear. The r_c=1.5 of LJ potential is higher than r_F=1.15 bond broken, which leads to the higher ultimate fracture strain under shear than that under uniaxial tension.

References:

C. Bennemann, W. Paul, K. Binder, Molecular-dynamics simulations of the thermal glass transition in polymer melts: α-relaxation behavior. Phys Rev E, 57 (1998) 843-851.

R.H. Boyd, R.H. Gee, Y. Jin, Conformational dynamics in bulk polyethylene: a molecular dynamics simulation study. J Chem Phys, 101 (1994) 788-797.

F.M. Capaldi, M.C. Boyce, G.C. Rutledge, Molecular response of a glassy polymer to active deformation. Polymer, 45 (2004) 1391-1399.

J.L. Faulon, Stochastic generator of chemical structure. (4) Building polymeric systems with specified properties. J Comput Chem, 22 (2001) 580-590.

R.S. Hoy, M.O. Robbins, Strain hardening of polymer glasses: Entanglements, energetics, and plasticity. Phys Rew E, 77(2008) 031801.

R.S. Hoy, M.O. Robbins, Strain hardening in polymer glasses: limitations of network models. Phys. Rev. Lett. 99 (2007) 117801.

K. Kremer, G.S. Grest, Dynamics of entangled linear polymer melts: A molecular‐dynamics simulation. J Chem Phys, 92 (1990) 5057-5086.

H.G.H. van Melick, L.E. Govaert, H.E.H. Meijer, On the origin of strain hardening in glassy polymers. Polymer, 44 (2003) 2493-2502.

S. Nose, A unified formulation of the constant temperature molecular dynamics methods. J Chem Phys, 81 (1984) 511-519.

M. Panico, S. Narayanan, L.C. Brinson. Simulations of tensile failure in glassy polymers: effect of cross-link density. Modelling Simul Mater Sci Eng, 18 (2010) 055005.

P.V.K. Pant, J. Han, G.D. Smith, R.H. Boyd, A molecular dynamics simulation of polyethylene. J Chem Phys, 99 (1993) 597-604.

S. Plimpton, Fast parallel algorithms for short-range molecular dynamics. J Comput Phys, 117 (1995) 1-19.

J.E. Shepherd, Multiscale modeling of the deformation of semi-crystalline polymers. Ph. D thesis. Georgia Institute of Technology, USA, 2006.

J. Zhao, S. Nagao, Z.L. Zhang, Thermo-mechanical properties dependence on chain length in bulk polyethylene: Coarse-grained molecular dynamics simulations, J Mater Res, 25 (2010a) 537-544.

J.H. Zhao, S. Nagao, Z.L. Zhang, H. Kristiansen, Coarse-grained molecular dynamics simulations on size effect of glassy polyethylene particles. J Nanosci Nanotech, 10 (2010b) 7340–7342.

J. Zhao, J.W. Jiang, N. Wei, Y. Zhang, T. Rabczuk, Thermal conductivity dependence on chain length in amorphous polymers. Appl Phys Lett, under review, 2013.

Chapter 8

Effects of the dispersion of polymer wrapped two neighbouring single walled carbon nanotubes (SWNTs) on nanoengineering load transfer*

Abstract

The influence of polymer wrapped two neighbouring single-walled nanotubes' (SWNTs) dispersion on their load transfer is investigated by molecular dynamics (MD) simulations. The influence of the SWNTs' position, the polymer chain length and the temperature on the interaction force between the two neighbouring SWNTs is systematically studied. There are four main findings from our simulations: (1) The dispersion angle dominates the amplitude and the interaction force evolution with or without polymer during the pulling process of two SWNTs. (2) The chain length doesn't affect the two SWNTs' interaction force within a short separation distance, the so called "Force enhancing point". The enhanced load effect of the polymer takes place after the load displacement goes across this point. (3) The temperature has a minor influence on the maximum pull force, while the increased temperature greatly decreases the pullout energy. (4) Based on the detailed analysis of the separation process, the self-repairing function of the system is found. The present results provide a guidance for understanding the load transfer of SWNT dispersion in phononic devices.

8.1 Introduction

After the discovery of carbon nanotubes (CNTs) by Iijima in 1991 (Iijima, 1991) almost two decades ago, the CNT based polymer nanocomposites have been received great interest due to the enhancement in mechanical (Sen et al., 2004), thermal (Clancy and Gates, 2006), optical (Kymakis and Amaratunga, 2002), electrical and magnetic properties (Sandler et al., 2003) with respect to neat polymer (Komarneni, 1992). They are used in the aerospace and automotive industries (Breuer and Sundararaj, 2004), as sensors (Kasumov et al., 1999), actuators (Baughman, 1999) and electrochemical capacitors in the electronics industry (Niu et al., 1997).

* The work was done by the cooperation with Dr. Yancheng Zhang and published on <<Composite part B: Engineering>> 45, 1714-1721 (2013), in which the most part of the work was done by Dr. Yancheng Zhang based on my much important guidance.

Recently, increased interest has also been received for the phononic devices, in which heat flow is manipulated and controlled in nanostructures (Chang et al., 2007; Chang et al., 2006), wherein the carbon nanostructures are excellent candidates for multi-functional thermal management network. However, the weak van der Waals interaction cannot reliably hold the nanotubes together under thermal fluctuations or due to elastic deformation of the material, leading to inferior mechanical stability. One experimentally feasible approach is to wrap the carbon nanotube junctions using polymer chains has been reported in literature (Dalton et al., 2004; Zhang et al., 2008). Nevertheless, some significant challenges remain in the design and understanding of the nanostructure, such as the dispersion of the CNTs within the considered polymer matrix (Zheng et al., 2008). Unfortunately, the insufficient dispersability of single-walled carbon nanotubes (SWNTs) occurs in most common solvents due to the van der Waals attraction among tubes. Locally, carbon nanotubes tends to bind and form energetically stable bundles (Dresselhaus et al., 2000), which makes it difficult to understand and explore their physical and chemical properties. Therefore, the phenomenon implies many limitations for their practical applications (Shin et al., 2009). Up to now, dispersion of CNTs in polymer (Shin et al., 2009; Zhao et al., 2009; Qian et al., 2000) and metal alloy media (Esawi et al, 2007) have been reported. These studies mainly focus on experiments and the global effect on the mechanical behavior of the nanocomposites. More detailed information about the interaction and separation between CNTs is needed. Analytical interface models have been developed for both opening and sliding modes, while both CNT and the polymer were assumed to be rigid (Jiang et al., 2006).

Molecular dynamics (MD) simulations have been performed to study the interfacial mechanical behavior between CNT/polymer (Awasthi et al., 2009): traction-displacement behavior of graphene-polyethylene interfaces for both opening and sliding separation mode, and the influence of constraint conditions were discussed. The influence of the curvature of the CNT wall was ignored. Kulmi and Basu (Kulmi and Basu, 2006) as well as Adnan and Sun (Adnan and Sun, 2008) investigated the competition between adhesive failure along the interface and cohesive failure within the polymer. Both molecular mechanics (MM) and MD simulations were conducted to explore the interfacial binding characteristics between SWNTs and polymer (Zheng et al., 2008; Gou et al., 2004). However, current models developed for CNT-polymer interfaces in the bulk can not be directly applied to a nano scale interface, specially to interfaces between

similar materials bonded through weak interactions (i.e., van derWaals forces) and can therefore not be used to study the performance of nano-structured junctions between SWNTs. Xu and Buehler (Xu and Buehler, 2009) have studied the two SWNTs interaction with and without polymer, which shows the wrapped polymer chain can enhance the binding range compared to the bare junction (pure SWNTs) for two parallel SWNTs. The main aim of this research is to study the dispersion effects on the load transfer of two pristine SWNTs without and with low density polymer wrapping in the absence of heat transfer. The paper is structure as follows: first we will introduce the details of the MD simulation, which includes the force field and arrangements of the polymer and SWNTs. Then we will explain the equilibrium and separation process of the polymer wrapped two single SWNTs. After that we give parametric study for different relative dispersion angels, polymer chain lengths and temperature. The paper ends with the discussion of results as well as implications of the future work.

8.2 Details of the simulation

8.2.1 Molecular model

In this research, MD simulations were conducted to extract the interface behavior between two SWNT with and without polymer wrapping. All MD simulations were performed with LAMMPS (Plimpton, 1995). The polymer matrix consists of PE is used in a variety of engineering applications (Jiang et al., 2012). To reduce the computational cost, the united atom (UA) approximation is utilized (Zhao et al., 2011), in which the methyl groups are represented by a single atom or unit (i.e., the CH2 monomer). The effect of the hydrogen atoms on the polymer configuration is accounted for in the present potentials, while the mass is included in the mass of the united atom. In this research, a total number of 600 UA monomers is kept constant for three different chain lengths with 20, 40 and 60 monomers respectively. Two SWNTs (armchair (5,5)) with a diameter of 6.78 Å and lengths of 59.03 Å are selected for simulations of SWNT-PE composites. The unsaturated boundary effect was avoided by adding hydrogen atoms at the end of the SWNTs.

8.2.2 Force field

8.2.2.1 Polymer

The functional form and the parameters of the force field are provided in Table 8.1 (Capaldi et al, 2004). Note that the non-bonded interactions are truncated at a distance of 10 Å (Capaldi et al, 2004).

Table 8.1 Function form of force field and potential parameters used for PE MD calculation (Capaldi et al, 2004).

Type of potential	Form	Parameters
Bond	$E=\frac{1}{2}k_b(r_b-r_0)^2$	k_b=2000 kJ/mol Å^2; r_0=1.53 Å
Angle	$E=\frac{1}{2}k_\theta\left(\cos(\theta)-\cos(\theta_0)\right)^2$	k_θ=510 kJ/mol; θ_0=110^0
Dihedral	$E=\frac{1}{2}\sum_{n=0,3}A_n\cos^n(\phi)$	A_1=17.477, A_2=-37.594, A_3=6.493, A_4=58.499 kcal/mol
Non-bonded	$E=4\varepsilon\left[\left(\frac{\sigma}{r}\right)^{12}-\left(\frac{\sigma}{r}\right)^{6}\right]$	ε=0.468 kcal/mol; σ=4.01 Å; r_c=10 Å (truncation radius)

8.2.2.2 SWNT

The interatomic (Carbon and hydrogen) interactions in carbon nanotubes are described with the adaptive intermolecular reactive empirical bond-order (AIREBO) (Plimpton, 1995; Brenner et al., 2002) potential function. This potential allows for covalent bond breaking and creation with associated changes in atomic hybridization within a classical potential.

8.2.2.3 Interfacial binding energy between polymer and SWNTs

The Lennard-Jones Potential $V(r)= 4\varepsilon((\sigma/r)^{12}-(\sigma/\varepsilon)^6)$ is adopted for characterizing the interatomic interaction between the polymer monomers and the SWNT which include both carbon and hydrogen. The mixing rule form parameters is performed for polymer monomers and hydrogen (CH2(UA)-H) as described in Table 8.2.

Table 8.2 Function form of the force field and the potential parameters used for the interaction between PE and SWNTs.

Type of potential	ε(kJ/mol)	σ (Å)
CH2(UA)-C	0.461	k_b=2000 kJ/mol Å^2; r_0=1.53 Å [32]
CH2(UA)-CH2(UA)	0.468	k_0=510 kJ/mol; θ_0=110^0 [30]
H-H	0.126	A_1=17.477, A_2=-37.594, A_3=6.493, A_4=58.499 kcal/mol [33]
CH2(UA)-H	0.243(=(ε_{CH2}*ε_H)$^{1/2}$)	3.215(=(σ_{CH2}+σ_H)/2) [34]

8.3 Equilibrium process

After the polyethylene chains are introduced close to the interface, the equilibrium MD simulations are initially performed at 500 K with the *NVT* ensemble of 8×10^5 steps (Δt = 0.5fs). The next relaxation cools the structure down to the desired temperature at a cooling rate of 0.8 K/ps steps (Capaldi et al, 2004) followed by further relaxation of 8×10^5 at the desired temperature. The following pulling separation is also performed under the NVT ensemble. Two typical configurations at equilibrium with the dispersion angle of 0 and 90 degrees are shown in Fig.1 for the chain length of 20 monomers. The polymer chains prefer to wrap around the SWNT surface, while they don't enter the interaction zone for both dispersion angles.

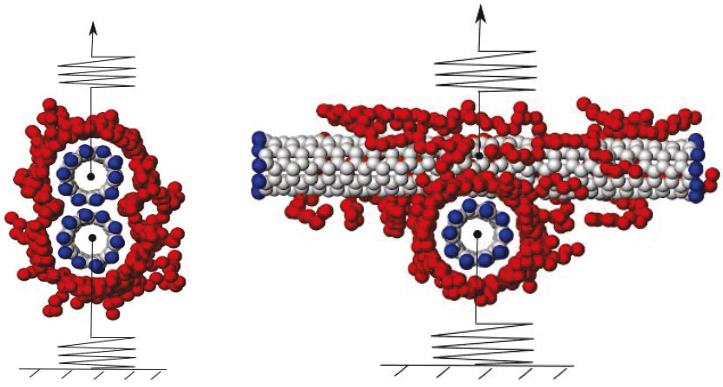

Fig. 8.1 Equilibrated double SWNTs with polymer at 300 K.

Note that various initial configurations of the polymer chains such as vertical, perpendicular, and random orientations are used in the simulation. The results show that the final configuration of the polymer chains at the carbon nanotube junction does not depend on the initial pattern.

8.4 Separation process

The separation process is performed between SWNTs, with or without polymer wrapping, through steered molecular dynamics (SMD) (Wei et al., 2002; Jorgensen et al., 1997; Bandyopadhyaya et al., 2011) for mechanically separating the interface, which permits one to efficiently extract equilibrium properties (mean force and the potentials of the mean force built in LAMMPS) from nonequilibrium processes (such as SMD simulations). One SWNT is pulled along the direction perpendicular to the interface by the virtual spring with the constant velocities of 0.001nm/ps and 0.0001nm/ps (Xu and Buehler, 2009; Park and Schulten, 2004), while the center of mass of the other SWNT is constrained by a spring to its original position, as presented in Fig. 8.1.

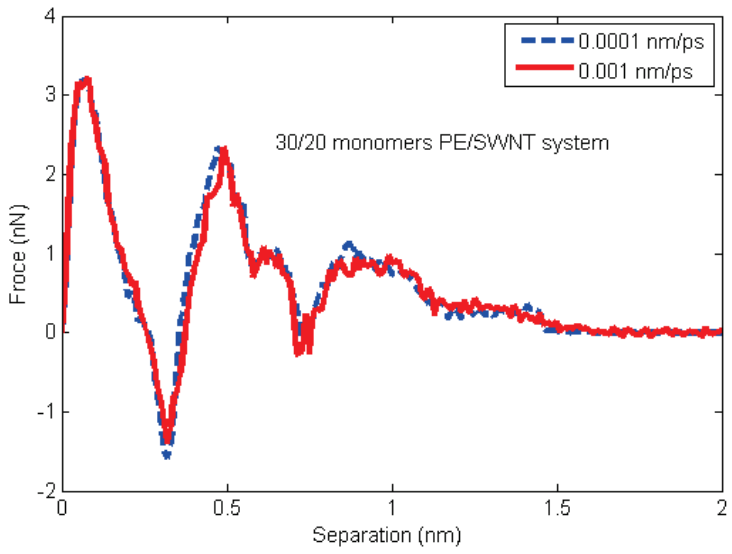

Fig. 8.2 Pulling velocity optimization for pulling double SWNTs at 300 K.

The results show that the pulling velocity of 0.001nm/ps is able to capture all the characteristics of the force evolution for the pulling process (Fig. 8.2), so this velocity (0.001nm/ps) is adopted in the following MD simulations. The elastic constant for the spring

between the constant tether point and the mass center of the SWNT is k = 1.6kN/m (Xu and Buehler, 2009). The force applied to the mass center of the SWNT by the virtual spring is:

$$F(t) = k_{spring}\left(x_{spring}(t) - x_{pull}(t)\right), \tag{1}$$

where χ_{spring} and χ_{pull} represent the spring and pulled group positions, respectively. During the pulling process, the integral operation over the pulling force in direction of the spring is recorded and then used to compute the PMF by averaging over multiple independent trajectories along the same pulling path [35].

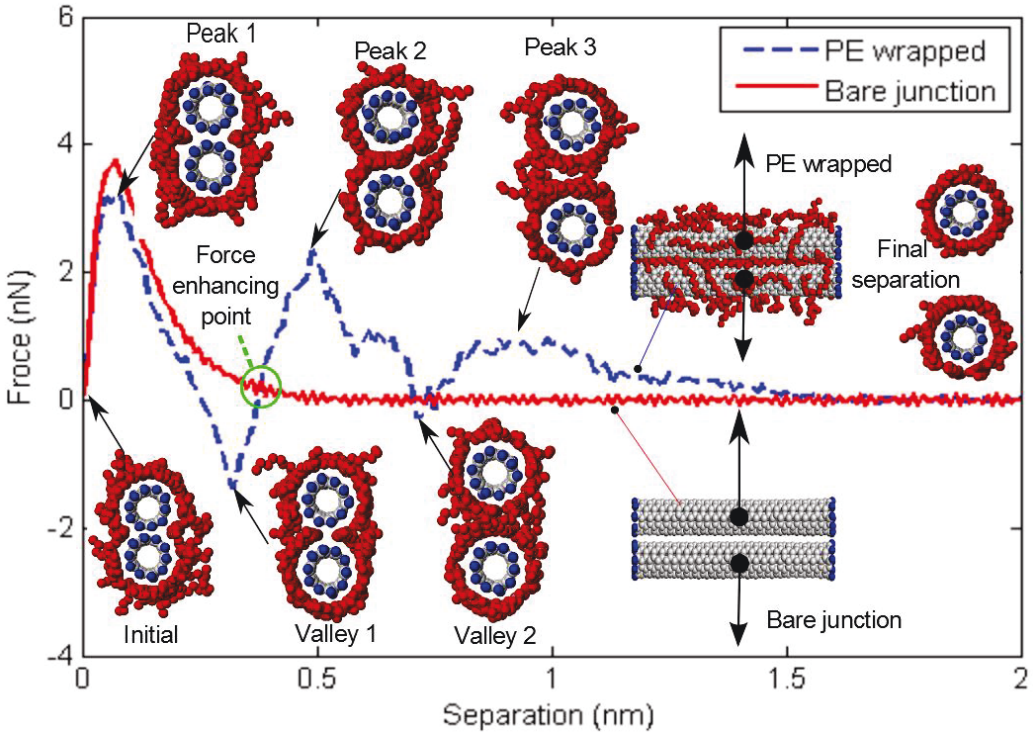

Fig. 8.3 Separation evolution for double SWNTs at 300 K.

The separation force evolutions of the bare junction (pure binding of two SWNTs) and 30 PE molecules of chain length with 20 monomers are illustrated in Fig. 8.3 for zero dispersion angle. In addition, the current configuration during the junction separation process of the wrapped polymer is also given in Fig. 8.3. Multi-peaks and valleys appear in the force-separation curve for the wrapped polymer chains. For two pure SWNTs, the force-separation curve exhibits only one maximum peak. However, the wrapped junction presents a much longer binding range than

the bare junction, while the "force enhancing point" locates at 0.38 nm (the interaction point after the first valley). Below this value, enhanced binding effect is not observed, which means that the substantial van der Waals attraction among tubes dominate the separation within a certain distance. Actually, the initial configuration shows a stronger van der Waals attraction force between SWNTs compared to the value among polymer and SWNTs, as polymer can not enter the interaction zone without using mechano-chemical driving forces at the primary stage pulling. The stronger attraction force between SWNTs continues until the polymer enters the interaction zone (position of "valley 1") with the increased separation distance. With the further increased separation, one close circle forms for the position of "peak 2", and double close circles appear at "valley 2". For the continuing separation, the two formed close circles start to detach, which will lead to the final detachment of the polymer wrapped SWNTs. We also observe self-repairing from three snapshots in the position of the initial, valley 1 and valley 2 configurations: one close circle splits into two close circles to obtain the stable state. Moreover, the configuration of the formed two circles is the last chance for self-repairing. Even the interaction strength is relatively low. The polymer chain will start to completely separate once the distance passes the position of peak 3.

8.5 Parametric study

8.5.1 CNT dispersion effect

Table 8.3 Dispersion angle influence on the interaction of neighbouring SWNTs.

Cases	Temperature (K)	Chain length (monomers)	Dispersion angle (degree)
1	300	bare junction	0-90, separated by 15
2	300	20	0-90, separated by 15

During the fabricating process without using mechano-chemical driving forces, the CNTs in the polymer matrix tends to locate at the position where the energy is minimized. Usually, the CNTs locate at the balance position with the relative distance wrapped with polymer chain.

To understand the dispersion angle effect on the SWNT interaction in nanocomposite, simulations were performed for a chain length of 20 monomers at room temperature 300K

through 7 groups orientation angle, varying from 0 to 90 degrees as presented in Table 8.3. For the bare junction of two SWNTs, the pulling forces and energies are are shown in Figs. 8.4a and 8.4b respectively. The relative dispersion angle greatly affects the load transfer of the bare junction of 2 SWNTs, as shown in Figs. 8.4a, 8.4b. Angles below 15 degrees provide larger forces and energies. There is almost no difference in these values for dispersion angles bigger than 45 degree. This observation holds for the bare junction as well as for the PE wrapped SWNTs. With the polymer chain, the interaction binding is enhanced for all the dispersion angles as presented for the pull energy evolution in Fig. 8.4d. The maximum value decrease for angles 0, 15 and 30 degrees (Fig. 8.4c) compared to the bare interaction in Fig. 8.4a, as the polymer can enter the increased distance between two SWNTs during the pulling operation, which contributes more repulsive force rather than attraction force. Due to the negative force at "valley 1" and "valley 2" (Fig. 8.4c), the corresponding valleys are found in the pull energy evolution in Fig. 8.4d. On the contrary, for the increased dispersion angles from 45 to 90 degrees, more polymer can wrap around the interaction surface at the initial configuration, which contribute more attractive force. Consequently, the maximum forces are increased compared to the bare SWNT pair.

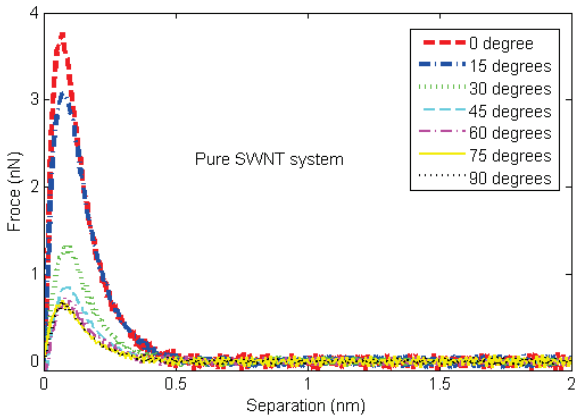

Pull force for bare junction

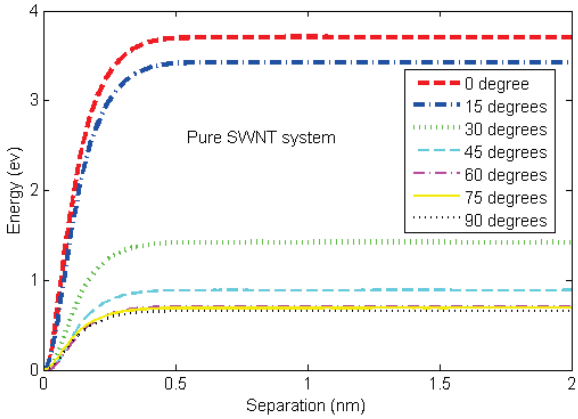

Pull force for bare junction

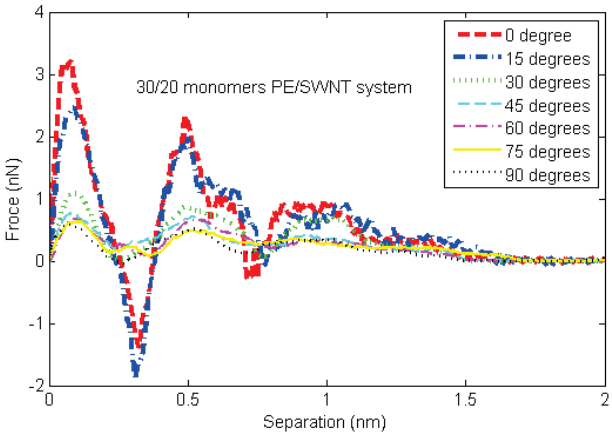

Pull force with polymer

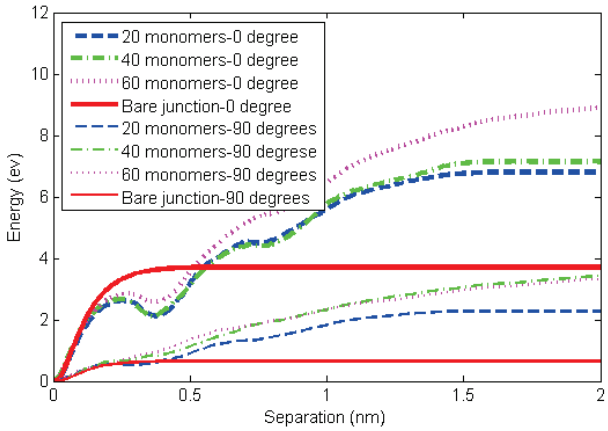

Pull energy with polymer

Fig. 8.4 Traction process for different dispersion angles at 300 K

The later enhanced force vibrations are above zero, which leads to a smoother pull energy evolution when the dispersion angles are larger than 30 degrees.

8.5.2 Chain length dependence

As described in the literature (Zhao et al., 2010; Hossain et al., 2010), the chain length of amorphous polyethylene greatly affects the mechanical behavior during the pull process. For the SWNT based nanocomposite, different PE chains with 20, 40 and 60 UA monomers are studied (see Table 8.4). At a relatively low polymer chain density, the polyethylene UA monomers tend to align at the groove between SWNTs.

Table 8.4 Chain length influence on the interaction of polymer wrapped SWNTs.

Cases	Temperature (K)	Chain length (monomers)	Dispersion angle (degree)
1	300	20/40/60	0
2	300	20/40/60	90

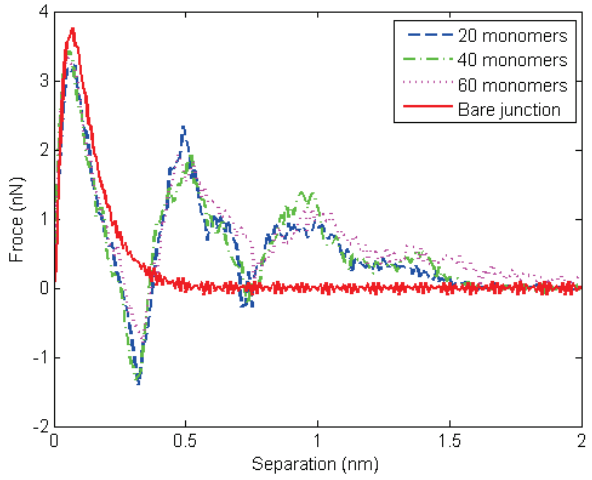

Dispersion angle-0 degree

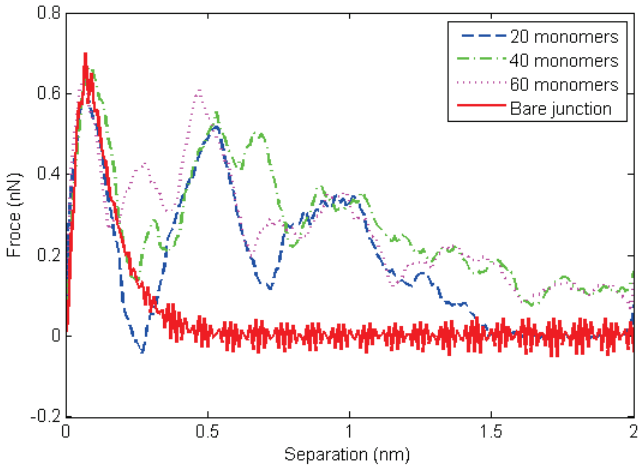

Dispersion angle-90 degree

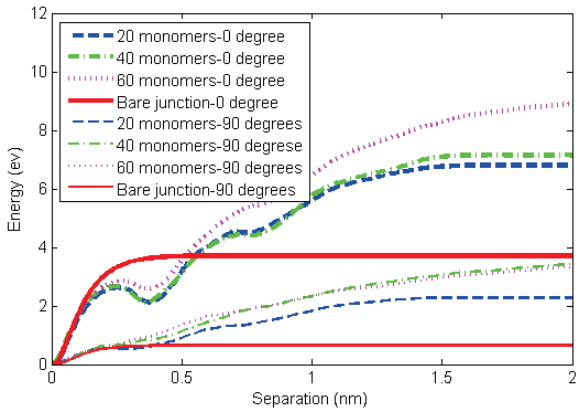

Pullout energy

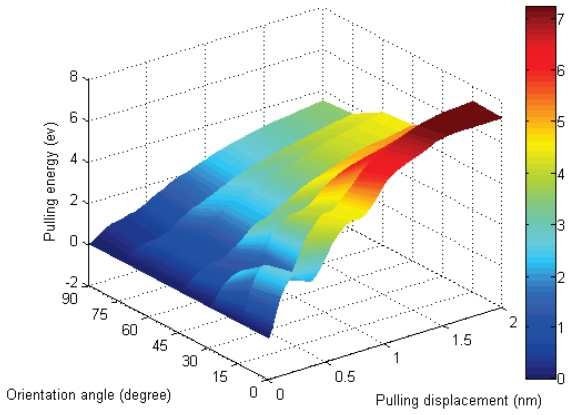

Energy distribution for chain length with 40 monomers

Fig. 8.5 Traction process with different chain lengths at temperature 300 K.

Two typical dispersion angles of 0 and 90 degrees for different chain length are presented, as shown in Fig. 8.5. For the cases of zero dispersion angles, it is found that there is no difference for the three chain lengths within the short separation distance, which means that the no-bond

van der Waals force dominates the attraction of the two SWNTs within the same number of polymer monomers in the six SWNT/polymer systems. For the further separation, the superiority of the long chain appears and the binding force increases with increasing chain length. The same phenomenon is observed the 90 degree angle. Hence, the chain length affects the pull out mechanical behavior slightly within a certain short distance corresponding to the relative position of two SWNTs, while the long chain polymers enhance the interaction binding once the distance of two SWNTs exceeds the critical value. The pullout energy for the zero dispersion angle is larger compared to the pullout energy of 90 degrees because of the larger interaction area, while more oscillation is observed in the cases of zero angle. The pulling energy distribution for all the dispersion angles for a chain length of 40 monomers is given in Fig. 8.5d. The pull energy for the other dispersion angle is between the cases of 0 and 90 degrees. The chain length doesn't change the trends of the pull energy evolution, compared to the chain length of 40 monomers as shown in Fig. 8.4d. Similar energy distributions are found for a chain length of 60 monomers.

8.5.3. Temperature influence

The temperature is one of the main factors which determine both mechanical and chemical properties of the CNT polymer composite, especially for the adhesion and reinforcement (Wei, 2006). In this section, the influence of the temperature on the interface strength is studied for different temperature with various chain lengths and dispersion angles, see Table 8.5.

Table 8.5 Temperature influence on the interaction of polymer wrapped SWNTs.

Cases	Temperature (K)	Chain length (monomers)	Dispersion angle (degree)
1	100/200/300	20	0
2	100/200/300	40	0
3	100/200/300	60	0
4	100/200/300	20	90
5	100/200/300	40	90
6	100/200/300	60	90

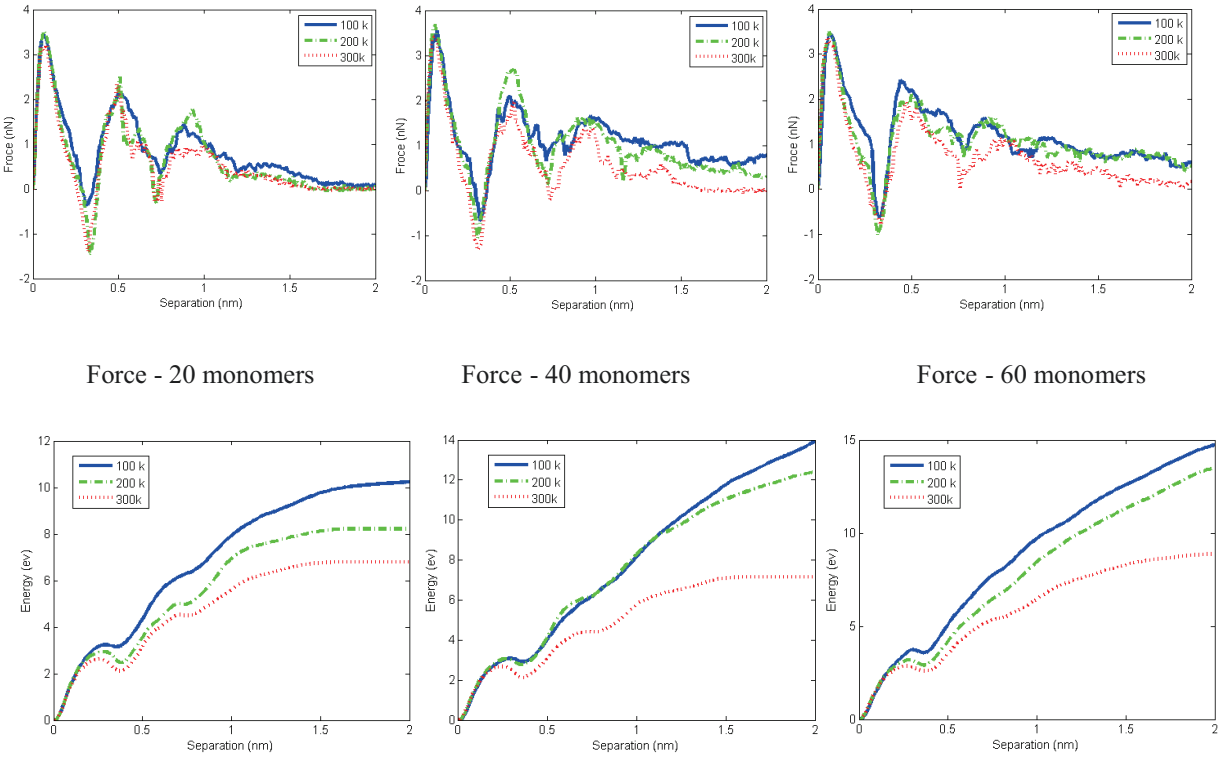

Force - 20 monomers Force - 40 monomers Force - 60 monomers

Energy - 20 monomers Energy - 40 monomers Energy - 60 monomers

Fig. 8.6 Traction process with different temperature at the dispersion angle of 0 degree.

As shown in Fig. 8.6, for a dispersion angle of 0 degree, the temperature has a minor effect on the maximum pull force. This observation holds independent of the chain length. The highest value of the minimum pull force (the first valley point) is obtained for a temperature of 100 K due to the inactive movement of the polymer monomers as less monomers can enter the interaction zone during the pulling process. The pull strength is less sensitive with respect to temperature and chain length, which are mainly determined by the interaction between two bare SWNTs. The polymer chains enhance the binding junction for the further separation when the distance is larger than the position of the minimum pulling force. The pull energy distribution clearly shows that the final separation is hard to be activated at low temperature, and the process is more difficult for the increased chain length as shown in Figs. 8.6e, 8.6f. Note that the energy curves almost overlap (the first half of curve) at chain length of 40 monomers for the low temperature (100 K and 200 K), this is maybe due to the similar initial configurations for the two cases.

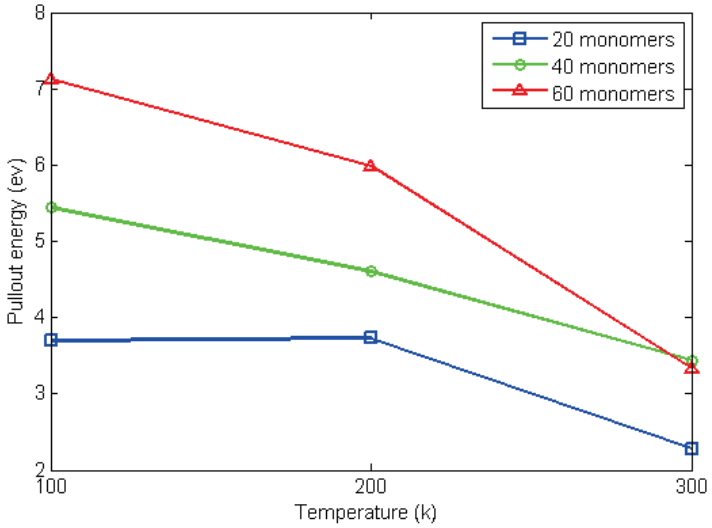

Fig. 8.7 Traction process with different temperature at the dispersion angle of 90 degrees.

Fig. 8.7 shows the final pullout energy for different temperature at the orientation angle of 90 degrees. As the interaction area is small and the interaction zone is immersed in the polymer matrix, the separation process requires less energy for the increased temperature with respect to three chains. Besides the slope of the decreased pullout energy is larger for the later part (range from 200 K to 300 K) compared to the former part (range from 100 K to 200 K), especially for the long chain polymer. By adjusting the dispersion of the SWNTs, we can obtain the controlled mechanical behavior with various chain length and temperature.

8.6 Conclusion

In this paper, the dispersion of polymer wrapped two single-walled nanotubes (SWNTs) on their load transfer was systematically investigated by molecular dynamics (MD) simulations. The separation process was analyzed by the pulling evolution with corresponding configuration. It is found that the polymer wrapped junction always presents a much longer binding range than the bare junction of SWNTs. Besides the multi-peaks and valleys are found in the force-separation curve for the polymer wrapped SWNTs. The valley means that the repulsive force dominates the interaction of the two SWNT, while the peak implies that the attractive force is dominant for the two SWNTs interacting, which presents the abilities of the wrapped structure to prevent the separation of two SWNTs, and the last peak is the final chance for the reinforcing effect compared to the bare junction of the SWNTs. It is also observed that the self-repairing function

can be obtained by splitting one close circle to two close circles in order to arrive at the other stable configuration, which actually leads to the phenomena of the multi-peaks and valleys. The self-repairing function is useful for designing phononic devices and synthesizing functional material with simple polymer and pristine SWNT.

The relative dispersion angle greatly affects the load transfer. The dispersion angles of 0 and 15 degrees give the lager pulling forces and energies, while there are almost no difference for these values when the dispersion angle exceeds 45 degrees. They are mainly determined by the interactionfarea, without or with polymer chains. Furthermore, a smooth pulling energy evolution is found when the dispersion angles are larger than 30 degrees. The chain length affects the pullout mechanical behavior slightly within a certain short separation distance corresponding to the relative position of two SWNTs, while the long chain polymers enhances the interaction binding once the distance of two SWNTs exceeds the critical value. In addition, the chain length doesn't change the trends of the pull energy evolution varying with dispersion angles of two SWNTs.

The temperature has a minor influence on the maximum pull force, while the increased temperature greatly decreases the pullout energy as the polymer deformation is easily activated at high temperature, especially for the long chain polymer. The future work will focus on the heat transfer performance of the polymer wrapped SWNTs with various SWNT dispersion angles and chain lengths of polymer under different temperature.

References

Adnan A and Sun CT, Effect of adhesive thickness on joint strength: A molecular dynamics perspective. J Adhesion 2008;84(5):401-420.

Awasthi PA, Lagoudas DC, and Hammerand DC. Modeling of graphenepolymer interfacial mechanical behavior using molecular dynamics. Modeling Simul Mater Sci Eng 2009;17:015002.

BaughmanR H, Cui CX, Zakhidov AA et al. Carbon Nanotube Actuators. Science 1999;284(5418):1340-1344.

Breuer O, Sundararaj U. Big returns from small fibers: A review of polymer/carbon nanotube composites. Polym Composite 2004;25(6):630-645.

Bandyopadhyaya A, Valavalab PK, Clancyc TC, Wised KE, Odegard GM. Molecular modeling of crosslinked epoxy polymers: The effect of crosslink density on thermomechanical properties. Polymer 2011;52(11):24452452.

Brenner DW, Shenderova1 OA, Harrison JA,Stuart SJ, Boris Ni B and Sinnott SB. A second-generation reactive empirical bond order (REBO) potential energy expression for hydrocarbons. J Phys: Condens Matter 2002;(14):783802.

Capaldi FM, Boyce MC, Rutledge GC. Molecular response of a glassy polymer to active deformation. Polymer 2004;45(4):13911399.

Chang CW, Okawa D, Garcia H, Majumdar A, and Zettl A, Nanotube phonon waveguide. Phys Rev Lett 2007;99:045901.

Chang CW, Okawa D, Majumdar A, and Zettl A. Solid-state Thermal Rectifier. Science 2006;314:1121-1124.

Dalton AB, Ortiz-Acevedo A, Zorbas V, Brunner E, Sampson WM, Collins S, Razal JM, Yoshida MM et al.

Clancy TC, Gates TS. Modeling of interfacial modification effects on thermal conductivity of carbon nanotube composites. Polymer 2006;47:59905996.

Dresselhaus MS, Dresselhaus G, Avouris P. Carbon Nanotubes: synthesis structure properties and applications. Springer: New York, 2000.

Esawi A, Morsi K. Dispersion of carbon nanotubes (CNTs) in aluminum powder. Composites:Part A 2007; 38:646650.

Gou JH, Minaie B, Wang B, Liang ZY, Zhang C. Computational and experimental study of interfacial bonding of single-walled nanotube reinforced composites. Comp Mater Sci 2004;31(34):225236.

Hierarchical Self-Assembly of Peptide-Coated Carbon Nanotubes. Adv Funct Mater 2004;14:11471151.

Hossain D, Tschopp MA, Ward DK, Bouvard JL, Wang P, Horstemeyer MF. Molecular dynamics simulations of deformation mechanisms of amorphous polyethylene. Polymer 2010; 51:6071-6083.

Iijima S. Helical microtubules of graphitic carbon. Nature 1991;354(6348):56-58.

Jorgensen WL. OPLS and OPLS-AA Parameters for Organic Molecules, Ions, and Nucleic Acids, Yale University, 1997.

Jiang JW, Zhao JH, Zhou K, and Rabczuk T. Superior thermal conductivity and extremely high mechanical strength in polyethylene chains from ab initio calculation. J Appl Phys 2012;111:124304. doi:10.1063/1.4729489.

Jiang LY, Huang Y, Jiang H, Ravichandran G, Gao H, Hwang K C and Liu B. J Mech Phys Solids 2006;54:24362452.

Kasumov AY,Deblock R, Kociak M, Reulet B,Bouchiat H, Khodos I, et al. Super currents Through Single-Walled Carbon Nanotubes. Science 1999;284:1508-1511.

Kulmi U and Basu S. A molecular dynamics study of the failure modes of a glassy polymer confined between rigid walls. Model Simul Mater Sci 2006;14(6):1071-1093.

Kymakis E, Amaratunga GAJ. Single-wall carbon nanotube/conjugated polymer photovoltaic devices. Appl Phys Lett 2002;80(1):112-115.

Komarneni S. Nanocomposites. J Mater Chem 1992;2:12191230.

Niu CM, Sichel EK, Hoch R, Moy D, Tennent H. High power electrochemical capacitors based on carbon nanotube electrodes. Appl Phys Lett 1997;70(11):1480-1482.

Park S and Schulten K. Calculating potentials of mean force from steered molecular dynamics simulations. J Chem

Phys 2004; 120(13):5946-5961.

Plimpton S. Fast Parallel Algorithms for Short-Range Molecular Dynamics, J Comp Phys 1995;117:1-19.

Qian D, Dickey EC, Andrews R and Rantell T. Load transfer and deformation mechanisms in carbon nanotube-polystyrene composites. Appl Phys Lett 2000;76:28682870.

Sandler JKW, Kirk JE, Kinloch IA, Shaffer MSP, Windle AH. Ultra-low electrical percolation threshold in carbon-nanotube-epoxy composites. Polymer 2003;44(19): 5893-5899.

Sen R, Zhao B, Perea D, Itkis ME, Hu H, Love J, Bekyarova E, and Haddon RC. Preparation of Single-Walled Carbon Nanotube Reinforced Polystyrene and Polyurethane Nanobers and Membranes by Electro-spinning. Nano Letters 2004;4(3):459464.

Shin J, Kim C, Geckeler KE. Single-walled carbon nanotubepolystyrene nanocomposites: dispersing nanotubes in organic media. Polym Int 2009;58(5):579583.

Wei CY, Srivastava D, Cho K. Thermal Expansion and Diffusion Coefficients of Carbon Nanotube-Polymer Composites. Nano Lett 2002;2(6):647650.

Wei CY. Adhesion and reinforcement in carbon nanotube polymer composite. Appl Phys Lett 2006;88:093108-3.

Xu Z, Buehler MJ. Nanoengineering heat transfer performance at carbon nanotube interfaces. ACS Nano 2009;3(9):2767-2775.

Zhang YC, Broekhuis AA, Stuart MCA, Landaluce TF, Fausti D, Rudolf P, Picchioni F. Cross-Linking of Multiwalled Carbon Nanotubes with Polymeric Amines. Macromolecules 2008;41:61416146.

Zhao JH, Nagao S, Zhang Zl. Thermomechanical properties dependence on chain length in bulk polyethylene: Coarse-grained molecular dynamics simulations. J Mater Res 2010;25(3):537-544.

Zhao JH, Guo WL, Zhang ZL, and Rabczuk T. Size-dependent elastic properties of crystalline polymers via a molecular mechanics model. Appl Phys Lett 2011;99 241902.

Zhao Y, Duan YX, Yuan L, Guan FX. The dispersion of SWCNTs treated by dispersing agents in glass fiber reinforced polymer composites. Compos Sci Technol 2009;69:21152118.

Zheng QB, Xue QZ, Yan KY, Gao XL, Li Q, Hao LZ. Effect of chemisorption on the interfacial bonding characteristics of carbon nanotube-polymer composites. Polymer 2008;49(3):800-808.

Chapter 9

Conclusions and Further work

9.1 Concluding remarks

In this thesis, the explicit solutions for the cohesive energy between carbon nanotubes (CNTs), graphene and substrates are obtained through continuum modeling of the van der Waals interaction between them. The dependence of the cohesive energy on their size, spacing and crossing angles is analyzed. The equilibrium distances between the nanotubes, graphene and substrates with minimum cohesive energy are also provided explicitly. Checking against full atom molecular dynamics (MD) calculations and available experimental results shows that the continuum solution has high accuracy.

Based on our analytical results of cohesive energy between two single-walled CNTs, the two kinds of coarse-grained (CG) non-bonded models between different CG beads are systematically analyzed. Checking against full atom MD calculations and our analytical results, we find that the first non-bonded CG model is only effective under small deformation since only the minimum potential energy at the equilibrium distance between two CNTs is fitted. However, the second non-bonded CG model has high accuracy under large formation when the equilibrium bond length (EBL) of two CG beads is not more than 5 Å, in which the accuracy strongly depends on the EBL and sharply decreases with increasing EBL (>5 Å). The explicit expressions of the CG stretching, bending and torsion potentials are obtained by the stick-spiral and the beam models.

Furthermore, the binding energy between two parallel (and two crossing) single-walled (and multi-walled) CNTs is obtained by continuum modeling of the van der Waals interaction between them. The dependence of the binding energy on their diameters, number of walls and crossing angles is systematically analyzed. The critical length for the mechanical stability and adhesion of the CNTs has been determined by the function of E_iI_i, h and γ, where E_iI_i, h and γ are the CNTs bending stiffness, distance and binding energy between them.

For crystalline polymers, an analytical molecular mechanics model is developed to obtain the size-dependent elastic properties of crystalline polyethylene. An effective “stick-spiral” model is

adopted in the polymer chain. Explicit equations are derived from the Lennard-Jones potential function for the van der Waals force between any two polymer chains. By using the derived formulas, the nine size-dependent elastic constants are investigated systematically. The present analytical results are in reasonable agreement with those from present united-atom MD simulations.

In particular, we show that the two molecular mechanics models, the stick-spiral and the beam models, predict considerably different mechanical properties of materials based on energy equivalence. The difference between the two models is independent of the materials since all parameters of the beam model are obtained from the harmonic potentials. We demonstrate this difference for finite width graphene nanoribbons and a single polyethylene chain comparing results of the MD simulations with harmonic potentials and the finite element method with the beam model. We also find that the difference strongly depends on the loading modes, chirality and width of the graphene nanoribbons, and it increases with decreasing width of the nanoribbons under pure bending condition. The maximum difference of the predicted mechanical properties using the two models can exceed 300% in different loading modes. Comparing the two models with the MD results of AIREBO potential, we find that the stick-spiral model overestimates and the beam model underestimates the mechanical properties in narrow armchair graphene nanoribbons under pure bending condition.

For amorphous polymers, the tensile and shear failure behavior dependence on chain length and temperature in amorphous polymers are scrutinized using molecular dynamics simulations. A wide range chain length of alkane is tested under tension and shear with various temperatures. We find that the broken rate (the broken bond number to all polymer chain number ratios) under tension and shear increases with increasing chain length and temperature. For a given chain length and temperature, the broken rates under shear are always higher than those under tension at a same large strain. For a given chain length, the tensile and shear stresses decrease with increasing temperature. We propose three typical fracture mechanisms to effectively elucidate the ductile fracture response based on the predominance of chain scission process.

Finally, the influence of polymer wrapped two neighbouring single-walled nanotubes' (SWNTs) dispersion on their load transfer is investigated by MD simulations. The influence of

the SWNTs' position, the polymer chain length and the temperature on the interaction force between the two neighbouring SWNTs are systematically studied. There are four main findings from our simulations: (1) The dispersion angle dominates the amplitude and the interaction force evolution with or without polymer during the pulling process of two SWNTs. (2) The chain length doesn't affect the two SWNTs' interaction force within a short separation distance, the so called "Force enhancing point". The enhanced load effect of the polymer takes place after the load displacement goes across this point. (3) The temperature has a minor influence on the maximum pull force, while the increased temperature greatly decreases the pullout energy. (4) Based on the detailed analysis of the separation process, the self-repairing function of the system is found.

9.2 Recommendations for future work

The CG potentials for multi-walled carbon nanotubes (MWCNTs) will be done soon. The mechanical properties and thermal conductivity of CNT networks dependence on CNT length, crosslink density and temperature will be done by MD simulations in the recent future. The mechanical properties and failure behavior as well as the thermal conductivity of amorphous polymers dependence on chain length and crosslink density will be done by MD simulations in the future. The mechanical and thermal properties of CNT and graphene based polymer nanocomposites could be done in the future. The quantitative fracture behavior of amorphous polymers could be accomplished by full atom MD simulations in the future, which is very important to the subsequent finite element method modeling the macroscale fracture behavior of the polymers.

Furthermore, the mechanical and physical functional CNTs with polymers are a potential study field in the future. The mechanical and physical CNT reinforced polymers composites could be also done in the future since they are important potential applications.